JOURNAL OF TELECOMMUNICATIONS AND INFORMATION TECHNOLOGY

2/2018

(Contents Continued on Back Cover)

ISSN 1509-4553 on-line: ISSN 1899-8852

Circulation: 300 copies Sowa – Druk na życzenie, www.sowadruk.pl, tel. 22 431-81-40

Ministry of Science and Higher Education
Republic of Poland

Improvement of language quality; Assigning DOIs; Subscription to the plagiarism detection system – tasks financed under 556/P-DUN/2017 agreement from the budget of the Ministry of Science and Higher Education under the science dissemination fund.

JOURNAL OF TELECOMMUNICATIONS AND INFORMATION TECHNOLOGY

Preface

Telecommunications is a vast field of technology and science. Considering only its technical aspects, it cover areas such as, *inter alia*, signal processing, transmission, or network commutation. What is more, telecommunications also includes various types of services. This diversity is visible in the subject matter of articles published in this issue. Eight papers of the *Journal of Telecommunications and Information Technology* are dedicated to the services, and more specifically to the quality of the telecom services.

Every year, in each issue, we devote a lot of attention to these issues. It's no different this time because in the current issue of the magazine, two articles are related to the quality of video signals. The first of them by Christian Hoppe and Tadeus Uhl deals with the using DASH techniques to transmit video signals via IP networks. The second paper presents a newly designed stereoscopic video quality metrics and was written by Grzegorz Wilczewski.

Two papers share the subject of voice signals, namely the paper titled *Model-Based Method for Acoustic Echo Cancelation and Near-End Speaker Extraction: Non-negative Matrix Factorization* by Pallavi Agrawal and Madhu Shandilya, and *Genetic Algorithm for Combined Speaker and Speech Recognition using Deep Neural Networks* by Gurpreet Kaur, Mohit Srivastava, and Amod Kumar.

The four following articles also touch QoS in the area of mobile networks: *Link Quality Assessment Algorithm for Heterogeneous Self-organizing Maritime Communications Network* by Krzysztof Bronk, Adam Lipka, and Rafał Niski, *Comparative Analysis of QoS Management and Technical Requirements in 3GPP Standards for Cellular IoT Technologies* by Valery Tikhvinskiy, Grigory Bochechka, Andrey Gryazev, and Altay Aitmagambetov. The third one is *Measurements and Statistical Analysis for Assessment of Availability of Mobile Network Services* by Grażyna Kadamus and Małgorzata Langer. The last paper from this group written by Szabolcs Szilágyi, Ferenc Fejes, Róbert Katona is dedicated to a compression of the MPT-GRE software and MPTCP protocol in the Fast Ethernet. The authors compare the path aggregation capabilities of these two technologies.

This issue of the magazine is complemented by five interesting articles about other topic, yet all of them are closely related to the propagation of radio waves. P. Vimala and G. Yamuna propose a new pilot search algorithm and elaborate on it. Their article is titled: *Pilot Design for Sparse Channel Estimation in Orthogonal Frequency Division Multiplexing Systems*.

In turn, in the article entitled *An Optimized Propagation Model based on Measurement Data for Indoor Environments* by Marco Morocho-Yaguana, Patricia Ludeña-González, Francisco Sandoval, Betty Poma-Vélez, and Alexandra Erreyes-Dota the authors present a new model of adjusting the loss coefficients based on empirical data. Also, the paper written by Alessandro Calcaterra, Fabrizio Frezza, Patrizio Simeoni, and Nicola Tedeschi relates to electromagnetic waves propagation. This paper is titled: *Numerical Evaluation of Electromagnetic-wave Penetration at Normal Incidence Through an Inhomogeneous-wave Approach*.

The title of the next article: *Minimum Array Elements for Resolution of Several Direction of Arrival Estimation Methods in Various Noise-Level Environments* by Ismail El Ouargui, Said Safi, and Miloud Frikel is not very closely related to the radio transmission; however, the issues presented in it are also applicable in radio communications.

Artur Maździarz is the author of the paper titled *Alarm Correlation in Mobile Telecommunications Networks based on k-means Cluster Analysis Method*. This paper deals with very important issues from the point of view of maintaining mobile networks.

I hope that the specialist will find these papers interesting and worthwhile their attention. I wish you pleasant reading experience.

Sławomir Kula
Guest Editor

https://doi.org/10.26636/jtit.2018.preface2

Paper

Video Streaming over IP using the DASH Technique

Christian Hoppe[1] and Tadeus Uhl[2]

[1] *Nextragen Solutions GmbH Flensburg, Handewitt, Germany*
[2] *Maritime University of Szczecin, Szczecin, Poland*

https://doi.org/10.26636/jtit.2018.125318

Abstract—Modern Internet serves as a high-performance platform for an ever-increasing number of services. Some of them – video services in particular – are of the broadband variety. So, it is not surprising that segments of networks can rapidly become congested, which may lead to a deterioration in quality. It is hoped that the new MPEG-DASH technique will alleviate congestion. This paper contains an analysis of the new technology's impact on the quality of service in IP networks. It also explains a new numerical tool QoSCalc(DASH) that has been used to analyze the DASH method in different scenarios. The results are presented graphically and interpreted.

Keywords—H.265, IP network technology, MPEG-DASH, QoS measurement techniques, QoS measurement environment, video streaming, VP9.

1. Introduction

There is currently no better communication technology available than IP. It is extremely flexible and has been implemented worldwide. The modern Internet of Things (IoT) concept is also based on IP technology. The number of applications is growing rapidly, with video applications especially on the increase recently. It is common knowledge that video services are extremely resource consuming. So, congestion will occur rapidly in certain segments of the Internet. Packet losses, end-to-end delays and jitter are the inevitable consequences. They will be reflected by a rapid deterioration in service quality, and customer satisfaction will plummet. New techniques will have to be adopted to address the situation. One such new technique is the MPEG-DASH method (Dynamic Adaptive Streaming over HTTP), that was standardized in 2012 as ISO/IEC 23009-1:2012 [1]. What effects does it have on QoS in IP networks? The work described in this paper aimed to find an answer to that question.

In general, two models are used to determine the quality of service/quality of experience (QoS/QoE) in a network: the dual-ended model and the single-ended model [2]. In the case of the dual-ended model, two signals are used: the original signal and the degraded signal. These two signals are available uncompressed. For this reason, measurements can be carried out for both QoE (a subjective evaluation) and Quality of Service (an objective evaluation). In the case of the single-ended model, only the impaired signal (compressed) is available. This allows only an objective evaluation of QoS to be made.

The most widely used QoE measurement techniques for video services over IP (VSoIP) are currently PEVQ (J.247) [3] and VQuad-HD (J.341) [4]. These techniques are very accurate. They are, however, time-consuming and can often only be implemented with a license. Both algorithms incorporate an emulation of the human eye, and so, one can justifiably speak of QoE values here. It is also the reason why these QoE methods were chosen for the analyses described in this paper.

This paper begins with a brief explanation of the MPEG-DASH technique. It then goes on to introduce a new numerical tool to analyze the DASH method. The analysis scenarios are then described. The results obtained are presented graphically and interpreted. The paper concludes with a summary and an outlook on future work.

2. How Does MPEG-DASH Work?

Dynamic Adaptive Streaming over HTTP (DASH), also known as MPEG-DASH, is an adaptive bitrate streaming technique that enables high-quality streaming of media content over the Internet hosted by conventional HTTP web servers. Like Apple's HTTP Live Streaming (HLS) solution, MPEG-DASH works by breaking the content into a sequence of small HTTP-based file segments, each segment containing a short interval of playback time of content that is potentially many hours in duration, such as a movie or a live broadcast of a sports event. The content is made available at a variety of different bitrates, i.e. alternative segments encoded at different bitrates covering aligned short intervals of playback time. While the content is being played back by an MPEG-DASH client, the client automatically selects, from the alternatives, the next segment to download and play based on current network conditions. The client selects the segment with the highest bitrate possible that can be downloaded in time for playback without causing stalls or re-buffering events in the playback. Thus, an MPEG-DASH client can seamlessly adapt to changing network conditions and can provide high-quality playback with fewer stalls or re-buffering events.

MPEG-DASH is the first adaptive bitrate HTTP-based streaming solution to become an international standard. MPEG-DASH should not be confused with a transport protocol - the transport protocol that MPEG-DASH uses is TCP. MPEG-DASH uses existing HTTP web server infrastructure that is used for delivery of essentially all online content. It allows devices such as Internet-connected TVs, set-top boxes, personal computers, smartphones, tablets, etc., to consume multimedia content (video, TV, radio, etc.) delivered via the Internet, coping with variable Internet receiving conditions. Standardizing an adaptive streaming solution was intended to promote confidence on the market that the solution can be adopted for universal deployment, compared to similar but proprietary solutions such as Microsoft Smooth Streaming, or Adobe HDS. DASH is codec-agnostic, which means it can use content encoded with any coding format, e.g. H.264, H.265, VP9 [5].

3. A New Tool QoSCalc(DASH)

The QoSCalc(IPTV) tool described in a previous paper [6] can take a reference video and encode it with a specified codec and different parameters. Afterwards, it can apply impairments in the form of packet loss and compare the resulting video with the reference. This tool serves as a basis for analyzing MPEG-DASH. However, MPEG-DASH introduces the need to change the workflow of the measurements as more than one format to encode is used.

The most significant changes to the tool QoSCalc(DASH) is the need to encode the reference video in different formats and to make sure that such encoded videos can be seamlessly switched by MPEG-DASH. That is why the configuration is split into multiple groups. When the measurements have been made, all group options are recombined. The settings for the reference video and the parameters have not changed much beyond the additional possibility of selecting multiple settings (see Fig. 1). The order of the encoding parameters is important for a later step in the measurement process. Figure 1 also shows the encoding settings.

The biggest change to the former tool becomes apparent when MPEG-DASH is enabled (see Fig. 2). First, analyzing MPEG-DASH requires multiple changes of the selected format over time, which is difficult to achieve on a short reference signal (e.g. 8 s). That is why the reference signal is first looped a selectable number of times to increase its duration. Afterwards, the tool encodes the reference video with different sets of parameters set in the tool (indicated in Fig. 1). With different qualities of encoded videos an additional option is required, which tells the tool how and when to change the selected video format during the measurement. Four options are available for the format selection and the order in which the encoding options are added is important:

- steps (deterministic) – the encoding formats are selected in the sequence in which they were added,

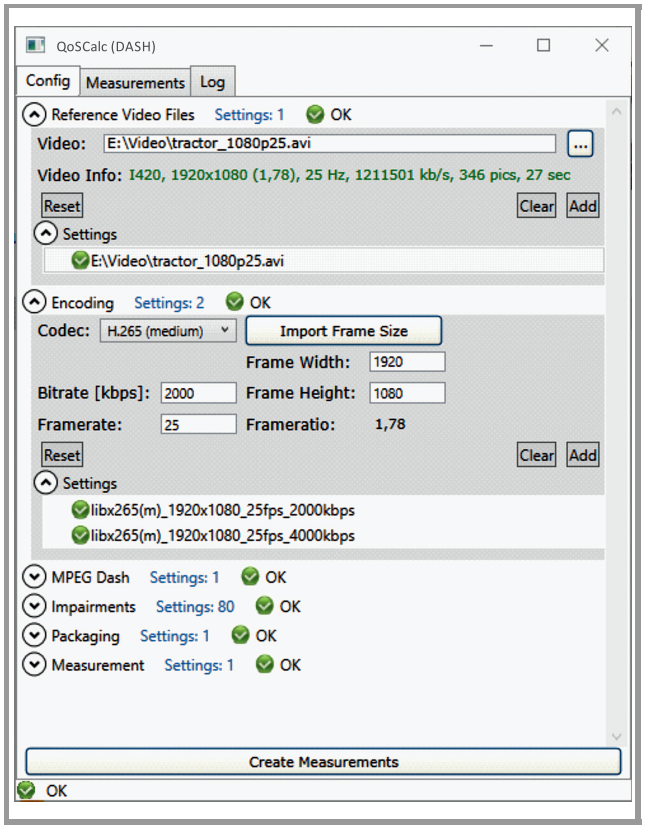

Fig. 1. Reference video and encoding settings for the QoSCalc(DASH) tool.

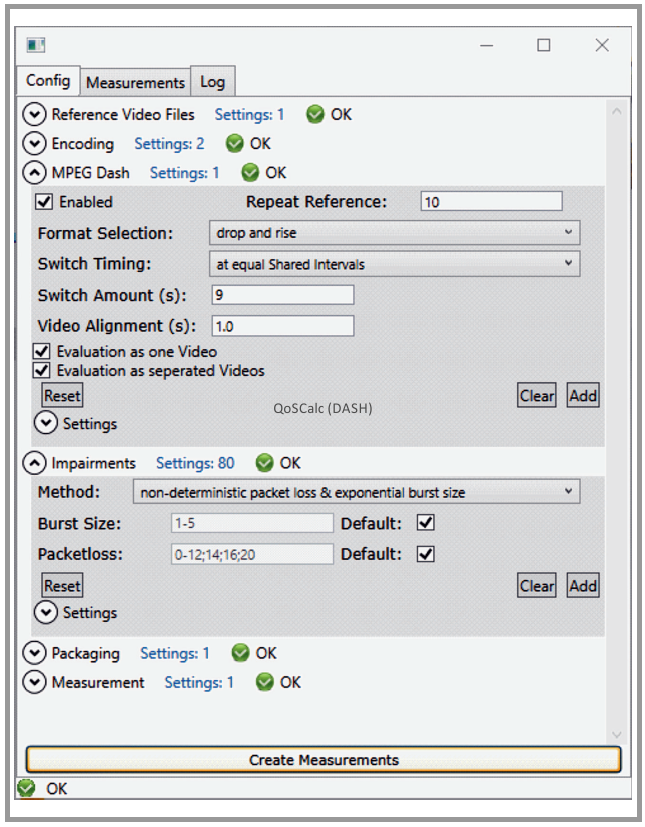

Fig. 2. MPEG-DASH and impairments settings for the QoSCalc(DASH) tool.

starting from the top again after the last has been reached,

- non-deterministic – the encoding format is selected randomly,
- drop and rise – the encoding formats are selected by using the first setting to the last and then in reverse order,
- rise and drop – opposite to drop and rise by selecting the last to the first and then back down again from the first to the last.

Selecting one of the following three settings determines when the format changes will occur:

- at reference boundary – this will change the format whenever the reference video is repeated (looped),
- at equally spaced intervals – the total length of the video is split in equally sized sequences determined by the number of changes set,
- at non-deterministic intervals – a selected number of changes are distributed randomly over the total time of the measurement (equal distribution).

To accomplish a seamless switch between formats the I-frames have to be available in each format at the same moment in time (frame). FFmpeg [7] as the underlying codec library can be told to force an I-frame at constant intervals, programmable in the new configuration window in the video alignment setting. Finally, there is the option in the MPEG-DASH settings with which to select whether the video should be evaluated as one video or each sequence individually or both.

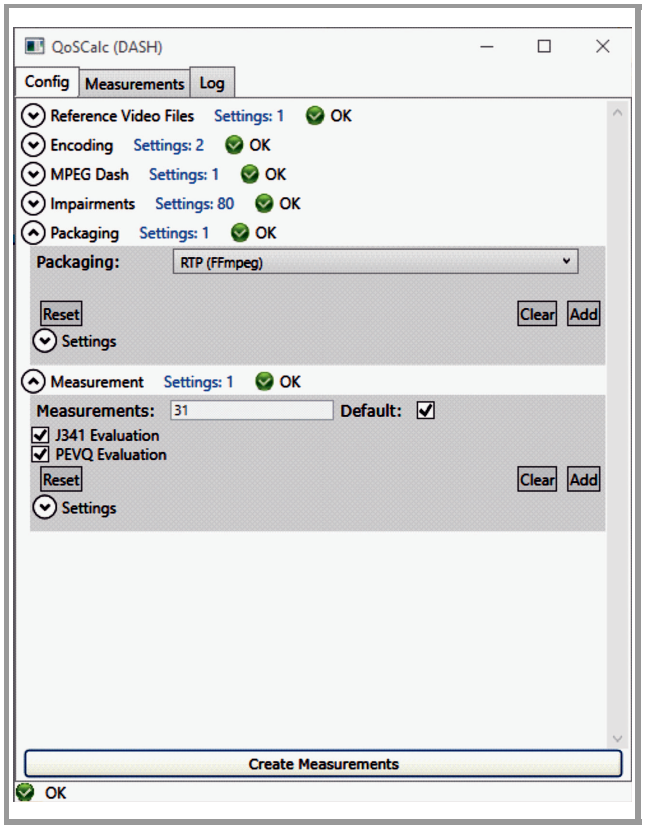

Fig. 3. Packaging and measurement settings for the QoSCalc(DASH) tool.

The next group of settings has also changed slightly. Different impairment methods can be selected which determine how packet loss is distributed. The distribution is a function of the selected burst and packet loss values and is applied to each packet of the video stream:

- deterministic packet loss and constant burst size,
- non-deterministic packet loss and constant burst size,
- non-deterministic packet loss and exponential burst size,
- 2-state Markov loss model/BurstR [8].

The packaging options have changed slightly, the three options being MPEG2-TS, RTP and native RTP. The last option provides an additional setting for the selection of the NAL size of each packet. Finally, in the group "measurement" a method can be selected with which to evaluate each measurement and how often each measurement is repeated to gain statistically relevant data (see Fig. 3).

4. Measurement Scenarios and Measurement Results

For the first measurements for MPEG-DASH, four slightly different scenarios are analyzed. To make them comparable, some common settings are applied to all scenarios. First, the same reference video from previous papers was used and repeated nine times to give adequately long segments to use five different encoding formats in each scenario in a drop and rise pattern. Drop and rise was selected as it simulates a temporary problem in a video stream in which the quality is first reduced and then increased again. In all scenarios the video was packaged in native RTP with a NAL size of 1500 bytes. An overview of the four scenarios is shown in Table 1.

Table 1
Measurement scenarios

Scenario	Codec	Resolution	Bitrate
1	H.265	Constant	Variable
2	H.265	Variable	
3	VP9	Constant	
4	VP9	Variable	

Scenarios 2 and 4 use five different resolutions and bitrate combinations which are common in popular web services (see Table 2).

Scenario 1

H.265 codec and constant resolution and variable bitrate were used. All encoding parameters except the bitrate remain unchanged for the different formats. The results are shown in Figs. 4 and 5.

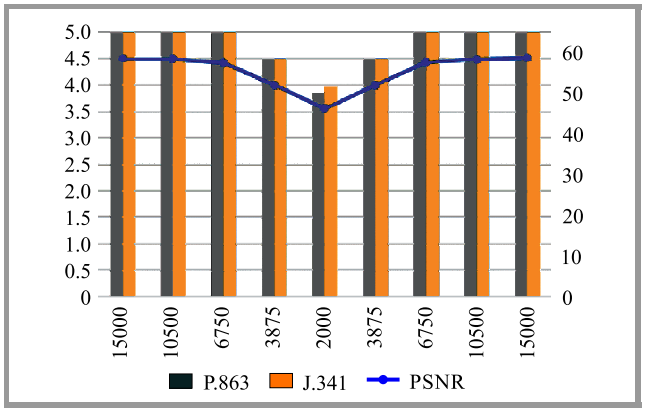

Fig. 4. QoE values as a function of coding rate for Scenario 1 at 0% packet loss.

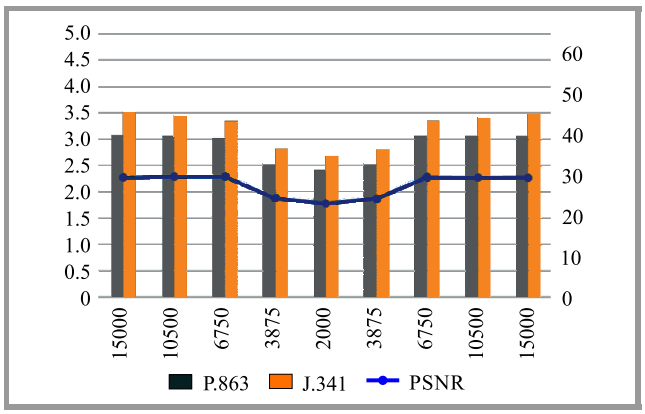

Fig. 5. QoE values as a function of coding rate for Scenario 1 at 1% packet loss.

As expected, with the decreasing bitrate, the quality of the video service decreases. Packet losses have a large impact on video quality. It is remarkable that even a low packet loss of approximately 1% has such a great influence on QoE. This behavior is also clearly shown by the PSNR curves. It is evident that there is a strong correlation between QoE values and PSNR values.

Scenario 2

H.265 codec and variable resolution as well as variable bitrate were used. In this scenario the resolution is changed along with the bitrate. The format details were shown in Table 2. The results are shown in Figs. 6 and 7.

The changes in resolution and bitrate result in a more balanced quality of the video service. Thus, higher quality can be achieved when packet loss occurs by simply changing the bitrate. It is also worth mentioning the strong correlation between QoE values and PSNR values. Additionally, the bandwidth used in Scenario 2 is significantly smaller than that in Scenario 1. This is of great practical benefit, for it reduces the cost of delivering video services.

Table 2
Encoding formats for variable resolution scenarios

Format	Resolution [pixels]	Bitrate [kbps]
1	1080×1920	4500
2	720×1280	2500
3	480×853	1000
4	360×640	500
5	260×427	300

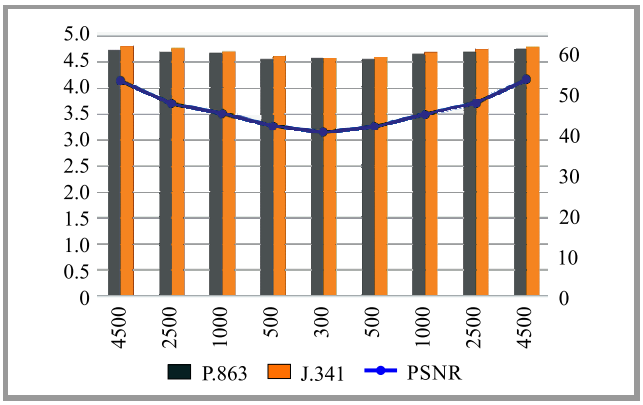

Fig. 6. QoE values as a function of coding rate and resolution for Scenario 2 at 0% packet loss.

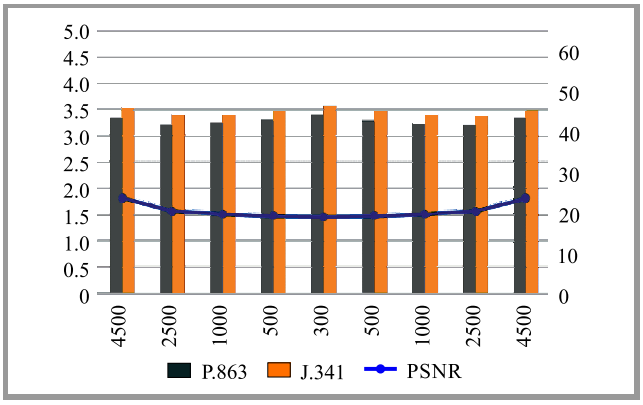

Fig. 7. QoE values versus coding rate and resolution for Scenario 2 at 1% packet loss.

Scenario 3

VP9 codec, constant resolution and variable bitrate were used. All encoding parameters except the bitrate remain the same for the different formats.

Scenario 4

VP9 codec, variable resolution and variable bitrate were used. In this scenario both the resolution and the bitrate were changed.

The results obtained with the VP9 codec in Scenarios 3 and 4 are very similar to the previously discussed results

using H.265. For this reason and for lack of space they are not presented graphically here. One thing is worth mentioning, however. The benefit of using VP9 is that this codec has a higher compression factor in the encoding process [9]. For this reason, a smaller amount of data needs to be transported. Again, this is of considerable benefit.

5. Summary and Outlook

This paper focused on the assessment of the influence of the new MPEG-DASH technique on QoS video streaming over IP. The new technique is flexible and can be implemented to relieve congestion in networks. That can improve the end-to-end QoS. The adaptive bandwidth, that was utilized here, at least ensures image flow even if a deterioration of some of the video sequences is to be expected. That is what makes this technique so strong and is the reason why numerous service providers, such as YouTube, Netflix, Hulu, Twitch, are using it. The analyses conducted during the work described in this paper have shown that it is especially beneficial to use the codec VP9 and to combine the MPEG-DASH technique with changes in image resolution and image coding bitrate.

For the analyses described in this paper the MPEG-DASH technique was used on the RTP transport stream. In practice, however, the technique is most often used in combination with the HTTP protocol. That provides another possibility of transporting video data over networks which further studies will take into consideration. The QoSCalc(DASH) tool will have to be modified first, however, so that it can accommodate the resending of lost video packets. This could be achieved by emulating an HTTP server and an HTTP client in the background of the tool. Further studies in this direction are already being planned.

References

[1] ISO/IEC DIS 23009-1.2, "Dynamic adaptive streaming over HTTP (DASH)" [Online]. Available: https://www.iso.org/standard/57623.html

[2] T. Uhl, "Quality of service everywhere", in *Proc. of the 9th Int. Conf. on Adv. Serv. Comput. Service Computation 2017*, Athens, Greece, 2017, pp. 28–30.

[3] ITU-T J.247 (08/2008), "Objective perceptual multimedia video quality measurement in the presence of a full reference" [Online]. Available: http://www.itu.int/rec/T-REC-J.247-200808-I/ 2017.11.03

[4] ITU-T J.341 (03/2016), "Objective perceptual multimedia video quality measurement of HDTV for digital cable television in the presence of a full reference" [Online]. Available: http://www.itu.int/rec/T-REC-J.341-201101-I/en/2017.11.03

[5] "Dynamic Adaptive Streaming over HTTP" [Online]. Available: https://en.wikipedia.org/wiki/Dynamic_Adaptive_Streaming_over_HTTP/2017.11.03

[6] T. Uhl and H. Jürgensen, "New tool for examining QoS in the IPTV service", in *Proc. of the World Telecom. Congr. WTC'14*, Berlin, Germany, 2014.

[7] "FFmpeg (current Window builds)" [Online]. Available: http://FFmpeg.zeranoe.com/builds/2017.11.03

[8] S. Paulsen, "QoS/QoE-Modelle für den Dienst Voice over IP (VoIP)", Dissertation, University Hamburg, Department of Information Technology, 2016 (in German).

[9] M. Řeřábek and T. Ebrahimi, "Comparison of compression efficiency between HEVC/H.265 and VP9 based on subjective assessments" [Online]. Available: https://infoscience.epfl.ch/record/200925/files/article-vp9-submited-v2.pdf/2017.11.03

Christian Hoppe received his B.Eng. in Communications Technology from the Flensburg University of Applied Sciences, Germany, in 2010 and his M.Sc. in Information Technology from the Kiel University of Applied Science, Germany, in 2016. Today, he works as a Software Engineer for Nextragen Solutions GmbH in Flensburg, Germany. His main activities cover the following areas: quality assurance for Triple Play services and medical imaging solutions.

E-mail: christian.hoppe@nextragen-solutions.de
Nextragen Solutions GmbH Flensburg
Heideland 1
D-24976 Handewitt, Germany

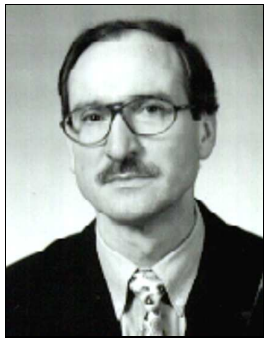

Tadeus Uhl received his M.Sc. in Telecommunications from the Academy of Technology and Agriculture in Bydgoszcz, Poland in 1975, his Ph.D. from Gdańsk University of Technology, Gdańsk, Poland in 1982 and his D.Sc. from University at Dortmund, Germany in 1990. Since 1992 he has worked as Professor at the Institute of Communications Technology, Flensburg University of Applied Sciences, Germany and, in addition, since 2013, as Professor at the Institute of Transport Engineering and Economics, Maritime University of Szczecin, Poland. His main activities cover the following areas: traffic engineering, performance analysis of communications systems, measurement and evaluation of communication protocols, QoS and QoE by Triple Play services, Ethernet and IP technology. He is an author or co-author of five books and 130 papers on the subjects of LAN, WAN and NGN.

E-mail: t.uhl@am.szczecin.pl
Maritime University of Szczecin
Henryka Pobożnego 11
70-507 Szczecin, Poland

Paper

Stereoscopic 3DTV Video Quality Metric: the Compressed Average Image Intensity

Grzegorz Wilczewski

Institute of Telecommunications, Faculty of Electronics and Information Technology, Warsaw University of Technology, Warsaw, Poland

https://doi.org/10.26636/jtit.2018.122917

Abstract— This paper presents a newly designed stereoscopic video quality metric. Overall insights towards the creation of mechanisms utilized within the genuine metric are presented herein. Delivery of the core information and motivation behind the features implemented, as well as functionality of the Compressed Average Image Intensity (CAII) quality metric are of utmost importance. The mechanisms created might be characterized as an objective, reliable and versatile quality evaluation tool for advanced analysis of the content delivery chain within stereoscopic video services.

Keywords—3D image analysis, image impairments, stereoscopy, video quality.

1. Introduction

The ever-improving performance of newly deployed multimedia content distribution networks enables customizable configuration of the end-to-end connectivity that offers even more control over the quality of the content delivered to the end-user. However, with the revenues generated by telecommunications services assigned a high priority, the last mile phenomenon implies specific behaviors concerning the content delivery scheme. Limitations regarding the available unicast bandwidth dedicated for a single user determines the overall quality over the path from the originating server towards the client's device. The study presented in [1] shows the predicted volumes of dedicated IP traffic or network capabilities required to support video-like services deployed. The fact that figures for such an application reveal an enormous rise in 3DTV and Ultra High Definition (UHD) availability (or IP traffic share) that is proclaimed to reach over 20% of the total, annual, global video IP traffic by the year 2020, may be very motivating. As a derivative of dynamic bandwidth and network management schemes, more and more multimedia services are deployed nowadays relying on adaptive bitrate streaming mechanisms, competing with different approaches, such as HTTP Live Streaming (HLS) or Motion Pictures Experts Group – Dynamic Adaptive Streaming over HTTP (MPEG-DASH) [2]. Introduction of such streaming technology mechanics implies multiple quality measurement-related considerations. From partitioning of content offered into appropriate video chunks that influence buffer saturation behavior, to stream zapping times whenever network dynamics imply a quality-wise switchover (i.e. from 1080p to 720p resolution and respective bitrate reduction), to quality restoration of the adaptive video stream whenever an updated client's manifest file is received – the overall mechanics of the quality measurement tool has to be properly designed to support reliable and codec-agnostic video analysis.

In order to prepare and implement such quality metric mechanics, it is crucial to employ appropriate evaluation of functionalities and inherent characteristics of the designed solution. As it is presented across [3], [4], assessment of basic components of the multimedia delivery chain, in terms of perceptual quality indicators within the stereoscopic 3DTV services, enables to create a cross-platform, responsive and versatile in terms of computational complexity, serving as a quality indicator for 3D, stereoscopic content. In the following sections, a detailed presentation of the objective quality metric mechanisms designed is given, along with examples of results from the CAII testing campaign.

2. Quality of 3DTV Service

Knowing the complexity of the stereoscopic content processing chain within the 3DTV service, one can analyze the problem of constructing the quality evaluation metric. Whenever key processes within such a system of service delivery are investigated, the understanding of quality factors enables to deliver a compound set of parameters and their behaviors to define how to derive and reason a coherent approach towards effective and reliable metric design. Presented in a graphical, tabular form in Fig. 1 are the fundamental elements representing crucial stages of the stereoscopic content processing flow.

As one may see, the overall composition of the quality evaluation scheme might be categorized into four baseline axes, as depicted in Fig. 1, and creates a complete definition of the phenomena defined for the stereoscopic content

Stereoscopic content processing chain within 3DTV service			
Content providers	Video service frame	Networking layer	Clients terminals
Acquisition: • stereoscopic 3D (SbS, L + R) • multi-camera rig • 2D + depth Creation (RAW): • dual stream • MVC	Asset management: • transcoding • stream forming • digital rights management • network-native encapsulation	Delivery: • push/download • streaming • adaptive streaming • unicast/multicast • single/multi stream	Reception: • decoding • filtering • display • environment clutter

Fig. 1. Anchor points in the evaluation of stereoscopic 3DTV content quality.

processing domain. Every single pillar of the positioning presented implies certain modifications of or updates to the processing scheme whenever end-to-end behavior of a 3DTV service is investigated or related to. Therefore, cross-investigation of the in-between relations is crucial in order to deliver an appropriate modeling approach towards quality definition within such a service.

2.1. Content Providers

The aforementioned core axes of the stereoscopic 3DTV service quality plane are as follows: content provider's side, video service frame, networking layer part, client's terminal zone. To start with, let one perform an evaluation of the content provider's side with respect to content manipulation flow. In this area, the greatest importance might be assigned to the process of acquiring stereoscopic visual data. At that point, the initial forming and shaping of quality, or further – the final quality of experience [5] of the actual video takes place. Thus, enabling possibly the highest, richest and undistorted imaging of the composition or logical scene is necessary.

To quantify the range of elements impacting the quality of the content acquisition stage, one may employ the following set of variables determining the overall quality-varying factors:

- formatting of stereoscopic pair (in a side-by-side composition or continuous left-and-right imaging) implies the overall resolution of the image, whenever the pixel stacking approach is available (i.e. limitation in vertical representation or capabilities in frame compression, given by selected standard of targeted format);

- discrepancies in the physical build of lenses and sensors used, causing deteriorating effects, such as fringing, vignetting, aspherical distortions and flaring alongside the sensors' dynamic range of captured luminance scale, sub-sampling of color space and noise footprint whenever a low light situation is captured.

Another aspect of multi-rig camera stacking involves pairing and synchronization of visual cue cameras used. However, there is still a vast range of stream reassembling methods that make it possible to achieve the desired result at the post production stage of content creation. Next, in the latter case of creation stage in the content provider's pillar, the forming part of the resulting video stream is kept. Delivering video content implies a certain composition of stereoscopic data streams. Therefore, several approaches exist towards assembling (and coding) the general video queue. The most frequently used ones are Multi-view Video Coding (MVC) [6] and dual stream aggregation. Both of the aforementioned approaches implement temporal and spatial image sampling (i.e. master-stream and slave-residual channel), thus guaranteeing a strong compression ratio and relatively direct investigation possibilities during video stream analysis.

2.2. Video Service Frame

The next stage of the stereoscopic content propagation chain is the video service frame axis. Here, the content is altered and manipulated in a number of manners, especially related to transcoding aspects of video stream compression. Management of 3DTV assets is closely connected with the type of media distribution or delivery relied upon. Thus, the main aim of the video service frame is to deliver a network native set of video streams. The asset management block is responsible for the creation of independent, quality-scaled stereoscopic video content to meet various adaptive streaming techniques (i.e. stream forming).

At this stage, the highest factor or compression ratio is observed, as the regular, straight-render movie assets are transcoded into low-weight multimedia files. In addition to this procedure, a complementary file, also referred to as a manifest file, is created. It contains a certain playlist-like network-native addressing scheme of where to find appropriate streams, or – in more sophisticated streaming systems – the list of chunk locations for network distribution. It may be also observed that such partitioning of the

original video stream might be based upon actual network congestion parameters, upon the reported workload of the certain network node or upon the given computing core (especially in modern day implementations of distributed cloud streaming services [7]). As for the consecutive activities, the Video Service Frame stands also for the digital rights management application. There, the appropriate certification and digital signing of video content is delivered, offering the final customer the selected media access methods (i.e. temporal, cyclic, per view, etc.).

2.3. Networking Layer

In the case of the third pillar of the stereoscopic 3DTV service core, namely the networking layer, as it was previously mentioned, whenever a certain approach towards media transmission is selected, appropriate mechanisms towards delivery technique are chosen. To support inherent functionalities of the transport mechanisms available, like the download/push technique or, more contemporarily, convenient streaming approaches, the difference in network-native phenomena determines the behavior of the selected mechanism and, as follows, its imminent impact upon the quality of distributed content. For instance, in the basic delivery scheme of a plain 3DTV video streaming service, one can enumerate four basic network phenomena causing instant QoE deterioration, specifically: bandwidth limitation, jitter, packet delay and stream synchronization.
Depending on the form of the buffer implemented, dropping packets in a form of bandwidth limitation may cause an influent multimedia playback, stuttering of an image or, if adaptive streaming is concerned, switchover to a lower bandwidth video stream.
In the case of the jitter phenomenon, whenever fluctuation in the ordering of a packet stream is observed, some plain mechanisms may not recover from rearrangements in the delivered data package, thus leading to discrepancies in the decoded video stream.
As far as the third and fourth of the aforementioned network phenomena are considered, the overall problem generated by their existence is the inability to synchronize the playback with the actual timing of the video stream data. Packet delay causes a vast buffer drainage, which implies either single stream corruption (i.e. only audio data) or more likely stereoscopic (i.e. MVC stream composite) video data line discontinuity [8]. Such phenomena might be concealed with encapsulated or expanded transport protocols that allow to reorder or recover packet arrangement with an appropriate stream synchronization, in order to avoid data discarding whenever the logical structure of the movie being played back is outdated (in fact, receiving video data afterwards its scheduled display timing makes the playback routine irrelevant).

2.4. Client's Terminal

The last, fourth axis of the stereoscopic content chain delivery scheme depicted on the graphical representation in Fig. 1 discovers the service customer domain. In that area there exist several aspects defining the final, overall quality of stereoscopic video content. To start with, the decoding process is a crucial and most important stage. Based on the data received throughout the previous axes of the content propagation scheme, whenever the logical structure of the content is incoherent, appropriate decomposition of the video stream is inaccessible. Thus, the QoE is not proclaimed, and the visual, perceptual outcome of the service is also limited [9]. In terms of further, quality impacting features, apart from the decoding process, the displaying technique and the accompanying stereovision filtering type generate complexity in recovering the originally captured scene. However, those two processes are mainly interfered by environmental clutter which is strictly dependent on the hardware setup used or the display technology itself.

2.5. Quality Evaluation

Having defined the pivot points of the quality domain within the stereoscopic content distribution chain, the consecutive step is to focus on the aspects of monitoring or evaluation of the quality of content, especially the one being perceived at the user's end. Basic organization of the quality evaluation domain is defined, with respect to video services, based on the following areas: objective quality metrics, subjective quality measurements and reference-type metrics, where a certain set of inherent parameters is considered, i.e. full reference information, reduced/limited or no-reference models where quality is evaluated strictly over the decoded stream outcome.
In the first video quality assessment method, the emphasis is placed on the reliability of measurement procedures and their outcome, their responsiveness and reproducibility or repeatability. The objective approach is widely acclaimed and highly demanded whenever digital video services are to be benchmarked, in terms of the quality offered. Nonetheless, the domain of the objective quality metrics, especially with respect to 3DTV, stereoscopic content, is barely initialized. As presented by the International Telecommunication Union (ITU) and its J-series recommendation found in [10], the domain is still under development. Proposals concerned with construction of the objective quality metric are funneled into a trilateral model of quality evaluation fundamentals.
The first one spans the analysis of actual, decoded image and pixel information conveyed alongside, i.e. image structure, optical composition, blurriness, etc. The next one is based upon network abstraction layer analysis, mainly in a form of packet investigation (so called bit-stream methodology). The third approach defines coding parameters as the basis for quality evaluation, thus the internal analysis of the codec configuration stream is assessed. Therefore, as one can observe, an objective methodology of video quality evaluation scheme delivers multiple resourceful indicators that can precisely and independently describe the actual quality of the stereoscopic, 3DTV content service rendered.

As far as subjective methodologies utilized for evaluation of quality within stereoscopic video services are concerned, a trending approach exists leaning towards objective methodologies. However, there is still a strong movement towards subjective judging regimes. Foremost, the undeniably requested feature of this kind is to evaluate quality of the perceived content with respect to the Human Visual System (HVS). That feature offers additional advantages of the subjective quality evaluation approach, namely delivers the measurement results in a conformed layout of Mean Opinion Score (MOS). Therefore, it is recognized in international academic research (for instance in [11]) as well as in the standardization activities of the ITU-R [12]. The vast workload presented in the aforementioned publications reveals the complexity of evaluation of the subjective quality of stereoscopic 3DTV content, involving appropriate procedures accompanying the standardization workflow. Nonetheless, in recent works presented in [13], there exists a strong aim to deliver a reasonable, reliable and effective methodology for the subjective metrics. Its outcome might greatly improve not only the subjective methodology domain, but may also expand the common field for comparative and benchmarking routines concerned with objective quality metrics.

3. CAII Metric

This section delivers insights towards the designed, genuine Compressed Average Image Intensity (CAII) metric. As the theoretical and engineering aspects of the quality metric creation were discussed in previous sections of the article, the aim of the design process was to implement an objective methodology scheme. The analysis performed by the mechanisms deployed is based on the assumptions presented strictly for the purpose of HVS. This implies that perceptive cues of the stereoscopic imagery need to be followed, thus realizing a resourceful algorithmic path – inquiry and analysis of 3D compound pairs of frames under the assumption of luminance stream investigation. Therefore, the criterion of perception of the HVS system, also referred to as the naturalness criterion, is proclaimed and fully supported. Processes that are present when stereoscopic information is perceived and ingested by HVS are based upon the dynamic range of the luma channel. As a result, outcomes produced by the CAII mechanism guarantee a direct representation of the actual perceptive sensitivity of the service's customer, and reflect what the HVS system may portray as a seemingly native image. The detailed algorithmic path of the designed objective quality metric is depicted in the graph presented in Fig. 2.

While analyzing the structure of the core mechanism of the CAII quality metric designed, one can distinguish eight independent but complementary, functional blocks within the processing scheme flow. Another characteristic features of the genuine mechanism might be noticed in Fig. 2, namely its modular, flexible construction and, most importantly, structural complexity minimized to create an independent

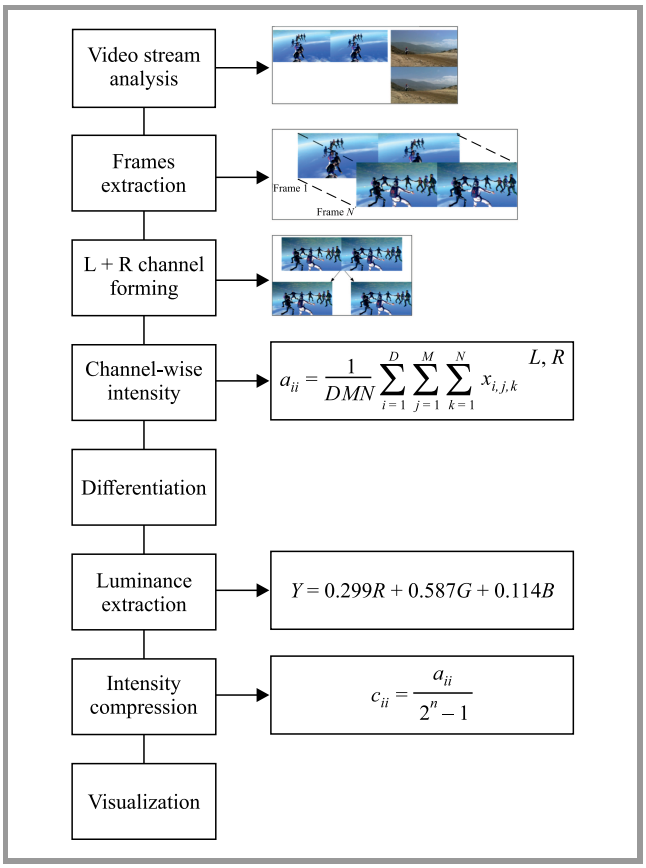

Fig. 2. Layout of the CAII quality metric core mechanism.

measurement tool, performing a quality analysis in spite of various types and formats of the video content injected. To elaborate on the functional blocks of the algorithm, the following list presents insights towards the designed stages of the algorithm:

- **Video stream analysis**: initialization of the algorithmic flow starts with investigation and identification of the ingested video stream parameters. Appropriate structures of information are created here – resolution, frame rate, duration, dynamic range of pixel information and other relevant data is directed into the object determining the further processing path (i.e. vertical or horizontal scanning of a structure).
- **Frames extraction**: this step is based upon the previously recovered information (for instance from the header of the multimedia file) that determines the extraction of the pixel structures of stereoscopic imagery into a selected stream or structure of frames given in a logical (i.e. display) order.
- **Channel forming**: while the unprocessed data structures are created over the previous steps in this particular stage of the algorithm, defined structures of visual cues (delivered for both, left and right HVS sensors) are being formed. Synchronization of such pairs is to be performed to avoid erroneous propagation.

- **Intensity calculation**: as presented in the diagram in Fig. 2, a special formula designed to appropriately calculate the image intensity is being deployed. The whole processing part is performed in the parallel regime, thus computational effectiveness might be achieved.
- **Differentiation**: it is a stage within which a base, residual image is constructed, thus delivering crucial data for the pair-wise disparity analysis. As far as the designed mechanism's workflow is considered, this stage delivers the most important data for further identification and investigation of core quality parameters (by means of the disparity measure) processed to evaluate the overall and actual quality of the decoded image.
- **Luminance extraction**: in this part of the algorithmic approach, image processing is performed by the implementation of the formula for Y parameter (also presented in Fig. 2), applied over the scope of pixel information to regain the luminance envelope of the input signal. A formula is therefore recommended to create a luminosity map of the analyzed pair of stereoscopic images, enabling further utilization of HVS-compatible measures to assess the achievement of the objective quality metric.
- **Intensity compression**: this step is realized in accordance with the set of parameters recovered at the initial stage of the algorithm. With respect to the depth of the pixel information or its dynamic range, appropriate scaling and therefore compression of the information is obtained. That enables to compare different realizations of the same original, logical 3DTV footage whenever its first-grade package is transcoded into a major set of resampled and highly compressed content.
- **Results visualization**: as far as the final stage of the algorithmic path is concerned, its aim is to deliver a graphical representation alongside live plotting of the results of the actual metric performance. Further investigation of the generated outcomes might be achieved by performing a detailed analysis with use of bundled tools available to the user.

To sum up, the insights concerned with the creation and delivery of the objective quality metric mechanism, as presented above, indicate its modular and flexible design. Whenever the need of special adjustments is present, the structural composition of the algorithm enables to set newly determined parameters, therefore meeting the range of features requested. Moreover, thanks to the ability to assess the algorithm presented, using parallel computing and efficient data structures, maximized efficiency may be achieved along with minimized complexity of the data processing performed. Furthermore, in the following sections, an in-depth description of the experimental testing stage and its results related to the CAII metric are presented.

4. Experimental CAII Testing

Deployment of the experimental testing stage for the CAII objective metric designed focused on the investigation of the behavior and responsiveness of the metric in the presence of simulated impairments. In order to prepare such a multipurpose testing scheme, the selected, initial conditions for the testing environment were defined as follows.

To start with, the test-bed of choice was utilizing the programming environment of the widely popular Mathworks Matlab solution (2013a release) installed on a mid-class PC workstation. In terms of the stereoscopic video content selected, a logical scene containing highly dynamic action with dense motion flows was chosen. As far as its technical parameters are concerned, the source video stream was constructed with the use of 152 images on a side-by-side frame stacking and with the display rate of 30 FPS. Furthermore, vertical resolution of the image reached 1080 pixels in a progressive mode, with half resolution within the horizontal orientation of the frame. The bitrate level evaluated was averaging 9 Mbps, while the pixel depth indicated information channel resolution of 8-bit.

Having stated the initial conditions, both for the environment and the content selected, the experimental tests are concerned with the core mechanism of the metric designed. In order to properly investigate its performance and the designed HVS or luminosity responsiveness (which proper objective metric should be characterized by), the next objective was to design an appropriate set of testing routines. The guidelines for synthetic benchmarking assumed following three independent test case scenarios, delivering multiple reactions of the CAII metric. An instant approach was selected: creation of synthetic image impairments, generated on-the-fly, simulating typical stereoscopic image deteriorations within the selected networking scheme.

The aforementioned content delivery approaches clearly state that the contemporarily deployed network solutions are based upon the adaptive streaming technology. Thus, one of the outcomes in the event of a network impairment is to switch the actual video stream over to a lower bitrate or a lower resolution. Therefore, to simulate such a behavior, a desirable approach was to implement the following set of impairments reflecting a real-life scenario of a networking environment:

- Scaling distortion – is realized by a function defined over the bilinear transform (with a set parameter k). It ensures scaling distortion by executing a cyclic action of step-down/step-up image transform. First, the original image is shrinking by a factor of 4 (i.e. $k = 0.25$) and is then scaled up by the same factor. The result is a blurry image, simulating a full screen boost of an 270p image to the 1080p format.
- Gaussian filtering – delivers similar impairment as the previous one, but is realized with use of the 2D filtering functionality, based on the Gaussian fil-

ter with the following parameter set: size $N = 11$ and generator variable $s = 2.0$. The video frame processed is rotationally and symmetrically blurred with the designed filter action. Thus, the image also resembles adaptive streaming impairment.

- Salt-and-pepper impairment – is realized by native, random saturation of pixel levels (in an 8-bit mode, with parameter $d = 0.2$). Therefore, a distortion similar to a pixellate scheme is created. It boosts a randomly selected picture element once it reaches its saturated state, but in one sub-channel (i.e. green component of an image).

All of the abovementioned impairments were morphed into the original video stream. The result of merging those image deteriorations, and the original frame, are presented in Fig. 3. In order to underline the image impairments, a local cropping of the same frame section was performed (Fig. 3).

Presented in Fig. 4 are synchronized test case scenario passes that indicate the behavior of the CAII metric in the presence of specifically designed impairments. The subplots included are constructed in the following manner. Out of the two main parts of each subplot, the section to the left depicts a stack of three frames representing the actual left and right channels, and the bottom one states the resid-

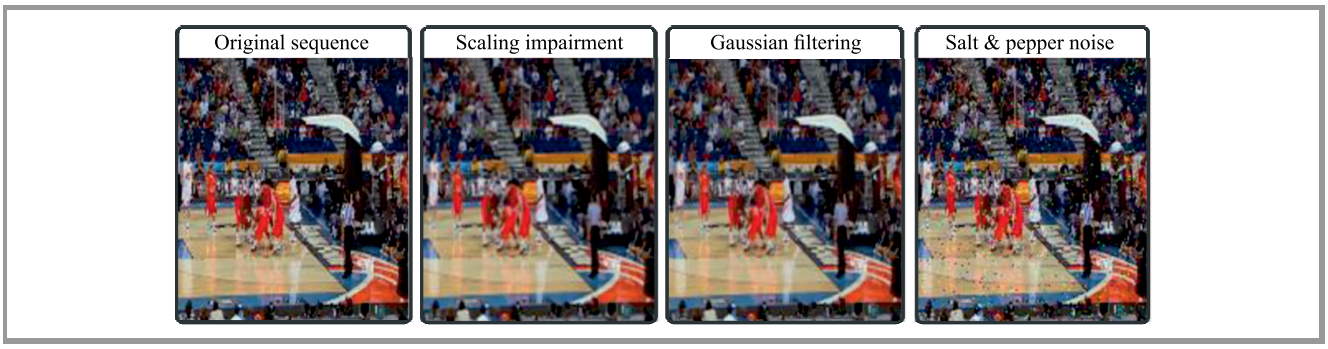

Fig. 3. Experimental impairments injection over the original image.

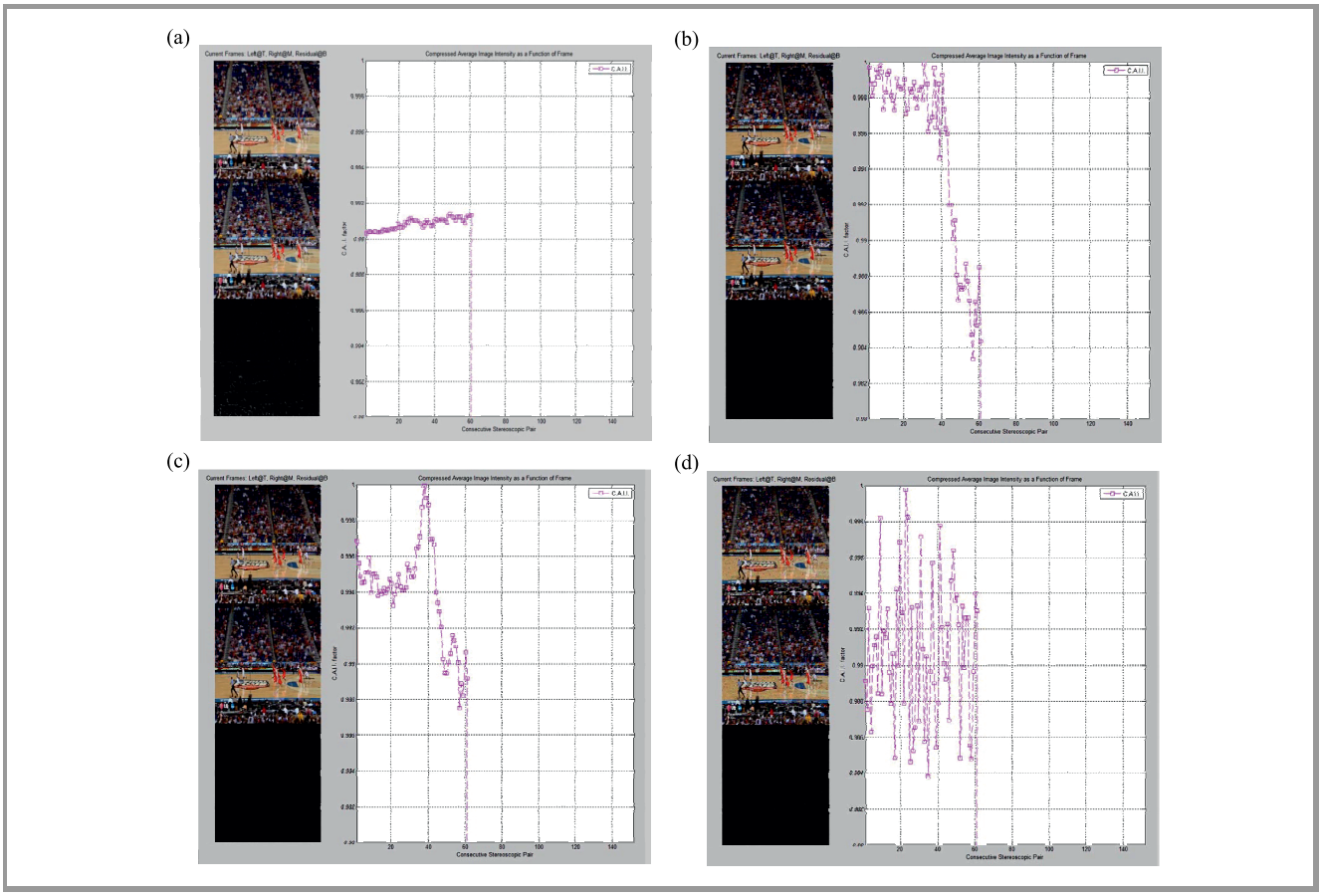

Fig. 4. Visualization of the results of the benchmarking routines to test the CAII quality metric.

ual frame (recall contents of the schematic diagram from Fig. 2). To the right of that stack is the synchronized, updated graph of the CAII metric plot indicating the present quality factor level.

Considering the experimental results obtained, as shown in the compound representation in Fig. 4 (partitions a–d) the CAII metric might be successfully stated to be a selective network probe, as it has identified video distortions amongst the infected structures of stereoscopic frames. The performance of the CAII mechanism shall be further characterized by its capability of indicating specific distortions (i.e. scaling outcomes against salt-and-pepper impairment). Fig. 4a reveals the reference, undistorted playback, which in fact is characterized by a steadily plotted line revealing the image of the stereoscopic pair is of the original quality. What is more, in Fig. 4b, at the exact, synchronized frame order, but imposed with the scaling impairment, the plotted characteristic shows the deterioration in video quality. The disrupted imagery (as depicted in Fig. 3) results in CAII metric value instability. Therefore, one can infer that fluent playback of an undistorted video cannot be achieved. Followed by the results shown in Fig. 4c, the Gaussian filtering process generates similar plots as the one with the scaling procedure invoked. Such a similarity in behavior might be based upon the effective algorithms used to simulate certain impairments, and in this particular case, it is due to the blurring effect procedures (comparable outcomes in the form of plotted graphs reveal similar distortions being generated). In terms of the last section, Fig. 4d, the oscillating plot line reflects the nature of the salt-and-pepper image distortion – clearly visible randomness. Analysis of the behavior of the plotted graphs might deliver multiple parameters, in the form of delivered information and overall characteristics, crucial for identification of the image distortion introduced; it enables the users of the designed tool to classify the impairment by means of the figure observed.

5. Conclusions

Insights towards the following stages: design, implementation, deployment and testing of the CAII metric revealed its effectiveness and reliability as an objective quality measure. The depicted mechanics perform accordingly to the HVS requirements, presenting perceptive quality aspects in parallel with responsiveness and multiple utilization aspects the CAII is capable of. To mention a few applications, it can be utilized as a network probe, as a system performance benchmarking routine and, most importantly, it might assess picture parameters concerning the luminance signal channel. The plotted outcomes deliver a rich set of indicators helpful in recognizing image distortion and identifying the significant deteriorations. Therefore, as far as the overall view of the topic of QoS and QoE is concerned, the genuine CAII designed reveals its comprehensive and versatile performance within stereoscopic 3DTV content distribution systems.

References

[1] Cisco Systems, "Cisco Visual Networking Index: Forecast and Methodology, 2015—2020", Jun 2016 [Online]. Available: http://bit.ly/295yXfL

[2] N. Fimic, S. Tanackovic, J. Kovacevic, and M. Temerinac, "Implementation of Multi-Format Adaptive Streaming Server", in *Proc. 5th IEEE ICCE Berlin Conference*, Berlin, Germany, 2015, pp. 218–220 (doi: 10.1109/ICCE-Berlin.2015.7391239).

[3] G. Wilczewski, "Analysis of Content Quality Evaluation within 3DTV Service Distribution Systems", *J. of Telecommun. and Inform. Technol.*, no. 1, pp. 16–20, 2014.

[4] G. Wilczewski: "An objective method for a video quality evaluation a 3DTV service", *Proc. Symp. on Photonics Applic. in Astr., Commun., and High-Energy Physics Exper. Wilga 2015*, Wilga, Poland, 2015, pp. 231–237 (doi: 10.1117/12.2205197).

[5] D. Minoli, *3DTV Content Capture, Encoding and Transmission*, New York: Wiley, 2010.

[6] A. Vetro, T. Wiegand, and G. J. Sullivan, "Overview of the Stereo and Multiview Video Coding Extensions of the H.264/MPEG-4 AVC Standard", *Proc. of the IEEE*, vol. 99, no. 4, pp. 626–642, 2011 (doi: 10.1109/IPROC.2010.2098830).

[7] G. Wilczewski, R. Mielowski, K. Perlicki, M. Siergiejczyk, and E. Kowalczyk, "Data Center resources monitoring for resilient telecommunication services", *Przegląd Elektrotechniczny*, no. 91, pp. 225–228, 2015 [in Polish] (doi: 10.15199/48.2015.10.47).

[8] T. H. Luan, L. X. Cai, and X. S. Shen, "Impact of Network Dynamics on User's Video Quality: Analytical Framework and QoS Provision", *IEEE Transact. on Multimedia*, vol. 12, no. 1, pp. 64–78, 2010 (doi: 10.1109.TMM.2009.2036294).

[9] R. A. Farrugia and C. J. Debono, "A Hybrid Error Control and Artifact Detection Mechanism for Robust Decoding of H.264/AVC Video Sequences", *IEEE Transact. on Circuits and Systems for Video Technol.*, vol. 20, no. 5, pp. 756–762, 2010 (doi: 10.1109/TCSVT.2010).

[10] "Objective perceptual multimedia video quality measurement of HDTV for digital cable television in the presence of a full reference", ITU-T J.341 Recommendation, 2016.

[11] T. Tian, X. Jiang, and X. Du, "Subjective quality assessment of compressed 3D video", in *Proc. 7th Int. Congress on Image and Signal Proces. CISP*, Dalian, Liaoning, China, 2014, pp. 606–611 (doi: 10.1109/CISP.2014.7003851).

[12] "Methodology for the subjective assessment of the quality of television pictures", ITU-R BT.500-13 Recommendation, 2012.

[13] "Subjective Assessment Methods for 3D Video Quality", ITU-T P.915 Recommendation, 2016.

Grzegorz Wilczewski received his B.Sc. and M.Sc. degrees in electrical and computer engineering from Warsaw University of Technology, Poland, in 2009 and 2011, respectively. He is currently a Ph.D. candidate at Warsaw University of Technology. His research interests include 3DTV service quality monitoring, 3D imagery and digital signal processing.

E-mail: g.wilczewski@tele.pw.edu.pl
Institute of Telecommunications
Faculty of Electronics and Information Technology
Warsaw University of Technology
Nowowiejska 15/19
00-665 Warsaw, Poland

Paper

Model-Based Method for Acoustic Echo Cancelation and Near-End Speaker Extraction: Non-negative Matrix Factorization

Pallavi Agrawal and Madhu Shandilya

Department of Electronics and Communication Engineering,
Maulana Azad National Institute of Technology, Bhopal, India

https://doi.org/10.26636/jtit.2018.122617

Abstract—Rapid escalation of wireless communication and hands-free telephony creates a problem with acoustic echo in full-duplex communication applications. In this paper a simulation of model-based acoustic echo cancelation and near-end speaker extraction using statistical methods relying on non-negative matrix factorization (NMF) is proposed. Acoustic echo cancelation using the NMF algorithm is developed and its implementation is presented, along with all positive, real time elements and factorization techniques. Experimental results are compared against the widely used existing adaptive algorithms which have a disadvantage in terms of long impulse response, increased computational load and wrong convergence due to change in near-end enclosure. All these shortcomings have been eliminated in the statistical method of NMF that reduces echo and enhances audio signal processing.

Keywords—adaptive algorithms, convergence, echo cancelation, non-negative matrix factorization (NMF).

1. Introduction

In the era of wireless communication, widespread use of hands-free telephony has been observed. This results in disturbances from acoustic echo and associated noise, which decreases the quality of speech [1]. Echo is a phenomenon in which a delayed and distorted original signal is reflected to its source. Echo in audio speech occurs when the sound is reflected from nearby objects, walls or from the floor. If these reflections are of a short duration and arrive in a very short time, they are referred to as [2] reverberations or the spectral distortion. Whereas if the same sound arrives back within a few tens of milliseconds, it is heard as a distinct reflected sound known as acoustic echo. In a telephony system, two types of echo may be distinguished: network echo [3], [4] and acoustic echo [5]–[7]. Network echo is mostly created along telephone lines due to an impedance mismatch between public switched telephone networks. The phenomenon of acoustic echo occurs mostly in hands free communications. Earlier work in the area of echo cancelation (EC) focused primarily on network echo cancelation. With advances in wireless communication technologies, cancelation of acoustic echo has captured attention of users. Figure 1 shows a scenario of acoustic echo affecting a teleconferencing system.

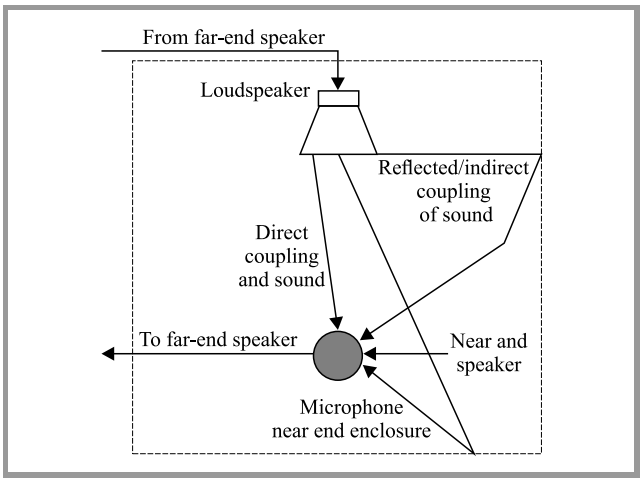

Fig. 1. Generation of acoustic echo.

Acoustic echo [8] occurs when audio from the far-end speaker comes arrives at the near-end enclosure via a loudspeaker and is picked up by the near-end microphone via both direct and indirect paths. To remove the echo, echo cancelers are developed which detect and remove the echo generated. In order to calculate the adaptive filter tap, various algorithms, such as least mean squares (LMS), normalized LMS and recursive LMS are employed. The main features of these algorithms are that they offer fast convergence, but at the cost of computational complexity observed with an increase of the number of filter taps. Also, any change in near-end enclosure may lead to wrong convergence, and additional filters may then be required for its removal [9]–[11].

Acoustic echo cancelation (AEC) and extraction of near-end signal is a challenging process, as the proposed method should emulate the inherent ability of the human auditory system, known as computational auditory scene analysis (CASA) [12]–[14].

In this paper, we extend the concept from the conventional method, to model-based statistical pattern recognition. This is motivated by the fact that in the spectral domain, distinct speakers have distinct patterns. To separate these features, machine learning and matrix factorization methods are applied. The main theme is to use, in advance, prior information from the sources, and to first train the model for each source, and then separate signals from a given mixture. Hence, such an approach is known as model-based near-end speaker extraction and echo cancelation. Model-based source separation can be a probabilistic model, or a matrix factorization-based method. The former method uses the Bayesian approach, while the latter uses such techniques as non-negative matrix factorization (NMF). In this paper, model-based methods of AEC, relying on matrix factorization-based methods, are proposed. It is shown that the proposed method outperforms the classic echo cancelation method.

The paper is organized as follows: Section 2 is devoted to problem formulation and contains a brief description of LMS, NLMS, RLS and NMF methods. The model-based AEC and near-end speaker extraction method is presented in Section 3. Algorithmic steps and their implementation are shown in Section 4. Performance analysis and experimental results are shown in Sections 5–6. Simulation results are discussed in Section 7. Section 8 summarizes the paper.

2. AEC and Near-End Speaker Extraction

The process of generating acoustic echo can be described with the use of a linear framework. Let us denote the signal coming from the far-end speaker as $x(n)$, where n is a sample index. Let this excite a linear system whose impulse response is given by $h(n)$. $h(n)$ is actually a superimposition of impulses, with each of them corresponding to an echo. In the near-end enclosure, echo is produced due to various propagation paths between the loudspeaker and the microphone. Let it be represented by $d(n)$, a linear convolution of $x(n)$ with $h(n)$, expressed as:

$$d(n) = \sum_{i=0}^{L_h-1} h(i)x(n-i)\,, \tag{1}$$

where i denotes the sample index and L_h denotes the length of the echo path impulse response. In a vector form, it can be expressed as:

$$\begin{aligned} d(n) &= \mathbf{h}^T\mathbf{x}(n),\ \mathbf{x}(n) \\ &= \left[x(n), x(n-1), \ldots, x(n-L_h+1)\right]^T, \end{aligned} \tag{2}$$

where T denotes the matrix's transpose operation symbol. The output of the near-end microphone signal or the far-end user's signal $y(n)$ is:

$$\begin{aligned} y(n) &= d(n)+u(n)+w(n) = && (3)\\ &= \sum_{i=0}^{L_h-1} h(i)x(n-i)+u(n)+w(n) = && (4)\\ &= \mathbf{h}^T\mathbf{x}(n)+u(n)+w(n)\,, && (5) \end{aligned}$$

where $u(n)$ denotes the desired near-end speech signal and $w(n)$ denote the noise sources (Fig. 2).

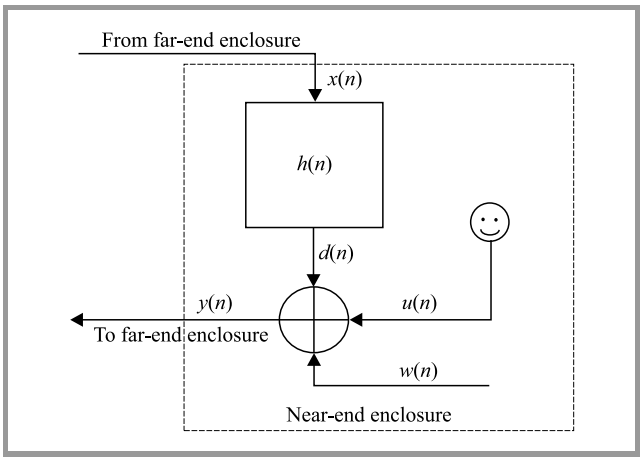

Fig. 2. Linear framework for hands-free communication.

The aim of acoustic echo cancelation is to present a clear near-end speech signal $u(n)$ to the far-end speaker, containing no echo and noise components, i.e. $d(n) = 0$ and $w(n) = 0$.

2.1. LMS Algorithm

The LMS algorithm, derived by Widow and Hoff [15], is one of the most efficient adaptive filtering algorithms. This algorithm has the property of adjusting the coefficients of a filter to reduce MSE between the desired signal and output of the filter. It is used for updating the taps of the adaptive filter during each iteration:

$$\mathbf{w}(n+1) = \mathbf{w}(n) + \mu e(n)\mathbf{x}^*(n)\,, \tag{6}$$

where $\mathbf{x}(n)$ is the input vector of time-delayed input values, $\mathbf{w}(n)$ is the weight vector at time n, and μ is the step-size parameter that controls the immediate change of the updating factor. Its value has an impact on the performance of the LMS algorithm. When μ is low, it takes a long time for the algorithm to converge and a high value of this factor causes the algorithm to diverge, leading to LMS instability.

2.2. NLMS Algorithm

The step-size parameter used in the LMS algorithm is normalized in the case of normalized least mean squares

(NLMS) [16] algorithm. In NLMS [17], [18], μ for computing the update is given by:

$$\mu(n) = \frac{\beta}{c + \|\mathbf{x}(n)\|^2}\,, \tag{7}$$

where $\mu(n)$ is the step-size parameter at sample n, β is a normalized step-size ($0 < \beta < 2$), and c is the smallest positive constant.

2.3. RLS Algorithm

The Recursive Least Square (RLS) algorithm has a fast convergence rate [30] and is widely used in EC, channel equalization, speech enhancement and radar applications. In this algorithm [25], we consider the following:

- $x(n)$ is the discrete time array $M \times 1$ array input vector,
- $y(n) = w^H x(n)$ is the output signal,
- $d(n)$ is the desired signal,
- w is the $M \times 1$ complex weight matrix.

2.4. NMF Algorithm

Non-Negative Matrix Factorization (NMF) [19] is a linear-based decomposition technique subject to the constraints of non-negativity of the data being decomposed. It actually decomposes the data of a non-negative matrix into two non-negative matrices and a residual matrix which does not necessarily have to be non-negative. A given data matrix $\mathbf{A} \in \mathbb{R}_+^{M\times N}$, it can be decomposed into two non-negative matrices $\mathbf{B} \in \mathbb{R}_+^{M\times K}$ $\mathbf{G} \in \mathbb{R}_+^{K\times N}$, $K < N$ and a residual matrix $E \in \mathbb{R}_+^{M\times N}$ representing the approximation to the error [20], [21].
It is an optimization problem which aims to minimize the cost function $\mathbf{C}(.)$ with respect to $\mathbf{B}$ and $\mathbf{G}$. This cost function measures the divergence between $\mathbf{A}$ and $\mathbf{BG}$.

$$\mathbf{A} = \mathbf{BG} + \mathbf{E},\ \ \mathbf{A} \approx \mathbf{BG}\,. \tag{8}$$

It is an optimization problem which aims at minimizing some cost function $\mathbf{C}(.)$ with respect to $\mathbf{B}$ and $\mathbf{G}$. This cost function measures the divergence between $\mathbf{A}$ and $\mathbf{BG}$.
One of the cost function measures is the Euclidean distance [22]:

$$D_{ED}(\mathbf{A},\mathbf{B},\mathbf{G}) = \frac{1}{2}\left\|\mathbf{A} - \mathbf{BG}\right\|^2. \tag{9}$$

The following multiplicative update rules are followed to balance convergence speed and complexity:

$$b_{ij} \leftarrow b_{ij}\frac{\left[\mathbf{AG}^T\right]_{ij}}{\left[\mathbf{BGG}^T\right]_{ij}},\ \ g_{ij} \leftarrow g_{ij}\frac{\left[\mathbf{B}^T\mathbf{A}\right]_{jk}}{\left[\mathbf{B}^T\mathbf{BG}\right]_{jk}}\,, \tag{10}$$

here $[.]_{ij}$ indicates that the given operations are performed on an element-by-element basis.

The second cost function in use is the generalized version of Kullback-Leibler divergence, also known as I-divergence [23], [24]:

$$D_{KL}(\mathbf{A}\|\mathbf{B},\mathbf{G}) = \sum_{ik}\left(a_{ik}\log\frac{a_{ik}}{[\mathbf{BG}]_{ik}} - v_{ik} + [\mathbf{BG}]_{ik}\right). \tag{11}$$

This cost function is not symmetric in $\mathbf{A}$ and $\mathbf{BG}$. It actually quantifies in bits that how close $\mathbf{A}$ is to $\mathbf{BG}$. Its value equals zero if the distributions match exactly, and infinite if there is no match at all.

3. Model-based AEC and Near-end Speaker Extraction Method

The model-based statistical pattern recognition technique was first proposed in [25]. In the spectral domain there is a distinct pattern of speech signals spoken by different speakers. Due to this regular and distinct pattern of speech signal, matrix factorization methods can be applied to differentiate between these speakers. The NMF [26] approach is formulated in the short-time Fourier transform domain [27], [28]. The near-end microphone signal $y(n)$ of the mixture signal is decomposed into two bases of spectral features. First, training on the magnitude spectra of many speakers is performed offline. This trained data can be called on as and when required. The other bases are created during operation and testing. These bases are continuously updated by the incoming far-end signal $x(n)$ and are actually specific to the far-end signal. Now, NMF is employed that minimizes the cost function. This cost function minimizes divergence of the trained vectors to the test vectors. Once the optimal vector is identified, echo reduction is conducted by performing an inverse transformation for the identified vectors, using the phase information received from the mixture signal.
The model of the acoustic echo which is mostly used in EC and given in the literature [29]–[32] is:

$$|Y(f,k)| = |D(f,k)| + |U(f,k)|\,, \tag{12}$$

where $|Y(f,k)$ is the STFT of $y(n)$, f is the discrete frequency, k is the frame index and $|.|$ is the magnitude of the complex value. For STFT of $y(n)$, hanning window of length N is used that advances in the steps of m. Similarly, $|D(f,k)|$ and $|U(f,k)|$ represent the $d(n)$ and $u(n)$ components of the mixture signal in the STFT domain. Such a model strictly follows non-negativity and linearity of the sample of the speech signals. This allows for easy implementation of NMF for EC.

4. Algorithm Implementation

The pseudocode of the algorithm for NMF-based AEC and near-end speaker extraction approach described above is presented as Algorithm 1. It comprises three stages: training, testing and reconstruction. Training is done for the

Algorithm 1: Algorithm pseudocode for NMF-based AEC and near-end speaker extraction

1. Process the incoming far-end signal $x(n)$
   Find STFT: $X(f,k)$
   $|X(f,k)|$, k is the frame index
   From $X(f,k)$, $d(f,k)$ is created
   Calculate the NMF of $D(f,k)$ and form the basis
   $B_d(k)$ $G_d(k)$
2. Process the speaker independent near-end signal $u(n)$
   Find STFT: $U(f,k)$
   $|U(f,k)|$, k is the frame index
   Calculate the NMF of $U(f,k)$ and form the basis
   $\mathbf{B}_u(k)$ $\mathbf{G}_u(k)$
3. Concatenate the basis of steps 1 and 2 to form composite basis $\mathbf{B}(k) = [\mathbf{B}_u\, \mathbf{B}_d(k)]$
4. Process the mixture signal $y(n)$
   Find STFT: $Y(f,k)$
   $|Y(f,k)|$, k is the frame index
   For $i = 1$ to ϕ (restricted NMF updates) $+\psi$ (unrestricted NMF updates) **do**
   (ϕ and ψ are the number of iterations)
   For ϕ iterations, composite basis $\mathbf{B}(k)$ is fixed and $\mathbf{g}(k)$ is updated as
   $$g(k) \leftarrow g(k)\frac{\mathbf{B}(k)\left[\frac{\mathbf{y}(k)}{\mathbf{B}(k)\mathbf{g}(k)}\right]}{\mathbf{B}(k)^T 1 + \delta},$$ δ is a positive regularization factor
   $y(k)$ can now be expressed as:
   $$\mathbf{y}(k) = \mathbf{B}(k)\mathbf{g}(k) + \mathbf{e}(k) = [\mathbf{B}_u\, \mathbf{B}_d(k)]\begin{bmatrix}\mathbf{g}_u(k)\\ \mathbf{g}_d(k)\end{bmatrix} + \mathbf{e}(k)$$
   For ψ iterations, both composite bases $[\mathbf{B}_u\, \mathbf{B}_d(k)]$ and $\mathbf{g}(k)$ are updated
   $$\mathbf{B}(k) \leftarrow \mathbf{B}(k)\frac{\left[\frac{\mathbf{y}(k)}{\mathbf{B}(k)\mathbf{g}(k)}\right]\mathbf{g}(k)^T}{1\mathbf{g}(k)^T + \delta}$$
   End for
   $\hat{\mathbf{u}}(k) = \mathbf{B}_u\mathbf{g}_u(k)$
5. Near-end speaker extraction
   $\hat{\mathbf{u}}(k) \angle Y(f,k)$

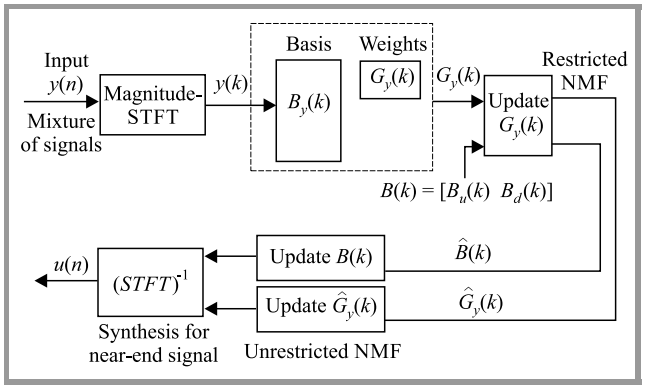

Fig. 3. Block diagram presenting AEC and near-end speaker extraction using NMF.

far-end speaker and for the near-end speakers. From the training phase, the base vectors $\mathbf{B}_d$ and $\mathbf{B}_u$ for far-end and near-end speaker signals are obtained. These bases are concatenated to form composite bases $\mathbf{B} = [\mathbf{B}_u\mathbf{B}_d]$. The composite base is derived during testing. Testing is done online for the incoming mixture signal. A block diagram presenting AEC relying on the NMF algorithm is shown in Fig. 3.

5. Performance Analysis

Spectrograph plot is a three-dimensional (3D) visual analysis of an acoustic signal, in which horizontal axis represents the time domain, the vertical axis represents frequency and

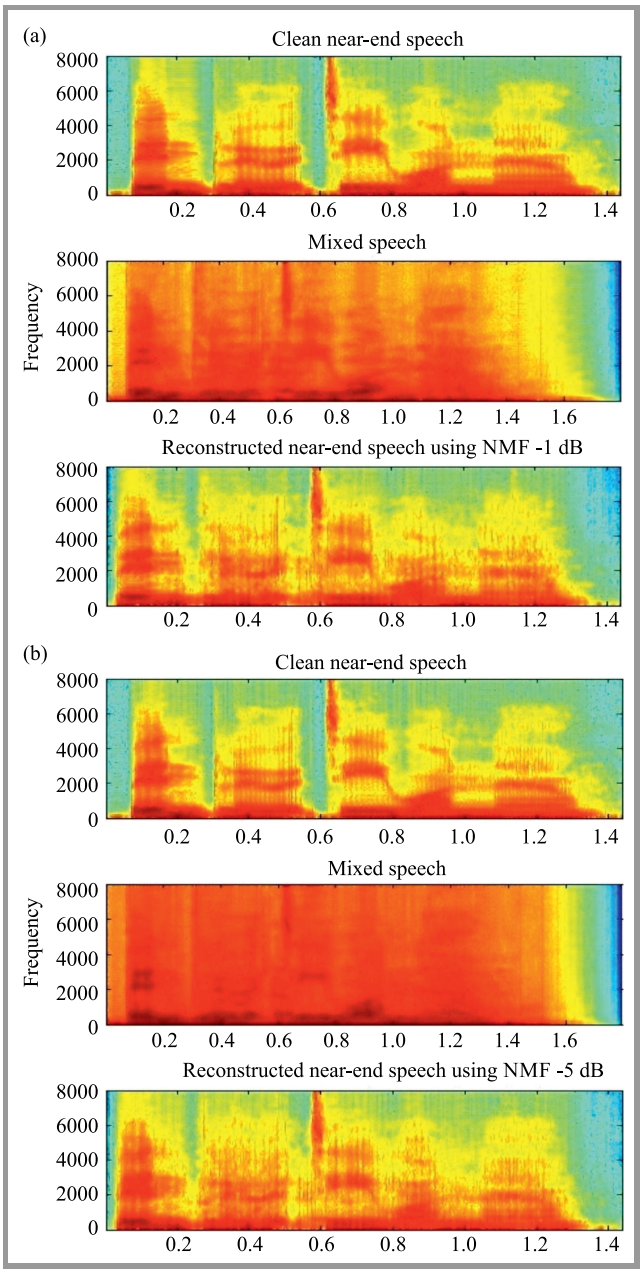

Fig. 4. Spectrogram of extracted near-end signal using NMF at ENR equal to: (a) –1 dB and (b) –5 dB. (For color pictures visit www.nit.eu/publications/journal-jtit)

the third dimension is amplitude at a frequency and time indicated by the color. Figure 4a shows the spectrogram of a near-end signal extracted using the NMF algorithm at ENR –1 dB. Figure 4b shows the spectrogram of a near-end signal extracted using the NMF algorithm at ENR –5 dB. In Figs. 4a-b, the top picture shows the spectrogram of a clean near-end signal, the middle image shows a mixed signal and the bottom picture shows a near-end signal reconstructed using NMF. Comparing the NMF algorithm at ENR –1 dB and ENR –5 dB, one may notice, visually, that a better reconstructed near-end speech signal is seen at ENR –5 dB, compared to ENR of –1 dB. This is due to the reduction in echo from –1 to –5 dB, and, hence, to better near-end speaker extraction.

5.1. Simulation Setup

During Matlab simulation, it was assumed that incoming far-end speech signals are segmented into 64 ms frames with a 50% overlap between the adjacent frames. The effect of background noise and local noise has been neglected. Room impulse response (RIR) is generated using the mirror image method with the room size of $10.4 \times 10.4 \times 4.2$ m. The reflection coefficient of the wall is selected as 0.8. Room parameters, such as volume, absorption, reflections from the walls, construction materials present in the room and distance between sources and the receiver, are all taken into consideration while generating RIR. Between the clean speech signal and RIR, convolution is done by considering the fixed distance between the source and the microphones. For audio recorded by several speakers, sampling is performed at 25 kHz. The experiment is conducted using audio data obtained from the GRID corpus database. Table 1 shows all choices of sentences from GRID [33]. The corpus consists of high-quality audio recordings of around 1000 sentences spoken by each of 34 talkers (18 males, 16 females).

Table 1
Possible choices in the sentences

Commands	Colors	Prepositions	Letters	Numbers	Adverbs
Bin (b)	Blue (b)	At (a)	A–Z	1–9 and	Again (a)
Lay (l)	Green (g)	By (b)	excluding W	zero (z)	Now (n)
Place (p)	Red (r)	In (i)			Please (p)
Set (s)	White (w)	With (w)			Soon (s)

Results are obtained by calculating echo to near-end signal ratio (ENR), which is the power ratio between the echo signal and the near-end signal. It is measured by varying the distance between the microphone and the source by keeping the source fixed and moving the microphone to various positions to generate different ENR values.

5.2. Performance Evaluation

This section gives experimental results that are conducted at different ENRs: –1, –3, – and –5 dB. The Mean Opinion Score (MOS) [34] obtained by evaluating the quality of speech after EC using the proposed NMF method, and its comparison with LMS, NLMS and RLS, are plotted in Fig. 5. As ENR decreases from –1 to –5 dB, MOS increases. Also when decreasing the ENR for all methods mentioned, MOS obtained using the NMF method proposed has the highest value.

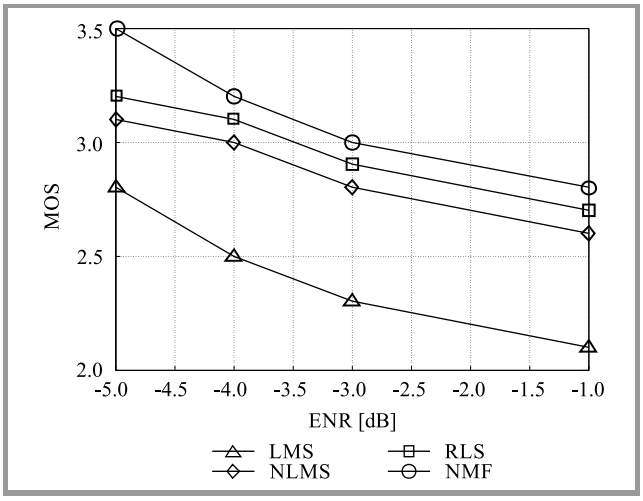

Fig. 5. MOS at different ENRs for LMS, NLMS, RLS and NMF.

5.3. Perceptual Evaluation of Speech Quality

Speech quality is evaluated using perceptual evaluation of speech quality (PESQ), and results with different ENRs are shown in Fig. 6. In this method the test signal and the corresponding reference signals are taken as input, and a set of features is extracted from both signals. They are then compared in perceptual space [35] by time-aligning these signals. Then, the speech signal is analyzed on a sample-by-sample basis for both the reconstructed output signal and the reference signal, after time-aligning it individually. This is done to compensate for any time shifts that can occur

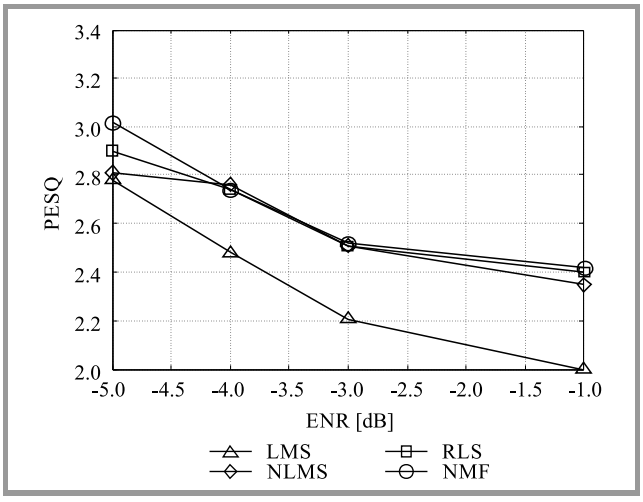

Fig. 6. PESQ at different ENRs for LMS, NLMS, RLS and NMF.

during processing. Then, the perceptual model incorporates a time frequency analysis procedure.

The experiment performed using test and reference signals is divided into 32 ms frames. The overlapping rate of the successive frames is 50%. Signals are transformed into the frequency domain using STFT. Linear frequency scale is transformed to the Bark scale for finer frequency resolution at lower rather than higher frequencies. From the perceived audio, audible differences in both domains are subtracted and accumulated over time. These are then weighted based on whether the distortion is additive in nature or whether the signal is missing. PESQ describes the audio quality using the scale of 1 (bad) to 5 (excellent). A higher PESQ value shows that the algorithm used is better suited to conduct echo cancelation [35]. From Fig. 6 it can be seen that NMF has a PESQ value that is approximately equal to or higher than all other methods, indicating a better perceptual similarity between clean and reconstructed signals. As ENR decreases from –1 to –5 dB, PESQ increases for the individual methods. Also, comparing the NMF method proposed for EC with LMS, NLMS and RLS, the PESQ value is the highest using NMF. Performance measured at ENR –5 dB obtained using NMF is found to be better than at ENR –1 dB.

5.4. Echo Return Loss Enhancement

Echo return loss enhancement (ERLE) measures the amount of additional signal loss applied by the echo canceler. It is defined as the ratio between send power in one direction and the power of a residual error signal obtained after the echo is canceled, i.e. in the steady state. It is usually measured in decibels:

$$\text{ERLE} = 10\log\frac{E\left(x^2(t)\right)}{E\left(e^2(t)\right)}, \tag{13}$$

where $x(t)$ is the send signal and $e(t) = \hat{u}(t) - u(t)$ is the residual error signal obtained after processing.

ERLE depends on the size of the adaptive filter and the algorithm which is designed to remove the echo. ERLE provides information about the behavior of the echo canceler convergence factor. The echo canceler system's input signal is an audio signal which is non-stationary in nature. In the case of adaptive filters, it is difficult to change the step size at a fast rate, which makes its implementation difficult. The NMF algorithm-based EC method presented herein overcomes those shortcomings. Figure 7 shows plots of ERLE at different ENRs. Results obtained for ERLE using NMF are higher than in the case of LMS, NLMS and RLS. As ENR decreases from –1 to –5 dB, the echo in the signal also decreases, thus the result obtained for ERLE increases. At a given ENR, statistical NMF-based EC methods produce better results. A higher ERLE indicates that speech if affected by lower echo rates. For example, at –3 dB, LMS produces ERLE 5, while NLMS 6 and RLS 7.2. The proposed NMF approach offers the result of 8.9, which is very high compared to other values. This clearly indicates that NMF has the least echo and, hence, clear audio is achieved.

5.5. Log Spectral Distortion

Log spectral distortion (LSD), also known as log spectral distance, measures the distance, in decibels, between the two spectra. It is proved in [35] that it is well suited for evaluation of algorithms. It is determined by the RMS value of the difference between log spectra of the original clean audio signal $x(n)$ and the signal that has to be evaluated $y(n)$, which is the outcome of the processing of the signal.

Let $\mathbf{S}(\omega)$ and $\hat{\mathbf{S}}(\omega)$ represent two power spectra. Then, $d(\mathbf{S}, \hat{\mathbf{S}}\omega)$ is the distance measure. LSD is given by:

$$d(\mathbf{S},\hat{\mathbf{S}})^P = (d_p)^P = \int_{-\pi}^{\pi} \left[\log\mathbf{S}(\omega) - \log\hat{\mathbf{S}}(\omega)\right]^P \frac{\mathrm{d}\omega}{2\pi}. \tag{14}$$

For $p = 1$, the above equation defines the mean absolute LSD and for $p = 2$, defines the LSD root mean square,

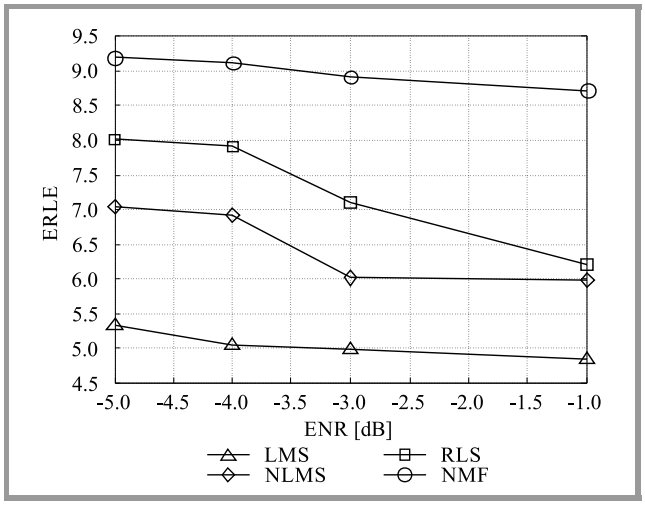

Fig. 7. ERLE vs. ENR for LMS, NLMS, RLS and NMF.

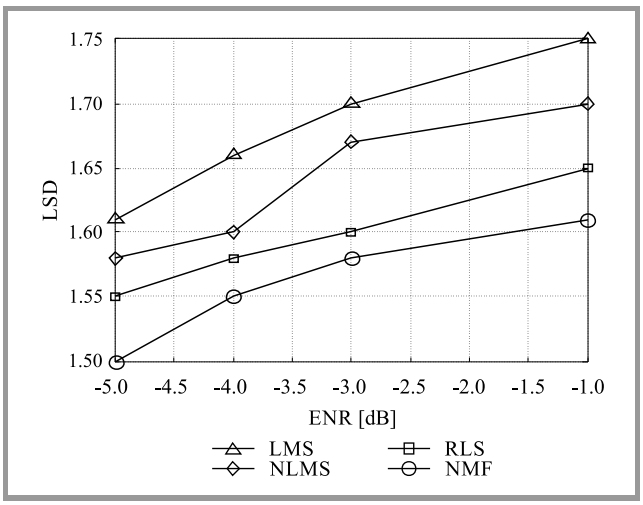

Fig. 8. LSD vs. ENR for LMS, NLMS, RLS and NMF.

which has applications in many speech processing systems and finally at $p = \infty$, the equation reduces to peak LSD. The lower the LSD value, the better the performance. Figure 8 shows LSD plots at different ENRs. At a given ENR, LSD results obtained for NMF are lower than for LMS and NLMS algorithms. At ENR –5 dB, there is less echo and thus the results obtained are better than at ENR –1 dB.

5.6. Comparison of Experimental Results

Table 3 illustrates comparisons between the proposed NMF method used for echo cancelation and LMS, NLMS and RLS algorithms using MOS, LSD, ELRE and PESQ at different ENRs. One may notice that NMF provides better EC and near-end speaker extraction. The proposed algorithm utilizes both restricted and non-restricted NMF, which results in a clean audio signal.

Table 2
Comparison of experimental results

		LMS	NLMS	RLS	NMF
ENR = –1 dB	MOS	2.1	2.6	2.7	2.8
	LSD	1.75	1.70	1.65	1.61
	ELRE	4.83	5.98	6.2	8.72
	PESQ	2	2.35	2.40	2.42
ENR = –3 dB	MOS	2.3	2.8	2.9	3.0
	LSD	1.70	1.67	1.60	1.58
	ELRE	4.98	6.01	7.10	8.90
	PESQ	2.21	2.51	2.51	2.52
ENR = –4 dB	MOS	2.5	3.0	3.1	3.2
	LSD	1.66	1.60	1.58	1.55
	ELRE	5.03	6.92	7.9	9.11
	PESQ	2.48	2.76	2.74	2.74
ENR = –5 dB	MOS	2.8	3.1	3.2	3.5
	LSD	1.61	1.58	1.55	1.50
	ELRE	5.31	7.03	8.01	9.18
	PESQ	2.78	2.81	2.9	3.02

6. Conclusion

This paper proposes a method of AEC and near-end speaker extraction using statistical NMF methods and compares it against classic LMS, NLMS and RLS methods. The results obtained with the use of the proposed NMF technique for AEC indicate that it can be implemented in real-time scenarios. Moreover, the proposed method paves the way for it to be implemented in real time scenarios using multi-resolution NMF, by taking into consideration spatial cues and reverberations. It is expected to achieve better results and to offer more accurate EC.

References

[1] E. Hansler and G. Schmidt, *Acoustic Echo and Noise Control: A Practical Approach*. John Wiley & Sons, 2005 (ISBN: 978-0-471-45346-8).

[2] P. A. Naylor and N. D. Gaubitch, Eds., *Speech Dereverberation*, 1st ed. Springer, 2010 (doi: 10.1007/978-1-84996-056-4).

[3] M. M. Sondhi and D. A. Berkley, "Silencing echoes on the telephone network", *Proc. of the IEEE*, vol. 68, no. 8, pp. 948–963, 1980 (doi: 10.1109/PROC.1980.11774).

[4] C. Paleologu, J. Benesty, and S. Ciochină, "An improved proportionate NLMS algorithm based on the L0 norm", in *Proc. IEEE Int. Conf. on Acoust., Speech and Sig. Process. ICASSP 2010*, Dallas, TX, USA, 2010, pp. 309–312 (doi: 10.1109/ICASSP.2010.5495903).

[5] S. Malik and G. Enzner "Recursive Bayesian control of multichannel acoustic echo cancellation", *IEEE Sig. Process. Lett.*, vol. 18, no. 11, pp. 619–622, 2011 (doi: 10.1109/LSP.2011.2166385).

[6] S. L. Gay and J. E. Benesty, Eds., *Acoustic Signal Processing for Telecommunication*. Boston: Kluwer Academic, 2000 (doi: 10.1007/978-1-4419-8644-3).

[7] J. Gunther and T. Moon "Blind acoustic echo cancellation without double-talk detection", *IEEE Worksh. on Appl. of Sig. Process. to Audio and Acoust.*, New Paltz, NY, USA, 2015 (doi: 10.1109/WASPAA.2015.7336925).

[8] J. Benesty, T. Gänsler, D. R. Morgan, M. M. Sondhi, and S. L. Gay, Eds., *Advances in Network and Acoustic Echo Cancellation*. New York: Springer-Verlag, 2001 (ISBN: 978-3-662-04437-7).

[9] Y. Hu and P. C. Loizou, "Evaluation of objective quality measures for speech enhancement", *IEEE Trans. on Audio, Speech, and Lang. Process.*, vol. 16, no. 1, pp. 229–238, 2008 (doi: 10.1109/TASL.2007.911054).

[10] A. H. Abdullah, M. I. Yusof, and S. R. M. Baki, "Adaptive noise cancellation: a practical study of the least-mean square (LMS) over recursive least-square (RLS) algorithm", in *Proc. Student Conf. on Res. and Develop. SCOReD 2002*, pp. 448–452, Shah Alam, Malaysia, 2002 (doi: 10.1109/SCORED.2002.1033154).

[11] X. Wang, T. Shen, and W. Wang, "An approach for echo cancellation system based on improved NLMS algorithm", in *Proc. Int. Conf. on Wirel. Commun., Netw. and Mob. Comput. WiCom 2007*, Shanghai, China, 2007 (doi: 10.1109/WICOM.2007.708).

[12] S. Wu, X. Qiu, and M. Wu, "Stereo acoustic echo cancellation employing frequency-domain preprocessing and adaptive filter", *IEEE Trans. on Audio, Speech, and Lang. Process.*, vol. 19, no. 3, pp. 614–623, 2011 (doi: 10.1109/TASL.2010.2052804).

[13] M. H. Maruo, J. C. M. Bermudez, and L. S. Resende, "Statistical analysis of a jointly optimized beamformer-assisted acoustic echo canceller", *IEEE Trans. on Sig. Process.*, vol. 62, no. 1, pp. 252–265, 2014 (doi: 10.1109/TSP.2013.2284138).

[14] R. C. Nongpiur and D. J. Shpak, "Maximizing the signal-to-alias ratio in non-uniform filter banks for acoustic echo cancellation", *IEEE Trans. on Circuits and Syst.: Regular Papers*, vol. 59, no. 10, pp. 2315–2325, 2012 (doi: 10.1109/TCSI.2012.2185333).

[15] D. L. Wang and G. J. Brown, Eds., *Computational Auditory Scene Analysis: Principles, Algorithms and Applications.* Wiley-IEEE Press, 2006 (ISBN: 978-0-471-74109-1).

[16] T. S. Wadaand and B.-H. Juang, "Enhancement of residual echo for robust acoustic echo cancellation", *IEEE Trans. on Audio, Speech, and Lang. Process.*, vol. 20, no. 1, pp. 175–189, 2012 (doi: 10.1109/TASL.2011.2159592).

[17] S. K. Nagendra and V. S. Kumar, "Echo cancellation in audio signal using LMS algorithm", in *Nat. Conf. on Recent Trends in Engin. and Technol. NCRTET 2011*, Anand, Gujarat, India, 2011.

[18] U. Mahbub, S. A. Fattah, W-P. Zhu, and M. O. Ahmad, "Single-channel acoustic echo cancellation in noise based on gradient-based adaptive filtering", *EURASIP Journal on Audio, Speech, and Music Processing*, vol. 20, pp. 1–16, 2014 (doi: 10.1186/1687-4722-2014-20).

[19] P. Paatero and U. Tapper, "Positive matrix factorization: A non-negative factor model with optimal utilization of error estimates of data values", *Environmetrics*, vol. 5, pp. 111–126, 1994 (doi: 10.1002/env.3170050203).

[20] A. Bansal, S. Choukse, K. Nathwani, and R. M. Hegde, "Acoustic echo cancellation using a multi-resolution non-negative matrix factorization method", in *Proc. 22nd Nat. Conf. on Commun. NCC 2016*, Guwahati, India, 2016, pp. 1–5, 2016 (doi: 10.1109/NCC.2016.7561119).

[21] D. D. Lee and H. S. Seung, "Algorithms for non-negative matrix factorization", in *Advances in Neural Information Processing Systems 13. Proceedings of the 2000 Conference*, T. K. Leen, T. G. Dietterich, and V. Tresp, Eds. MIT Press, 2001, pp. 556–562.

[22] P. O'Grady, "Sparse Separation of Underdetermined Speech Mixtures", Ph.D. Dissertation, Hamilton Institute, National University of Ireland Maynooth, Ireland, 2007 [Online]. Available: https://www.hamilton.ie/publications/ogrady2007_phd.pdf

[23] S. Ciochină, C. Paleologu, J. Benesty, and C. Anghel, "An optimized affine projection algorithm for acoustic echo cancellation", in *Proc. Int. Conf. on Speech Technol. and Human-Comp. Dialogue SpeD 2015*, Bucharest, Romania, 2015, pp. 1–6 (doi: 10.1109/SPED.2015.7343092).

[24] C. Fevotte, N. Bertin, and J. L. Durrieu, "Nonnegative matrix factorization with the Itakura-Saito divergence: with application to music analysis", *Neural Computation*, vol. 21, no. 3, pp. 793–830, 2009 (doi: 10.1162/neco.2008.04-08-771).

[25] S. Roweis, "One microphone sound source separation", in *Advances in Neural Information Processing Systems 13*, T. K. Leen, T. G. Dietterich, and V. Tresp, Eds. MIT Press, 2001, pp. 793–799.

[26] F. Yang, M. Wu, and J. Yang,"Stereophonic acoustic echo suppression based on Wiener filter in the short-time Fourier transform domain", *IEEE Sig. Process. Lett.*, vol. 19, no. 4, pp. 227–230, 2012 (doi: 10.1109/LSP.2012.2187446).

[27] S. Rickard and O. Yilmaz, "On the approximate W-disjoint orthogonality of speech", in *Proc. IEEE Int. Conf. on Acoust., Speech, and Sig. Process. ICASSP 2002*, vol. 1, pp. I-529–I-532, 2002, Orlando, FL, USA, 2001 (doi: 10.1109/ICASSP.2002.5743771).

[28] O. Yilmaz and S. Rickard, "Blind separation of speech mixtures via time-frequency masking", *IEEE Trans. on Sig. Process.*, vol. 52, no. 7, pp. 1830–1847, 2004 (doi: 10.1109/TSP.2004.828896).

[29] C. Avendano, "Acoustic echo suppression in the STFT domain", in *Proc. IEEE Worksh. on Appl. of Sig. Process. to Audio and Acoust.*, New Paltz, NY, USA, pp. 175–178, 2001 (doi: 10.1109/ASPAA.2001.969571).

[30] C. Faller and J. Chen, "Suppressing acoustic echo in a spectral envelope space", *IEEE Trans. on Speech and Audio Process.*, vol. 13, no. 5, pp. 1048–1062, 2005 (doi: 10.1109/TSA.2005.852012).

[31] E. A. P. Habets, S. Gannot, and I. Cohen, "Robust early echo cancellation and late echo suppression in the STFT domain", in *Proc. of 11th Int. Worksh. on Acoust. Echo and Noise Control IWAENC 2008*, Seattle, VA, USA, 2008.

[32] P. Yun-Sik and C. Joon-Hyuk, "Frequency domain acoustic echo suppression based on soft decision", *IEEE Sig. Process. Lett.*, vol. 16, no. 1, pp. 53–56, 2009 (doi: 10.1109/LSP.2008.2008571).

[33] M. Cooke, J. Barker, S. Cunningham, and X. Shao, "An audio-visual corpus for speech perception and automatic speech recognition", *The J. of the Acoustical Soc. of America*, vol. 120, no. 5, pp. 2421–2424, 2006 (doi: 10.1121/1.2229005).

[34] Y.-X. Wang and Y-J. Zhang, "Nonnegative matrix factorization: A comprehensive review", *IEEE Trans. on Knowl. and Data Engin.*, vol. 25, no. 6, pp. 1336–1353, 2013 (doi: 10.1109/TKDE.2012.51).

[35] A. W. Rix, J. G. Beerends, M. P. Hollier, and A. P. Hekstra, "Perceptual evaluation of speech quality (PESQ) – A new method for speech quality assessment of telephone networks and codecs", in *Proc. IEEE Int. Conf. on Acoust., Speech and Sig. Process. ICASSP 2001*, Salt Lake City, UT, USA, 2001, vol. 2, pp. 749–752 (doi: 10.1109/ICASSP.2001.941023).

Pallavi Agrawal received her B.Eng. (Hons) in Electronics and Communication Engineering from RGPV, Bhopal, India and M.Tech. in Digital Communications from Maulana Azad National Institute of Technology (MANIT), Bhopal, India. She is now a Ph.D. candidate at the Electronics and Communication Department at MANIT. Her areas of interest include digital speech signal processing, digital communication and statistical signal processing.
E-mail: pallaviagrawal4@gmail.com
Department of Electronics and Communication Engineering
Maulana Azad National Institute of Technology
Bhopal (M. P.), India

Madhu Shandilya is currently working as a Professor at the Department of Electronics, MANIT, Bhopal, Deemed University and at the National Institute of Technology of India. She has more than 20 years teaching and research experience. Her areas of interest include image processing, information security and watermarking. She has more than 30 papers published in various national and international journals and in various IEEE-sponsored national and international conferences. She is a member of various Societies, such as IETE, CSI, and ISTE.
E-mail: madhu_shandilya@yahoo.in
Department of Electronics and Communication Engineering
Maulana Azad National Institute of Technology
Bhopal (M. P.), India

Paper

Genetic Algorithm for Combined Speaker and Speech Recognition using Deep Neural Networks

Gurpreet Kaur[1,2], Mohit Srivastava[3], and Amod Kumar[4]

[1] *I. K. Gujral Punjab Technical University, Kapurthala, Jalandhar, India*
[2] *University Institute of Engineering & Technology, Panjab University, Chandigarh, India*
[3] *Chandigarh Engineering College, Landran, Mohali, Punjab, India*
[4] *Central Scientific Instruments Organisation, Chandigarh, India*

https://doi.org/10.26636/jtit.2018.119617

Abstract— Huge growth is observed in the speech and speaker recognition field due to many artificial intelligence algorithms being applied. Speech is used to convey messages via the language being spoken, emotions, gender and speaker identity. Many real applications in healthcare are based upon speech and speaker recognition, e.g. a voice-controlled wheelchair helps control the chair. In this paper, we use a genetic algorithm (GA) for combined speaker and speech recognition, relying on optimized Mel Frequency Cepstral Coefficient (MFCC) speech features, and classification is performed using a Deep Neural Network (DNN). In the first phase, feature extraction using MFCC is executed. Then, feature optimization is performed using GA. In the second phase training is conducted using DNN. Evaluation and validation of the proposed work model is done by setting a real environment, and efficiency is calculated on the basis of such parameters as accuracy, precision rate, recall rate, sensitivity, and specificity. Also, this paper presents an evaluation of such feature extraction methods as linear predictive coding coefficient (LPCC), perceptual linear prediction (PLP), mel frequency cepstral coefficients (MFCC) and relative spectra filtering (RASTA), with all of them used for combined speaker and speech recognition systems. A comparison of different methods based on existing techniques for both clean and noisy environments is made as well.

Keywords— deep neural network, genetic algorithm, LPCC, MFCC, PLP, RASTA-PLP, speaker recognition, speech recognition.

1. Introduction

The study of speech signals and their processing methods is known as speech processing [1]. Speech processing is an immensely vast area and much research has been performed in this field over the past sixty years [2]. Important fields of speech processing are synthesis, recognition and coding of speech signals. Recognition itself is a wide topic consisting of three areas of recognition, i.e. speech, speaker and language. As the name implies, speech recognition aims to recognize the words spoken, while language recognition aims to recognize the language spoken and speaker recognition aims to recognize the speaker. Speech recognition may be speaker dependent and independent. In the speaker dependent mode, the system is trained to recognize one speaker only, but in the speaker independent mode, the system is trained to work with multiple speakers. The field of speaker recognition is also divided into two categories, i.e. text dependent and text independent. In the text dependent speaker recognition mode, the speaker is required to utter words which are known to the system, but in the text independent mode, the speaker may speak any words [3].

A speech signal consists of different attributes, such as loudness, voiced/unvoiced sounds, pitch, fundamental frequency, spectral envelope, formants etc. These attributes help identify the speaker and speech features [4]. Although speech recognition and speaker recognition are different fields, the feature extraction methods in both fields overlap [5]. These methods include predictive models based on the linear predictive coding coefficient (LPCC), perceptual linear prediction (PLP), mel frequency cepstral coefficient (MFCC) and relative spectra filtering (RASTA). These methods can be implemented in speech recognition as well as in speaker recognition [6]–[10]. Speech features can be optimized for improving recognition accuracy with the help of various optimization algorithms, like the genetic algorithm (GA), particle swarm optimization, ant colony search algorithm, etc. [12]. GA can be used, in deep neural networks, for improvement in recognition accuracy [13]–[17]. In past studies, many researchers have implemented GA with an artificial neural network (ANN), i.e. Lan *et al.* [18]. They have implemented GA, instead of the steepest descent method, for updating weights and achieved a 91% recognition accuracy. Balochian *et al.* [19] claimed a 96.49% accuracy level by using GA with the multi-layer perceptron (MLP) classifier.

In this paper, we first implemented some state-of-the-art feature extraction methods for combined speaker and

speech recognition. Out of these methods we have selected the best feature extraction method based upon the results obtained, i.e. MFCC for our application. Further, combined speaker and speech recognition using MFCC with the genetic algorithm and a deep neural network was performed with improved accuracy results achieved.

2. Feature Extraction Techniques

The speech production mechanism can be modeled by a linear separable equivalent circuit [20]–[22]. This model is equivalent to a sound source $G(\omega)$ inputting into the articulation filter (vocal tract) to produce speech. The sound source $G(\omega)$ can be categorized as a train of impulses (voiced) and random noises (unvoiced). Voiced sounds include /a/, /e/, /i/, /o/, /u/. On the other hand, unvoiced sounds are noise generated sounds, such as /t/, /s/. The articulation $H(\omega)$ is a transfer function which models the vocal tract of the human speech organ. The output speech wave $S(\omega)$ is the combination of the sound source multiplied with the articulation given by the equation:

$$S(\omega) = G(\omega)H(\omega). \tag{1}$$

Feature extraction techniques, like LPCC, etc., and models exploit the vocal tract articulation filter $H(\omega)$.

2.1. Linear Predictive Coding Coefficient

LPCC is one of the early algorithms that represent the spectral magnitude of speech signal and generates the vocal tract coefficients. In this method, a speech utterance at the current time can be approximated as linear combination of past speech samples [23]–[25]. The steps are as shown below in Fig. 1.

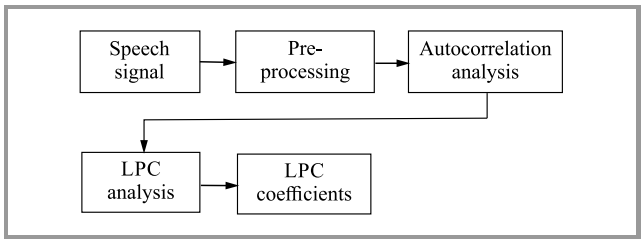

Fig. 1. LPCC technique.

Pre-processing is performed in almost every feature extraction method. The steps of pre-processing include: silence removal from the speech signal, pre-emphasis, framing and windowing. In silence removal, the digitized signal is scanned and the silence zones are removed. Pre-emphasis of the signal is done to enhance the high frequency component of the spectrum. This is performed by passing the speech signal through a digital filter, so that the energy level of the speech signal at higher frequencies is increased:

$$Y[n] = X[n] - 0.95X[n-1]. \tag{2}$$

In framing and windowing, the speech signal is divided into the analysis frames, where the signal can be assumed to be stationary. A window is applied to the emphasized speech signal. Usually the Hamming window is used.

$$W[n] = \begin{cases} 0.56 - 0.46\cos\left(\frac{2\pi m}{L-1}\right), & 0 \le m \le L-1 \\ 0, & \text{elsewhere} \end{cases}. \tag{3}$$

Linear prediction is based on the fact that the present sample $S[n]$ can be linearly predicted using the previous samples $S[n-k]$:

$$S[n] = \sum_{k=1}^{p} \alpha_k S[n-k]. \tag{4}$$

This linear prediction will introduce errors into the sequence of speech samples. This error is known as the residual error $e[n]$:

$$e[n] = s[n] - \sum_{k=1}^{p} \alpha_k S[n-k]. \tag{5}$$

Equation (5) is then transformed into z domain as:

$$E(z) = \left(1 - \sum_{k=1}^{p} \alpha_k z^{-k}\right) S(z). \tag{6}$$

The auto correlation method can be used for estimating LP coefficients. Fundamental frequency or pitch can be identified using an auto correlation analysis. It is based upon determining the correlation between the signal and a delayed version thereof. The next processing step involves a linear prediction coding (LPC) analysis, which converts the auto correlation coefficients into the LPC parameters. The Levinson-Durbin recursive algorithm can be used to identify the coefficients.

2.2. Perceptual Linear Prediction

Perceptual Linear Prediction (PLP) is a method used to obtain more auditory like spectrum based on linear LP analysis of speech. This is a combination of discrete Fourier transform (DFT) and LP techniques and this method is more suitable for the speaker independent mode [26]–[28] (Fig. 2).

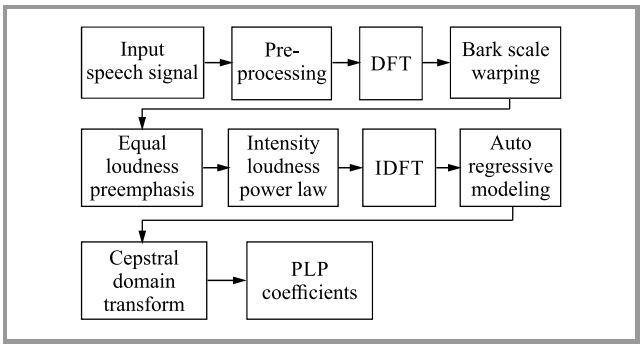

Fig. 2. Perceptual linear prediction technique.

2.3. Rasta Perceptual Linear Prediction (RASTA-PLP)

A band pass filter is added to the PLP algorithm to remove short term noise variations. The individual steps are shown in Fig. 3.

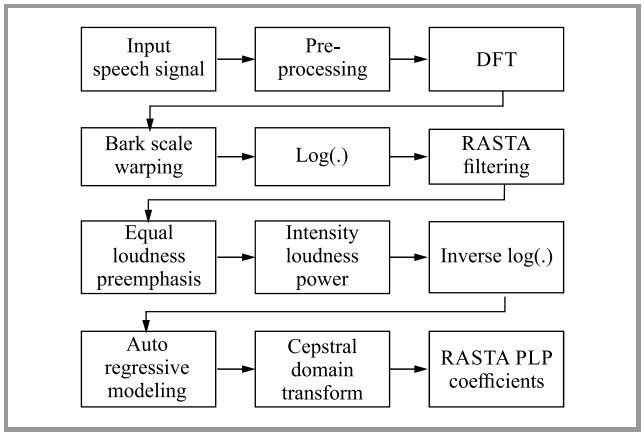

Fig. 3. Relative spectra filtering PLP technique.

2.4. Mel Frequency Cepstral Coefficient (MFCC)

It is the most popular method used for feature extraction [29], [30]. The steps involved are: fast Fourier transform (FFT) is applied first on the frame, and then power spectrum is converted into a mel frequency spectrum. Then, the logarithm of that spectrum is taken and its inverse Fourier transform is taken as shown in Fig. 4.

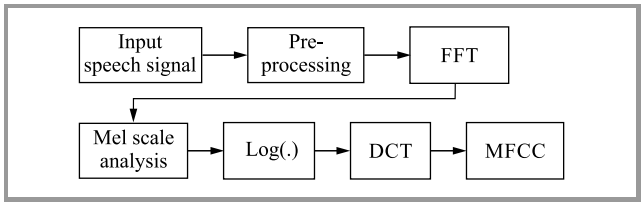

Fig. 4. MFCC extraction.

3. Experiment and Implementation

The speech database is recorded on the sound recorder with the use of headphones, in a room environment, in the mono format. The dataset contains a thousand of words recorded by four speakers aged 27–34, two females (F1, F2) and two males (M1, M2). The recorded words are: *forward*, *backward*, *left*, *right* and *stop*. For each word, fifty samples are taken. All samples are stored in .wav files (16 bps bitrate). All methods, i.e. LPCC, PLP, RASTA PLP and MFCC, are implemented to extract speaker- and speech-specific. Accuracy is calculated in terms of clean signals, as well as of those affected by adding white Gaussian noise (WGN). Further, the MFCC technique is used for feature extraction with GA, and DNN is trained using the optimized features. GA is used for determining the weights and biases of DNN. The fitness function of GA can be defined according to specific requirements.

In the proposed work, f_s is the current selected feature and f_t is the threshold value of feature points. On the basis of a given condition, the fit value is checked which can exist in a new feature set:

$$f(fit) = \begin{cases} 1, & f_s < f_t \\ 0, & f_s \geq f_t \end{cases}, \tag{7}$$

where $f(fit)$ is the fit value according to the fitness function. If the condition is true (1), then GA creates an optimal feature set. The genetic parameters and operators used are: population size, crossover function, mutation function and selection function. To organize the feature sets according to the requirements, selection of individual features is performed by means of the selection function. The selection of individual features is done according to their fitness value represented as f_s and is given by:

$$f_s = \sum_{i=1}^{popsize} f(i), \tag{8}$$

where $f(i)$ describes the individually selected features and $popsize$ denotes the population size of GA. The fitness

Algorithm 1: Optimization technique for DNN training

1: Load speech feature sets
2: Calculate the length of feature $[r,c]$
3: Define genetic parameters and operators to initialized the genetic algorithm
4: Set population size $popsize = 50$ (when number of variables is lower than 50 then value of 50 is still sufficient for optimization)
5: Selection function = handle to the function that selects parents of crossover from feature sets
6: Crossover function = handle to the function that the genetic algorithm uses to create the optimal solution
7: Mutation function = handle to the function that produces mutation children which are called optimized features
8: Define fitness function using Eq. (8)
9: **For all components of feature according to rows**
For all components of feature according to columns

$$fs = \sum_{i=1}^{popsize} f(i)$$

$$ft = \frac{\sum_{i=1}^{popsize} f(i)}{Length\ of\ feature}$$

$$f(fit) = \begin{cases} 1, & fs < ft \\ 0, & fs \geq ft \end{cases}$$

$$No.\ of\ variables = 1$$

$$O_{value} = GA[f(fit), no.\ of\ variables,\ initialized\ parameters]$$

End
End
Training data = O
For each set of *Training data*
$Group = Training\ data(i)$
End
10: Initialize the DNN using Training data and Group
11: Train and save the DNN and create a trained structure for classification

function is defined in terms of the distance measured between the selected value and threshold values of features based on the crossover function. Crossover and mutation function are the operators used to establish the relationship between the selected feature f_s and the threshold feature value f_t. A crossover function is based on an individual feature (parents) and a new individual feature (children), while mutation changes the genes of one individual to produce a new feature (mutant), according to the fitness function [35]–[36]. New optimized feature sets are transferred to DNN as input or a training set, to create a trained DNN structure for classification. The methodology of the proposed genetic algorithm with DNN is described as Algorithm 1.

We have used the *trainlm* training function because it is the fastest back propagation algorithm. It is based on the Levenberg-Marquardt optimization algorithm [31]–[34]. During the training phase, we have used a set of 5 hidden layers and weights, and bias values were updated according to the Levenberg Marquardt optimization algorithm. After training, we have performed a simulation with a test speech signal and the process was repeated for training and testing

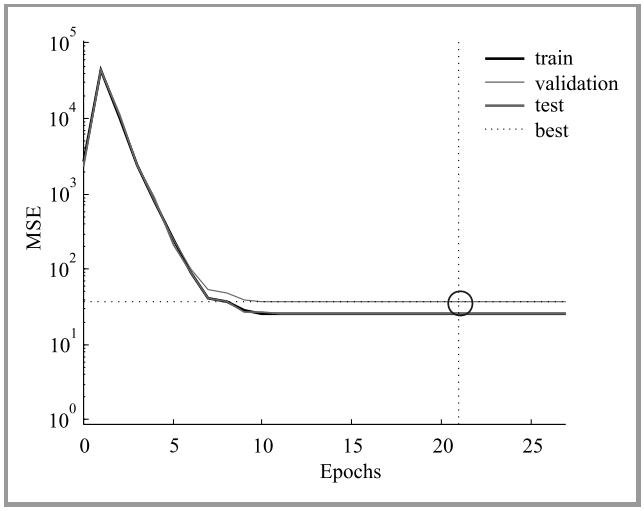

Fig. 5. MSE curve.

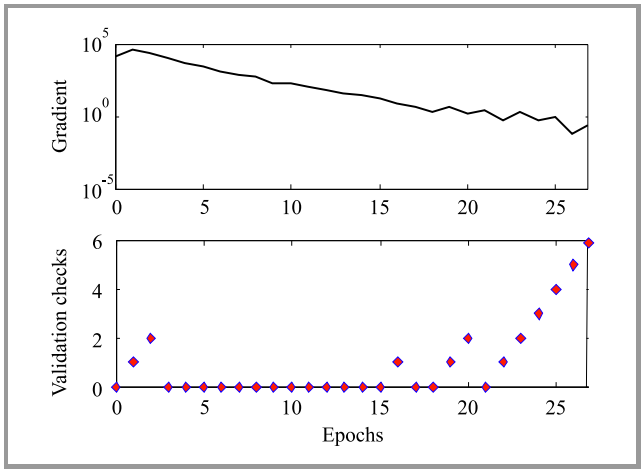

Fig. 6. DNN parameters.

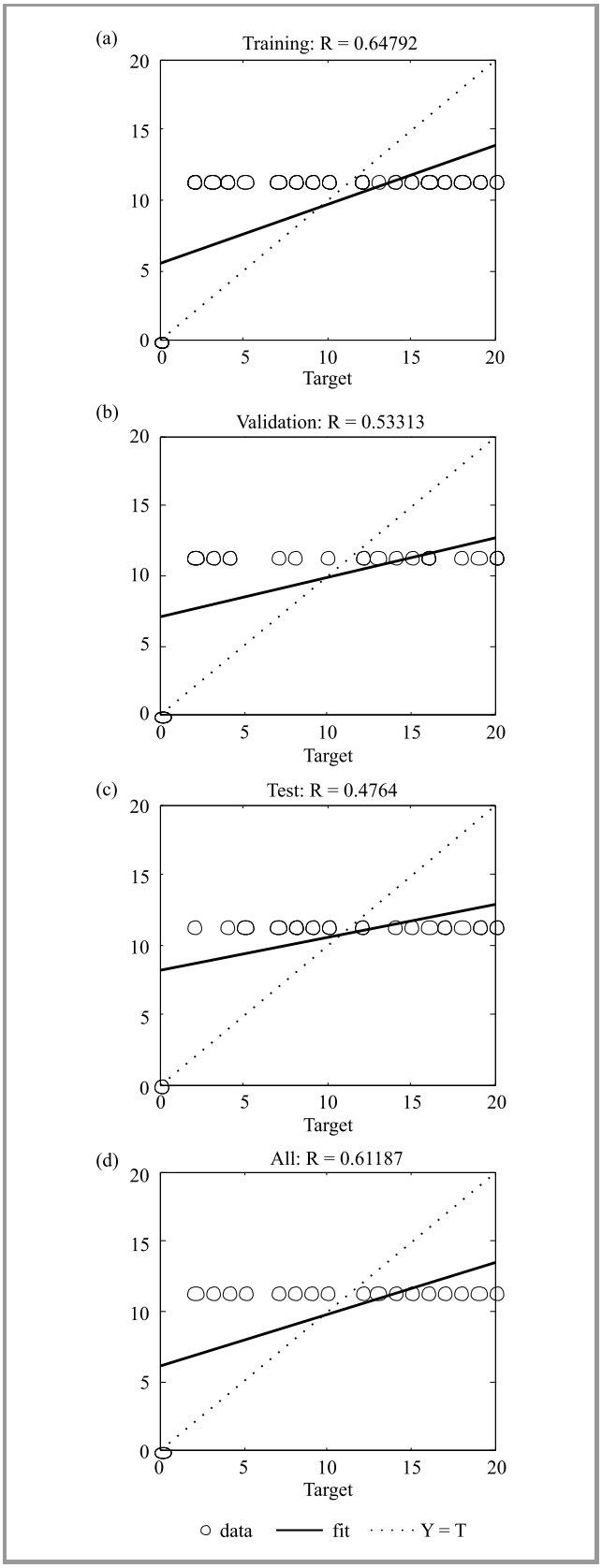

Fig. 7. DNN dataset: (a) training, (b) validation, (c) test, and (d) training output.

phases. We have checked the performance on the basis of mean of square errors (MSE). The MSE graph of the pro-

posed work is given in Fig. 5 with respect to the epochs. The epochs denote the number of iterations which is used by DNN during the speech feature training phase.
The circle shows the best performance in terms of MSE (37.4629 at iteration number 21). Validation and test curves are very similar. If the test curve increases drastically before the validation curve increases, then it is possible that overfitting might have occurred. The next step is to validate the network for which a decay plot is generated to show the association between the outputs of the network and the targets. If training is ideal, network outputs and targets would be equal, but the connection is rarely perfect in practice.
Figure 6 shows a graph presenting different types of parameters, such as gradient value and validation check, with respect to the epochs which are generated during the dataset training phase, using the DNN as a classifier.
Figure 7 shows a description of datasets which are used for the purpose of training. The solid line shows the finest fit linear decay line between outputs and targets. The R value is a signal of the bond between outputs and targets. If $R = 1$, there is an exact direct relationship between outputs and targets. If R is close to zero, then there is no direct relationship between outputs and targets

4. Results and Discussions

All feature extraction methods discussed, i.e. LPCC, PLP, RASTA PLP and MFCC, are used with the recorded database to extract the speaker- and speech-specific features, and results are evaluated in Matlab. Accuracy is calculated in the clean version, as well as in one with WGN added to the speech samples, as shown in Tables 1–4.
Table 1 shows that the average recognition rate related to speaker and words, achieved by using LPCC, equals, for a clean environment, 93.12%. However, by adding WGN to the speech signal, the recognition rate decreases to 83.48%. In Table 2 the feature extraction method used is PLP,

Table 1
Accuracy [%] in clean and with WGN
using LPCC technique and speech recognition
for two males (M1, M2) and two females (F1, F2)

Speaker	M1	M2	F1	F2
Backward	93.18	92.78	92.63	93.65
Backward with WGN	83.50	83.53	84.31	84.22
Forward	94.58	93.56	94.59	92.62
Forward with WGN	81.19	81.20	85.36	82.34
Left	95.50	94.37	91.14	94.41
Left with WGN	80.62	84.76	82.02	82.01
Right	91.17	91.27	95.44	91.79
Right with WGN	83.94	83.46	84.45	84.15
Stop	94.64	92.35	91.33	91.48
Stop with WGN	85.34	84.82	84.39	84.22

Table 2
Accuracy [%] in clean and with WGN
using PLP technique

Speaker	M1	M2	F1	F2
Backward	92.59	94.47	92.60	93.24
Backward with WGN	84.62	83.73	82.21	85.17
Forward	95.52	90.12	92.24	94.43
Forward with WGN	84.43	85.32	82.35	82.76
Left	90.66	94.09	92.54	91.54
Left with WGN	84.11	83.00	81.15	81.06
Right	90.90	92.57	94.59	95.37
Right with WGN	84.37	85.06	83.36	84.43
Stop	94.46	93.54	94.22	93.89
Stop with WGN	84.93	81.97	82.49	84.74

Table 3
Accuracy [%] in clean and with WGN
using RASTA-PLP technique

Speaker	M1	M2	F1	F2
Backward	91.18	92.35	95.43	91.31
Backward with WGN	84.59	85.46	81.71	84.58
Forward	91.32	93.09	94.49	92.19
Forward with WGN	82.39	82.51	80.95	82.26
Left	91.98	93.92	92.54	94.49
Left with WGN	85.47	83.99	84.96	82.83
Right	92.81	93.72	93.35	92.54
Right with WGN	81.63	82.73	82.21	84.58
Stop	93.59	94.87	92.37	93.12
Stop with WGN	82.45	81.35	81.64	83.86

Table 4
Accuracy [%] in clean and with WGN
using RASTA-PLP technique

Speaker	M1	M2	F1	F2
Backward	94.19	94.42	94.66	92.51
Backward with WGN	82.14	84.12	83.95	84.21
Forward	94.69	93.58	94.31	95.55
Forward with WGN	83.38	84.95	81.57	85.29
Left	94.73	94.61	94.22	93.66
Left with WGN	83.86	82.16	83.12	85.22
Right	94.63	94.45	94.41	93.96
Right with WGN	82.89	84.81	84.70	84.38
Stop	93.47	94.19	94.33	94.66
Stop with WGN	83.29	85.40	85.23	83.57

and the average speaker and word recognition rate equals, for a clean environment, 93.17%. However, by adding

WGN to the speech signal, the rate of recognition decreases to 83.56%. Similarly, Table 3 shows that the average speaker and word recognition rate achieved using RASTA PLP equals, for a clean environment, 93.16 and 83.10% respectively. The last Table 4 shows that the average speaker and word recognition rate achieved by using MFCC for a clean environment equals 94.25% and 83.98% with WGN. Figures 8 and 9 show the results of Tables 1–4. Based on the results, we have found that MFCC feature extraction method is best for our application in clean and noisy .

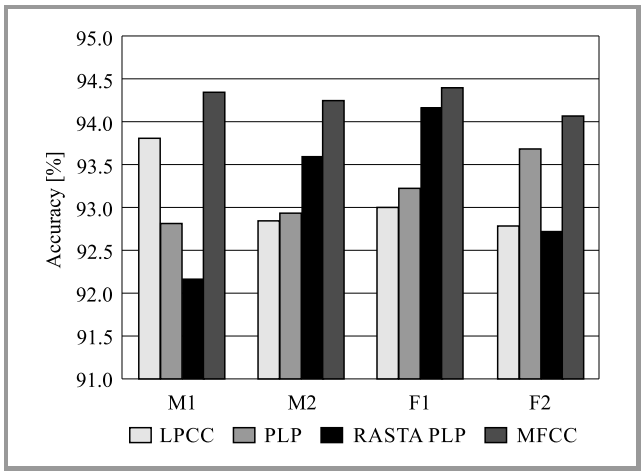

Fig. 8. Accuracy in clean environment.

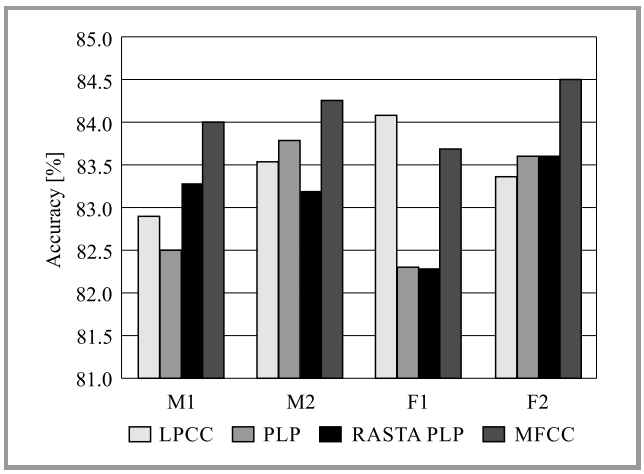

Fig. 9. Accuracy with WGN added.

5. Optimization using GA to assist in DNN Training

In this section results are shown for a system using GA and DNN. It is quite difficult to recognize speech in the presence of noise. The proposed work is tested with various types of noise, such as White Gaussian Noise (WGN), Additive White Gaussian Noise (AWGN), etc. Due to noise, recognition becomes difficult. Therefore, we have used GA for feature optimization. The experimental results have confirmed our expectations by giving good values in terms of such measurement metrics as precision rate, recall rate, accuracy, sensitivity and specificity, defined as:

$$Accuracy = \frac{TP+TN}{TP+FP+TN+FN},$$

$$Precision\ rate = \frac{TP}{TP+FP},$$

$$Sensitivity = \frac{TP}{TP+FN},$$

$$Specificity = \frac{TN}{FP+TN},$$

where true positive (TP) represents the truly selected feature sets using and false positive (FP) are the falsely selected feature sets during the classification of signals. True negative (TN) are all negative features which are really true and false negative (FN) are all negative features which are really false. Figure 10 shows the Receiver Operating Characteristics (ROC) curve. It is a graphical method for comparing two empirical distributions. In this work, true positive and false negative parameters have been taken.

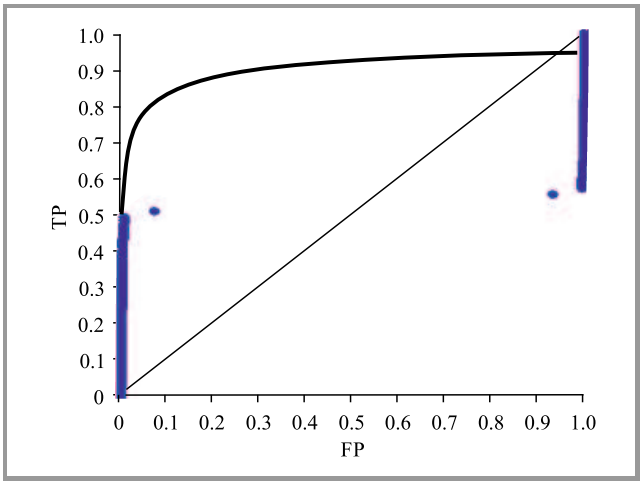

Fig. 10. ROC curve for the proposed work.

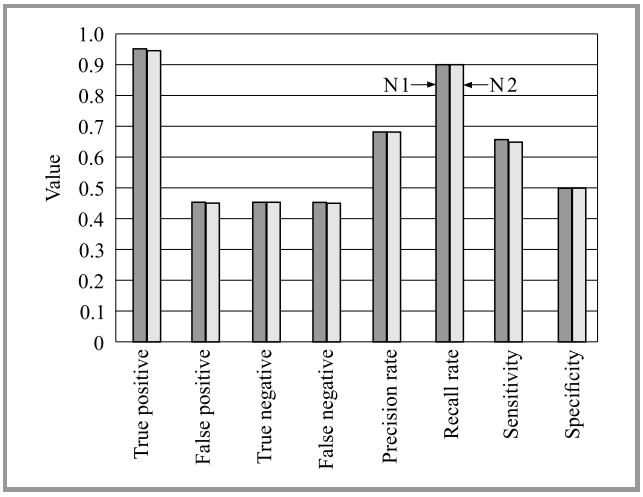

Fig. 11. Result evaluation for proposed methodology.

Table 5
Analysis of proposed metric results

Speaker	N1	N2
TP	0.949	0.945
FP	0.448	0.447
TN	0.449	0.449
FN	0.448	0.445
Precision rate	0.679	0.678
Recall rate	0.901	0.901
Accuracy	97.05	97.11
Sensitivity	0.655	0.645
Specificity	0.500	0.501

Figure 11 and Table 5 present the parameters calculated in the proposed work for two different speakers. N1 represents Speaker 1 and N2 is Speaker 2.
A comparison is also made between MFCC+DNN and MFCC+GA+DNN, as shown in Table 6 and Fig. 12. Recognition accuracy is higher when GA is used for the optimization of features.

Table 6
Comparison of accuracy between
MFCC+DNN and MFCC+GA+DNN

No. of iterations	MFCC+DNN	MFCC+GA+DNN
1	94.48%	97.19%
2	93.23%	98.73%
3	94.11%	95.57%
4	94.15%	96.45%
5	94.47%	94.57%
Average	94.08%	96.51%

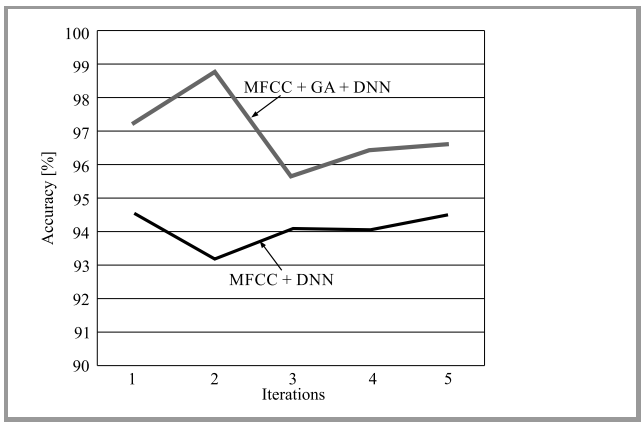

Fig. 12. Accuracy comparison.

6. Conclusions

The existing feature extraction techniques, such as LPCC, PLP, RASTA PLP and MFCC, used for combined speaker and speech recognition, are implemented for five words recorded by four persons in clean and noisy environments. The results show that out of four techniques, MFCC offers the best results in clean, as well as in noisy environments, i.e. the average percentage accuracy for combined speaker and speech recognition in a clean environment is higher than 94%, and with WGN added to the signal – it is higher than 83.5%. We have shown that speaker and speech recognition systems with MFCC and GA using DNN are helpful in achieving a higher accuracy. The experimental results indicate that the proposed method has provided good results, offering the following values: true positive 0.949, false positive 0.448, true negative 0.449, false negative 0.448, precision rate 0.679, and the following rates: recall 0.901, accuracy 96.51, sensitivity 0.655 and specificity 0.500. All these values are an improvement over the existing methods.

References

[1] D. R. Reddy, "Speech recognition by machine: A review", *Proc. of the IEEE*, vol. 64, no. 4, pp. 501–531, 1976 (doi: 10.1109/PROC.1976.10158.

[2] S. Furui, "50 Years of Progress in Speech and Speaker Recognition Research", *ECTI Transact. on Comput. and Infor. Technol.*, vol. 1, no. 2, pp. 64–74, 2005.

[3] J. Campbell, "Speaker recognition: A tutorial", *Proc. of the IEEE*, vol. 85, no. 9, pp. 1437–1462, 1997 (doi: 10.1109/5.628714).

[4] L. Mary and B. Yegnanarayana, "Extraction and representation of prosodic features for language and speaker recognition", *Speech Communic.*, vol. 50, no. 10, pp. 782–796, 2008 (doi: 10.1016/j.specom2008.04.010).

[5] I. Bhardwaj, "Speaker dependent and independent isolated Hindi word recognizer using hidden Markov model (HMM)", *Int. J. of Comp. Applic.*, vol. 52, no. 7, pp. 34–40, 2012.

[6] S. Squartini, E. Principi, R. Rotili, and F. Piazza, "Environmental robust speech and speaker recognition through multi-channel histogram equalization", *Neurocomputing*, vol. 78, no. 1, pp. 111–120, 2012 (doi: 10.1016/j.neurocom.2011.05.035).

[7] N. S. Dey, R. Mohanty, and K. L. Chugh, "Speech and speaker recognition system using artificial neural networks and hidden Markov model", in *Proc. IEEE Int. Conf. on Communic. Sys. and Network Technol. CSNT*, Bhopal, Madhya Pradesh, India, 2012, pp. 311–315 (doi: 10.1109/CSNT.2012.221).

[8] T. Gaafar, H. Bakr, and M. Abdalla, "An improved method for speech/speaker recognition", in *Int. Conf. on Infor., Electr. and Vision ICIEV*, Dhaka, Bangladesh, 2014 (doi: 10.1109/ICIEV.2014.6850693).

[9] T. A. Smadi, "An improved real-time speech signal in case of isolated word recognition", *Int. J. of Engineer. Research and Applic.*, vol. 3, no. 5, pp. 1748–1754, 2013.

[10] V. Fontaine and H. Bourlard, "Speaker dependent speech recognition based on phone–like units models application to voice dialing", in *Proc. IEEE Conf. on Acoustics, Speech, and Signal Proces. ICASSP'97*, Munich, Bavaria, Germany, 1997, pp. 2–5 (doi: 10.1109/ICASSP.1997.596241).

[11] S. J. Wright, D. Kanevsky, and L. Deng, "Optimization algorithms and applications for speech and language processing", *IEEE Transact. on Audio, Speech and Lang. Proces.* vol. 21, no. 11, pp. 1527–1530, 2013 (doi: 10.1109/TASL.2013.2283777).

[12] M. Mitchell, "Genetic algorithms: An overview 1", *Complexity*, vol. 1, pp. 31–39, 1995 (doi: 10.1102/cplx.6130010108).

[13] M. Sarma, "Speech recognition using deep neural network – recent trends", *Int. J. of Int. Sys. Design and Computing*, vol. 1, no. 12, pp. 71–86, 2017 (doi: 10.1504/IJISDC.2017.082853).

[14] L. Deng, M. Seltzer, D. Yu, A Acero, A. Mohamed, and G. Hinton, "Binary coding of speech spectrograms using a deep auto – encoder", in *Proc. 11th Int. Conf. on Speech Commun. Assoc.*, Makuhari, Chiba, Japan, 2010, pp. 1692–1695, 2010.

[15] F. Guojiang, "A novel isolated speech recognition method based on neural network", *2nd Int. Conf. on Network. and Infor. Technol.*, Singapore, 2011, vol. 17, pp. 264–269.

[16] I. Lopez-Moreno *et al.*, "On the use of deep feed forward neural networks for automatic language identification", *Computer Speech Lang.*, vol. 40, no. C, pp. 46–59, 2016 (doi: 10.1016/j.csl.2016.03.001).

[17] M. Mimura, S. Sakai, and T. Kawahara, "Reverberant speech recognition combining deep neural networks and deep auto encoders augmented with a phone-class feature", *EURASIP J. on Advances in Signal Proces.*, vol. 62, p. 13, 2015 (doi: 10.1186/s13634-015-0246-6).

[18] M. L. Lan, S. T. Pan, and C. C. Lai, "Using genetic algorithm to improve the performance of speech recognition based on artificial neural network", in *1st Int. Conf. on Innovative Computing, Infor. and Control – Vol. I ICICIC'06*, Beijing, China, 2006, vol. 2, no. 1, pp. 6–9 (doi: 10.1109/ICICIC.2006.372).

[19] S. Balochian, E. A. Seidabad, and S. Z. Rad, "Neural network optimization by genetic algorithms for the audio classification to speech and music", *Int. J. of Signal Proces., Image Proces. and Pattern Recog.*, vol. 6, no. 3, pp. 47–54, 2013.

[20] S. King, J. Frankel, K. Livescu, and E. Mcdermott, "Speech production knowledge in automatic speech recognition", *J. of the Acoustic. Soc. of America*, vol. 121, no. 2, pp. 723–742, 2007 (doi: 10.1121/1.2404622).

[21] S. I. Levitan, T. Mishra, and S. Bangalore, "Automatic identification of gender from speech", in *Proc. Conf. on Speech Prosody*, Boston, MA, USA, 2016 pp. 84–88 (doi: 10.21437/SpeechProsody.2016-18).

[22] M. Honda, "Human speech production mechanisms", *NTT Technic. Rev.*, vol. 1, no. 2, pp. 24–29, 2003.

[23] N. S. Nehe and R. S. Holambe, "DWT and LPC based feature extraction methods for isolated word recognition", *EURASIP J. on Audio, Speech, and Music Proces.*, vol. 7 pp. 1–7, 2012 (doi: 10.1186/1687-4722-2012-7).

[24] A. Pramanik and R. Raha, "Automatic speech recognition using correlation analysis", in *Proc. World Cong. on Infor. and Commun. Technol. WICT*, Trivandnum, Kerala, India, 2012 (doi: 10.1109/WICT.2012.6409160).

[25] X. Zhang, Y. Guo, and X. Hou , "A speech recognition method of isolated words based on modified LPC cepstrum", in *IEEE Granular Computing Conf.*, San Jose, CA, USA, 2007 (doi: 10.1109/GrC.2007.96).

[26] I. Hermansky, K. Tsuga, S. Makino, and H. Wakita, "Perceptually based processing in automatic speech recognition", in *Proc. IEEE Conf. on Acoustics, Speech, and Signal Proces. ICASSP'86*, Tokyo, Japan, 1986 (doi: 10.1109/ICASSP.1986.1168649).

[27] S. Swamy and K. V. Ramakrishnan, "An efficient speech recognition", *Int. J. of Comp. Science and Engineer.*, vol. 3, no. 4, pp. 21–27, 2013 (doi: 10.5121/cseji.2013.3403).

[28] H. Ali, N. Ahmad, X. Zhou, K. Iqbal, and S. M. Ali, "DWT features performance analysis for automatic speech recognition of Urdu", *Springer Plus*, vol. 3, pp. 1–10, 2014 (doi; 10.1186/2193-1801-3-204).

[29] G. Kaur, R. Khanna, and A. Kumar, "Automatic speech and speaker recognition using MFCC: Review", *Int. J. of Advances in Science and Technol.*, vol. 2, no. 3, 2014.

[30] G. Kaur, R. Khanna, and A. Kumar, "Implementation of Text Dependent Speaker Verification on Matlab", in *Proc. 2nd Conf. on Recent Adv. in Engineer. and Comput. Sciences RAECS*, Chandigarh, India, 2015 (doi: 10.1109/RAECS.2015.7453344).

[31] R. Price, K. Iso, and K. Shinoda, "Wise teachers train better DNN acoustic models", *EURASIP J. of Audio, Speech, Music Proces.*, vol. 10, art. no. 88, 2016 (doi: 10.1186/s13636-016-0088-7).

[32] D. Reynolds, T. Quatieri, and R. Dunn, "Speaker verification using adapted gaussian mixture models", *Digital Signal Proces.*, vol. 10, pp. 19–41, 2000 (doi: 10.1006/dspr.1999.0361).

[33] F. Seide, G. Li, and D. Yu, "Conversational speech transcription using context-dependent deep neural networks", *Interspeech*, pp. 437–440, 2011.

[34] M. L. Seltzer, D. Yu, Y. Wang, "An investigation of deep neural networks for noise robust speech recognition", in *IEEE Int. Conf. on Acoust. Speech Signal Proces. ICASSP'13*, Vancouver, BC, Canada, 2013 (doi: 10.1109/ICASSP.2013.6639100).

[35] S. Casale, A. Russo, and S. Serrano, "Classification of speech under stress using features selected by genetic algorithms", in *Proc. 14th European Signal Proces. Conf.*, Florence, Tuscany, Italy, 2006 pp. 1–4.

[36] I. Perikos and I. Hatzilygeroudis, "Recognizing emotions in text using ensemble of classifiers", *Engineer. Applic. of Artif. Intel.*, vol. 51, pp. 191–201, 2016 (doi: 10.1016/j.engappai.2016.01.012).

Gurpreet Kaur is an Assistant Professor at the Department of Electronics and Communication Engineering at University Institute of Engineering and Technology, Panjab University, Chandigarh, India. She received her B.Tech. (with honors) in Electronics and Communication Engineering from Kurukshetra University, Haryana in 2004, M.Eng. (with distinction) in Electronics and Communication from the University Institute of Engineering and Technology, Panjab University, Chandigarh in 2007 and is pursuing Ph.D. in Electronics Engineering from IKG Punjab Technical University, Jalandhar. Her current research interests are speech processing and neural networks.
E-mail: regs4gurpreet@yahoo.co.in
I. K. Gujral Punjab Technical University
Kapurthala, Jalandhar, India

University Institute of Engineering & Technology
Panjab University
Chandigarh, India

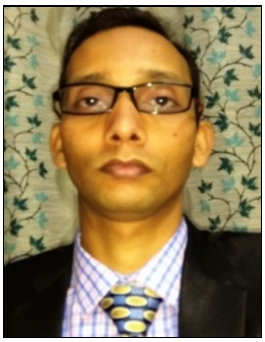

Mohit Srivastava is a Professor at the Department of Electronics and Communication Engineering and R&D Dean at Chandigarh Engineering College, Landran, Mohali, Punjab, India. He received his B.Tech. in Electronics and Communication Engineering from Magadh University, Bodh Gaya, M.Tech. in Digital Electronics and Systems from K.N.I.T. Sultanpur and Ph.D. in Image processing & Remote Sensing from Indian Institute of Technology Roorkee in 2000, 2008 and 2013 respectively. He has more than 15 years of work experience in various environments, including industry, as well as educational and research centers. He has completed two IEDC (DST) funded projects. His current research interests are digital image and speech processing, remote sensing and their applications in land cover mapping, as well as communication systems.
E-mail: mohit.ece.@cgc.edu.in
Chandigarh Engineering College
Landran, Mohali, Punjab, India

Amod Kumar received his B.E. (Hons) in Electrical and Electronic Engineering from Birla Institute of Technology and Science, Pilani, M.E. in Electronics from Punjab University, Chandigarh and Ph.D. in Biomedical Signal Processing from IIT Delhi. He has about 38 years of experience in research and development of different instruments in the area of process control, environmental monitoring, biomedical engineering and prosthetics. He is currently working as Chief Scientist at Central Scientific Instruments Organisation (CSIO), Chandigarh, which is a laboratory of CSIR. He has more than 70 publications in reputed national and international journals. His areas of interest are digital signal processing, image processing and soft computing.
E-mail: csioamod@yahoo.com
Central Scientific Instruments Organisation
Chandigarh, India

Paper

Link Quality Assessment Algorithm for Heterogeneous Self-organizing Maritime Communications Network

Krzysztof Bronk, Adam Lipka, and Rafał Niski

National Institute of Telecommunications, Wireless Systems and Networks Department, Gdańsk, Poland

https://doi.org/10.26636/jtit.2018.121217

Abstract—The article introduces a method of performing a radio link quality assessment based on the Link Quality Indicator (LQI) which will be calculated for every system that is available. The method presented has been developed during the netBaltic project completed in Poland and generally applies to the so-called maritime zone A, i.e. the sea area where ships are still within the range of shore-based radio communication systems, particularly 3G/LTE cellular networks. The algorithm was developed based on the results of measurements obtained during two separate campaigns. That measurement data served as a basis for the method's initial assumptions and was utilized during the method's verification.

Keywords—3G, cellular systems, link quality indicator, LTE, maritime radiocommunications.

1. Introduction

The main purpose of the netBaltic project is to develop a multi-system, self-organizing wideband maritime communications network which will support modern e-navigation features and improve the overall safety of maritime navigation. The network will offer fast data transmission between vessels, vessels and on-shore infrastructure, as well as between vessels and the Internet, using the most suitable link selected from among those available. For the purpose of the project, it is assumed that the entire sea area is divided into three separate zones to which various communication mechanisms apply. That arrangement is illustrated in Fig. 1 [1]:

- in zone A, ships are close enough to the coast to be within range of the shore-based communication systems (mostly cellular networks) and can utilize such systems to communicate with one another (the following paper applies only to zone A),
- in zone B, ships can only communicate with the shore via other ships that are within zone A,
- in zone C, ships are out of any network's range and the main option in this case is a buffered transmission (ship-to-ship communication is also possible, however).

One of the major tasks performed in the course of the netBaltic project is the development of an algorithm enabling to assess quality of the wireless communication links available. The analysis of the links' quality and stability is undoubtedly an important issue and, as such, it is frequently addressed in projects and publications related to contemporary radio communications [2], [3]. The mechanism introduced here will enable the selection of the most suitable (optimal) wireless communication link for the specific type of service. The link's quality will be evaluated based on the so-called Link Quality Indicator (LQI) metric, whose value will be calculated for every system available. The autonomous analysis functionality enabling to assess the quality of various communication links, as well as seamless roaming between them are some of the most important features of the netBaltic network.

The network switches between various communications standards/systems and operators to provide the best quality of the connection and to avoid – to the extent possible – expensive satellite links.

The link quality assessment concept presented in this paper was developed following a thorough analysis of the measurement data obtained during two campaigns that were performed on the Baltic Sea in the course of the netBaltic project. The first took place in the summer of 2015 and its scope mostly included range and quality measurements of the selected cellular systems. As a result, almost 15,000 measurement points were obtained for LTE networks, and roughly 5,000 measurement points for 3G. The results of this campaign helped define the initial assumptions for the LQI algorithm and were utilized during preliminary verification of the method.

The second campaign was held in the winter of 2017 and its main purpose was to gather more detailed results regarding LTE and 3G networks under maritime conditions. This time, the measurement points were obtained with a much greater frequency and, as a result, nearly 30,000 points were collected for LTE and over 42,000 points for 3G networks. These results were sufficient to introduce some modifications into the original version of the LQI algorithm and were later used during its second and final verification.

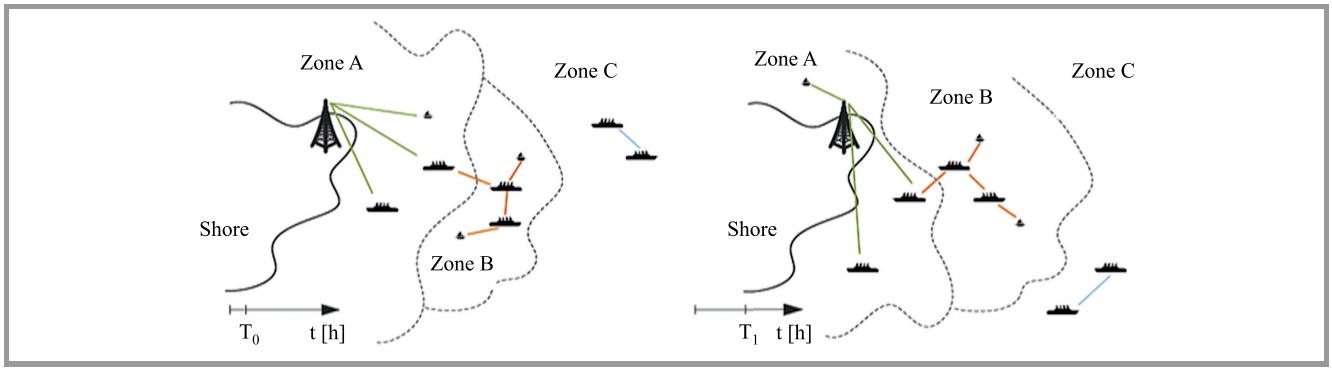

Fig. 1. Operating principle of zones A, B and C introduced for the purpose of the netBaltic project.

2. Measurement Methodology

As it was previously mentioned, the results of the measurement campaigns have been relied upon to define the LQI algorithm. Below, we will provide some explanations concerning the methodology used.

Both measurements were performed on a ship-to-shore basis, meaning that the ship participating in the campaign maintained communications with the infrastructure of shore-based cellular systems (i.e. base stations). No ship-to-ship communication was tested at this stage.

The main component utilized during the campaigns was a Mobile Measurement Platform [4] which was developed by the National Institute of Telecommunications to facilitate measurements of various quality-related parameters of radio communications systems (data rate, delays, received signal level, etc.). Its general architecture is depicted in Fig. 2.

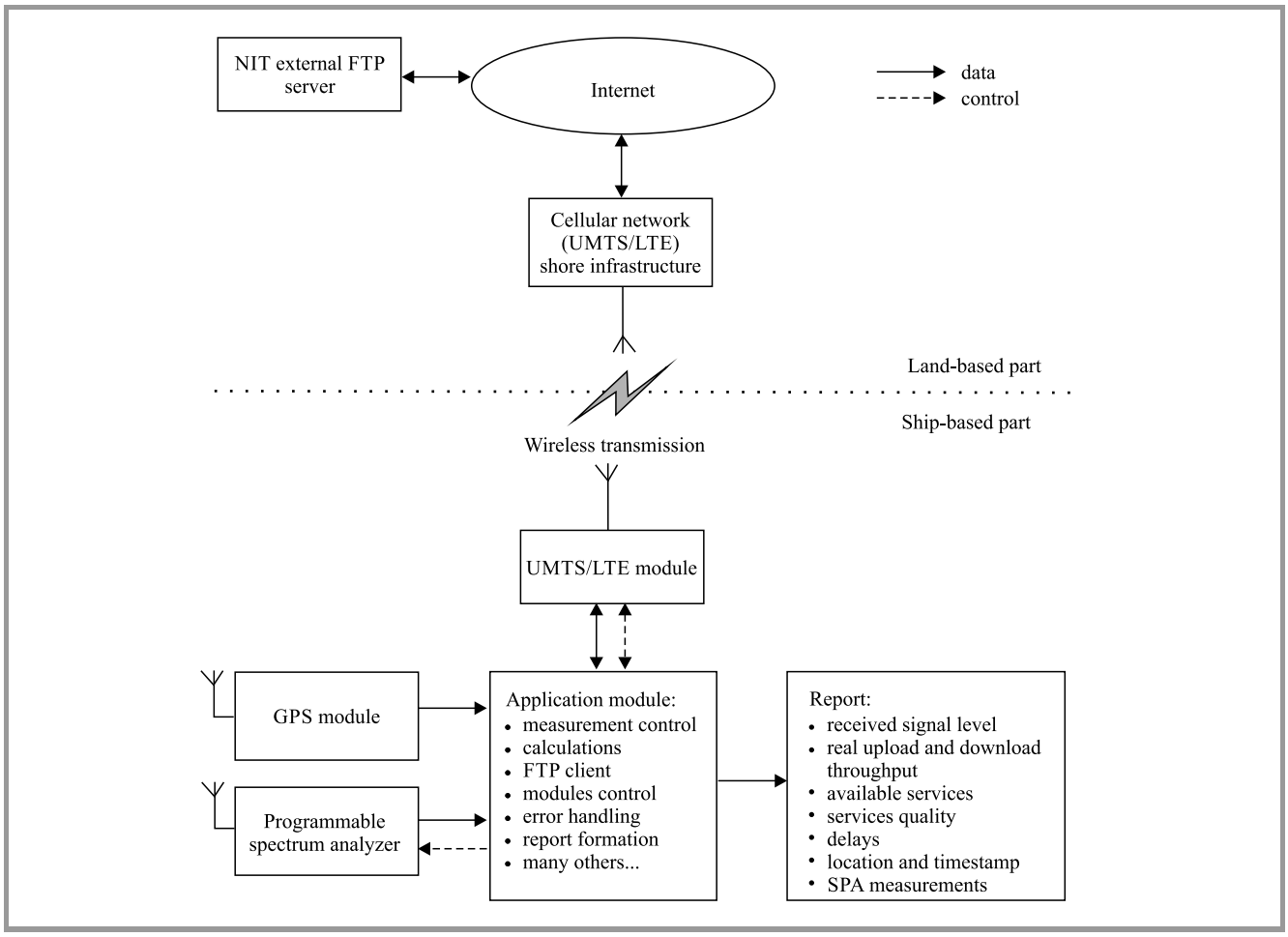

Fig. 2. Mobile Measurement Platform architecture.

Using the 3G/LTE module[1], a radio link between the ship and an external FTP server was set up. Having established the connection, it was possible to initiate a bi-directional data transmission between FTP and the ship, and to measure its duration. To test the downlink transmission, the application module started to download a file from the FTP server. To test the uplink transmission, another file was uploaded into the FTP. The size of the file that was being transmitted at a given moment was not random, but it was selected by the application module using a special algorithm. If the available throughput was low, the file size was gradually decreased to avoid excessive duration of a single measurement. If the throughput increased, it was also possible to increase the test file size. So, we might say that in this case the file size was being changed adaptively. After the transmission was completed, the software calculated actual throughput (separately for downlink and uplink transmissions), by dividing the file size by the transmission duration measured. The 3G/LTE modem used enabled to obtain some additional system parameters as well, i.e. signal power parameters (RSRP, RSCP) and quality parameters (RSRQ, Ec/Io). Using the ICMP protocol, the ping value could be determined as well.

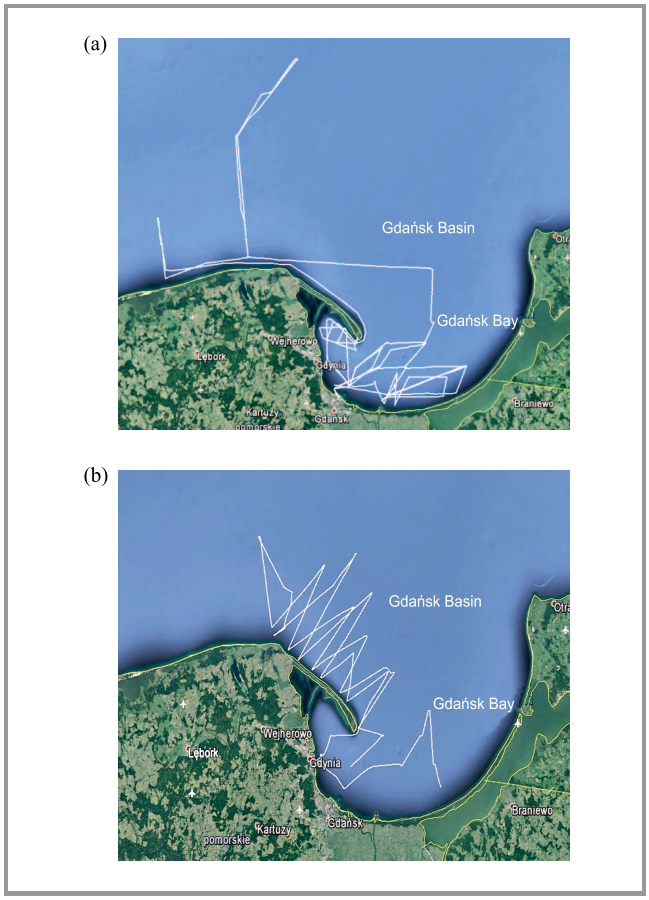

Fig. 3. The ship's routes during the campaigns: (a) in 2015 and (b) in 2017.

[1] LTE USB access head UAH-MC7710-1800-STD, equipped with the Sierra Wireless AirPrime MC7710 LTE/HSPA+ card was used.

The ship that was used during the campaign enabled the antenna to be installed 4 and 10 m above sea level. That made it possible to model two sizes of a vessel (a "small" ship and a "big" ship). The antenna used during the measurements was of the Apex Magforce MB.TG30.A.305111. It supports the most important bands used by cellular 3G/4G systems, namely 698-960 MHz, 1575.42 MHz and 1710–2700 MHz.
In Fig. 3, the ship's routes during the two measurement campaigns (in 2015 and 2017) are presented.

3. LQI Parameter

The LQI parameter grades the quality of the wireless radio links and can be used to compare the quality of various systems, as well as to select the system that is most suitable (i.e. "the best") for a given service/application.
The measurement results obtained on the Baltic Sea during the campaign [5], [6] were used to perform a thorough analysis of the parameters that may affect transmission quality. It was established that in the case of 3G and LTE networks in zone A, quality is best reflected by the data rate and the received signal power. Other parameters, such as transmission delay, jitter or packet loss ratio, also exert some influence on quality, but the instants when their actual values were significantly different from their mean values were usually observed for low data rates, in areas close to the network's coverage border.
While defining the LQI parameter, it was decided that its value would be in the 0–255 range, representing the system's quality. The following initial assumptions have been made in that respect:

- 0–5 Mbps: LQI < 150,
- 5–10 Mbps: $150 <$ LQI < 220,
- 10–15 Mbps: $220 <$ LQI < 255,
- over 15 Mbps: LQI = 255.

The rationale adopted is that low data rates are most crucial for e-navigation and, consequently, they need to be modeled with the highest level of precision.
Using the above assumptions, the $f(R)$ function can be defined to illustrate the relation between LQI and data rate R (in Mbps) (Fig. 4):

$$f(R) = \begin{cases} 0.025R^3 - 1.65R^2 + 36R & \text{for } 0 \le R \le 15 \\ 255 & \text{for } R > 15 \end{cases}. \quad (1)$$

The relation introduced in Eq. (1) is compliant with the initial assumptions and ensures the continuity of the $f(R)$ function around the point $R = 15$ Mbps.
As a result, LQI will correspond to the data rate which is available in the system analyzed. Obviously, that value will depend on the present state of the system, and such a state will be evaluated based on the messages broadcast by base stations. Parameters corresponding to the received signal level and to service quality will then be compared

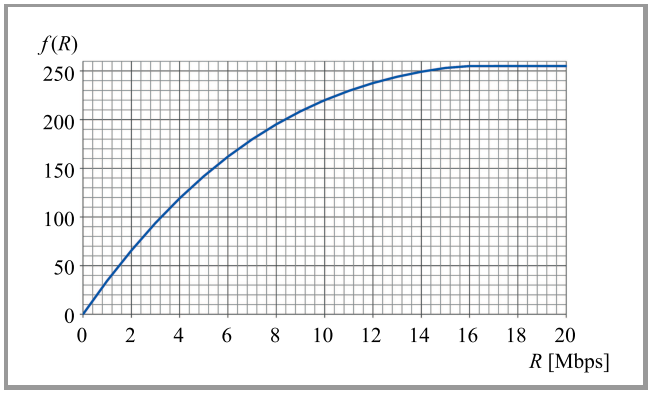

Fig. 4. The $f(R)$ function.

with the measurement data collected during the campaigns, in order to assess the expected system quality and – most importantly – to calculate LQI.

To apply the proposed algorithm, two parameters calculated for the t time need to be known:

- $P_D(t)$ – parameter corresponding to the received signal power and the shortest distance from the shore,
- $P_Q(t)$ – parameter corresponding to the system quality.

Their values are determined through periodic measurements, but the exact calculation procedure varies depending on the network type (3G vs. LTE). $P_D(t)$ and $P_Q(t)$ varies in time due to a number of factors (e.g. changes in propagation conditions or network load), so it is necessary to include also (with appropriate weights) the mean values of such factors, as well as their changes over a long period of time. Consequently, the LQI parameter shall be defined in the following way:

$$LQI(t) = A \cdot \overline{P}_D(t) + B \cdot \overline{P}_Q + C \cdot \widetilde{P}_Q(t) + D \cdot P_Q(t), \quad (2)$$

where: A, B, C, D – weight coefficients, $\overline{P}_D(t)$ – mean value of the parameter corresponding to the received signal power and the distance, $\overline{P}_Q(t)$ – mean value of the parameter corresponding to quality, $\widetilde{P}_Q(t)$ – change in the quality parameter's mean value observed over time.

Let us assume Δt denotes the duration of a single measurement (i.e. the interval time between two consecutive measurement cycles). In that case the period over which the mean values of $P_D(t)$ and $P_Q(t)$ are calculated can be expressed as $N \cdot \Delta t$, where N is the total number of the collected measurements.

Given the above:

$$\overline{P}_D(t) = \frac{1}{N} \sum_{n=0}^{N-1} P_D(t - n \cdot \Delta t), \quad (3)$$

$$\overline{P}_Q(t) = \frac{1}{N} \sum_{n=0}^{N-1} P_Q(t - n \cdot \Delta t), \quad (4)$$

$$\widetilde{P}_Q(t) = \overline{P}_Q(t) - \overline{P}_Q(t - \Delta t). \quad (5)$$

As per initial assumptions, the LQI value is in the range of 0–255, so whenever the value calculated using Eq. (2) is greater than 255 or lower than 0, it shall be equal to 255 or 0, respectively. The weight coefficients A–D might vary for each of the systems analyzed, and the way they are obtained will be explained in the following section.

4. Calculation of LQI for LTE Cellular Networks

Once the measurement results have been analyzed, it was established that parameters $P_Q(t)$ and $P_D(t)$ for the LTE networks should be derived from the Reference Signal Received Quality (RSRQ) and Reference Signal Received Power (RSRP) values [7].

The measurement campaigns indicate that the expected data rate R can be estimated based on the RSRQ level. In Fig. 5, the measured values of the mean RSRQ are presented as a function of the downlink data rates for various frequency bands and channel bandwidths. The curve representing LTE "free mode" serves as a basis for the generic approximation function which will be used to determine the data R. The term "free mode" represents a situation where exact frequency parameters of the LTE network are unknown and are selected automatically by the network.

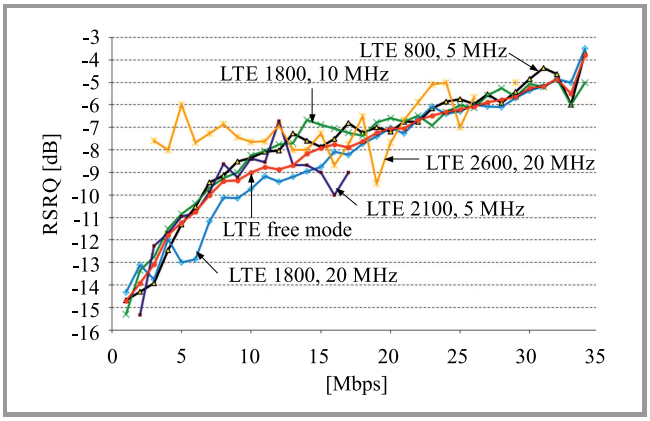

Fig. 5. Mean RSRQ as a function of data rate for different frequency bands and channel bandwidths. (See color pictures online at www.nit.eu/publications/journal-jtit)

For data rates above 15 Mbps, the LQI value saturates at 255. The same constraint had to be introduced for the approximation function as well. The relation between the value of the approximation function and RSRQ can be expressed as (Fig. 6):

$$R\,[\text{Mbps}] = \begin{cases} 10^{\frac{\text{RSRQ}+16.25}{7.1}} & \text{for RSRQ} \le -8\ \text{dB} \\ 15 & \text{for RSRQ} > -8\ \text{dB} \end{cases}. \quad (6)$$

Using the value of the data rate R expected in time t, the $P_Q(t)$ can be determined on the basis of the $f(R)$ function defined in Eq. (1), i.e.:

$$P_Q(t) = f\big(R(t)\big). \quad (7)$$

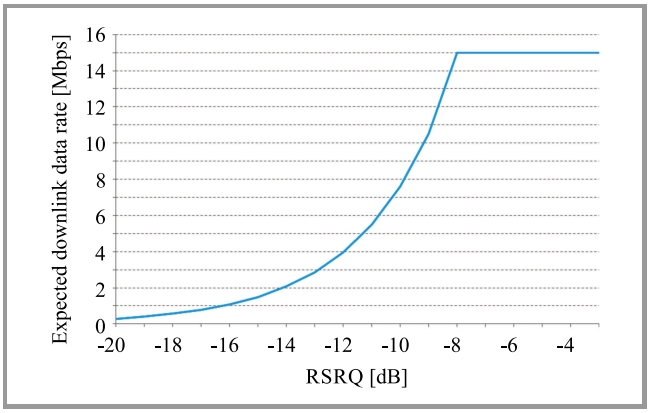

Fig. 6. Approximation function for the LTE networks defined by Eq. (6).

As a result, the $P_Q(t)$ will also have its values limited to the 0–255 range.
In the next step, the $\overline{P}_Q(t)$ and $\widetilde{P}_Q(t)$ values are calculated using Eqs. (4) and (5), respectively. Having completed that, three out of four parameters required for the LQI evaluation are available.

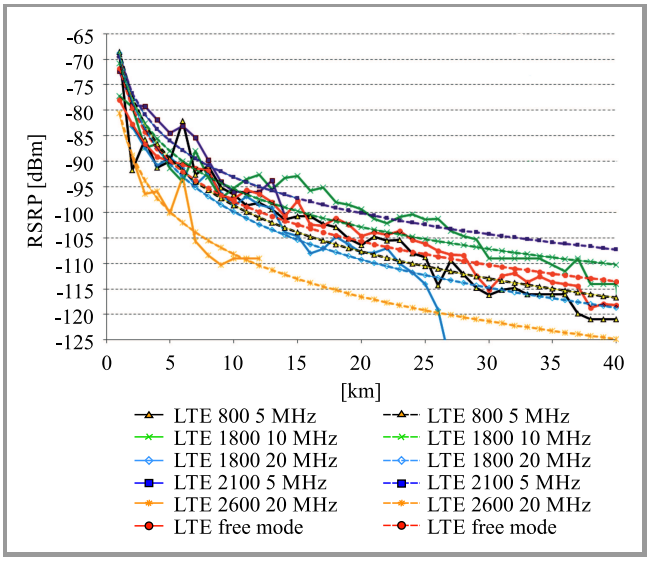

Fig. 7. Relationship between RSRP and the distance from the shore.

The last unknown factor $\overline{P}_D(t)$ is related to the received signal power and depends on the distance from the shore. It is calculated using the RSRP. The importance of the $\overline{P}_D(t)$ is particularly high in the areas close to the networks' coverage border. Results obtained during the measurement campaigns did not provide a clear and unambiguous relationship between RSRP and the data rate (as it was the case for the RSRQ). On the other hand, a distinct relationship between the RSRP and the distance from the shore has been noticed and it is presented in Fig. 7. The solid lines depict actual measurement results, whereas dotted ones represent the functions that approximate those results.

During the measurement campaigns, it was sometimes the case that the RSRP level and the data rate decreased significantly as the terminal's distance from the shore increased, but at the same time the RSRQ level did not change or even gained a little. The results obtained indicate that in such cases a 5 dB decrease of RSRP resulted in a mean data rate dropping by approximately 10%. That observation helped establish the relationship between RSRP and the data rate using the following procedure. First, the RSRP level anticipated at a given distance from the shore needs to be calculated using the approximation function shown in Fig. 7. The analytical formulas of these functions are:

$$\mathrm{RSRP}\big(d\ [\mathrm{km}]\big)[\mathrm{dBm}] = \begin{cases} -30.095\cdot\log(d)-66.50 & \text{for LTE 800, 5 MHz} \\ -24.615\cdot\log(d)-70.81 & \text{for LTE 1800, 10 MHz} \\ -31.131\cdot\log(d)-68.76 & \text{for LTE 1800, 20 MHz} \\ -23.509\cdot\log(d)-69.57 & \text{for LTE 2100, 5 MHz} \\ -27.608\cdot\log(d)-80.58 & \text{for LTE 2600, 20 MHz} \\ -26.065\cdot\log(d)-71.76 & \text{for LTE free mode} \end{cases}. \quad (8)$$

The approximation functions have been assigned to each of LTE network types analyzed during the measurements (the type is described by network frequency and channel bandwidth). In the next step, the $\mathrm{RSRP}_{\mathrm{approx}}(d)$ value obtained using Eq. (8) compared with the $\mathrm{RSRP}_{\mathrm{meas}}(t)$ value measured at a given time t. If the approximated value is greater than the measured one, transmission quality degradation can be expected and the value of $P_D(t)$ should be negative. If the opposite is true, one might expect that transmission conditions will improve and, consequently, the $P_D(t)$ will assume a positive value. Given the above, the change of the expected data rate can be expressed as:

$$\Delta R = \frac{\mathrm{RSRP}_{\mathrm{meas}}(t) - \mathrm{RSRP}_{\mathrm{approx}}(d)}{50}\cdot 100\%, \quad (9)$$

where $\mathrm{RSRP}_{\mathrm{meas}}(t)$ and $\mathrm{RSRP}_{\mathrm{approx}}(d)$ are in dBm.
The measurement results showed also that the RSRP level near the end of the coverage area usually fluctuated between –110 and –120 dBm. The fact that the terminal is getting closer to the border of the network's coverage can be modeled by introducing a new parameter G_{LTE} which will additionally decrease the expected data rate by 10, 20 or 30%:

$$G_{LTE}\ [\%] = \begin{cases} 0 & \text{for } -110\ \mathrm{dBm} < \mathrm{RSRP}_{\mathrm{meas}}(t) \\ 10\% & \text{for } -115\ \mathrm{dBm} \le \mathrm{RSRP}_{\mathrm{meas}}(t) < -110\ \mathrm{dBm} \\ 20\% & \text{for } -120\ \mathrm{dBm} \le \mathrm{RSRP}_{\mathrm{meas}}(t) < -115\ \mathrm{dBm} \\ 30\% & \text{for } \mathrm{RSRP}_{\mathrm{meas}}(t) \le -120\ \mathrm{dBm} \end{cases}. \quad (10)$$

Now $P_D(t)$ can be defined as:

$$P_D(t) = f\big(R(t)\cdot(1+\Delta R - G_{LTE})\big) - f\big(R(t)\big). \quad (11)$$

In the subsequent step, the value of $\overline{P}_D(t)$ can be calculated by applying Eq. (3). Hence, all four parameters necessary to obtain the LQI for the LTE network in zone A are now known and available for further processing.

5. Calculation of LQI for 3G Cellular Networks

On the basis of the measurement results, it was established that parameters $P_Q(t)$ and $P_D(t)$ for UMTS networks should be derived using the values of the Received Signal Code Power (RSCP) and Ec/Io [8], respectively.

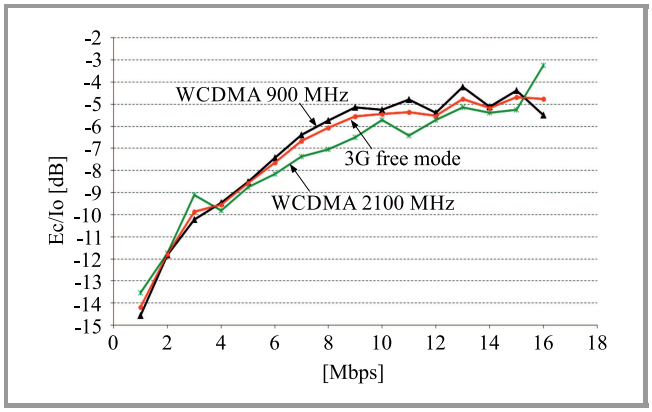

Fig. 8. Relationship between Ec/Io and the downlink data rate.

Similarly to the LTE network, the expected UMTS data rate R can be determined from the measurement data. The relationship between the mean value of Ec/Io and the downlink data rate is presented in Fig. 8 for two frequency bands (900 and 2100 MHz). As one can observe, those characteristics are relatively similar, so the approximation function was defined on the basis of the 3G free-mode characteristic. This will make it possible to determine the expected value of the data rate R. Just as it was the case for LTE, the 3G approximation function saturates for data rates

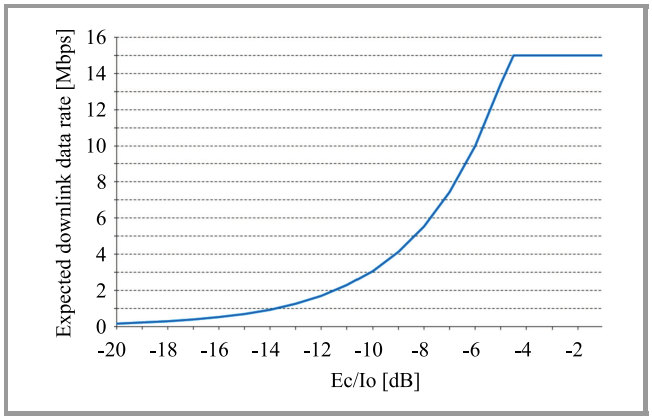

Fig. 9. Approximation function characteristics for the 3G networks, defined by Eq. (12).

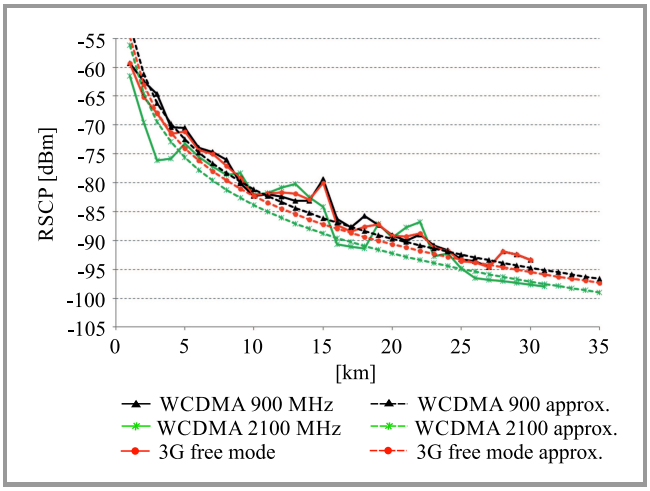

Fig. 10. Relationship between RSCP and the distance from the shore.

above 15 Mbps, and its analytical formula can be expressed as (Fig. 9):

$$R\,[\text{Mbps}] = \begin{cases} 10^{\frac{\text{Ec/Io}+13.8}{7.8}} & \text{for Ec/Io} \le -4.5\ \text{dB} \\ 15 & \text{for Ec/Io} > -4.5\ \text{dB} \end{cases}. \quad (12)$$

Having calculated the value of the data rate predicted for time t, it is now possible to calculate $P_Q(t)$ using Eq. (7). As a result, $P_Q(t)$ is limited to 0–255.

Next, the $\overline{P}_Q(t)$ and $\widetilde{P}_Q(t)$ are calculated using Eqs. (4) and (5), respectively.

The last unknown parameter $\overline{P}_D(t)$ is related to the received signal power and depends on the distance from the shore. It is calculated using the RSCP. The importance of $\overline{P}_D(t)$ is particularly vital in areas close to the coverage border. The measurement did not provide a clear and unambiguous relationship between RSCP and data rate (as it was the case for Ec/Io). On the other hand, a distinct relationship between RSCP and distance from the shore has been observed and is presented in Fig. 10, where solid lines depict measurement results, and dotted ones represent functions that approximate those results. The analytical formulas of these functions are:

$$\text{RSCP}\big(d\ [\text{km}]\big)[\text{dBm}] = \\ = \begin{cases} -28.5 \cdot \log(d) - 52.6 & \text{for WCDMA 900} \\ -27.7 \cdot \log(d) - 56.2 & \text{for WCDMA 2100} \\ -27.6 \cdot \log(d) - 54.7 & \text{for 3G free mode} \end{cases}. \quad (13)$$

The approximation functions have been assigned to each of the 3G network types analyzed during the measurement (the type is described by the frequency utilized by a given 3G network). In the next step, the $\text{RSCP}_{\text{approx}}(d)$ value obtained using Eq. (13) is compared with the $\text{RSCP}_{\text{meas}}(t)$ value measured in time t. If the approximated value is greater than the measured one, transmission quality degradation can be expected and the value of $P_D(t)$ should be negative. If the opposite is true, one may expect that

transmission conditions will improve and, consequently, $P_D(t)$ will be assume a positive value. Given the above, the change in the expected data rate can be expressed as:

$$\Delta R = \frac{\mathrm{RSCP}_{\mathrm{meas}}(t) - \mathrm{RSCP}_{\mathrm{approx}}(d)}{50} \cdot 100\%, \qquad (14)$$

where $\mathrm{RSCP}_{\mathrm{meas}}(t)$ and $\mathrm{RSCP}_{\mathrm{approx}}(d)$ are in dBm.

The measurements have also shown that the RSCP level near the coverage border usually fluctuated between –100 and –120 dBm. The fact that the terminal is getting closer to the network's coverage border can be modeled by introducing a new parameter, $G_{3\mathrm{G}}$, which will additionally decrease the expected data rate by 10, 20 or 30%, according to the formula:

$$G_{3\mathrm{G}}\,[\%] = \begin{cases} 0 & \text{for } -90 \text{ dBm} < \mathrm{RSCP}_{\mathrm{meas}}(t) \\ 10\% & \text{for } -105 \text{ dBm} \le \mathrm{RSCP}_{\mathrm{meas}}(t) < -90 \text{ dBm} \\ 20\% & \text{for } -120 \text{ dBm} \le \mathrm{RSCP}_{\mathrm{meas}}(t) < -105 \text{ dBm} \\ 30\% & \text{for } \mathrm{RSCP}_{\mathrm{meas}}(t) \le -120 \text{ dBm} \end{cases}. \qquad (15)$$

The $P_D(t)$ can now be defined as:

$$P_D(t) = f\big(R(t) \cdot (1 + \Delta R - G_{3\mathrm{G}})\big) - f\big(R(t)\big)\,. \qquad (16)$$

In the final step, the $\overline{P}_D(t)$ can be calculated by using Eq. (3).

6. Calculation of LQI Weight Coefficients

Using research presented in Sections 4 and 5, a more thorough analysis of the proposed algorithm has been performed based on the following assumptions:

- weight coefficients that appear in Eq. (2) will be calculated independently for 3G and LTE networks;
- analysis will cover downlink transmission only;
- three different averaging periods for P_Q and P_D parameters have been adopted (3, 5 and 10 min);
- the measurement series lasting at least 15 min have been extracted from the measurement data. Those series account for approximately 90% of all the data obtained during the campaigns;
- some data was discarded before further analysis. That includes those pieces of data for which the relationship between RSRQ (Ec/Io) and the data rate varied significantly from the overall relationship observed throughout the entire campaign. Once this step has been performed, the data left for further analysis comprised approximately 80% of the initial data set.

Next, the following elements were calculated for each of the measurement series extracted:

- three values of the LQI corresponding to three different averaging periods, denoted as LQI 3/5/10;
- based on the measurements, the LQI value corresponding to a given data rate was calculated: $\mathrm{LQI}(R_{\mathrm{current}}) = f(R_{\mathrm{current}})$, and compared with the expected LQI 3/5/10 calculated using the system parameters;
- for each measurement point collected, the average error of LQI calculation was determined: $\Delta\mathrm{LQI} = \mathrm{LQI\ 3/5/10} - \mathrm{LQI}(R_{\mathrm{current}})$;
- for each measurement series, the average error ΔLQI and its standard deviation were calculated;
- for all the series, the weighted average value and average standard deviation were calculated.

Coefficients A–D from Eq. (2) were derived empirically, in such a way that the average error of LQI calculation was equal to zero and the value of its standard deviation was kept as low as possible. During the first stage of the LQI algorithm verification, it was proven that this method models the actual performance of LTE/3G networks quite faithfully, and that the best results can be achieved for a 3-minute averaging period. Those observations served as a starting point for further activities. The analysis conducted has also shown that quality parameters of cellular networks should be monitored with a higher frequency (at that point such measurements were taken every 30 s). As a result, before further analysis, it was necessary to introduce some modifications to the measurement procedures implemented in the Mobile Measurement Platform [4].

During the second measurement campaign, the 3-second interval was used, which significantly increased the amount of the data collected. The way that data was analyzed was quite similar to the method adopted in the first step of the verification process. However, the averaging period for $P_D(t)$ and $P_Q(t)$ was 3 minutes, and the duration of the data series that was taken into account had to exceed 5 minutes.

The most significant difference between the first and the second verification was that in the latter we did not compare the ΔLQI error, but the difference between the expected data rate derived from LQI and the actual (real) data rate observed at a given time. Additionally, it was assumed that whenever the real data rate exceeded 15 Mbps, the value used for the purpose of comparison was equal to 15 Mbps, which results from the adopted definitions of LQI and the $f(R)$ function.

Having completed this entire procedure, the final formulas defining the LQI for 3G and LTE, respectively (which take into account the empirical coefficients A–D), are:

$$LQI_{3\mathrm{G}}(t) = 0.57 \cdot \overline{P}_D(t) + 0.95 \cdot \overline{P}_Q(t) + \\ +0.56 \cdot \widetilde{P}_Q(t) + 0.14 \cdot P_Q(t)\,, \qquad (17)$$

$$LQI_{LTE}(t) = 0.53 \cdot \overline{P}_D(t) + 0.89 \cdot \overline{P}_Q(t) + \\ +0.50 \cdot \widetilde{P}_Q(t) + 0.12 \cdot P_Q(t)\,. \qquad (18)$$

In both cases the average error of the data rate estimation was equal to zero, and the standard deviation was 1.8 Mbps for the 3G network and 3.7 Mbps for LTE.

7. Conclusions

Versatility is one of the unquestionable advantages of the method introduced in this paper. The algorithm is not based on a single factor, but rather takes into account both power and quality factors. To a certain extent, it can also be adapted and tailored for the purpose of assessment of other links (e.g. WiMAX). It should be underlined that the correct operation of the algorithm has been verified and confirmed in the course of an extended measurement campaign that was performed in the target environment – i.e. at sea. On the other hand, it has to be strongly stated that the values on which the algorithm is based – power and quality – as important as they are, are not the only factors that affect the actual quality of a radio link. The final output of the LQI algorithm is hence an approximation of the real value. Another limitation of the method is the fact that due to the averaging process, quality estimation is slightly delayed. An attempt has been made to mitigate that issue by using an additional power-related parameter which enables to "predict" that the terminal is approaching the cell's border.

In general, the LQI algorithm proposed is applicable mostly to the systems for which the measurable quality and power parameters have been defined, i.e. 3G/HSPA and LTE/LTE-A cellular networks or WiMAX networks. The algorithm has been verified both in the coastal waters (the Bay of Gdańsk) and at open sea (see Fig. 3). Basically, the method can be utilized for any type of shore-based infrastructure and for any telecommunications providers, but in the latter case the specific features of their networks should be taken into account. It has to be underlined that the measurements described in this paper were conducted for two different cellular operators.

Obviously, besides the systems for which the LQI method is applicable, there exist other communication solutions that might be utilized in the netBaltic network as well. That is particularly the case in zone B, for which Wi-Fi communication is likely to be the major transmission mechanism. As opposed to cellular systems, Wi-Fi networks do not offer any unambiguous quality parameters and their characteristics are very different from 3G/LTE (e.g. small distances between stations, low antenna heights at both radio link ends, license-free ISM band utilization, etc.). In light of the above, an attempt has been made to define a universal quality parameter for the netBaltic zone B, which would be based on the measured intervals between consecutive control packets. Those packets will be introduced in the netBaltic network and they will be primarily used to maintain the network's topology.

It should be noted that, to a certain extent, the LQI algorithm presented in this paper can be considered a special type of cognitive radio (CR). In CR, the frequency channel is selected automatically, depending on its availability, to avoid congestion and interference with primary users. In the case of the LQI algorithm, this "automatic selection" refers not only to the frequency, but most notably to the standard of wireless transmission. So, here, the primary goal is to ensure the best possible transmission conditions for the user (by maximizing the LQI metric). On the other hand, it can also be stated that in the case of CR, the algorithm is relatively simpler, because the same measure can be used to achieve the goal (i.e. to select the optimum frequency channel), whereas in the LQI algorithm, the selection is made from among several various, incomparable transmission standards. Consequently, in this case, the same measure cannot be used for LTE, 3G, Wi-Fi or any other system discussed. That is why the authors provided, in the paper, two separate LQI formulas for LTE and 3G – see Eqs. (17) and (18). This accentuates the fact that on the conceptual level, the LQI algorithm is rather complex and requires analysis of many input parameters which vary in time.

Even though this is beyond the scope of this article, it should be also noted that the range (service coverage) of radio systems in zone A is generally limited. Currently, organizations such as IALA and ITU are working on a novel maritime communication standard known as VHF Data Exchange System (VDES) [9], [10] which should substantially help overcome that limitation. Another factor that will strongly contribute to the enhancement of quality of maritime communication is e-navigation. This concept has been developing rapidly over the past years, which is demonstrated by a large number of relevant publications and projects and by a general interest shown by the maritime community (including IMO and IALA). One of the projects dealing with that area is EfficienSea 2.0 [11], in which the National Institute of Telecommunications is deeply involved.

Acknowledgments

This work has been partially supported by the (Polish) Applied Research Program under the Grant No. ID PBS3/A3/20/2015, founded by the National Center for Research and Development.

References

[1] netBaltic project website (in Polish) [Online]. Available: www.netbaltic.pl (accessed: 29 Jan. 2018).

[2] Z. Jinglong, M. Jacobsson, E. Onur, and I. Niemegeers, "A novel link quality assessment method for mobile multi-rate multi-hop wireless networks", in *Proc. 6th IEEE Consumer Commun. and Netw. Conf. CCNC 2009*, Las Vegas, NV, USA, 2009 (doi: 10.1109/CCNC.2009.4784751).

[3] B. C. YI, X. Jin, C. Liu, X. Li, and Y. Wei, "Relative link quality assessment and hybrid routing scheme for wireless mesh networks", in *Proc. IEEE Int. Conf. on Commun. ICC 2011*, Kyoto, Japan, 2011 (doi: 10.1109/icc.2011.5963284).

[4] K. Bronk, R. Niski, and B. Wereszko, "Measurement of data transmission quality in the area of Tri-City in the networks of selected cellular operators", *Przegląd Telekomun. + Wiadomości Telekomun.*, no. 4, 2015, pp. 197–200 (in Polish).

[5] Report from the measurement campaign on the Baltic Sea, 2015, netBaltic project documentation, National Institute of Telecommunications.

[6] Report from the measurement campaign on the Baltic Sea, 2017, netBaltic project documentation, National Institute of Telecommunications.

[7] 3GPP TS 36.214 V14.2.0 (2017) Technical Specification Group Radio Access Network; Evolved Universal Terrestrial Radio Access (E-UTRA); Physical layer; Measurements (Release 14).

[8] 3GPP TS 25.215 V14.0.0 (2017) Technical Specification Group Radio Access Network; Physical layer; Measurements (FDD) (Release 14).

[9] ITU-R M.2092-0 (10.2015) "Technical characteristics for a VHF data exchange system in the VHF maritime mobile band".

[10] K. Bronk, M. Mazurowski, D. Rutkowski, and B. Wereszko, "Badania symulacyjne warstwy fizycznej naziemnego segmentu systemu VDES (Simulation analysis of the physical layer of the VDES terrestrial segment)", *Przegląd Telekomun. + Wiadomości Telekomun.*, no. 6, 2016, pp. 467-470 (in Polish).

[11] K. Bronk, A. Lipka, R. Niski, B. Wereszko, and K. Wereszko, "Hybrid communication network for the purpose of maritime applications", *Int. J. of Maritime Engin.*, vol. 159, part A1, pp. 115–122, 2017 (doi: 10.3940/rina.ijmme.2017.a1.396tn).

Krzysztof Bronk holds a Ph.D. degree (2010) and is an Assistant Professor at the National Institute of Telecommunications. He is an author or co-author of more than 60 reviewed scientific articles and publications, technical documents and studies. His research focuses mainly on radio communication systems, networks design and planning, development of software-defined and cognitive radio systems, multi-antenna technology, cryptography, propagation analysis, transmission and coding techniques, as well as positioning systems and techniques. His interests include also multi-thread and object-oriented applications, devices controlling applications, DSP algorithms and quality measurement solutions.

ORCID ID: https://orcid.org/0000-0002-3594-8462
E-mail: K.Bronk@itl.waw.pl
National Institute of Telecommunications
Wireless Systems and Networks Department
Jaśkowa Dolina 15
80-252 Gdańsk, Poland

Adam Lipka received his M.Sc. and Ph.D. degrees in Telecommunications from the Gdańsk University of Technology in October 2005 and June 2013, respectively. Since January 2006, he has been working at the National Institute of Telecommunications at its Wireless Systems and Networks Department in Gdańsk (currently as an Assistant Professor). His scientific interests include contemporary transmission techniques, MIMO systems and radio waves propagation. He is an author or co-author of over 50 scientific papers and publications.

ORCID ID: https://orcid.org/0000-0002-2919-4270
E-mail: A.Lipka@itl.waw.pl
National Institute of Telecommunications
Wireless Systems and Networks Department
Jaśkowa Dolina 15
80-252 Gdańsk, Poland

Rafał Niski graduated from Gdańsk University of Technology in 2001, receiving an M.Sc. in radio communications. Since then, he has been working at the National Institute of Telecommunications in Gdańsk, at first as an Assistant Professor, and after receiving his Ph.D. degree in 2006, as an Associate Professor. Between 2005 and 2012 he was the Head of Wireless Systems and Networks Department, and since 2016 he has been the Head of the Network and Equipment Measurement section. His scientific research concerns the theory and techniques of mobile communication, radio networks design and planning, as well as measurements of transmission and quality-related parameters in radio networks. He is an author or co-author of nearly 90 scientific publications. Since 2007 he has been a member of the Scientific Council of the National Institute of Telecommunications.

ORCID ID: https://orcid.org/0000-0002-5106-9046
E-mail: R.Niski@itl.waw.pl
National Institute of Telecommunications
Wireless Systems and Networks Department
Jaśkowa Dolina 15
80-252 Gdańsk, Poland

Paper

Comparative Analysis of QoS Management and Technical Requirements in 3GPP Standards for Cellular IoT Technologies

Valery Tikhvinskiy[1,2], Grigory Bochechka[1,2], Andrey Gryazev[3], and Altay Aitmagambetov[4]

[1] *LLC Icominvest, Moscow, Russian Federation*
[2] *Moscow Technical University of Communications and Informatics, Moscow, Russian Federation*
[3] *Federal State Unitary Enterprise Central Science Research Telecommunication Institute, Moscow, Russian Federation*
[4] *International IT University, Almaty, Kazakhstan*

https://doi.org/10.26636/jtit.2018.122717

Abstract—Optimization of 3GPP standards that apply to cellular technologies and their adaptation to LPWAN has not led to positive results only enabling to compete on the market with the growing number non-cellular greenfield LPWAN technologies – LoRa, Sigfox and others. The need to take into consideration, during the 3GPP standard optimization phase, the low-cost segment of narrow-band IoT devices relying on such new technologies as LTE-M, NB-IoT and EC-GSM, has also led to a loss of a number of technical characteristics and functions that offered low latency and guaranteed the quality of service. The aim of this article is therefore to review some of the most technical limitations and restrictions of the new 3GPP IoT technologies, as well as to indicate the direction for development of future standards applicable to cellular IoT technologies.

Keywords—3GPP, EC-GSM, LTE, NB-IoT, QoS, standardization, RAT.

1. Introduction

The global economy is rapidly becoming digital. The creation of a digital single market is currently one of European Union's key priorities [1]. With the technological aspect of digital economy considered, one comes to the conclusion that ICT technologies have become a basis of the modern digital economy, as they connect nearly everything in the world. The Internet of Things (IoT) is the most prominent one. Applications for vertical markets require development of new wireless access technologies based on modern 3GPP cellular solutions, optimized for low-power wide area (LPWA) technology requirements. LPWA applications are characterized by the sending of small payloads of data at infrequent intervals (perhaps just a few times an hour).

The attractiveness of the concept of creating and standardizing the low-power wide area technology based on 3GPP has been proved by the infrastructure that is already operational and by the explosive growth in demand for IoT services with CAGR, expected to reach over 33–50% by 2022 [2], [3].

However, in addition to positive results, such as reduction of the cost of devices and meeting the requirements for LPWA, the transition to narrowband technologies has also brought about significantly limited opportunities, such as Quality of Service (QoS), mobility and a number of others. Narrowband IoT is a machine type communication (MTC) technology that is specifically optimized for IoT.

This article is devoted to a comparative analysis of the impact that 3GPP standards applicable to new narrowband IoT access technologies exert on QoS in IoT access networks, as well as to the impact of these technologies on the IoT business model.

2. Analysis of 3GPP Cellular IoT Standardization of LPWA Requirements

In November 2015, 3GPP provided for specifications for Narrowband IoT (NB-IoT). New radio access technologies (RAT) for cellular IoT, based, to a great extent, on the non-backward-compatible variant of E-UTRA/GERAN, address improved indoor coverage, support a massive number of low throughput devices, as well as offer low delay sensitivity, ultra-low device cost, low device power consumption and optimized network architecture.

LPWANs are low-power wireless wide area networks technologies that specialize in interconnecting devices with IoT/M2M applications that have low data rates, require long battery lives and operate unattended over prolonged periods time, often at remote locations.

Table 1
Cellular IoT technology parameters

Parameters	LTE-M (1.4 MHz)	NB-IoT (180 kHz)	EC-GSM (200 kHz)
Improved coverage including indoor	156 dB MCL (+15 dB improvement)	164 dB MCL (+20 dB improvement)	164 dB MCL (+20 dB improvement)
Range (outdoor)	$<$ 11 km	$<$ 15 km	$<$ 15 km
Massive IoT capacity	$>$ 52 kdev./cell/180 kHz	$>$ 52 kdev./cell/180 kHz	$>$ 52 kdev./cell/180 kHz
Data rate	$<$ 1 Mbps	$<$ 200 kbps	$<$ 70 kbps
Battery life	$>$ 10 years	$>$ 10 years	$>$ 10 years
Latency	$<$ 10 s	$<$ 10 s	$<$ 10 s
Low cost IoT module	5 USD (2016)/ 3.3 USD (2020)	4 USD (2016)/ 2–3 USD (2020)	5.5 USD (2016)/ 2.9 USD (2020)
Spectrum deployment scenario	In-band	In-band, stand alone, guard-band	Stand-alone
Network upgrade	To be determined	Yes (HW/SW?)	Yes (HW/SW?)

3GPP Requirements include some important market and technological parameters [4]:

- low-cost devices should be less than 5 USD,
- long battery life in order of 10 years,
- extreme low data rate network support,
- extended coverage similar to GPRS, with the maximum coupling loss (MCL) of approx. 164 dB,
- support of a massive number of devices, requiring high cell capacity (40 devices per household, 55,000 devices per cell),
- low data and low latency support (a few kbps and below 10 s),
- low deployment and operation cost, and very high network availability,
- consistent and meaningful user experience – QoS.

Three different cellular IoT technologies (Table 1) are standardized in 3GPP, with two of them based on E-UTRAN and one – on GERAN [5]:

- the first solution was LTE-M, released in 2014, under Release 12, as an evolution of LTE Advanced, optimized for IoT in the 3GPP RAN working group. Further optimization was continued in Release 13, with specifications completed in 2016;
- NB-IoT is the narrowband evolution of E-UTRAN for IoT, developed in the 3GPP RAN working group. It was included in Release 13, with technical specifications completed in 2016;
- EC-GSM-IoT is an evolution of GERAN, optimized for IoT in the 3GPP GERAN working group, included in Release 13, with specifications completed in 2016.

The first solution, i.e. LTE-M or eMTC, differs from the LPWA solutions in that it uses a standard LTE air interface and a broadband radio channel with the bandwidth of 1.4 MHz in relation to other technologies. LTE-M offers a new power-saving functionality, suitable for serving a IoT applications. In LTE-M, the power saving mode and eDRX [6] extend battery life for LTE-M to 10 years or more. LTE-M has a reduced peak rate. This can be achieved by limiting the maximum block size to less than 1000 bits, or the number of physical resource blocks (PRBs) allocated each time to 6 or less, or by reducing the modulation order, i.e. QPSK only.

LTE-M traffic is multiplexed over the full LTE carrier, and it is therefore able to tap into the full capacity of LTE. New functionalities for substantially reduced device cost and extended coverage for LTE-M are also specified within 3GPP.

NB-IoT is a 3GPP RAT that forms a part of the cellular IoT network. It provides access to network services via E-UTRA, with the channel bandwidth limited to 180 kHz, corresponding to one physical resource block (PRB). NB-IoT is a subset of E-UTRAN. The NB-IoT technology provides lean setup procedures, while capacity evaluation indicates that each 180 kHz NB-IoT carrier can support more than 200,000 subscribers. The solution can be easily scaled up by adding multiple NB-IoT carriers. NB-IoT also comes with an extended coverage of up to 20 dB, and battery saving features.

Table 2
Bandwidth of NB-IoT channel in compared to LTE channels

Channel bandwidth NB-IoT [MHz]	0.18	1.4	3	5	10	15	20
LTE [MHz]	1	6	15	25	50	75	100

The bandwidth of one NB-IoT channel is equal to that of one resource block (RB), and 6-100 times smaller than that of an LTE legal channel (Table 2) [7].
NB-IoT shall support 3 different operating spectrum scenarios (Fig. 1):

- stand-alone operation utilizing, for example, the spectrum currently being used by GERAN systems, as a replacement for one or more GSM carriers (Fig. 1a),
- guard band operation utilizing the unused resource blocks within the LTE carrier's guard-band (Fig. 1b),
- in-band operation utilizing resource blocks within a normal LTE carrier (Fig. 1c).

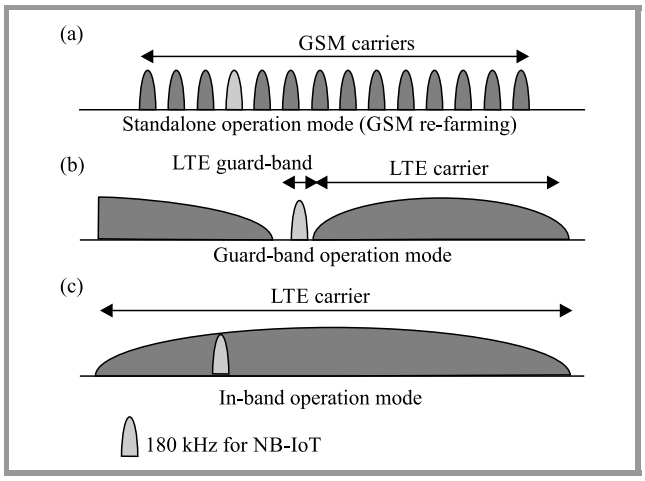

Fig. 1. Spectrum scenarios for operation of NB-IoT.

NB-IoT will support the following features:

- 180 kHz user equipment (UE) RF bandwidth for both downlink and uplink,
- each resource element of NB-IoT can accommodate 1 modulation symbol, e.g. 2 bits for QPSK,
- the modulation symbol rate per resource block is 144 ksps or 168 ksps,
- single synchronization signal design for the different modes of operation, including techniques to handle overlap with legacy LTE signals.

The EC-GSM functionality enables coverage improvements of up to 20 dB with respect to GPRS on the 900 MHz band. EC-GSM defines new control and data channels mapped over legacy GSM. The EC-GSM operation spectrum scenario assumes stand-alone operation only. EC-GSM provides a combined capacity of up to 50,000 devices per cell on a single transceiver.
The introduction of LPWAN requirements to 3GPP standards has led not only to positive results, but has also significantly limited the use of cellular IoT devices in critical cases for such applications. Therefore, it is advisable to further analyze the consequences of optimization of 3GPP technologies to LPWAN, and to assess their impact on the IoT application market.

3. Results of 3GPP RAT Standards' Optimization to LPWAN

Analysis of the optimization of 3GPP technical specifications to LPWAN reveals some limitations and restrictions for technical features of narrow-band technologies optimized for IoT (i.e., 3GPP TS 36.300, 3GPP TS 23.401, 3GPP TS 23.203 [7]-[9]).

3.1. NB-IoT

NB-IoT is the first of such technologies, and it provides access to network services via E-UTRA with channel bandwidth limited to 180 kHz (Table 2). The downlink transmission scheme for NB-IoT in the frequency domain uses one resource block per NB-IoT carrier, with the OFDM sub-carrier spacing of $\Delta f = 15$ kHz, at all times, and with half-duplex operation being the only one supported.
For NB-IoT uplink transmission, both single-tone transmission and multi-tone transmission are possible. For single-tone transmission, there are two numerologies defined: 3.75 kHz and 15 kHz subcarrier spacing, based on single-carrier FDMA. Multi-tone transmission is based on a single-carrier FDMA. There are 12 consecutive uplink sub-carriers with the uplink sub-carrier spacing of $\Delta f = 15$ kHz.
A number of functions including inter-RAT mobility, handover, measurement reports, public warning functions, guaranteed bit rate (GBR), closed subscriber group (CSG) mode, support of Home eNode B (HeNB), relaying, carrier aggregation, dual connectivity, multimedia broadcast multicast services, real-time services, interference avoidance for in-device coexistence, RAN assisted WLAN interworking, sidelink communication/discovery, emergency call, VoLTE, self-configuration/self-optimization, congestion control for data communication - are not supported in NB-IoT. A number of E-UTRA protocol functions supported by all Rel-8 devices are not used in the NB-IoT technology and need not be supported by eNBs and IoT-devices only using NB-IoT. Restrictions of the NB-IoT technology in the LTE user plane include:

- the user plane is not used when transferring data over a non-access stratum,
- multiplexing of the common control channel and the dedicated traffic channel in the transition from the radio resource control (RRC) idle mode to the RRC connected mode is not supported,
- a non-anchor carrier can be configured when an RRC connection is re-established, resumed or reconfigured additionally when an RRC connection is established.

Restrictions of the NB-IoT technology in LTE control plane include:

- NB-IoT devices don't make reporting and control measurements for RRC,
- data radio bearer (DRB) is not used,
- access stratum (AS) security is not used,
- there is no differentiation between the different data types (i.e. IP, non-IP or SMS) in the access stratum,
- RRC connection reconfiguration and RRC connection re-establishment are not supported.

Handover, measurement reports and inter-RAT mobility are not supported in NB-IoT.
LTE optimization towards NB-IoT has led to a situation in which GBR bearers are not supported by NB-IoT. The PDN gateway (P-GW) uses the RAT type to ensure that GBR bearers are not active when the cellular IoT device is using the NB-IoT technology [8].
The mobility of UE is handled by the handover procedure, except for when the NB-IoT is being used, in which case there are no handover procedures.
Inter-RAT mobility to and from NB-IoT is not supported. In Release 13, NB-IoT does not support TDD operation.

3.2. EC-GSM

Extended coverage GSM (EC-GSM) technology is an evolution of EGPRS providing a streamlined protocol implementation and reducing IoT device complexity, while simultaneously supporting energy efficient operation with extended coverage compared to GPRS/EGPRS. IoT access network with EC-GSM could use as little as 600 kHz of the spectrum.
EC-GSM also mandates the use of an improved security framework by both the network and the IoT-device. In EC-GSM, the IoT device is able to operate in an extended coverage mode, in both uplink and downlink, which is means an improved IoT device and BTS sensitivity and interference performance. The feature has been designed to improve coverage by 20 dB and also the interference level by 20 dB compared to GPRS/EGPRS.
IoT devices supporting EC-GSM may support extended discontinuous reception (eDRX) and/or the power saving mode (PSM), and shall support the use of relaxed mobility related requirements. The EC-GSM technology is functional only when all three network nodes: SGSN, IoT devices and base station system (BSS), are compliant with the feature requirements of EC-GSM.
EC-GSM realizes extended coverage (EC) through coverage classes. A coverage class determines the total number of blind repetitions to be used when transmitting/receiving radio blocks. An uplink/downlink coverage class applicable at any point in time can differ between different logical channels. EC-GPRS devices operate in four different coverage classes, where each class is approximated with a level of extended coverage compared to GPRS/EGPRS operation denoted as CC1, CC2, CC3 and CC4 respectively [10]–[12].
Limitations and restrictions of the EC-GSM technology include:

- EC-GSM does not support dynamic absolute radio-frequency channel number (ARFCN) mapping,
- in networks where EC-GSM is supported, the frequency re-use cluster size is expected to be smaller than in networks not supporting EC-GSM,
- dual transfer mode is not supported in EC-GSM operation,
- no simultaneous uplink and downlink packet transfer is supported in EC-GSM,
- EC-GSM makes use of fixed uplink allocation for allocating uplink resources for EC packet data traffic channels and hence does not support the uplink status flag (USF) base uplink allocation.

GSM standards define the GPRS QoS classes that can be requested by GPRS devices, including EC-GSM IoT devices. GPRS QoS profiles are considered a single parameter that defines the following data transfer class attributes, according to the GSM/GPRS standard [11]:

- precedence class,
- delay class,
- reliability class,
- peak throughput class,
- mean throughput class.

This means that the EC-GSM technology, used as GSM/GPRS, has to employ the "best effort" principle for QoS management, which is not sufficient to offer real time IoT services. Therefore, in spite of the limitations and restrictions related to the optimization of 3GPP RAT standards, the solutions obtained make it possible to cover all IoT applications existing on the market, with the LTE-M technology used for critical (real time) IoT applications and NB-IoT/EC-GSM technologies used for other, non-critical IoT applications.

4. Impact of 3GPP Standard Optimization on QoS Management

Each 3GPP technology – 2G (GSM), 3G (UMTS) and 4G (LTE) is characterized by QoS classes, and the evolution from 2G to 4G has resulted in a two-fold increase of QoS

class numbers, to 9 [6]. QoS priority queuing and QoS bandwidth management, the fundamental mechanisms of a QoS configuration, are configured within the QoS class definition. QoS priority queuing and bandwidth management determine the order of traffic and how traffic is handled upon entering or leaving a network.

QoS classes distinguish the ability of 3GPP networks to provide services without quality assurance (best effort or non-GBR) and with guaranteed bit rate (GBR). QoS in 3GPP networks is the ability of the network to enforce different priorities for different application types, subscribers or data sessions, while guaranteeing a certain level of performance of a data session.

A steady increase in the number of mobile applications that control QoS based on the service quality requirements requires implementation of QoS management principles at the network level, and calls for the bearer services to offer the necessary, high-level data exchange.

LTE and UMTS networks propose two major types of bearers:

- guaranteed bit rate (GBR) used for dedicated bearers,
- non-guaranteed bit rate (Non-GBR) used for default or dedicated bearers.

QoS classes allow both 3GPP RAT-compliant subscribers and services to be differentiated. Premium subscribers can be prioritized over basic ones. Real time services can be prioritized over non-real time services.

GBR offers QoS support for the following:

- for real-time services,
- minimum amount of reserved bandwidth,
- always consumes resources in a eNB, regardless of whether it is used or not,
- GBR bearers will be defined with the lower latency and jitter tolerances which are typically required by real-time services.

Each bearer is associated with a predetermined GBR QoS parameter value. If the traffic carried by the GBR bearer conforms to the value associated with the GBR bearer, then there is no chance of congestion-related packet loss in the service utilizing the GBR bearer. A GBR bearer usually is established on an "on-demand basis", because it blocks all transmission resources by reserving them while performing the admission control function.

Non-GBR offers limited support of QoS-related issues:

- no specific network bandwidth allocation,
- for best-effort services (file downloads, email, and Internet browsing),
- packet loss experienced in the case of congestion,
- the maximum bit rate for non-GBR bearers is not specified on a per-bearer basis. However, an aggregate maximum bit rate (AMBR) will be specified on a per-subscriber basis for all non-GBR bearers.

This bearer is mainly used for such applications as web browsing and FTP transfer. Services utilizing non-GBR bearers are prone experience to congestion-related packet losses. No specific transmission resources are blocked. A non-GBR bearer is established in the default or dedicated bearer, and remains established for a longer period of time.

LTE networks include the following: LTE evolved packet system (EPS) bearer, external bearer, E-RAB, S1 interface bearer, S5 interface bearer, S8 interface bearer, LTE radio bearer, etc. [6], which are basically a virtual concept and are a set of network configurations to provide special treatment to traffic. The bearer is a kind of a pipe or tunnel in which message transfers between network entities occurs, and the pipe is identified through a unique ID.

An LTE EPS bearer provides user plane connectivity between the UE and the PDN gateway. This EPS bearer is known as a default EPS bearer, and it is used to provide "always-on" connectivity.

Other EPS bearers can be established to connect to other PDN gateways or to provide different LTE QoS to the same PDN gateway. These EPS bearers are known as dedicated EPS bearers. All user plane data transferred using the same EPS bearer has the same QoS.

The bearers have two or four QoS ID parameters depending on whether they are providing real time or best effort services (Table 3):

- QoS class indicator (QCI),
- allocation and retention priority (ARP),
- GBR – real-time services only,
- maximum bit rate (MBR) – real-time services only.

Table 3
LTE QoS parameters

LTE QoS parameters	GBR	Non-GBR
QoS class identifier	Supported	Supported
Allocation and retention priority	Supported	Supported
Guaranteed bit rate	Supported	
Maximum bit rate	Supported	
APN aggregate maximum bit rate		Supported
UE aggregate maximum bit rate		Supported

The analysis of 3GPP RAT optimization shown above indicates that the limitations and restrictions created during optimization of the LTE standard to NB-IoT for LPWAN

networks lead to a loss of the ability to use 1-4 classes of QoS supporting real-time services (Fig. 2). In the table of QoS classes shown in Release 13, Note 13 appeared which indicates that the packet delay budget is not applicable to the NB-IoT technology or does not apply when EC is used for WB-E-UTRAN (see TS 36.300 [8] and TS 23.302 [9]). This indicates that no packet delay budget is guaranteed and, consequently, GBR is not guaranteed as well.

The QoS mechanism working with GBR services will be essential for the development and implementation of many IoT applications. Cellular RAT technologies have a mature QoS functionality, and this allows to use cellular RAT in spite of wide frequency channels for critical IoT applications.

QCI	Resource type	Priority	Packet delay budget	Packet error loss rate	Example services
1	Guaranteed bit rate (GBR)	2	1[illegible]		Conversational voice
2		4			Conversational video (live streaming)
3		5			Non-conversational video (buffered streaming)
4		3	50		Real time gaming
5	Non-GBR	1	100 ms	10^{-6}	IMS signalling
6		7	100 ms	10^{-3}	Voice, video (live streaming), interactive gaming
7		6	300 ms	10^{-6}	Video (buffered streaming) TCP-based (e.g. www, e-mail, chat, FTP, P2P file sharing, progressive video, etc.)
8		8			
9		9			

Fig. 2. Loss of LTE QoS classes for NB-IoT .

Critical IoT applications will have very high demand for reliability, availability and low latency. The biggest barrier to using IoT for driverless cars is the absence of GBR services. Vehicle-to-vehicle communication is a typical delay-sensitive service with a millisecond-level latency constraint. It also requires extreme reliability, e.g. a nearly 100% success rate for decoding when the combined speed of vehicles passing each other is about 300 kph.

Extremely low latency, in combination with high availability, reliability and security, will be required by Tactile Internet [13]. Tactile Internet will set demanding requirements for cellular IoT networks. The outlined use cases will require round-trip latencies of as little as 1 ms. From the physical layer perspective, each packet must not exceed a duration of 33 μs to enable a one-way physical layer transmission of 100 μs [14]. However, the modulation used in LTE networks is not capable of achieving this requirement, as each OFDM symbol is approximately 70 μs long. The current 1 ms transmission time interval (TTI) of LTE produces, in practice, a 10–20 ms round trip time, while a future LTE Advanced Pro solution should provide even less than 2 ms round trip time and a less than 1 ms one-way delay. However, shorter TTI requires higher available bandwidth.

The abovementioned limitations and restrictions concerned with the use of cellular IoT technologies force the standardization bodies (3GPP, ETSI) to work on improving them.

The STQ mobile working group, ETSI, has opened a new working item with reference number DTR/STQ-0062 – focusing on TR speech and multimedia transmission quality (STQ); Quality of Service for IoT, Discussion on QoS aspects of services related to the IoT ecosystem, and has started the work on QoS aspects of cellular IoT technologies.

The SA WG2 3GPP working group plans to provide additional input to the evaluation and intends to conclude solution 15 for key issue 6 – "Inter-UE QoS for NB- IoT control plane optimization". This solution will be based on a mechanism where eNB fetches QoS information from MME after reception of the UE's indicator S-TMSI in the RRC connection request message. Additional input is provided clarifying the magnitude of the impact from the additional eNB – CN round-trip-time.

5. Conclusions

The 3rd Generation Partnership Project successfully completed standardization of two RATs: NB-IoT (Narrowband-IoT) and EC-GSM in June 2016, with the new 3GPP RAT-based narrowband technologies optimized for IoT. These technologies are competitors of non-cellular IoT – access technologies from the LPWAN family (LoRa, Sig-fox, etc.).

NB-IoT and EC-GSM RAT offer enhancements in both LTE/GERAN air interfaces and networks that will provide new levels of efficiency for low-throughput, delay-tolerant communications common in many IoT applications. Optimization of 3GPP RAT and its adaptation to narrow band cellular IoT RATs has led to some limitations and restrictions, which prevent it from being used in most real-time IoT applications in consumer-based and industrial IoT. Two of out of three 3GPP IoT RATs support only Non-GBR (best effort) classes of QoS, due to their inability to transmit control traffic in the narrow 180–200 kHz channel band of NB-IoT and EC-GSM.

Further optimization of cellular IoT RATs, offer under Releases 14 and 15, will place higher priority on critical IoT communication and QoS.

References

[1] GSMA Report. The Mobile Economy, 2017 [Online]. Available: www.gsma.com/mobileeconomy/

[2] "Digital Single Market Strategy for Europe", European Commission, Brussels, Belgium, 2015.

[3] Global Narrowband – IoT Market Research Report – Forecast to 2022, MRFR, Market Research Future, Maharashtra, India, 2017.

[4] 3GPP TR 36.888 "Study on provision of low-cost Machine-Type Communications (MTC) User Equipments (UEs) based on LTE".

[5] "LTE evolution for IoT connectivity", Nokia, White Paper, 2016.

[6] V. O. Tikhvinskiy, S. V. Terentiev, V. P. Visochin, *LTE/LTE Advanced Mobile Communication Networks: 4G Technologies, Applications and Architecture*. Moscow: Media Publisher, 2014.

[7] TS 36.300 3GPP Project; Evolved Universal Terrestrial Radio Access (E-UTRA) and Evolved Universal Terrestrial Radio Access Network (E-UTRAN); Overall description; Stage 2 (Release 13).

[8] TS 23.401 3GPP Project; Technical Specification Group Services and System Aspects; General Packet Radio Service (GPRS) enhancements for Evolved Universal Terrestrial Radio Access Network (E-UTRAN) access (Release 13).

[9] TS 23.302 3GPP Project; Technical Specification Group Services and System Aspects; Policy and charging control architecture (Release 13).

[10] TS 36.331 3GPP Project; Evolved Universal Terrestrial Radio Access (E-UTRA); Radio Resource Control (RRC); Protocol specification (Release 13).

[11] TS 45.002 3GPP Project; Technical Specification Group Radio Access Network; GSM/EDGE Multiplexing and multiple access on the radio path (Release 13).

[12] TS 44.060 3GPP Project; General Packet Radio Service (GPRS); Mobile Station (MS) – Base Station System (BSS) interface; Radio Link Control/Medium Access Control (RLC/MAC) protocol.

[13] "The Tactile Internet", ITU-T Technology Watch Report, Geneva, Switzerland, August 2014.

[14] A. Aijaz, M. Simsek, M. Dohler, and G. Fettweis, "5G radio access for the Tactile Internet", in "5G Mobile Communications", W. Xiang, K. Zheng, X. Shen (Sherman), Eds. Springer, 2016.

Valery O. Tikhvinskiy is a Deputy General Director of Icominvest LLC, a finance investment company operating in the telecommunications sector, He is the chairman of the Information and Telecommunications Technologies branch of the Russian Academy of Natural Sciences, and a Doctor of Economic Sciences (2003). He received a Ph.D. in Radio Engineering (1988), is a Government Prize laureate (2002), a Member of the State Duma Committee Expert Council (since 2002). He is an Editorial Board Member of the Mobile Telecommunications (since 2002) and T-Com Journals (since 2007). He works as a Professor at the Moscow Technical University of Communications and Informatics (MTUCI, since 2001) and is a Visiting Professor at the Tunisian Telecommunications Institute (IsetCom) (since 2005).
E-mail: v.tikhvinskiy@icominvest.ru
LLC Icominvest
Ostozhenka 28
119034 Moscow, Russia

Moscow Technical University of Communications
and Informatics
Aviamotornaya 8a
111024 Moscow, Russian Federation

Grigory Bochechka is a Head of the Innovation Center Department of Icominvest LLC and Chairman of the WG14 Innovation Management Committee at the information and telecommunications branch of the Russian Academy of Natural Sciences. He received his Ph.D. degree in Specialty Systems, Networks and Telecommunication Devices.
E-mail: g.bochechka@icominvest.ru
LLC Icominvest
Ostozhenka 28
119034 Moscow, Russia

Moscow Technical University of Communications
and Informatics
Aviamotornaya 8a
111024 Moscow, Russian Federation

Andrey Gryazev received his Ph.D. degree in Management and Communication Systems in 2015. He is now acting General Director of the Russian Federal State Unitary Enterprise – the Central Telecommunication Scientific and Research Institute. His scientific research interests are in the fields of modern telecommunication technologies, economy and regulation in the field of radio communications, quality of service for fixed and mobile communications.
E-mail: agryazev@zniis.ru
Federal State Unitary Enterprise Central Science
Research Telecommunication Institute
First Passage of Perovo Pole 8
111141 Moscow, Russia

Altay Aitmagambetov is a Professor at the International University of Information Technology, a candidate of technical sciences, and a member of the International Telecommunications Academy.

E-mail: altayzf@mail.ru
International IT University
Almaty, Kazakhstan

Paper

Measurements and Statistical Analysis for Assessment of Availability of Mobile Network Services

Grażyna Kadamus[1] and Małgorzata Langer[2]

[1] *International Faculty of Engineering, Lodz University of Technology, Łódź, Poland*
[2] *Institute of Electronics, Lodz University of Technology, Łódź, Poland*

https://doi.org/10.26636/jtit.2018.125218

Abstract— Availability is an essential feature of telecommunication services. It influences the quality of experience (QoE) associated with individual networks and with the services offered. Therefore, it needs to be allowed for at each level of network design, and has to be controlled at the operation stage. This is achieved by means of various mathematical and numerical tools. In this project listening quality and speech level, which are quality-related features of mobile network services, are measured and analyzed with the Monte Carlo simulation method. Measurements are taken with assistance of the Diversity Benchmarker, a reliable device designed for mobile network testing. Finally, results obtained are compared to assess the applicability of the Monte Carlo method.

Keywords— availability, Diversity Benchmarker, Monte Carlo, quality of experience.

1. Introduction

The idea of Quality of Service (QoS) is widely recognized as a feature that may decide whether given offering proves successful or fails to attract customers. This rule served as a starting point for this work. In telecommunications, availability constitutes a basic element of QoS and thus of Quality of Experience (QoE), and is included in the design of telecommunication networks. Mathematical solutions that are used to achieve it include various probability distributions and the Monte Carlo method.

This work verities the combination of the two in practice, and aims to show whether application of the Monte Carlo simulation can be beneficial, not only for the statistical simulation, but also for predicting expected values. It was accomplished by means of the statistical analysis of parameters that influence QoE – listening quality and signal level.

However, before the simulation could be performed, measurement data that would serve as a basis for the analysis was obtained. The testing was completed with assistance of the Diversity Benchmarker, a modern system for wireless network testing. This system, newly obtained by the Lodz University of Technology, provides its user with a wide range of measurement and analysis options.

2. Service Quality Management

Although services offered by telecommunications networks are characterized by many specific features, their quality and quality management are subject to the same rules as other products. They also have to undergo constant improvement, which in fact requires, proper network management. This term refers to actions, methods and procedures that enable the system to be operated, administrated, monitored and maintained. It is also required to adhere to certain quality standards while providing the service.

The way network management is dealt with is of paramount importance and it determines the QoS as the degree to which features of provided service support customer satisfaction. Supplement No. 10 to ITU-T E-series Recommendations ITU-T E.800 [1] provides a more precise explanation as: "Totality of characteristics of a telecommunications service that bear on its ability to satisfy stated and implied needs of the user of the service" (p. 1). QoS measures the performance of services provided; includes mechanisms improving performance, network traffic management optimization and management of network resources.

This collective effect comprises numerous single performances, and there are many standards regarding this issue. The fact that only objective measurement means constitute the QoS is of great significance. The so-called end-to-end QoS is about the complete transmission chain. However, the user is omitted in this assessment. Moreover, QoS is very often about characteristics related to the service itself and does not consider information about specific network sections.

QoS criteria are determined for four viewpoints [2] (Fig. 1). The first point of view is related to the customer's QoS requirements. Non-technical, casual language is used to describe them. The next viewpoint is related to the service provider's QoS offering and this is in fact planned or targeted QoS. Here, definitions together with respective values to be reached are given separately for each service type parameter. The criteria regarding QoS achieved or delivered is provided QoS. They enable to compare the offered QoS against delivered QoS, which allows to assess provider's

the capability to deliver declared values. The final viewpoint criteria consider customer perception and how QoS is experienced by the customer. It is a non-technical description received by asking for feedback, for example through however, because this is a personal point of view and it is included into QoE.

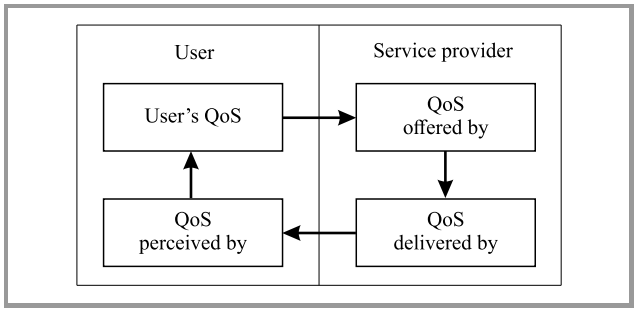

Fig. 1. Four-viewpoint QoS model.

Contrary to the objective QoS, QoE is a highly subjective measure as it is a user's perception of the overall quality of service. QoE takes into consideration both technical and non-technical factors and is influenced, to a great extent, by the customer's personal experiences and expectations, as well as by their emotions, environment, attitude and motivation. It is the QoE that impacts customer satisfaction and this fact should not be underestimated. The level of satisfaction is what virtually shapes their attitude towards the offering and it may result in the customer's decision to drop it when making the choice next time. Although, due to its high subjectivity, the measurable criteria for QoE are difficult to name, QoS gives a better understanding of QoE. Various QoS levels influence it and the empirically obtained relation between them are presented in Fig. 2 [2].

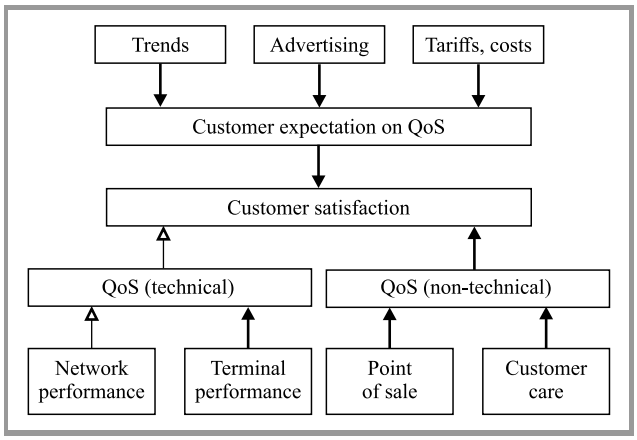

Fig. 2. Relationship between user QoE and QoS.

The model of QoS parameters in telecommunications has, according to the ITU-T E.804 standard, four layers (Fig. 3) [2]. The first one is network availability defined by Eq. (1), the second is network accessibility. The third layer is a combination of service accessibility, service integrity and service retainability. The fourth layer consists of different services.

$$\text{Availability} = \\ = 1 - \frac{\sum_{\text{Outage events}} \text{Capacity loss} \times \text{Outage duration}}{\text{Inservice time}} \quad (1)$$

Although from the customer's point of view accessibility is the first basic QoS parameter, availability, as the first layer, is in fact of paramount importance and determines accessibility and elements in other layers.

3. Measurement and Analysis System

SwissQual Diversity Benchmarker [3] is a measurement system based on a dedicated hardware platform and software used in this project offering high quality equipment for mobile network testing. It is capable of testing multiple technologies. Special models of mobile phones are used as an interface to the mobile network and allow to get an insight into network parameters [4]. The system is controlled externally by a PC computer connected to the Ethernet port in the hardware's control unit. The tests offered by the Diversity Benchmarker played a significant role in the course of this project. The test in question is based on Perceptual Objective Listening Quality Assessment (POLQA), which is an objective voice quality model standard used for benchmarking. POLQA was standardized in 2011 pursuant to Recommendation P.863. The model assumes that the measurement sample is compared with a high-quality signal. The fact that it is referred to as perceptual means that subjective users would assess the quality based on their subjective perception. On the other hand, the term *objective* means that measurements are performed by a device. POLQA combines the two options and is supposed to measure quality as it would be perceived by humans. Voice quality is predicted as in the ITU T P.800 subjective Listening Only Test (LOT), where the sample is compared to the listener's internal reference, and the assessment ranges from 1 (bad) to 5 (excellent). There are two operational modes offered by POLQA. They are narrowband and wideband modes and differ only in the reference signal used.

The measurements were performed in one of the university buildings (B9) of the Lodz University of Technology, Łódź, Poland. The tests were performed around 10 a.m.

Six POLQA tests were performed. For five of them, listening quality data was collected. Before a more detailed analysis is performed, it needs to be mentioned that the operational mode and the effective bandwidth of all tests were of the narrow band variety. Consequently, in terms of listening quality the highest value that could be possibly obtained was 4.5. In Table 1 one can notice that none of the tests recorded a high value. Nevertheless, three of the five results are marked as excellent. Apart from listening quality, the table includes other parameters defined during speech tests, along with their average $\bar{x}$ and median values, variances and standard deviation. Furthermore, the data gathered served also as a basis for Monte Carlo simulation.

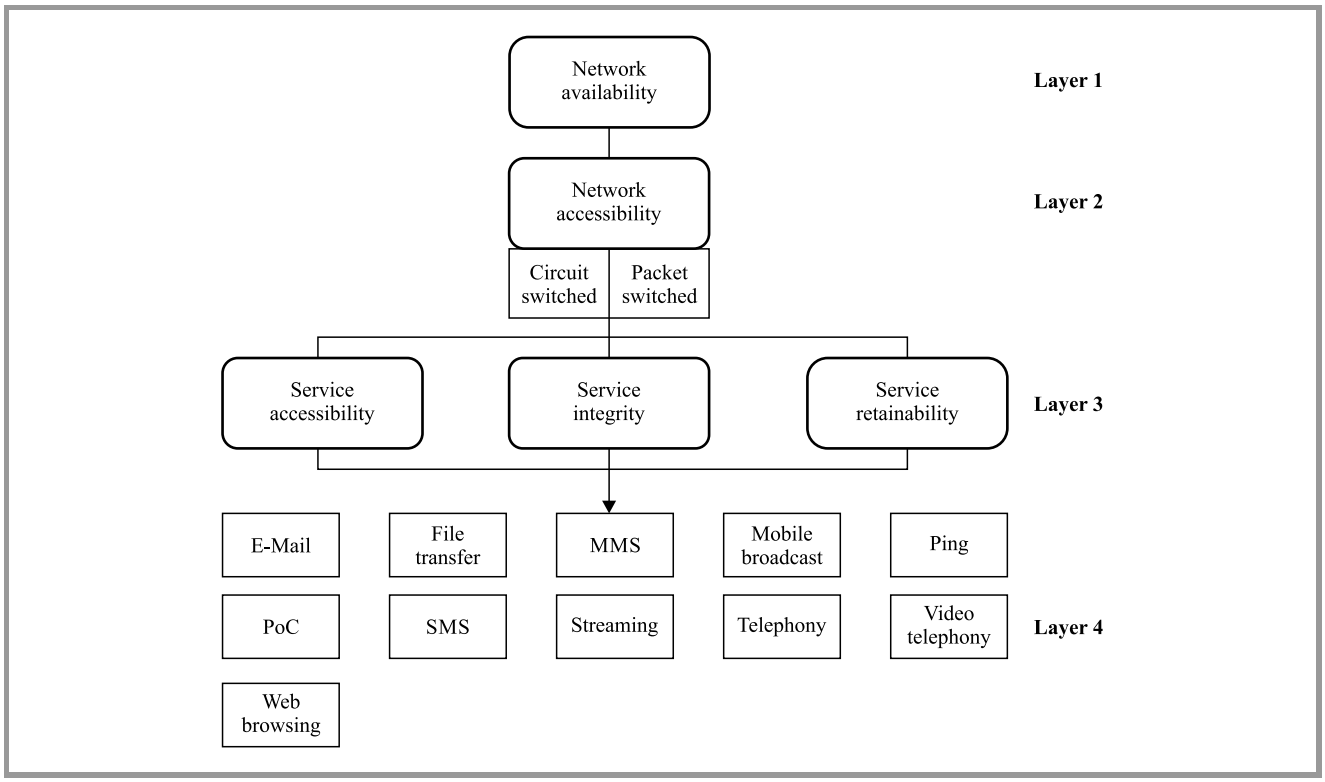

Fig. 3. QoS service parameters model.

Table 1
Five POLQA test results

Test ID/value	Listening quality P.863	Meaning	Speech level [dB]	Noise level [dB]	Static SNR [dB]	Total gain [dB]
159	3.66	Good	−25.5	−79.8	**54.3**	1.4
160	3.79	Excellent	**−25.2**	**−78.6**	53.5	**1.8**
161	**3.54**	Good	**−26.1**	**−79.9**	53.8	**0.8**
162	3.71	Excellent	−25.2	−78.7	53.6	1.7
163	**3.81**	Excellent	−26	−79.5	**53.5**	0.9
Average ($\bar{x}$)	3.702	Excellent	−25.60	−79.30	53.74	1.32
Median	3.71	Excellent	−25.50	−79.50	53.60	1.40
Standard deviation (s)	0.10894953	x	0.43011626	0.612372	0.336155	0.4549725
Variance (s^2)	0.01187	x	0.185	0.375	0.113	0.207

Two parameters were subject to the simulation and they were listening quality and speech level.

4. Monte Carlo Simulation

For availability evaluation, numerical methods constitute an alternative to the analytical approach. One of them is the Monte Carlo simulation. It uses randomly generated numbers in order to assess output parameters. No specified assumptions for input values are required and, additionally, distributions that are considered very difficult to solve can be addressed with the use of Monte Carlo, which makes it an attractive option [5].

Logic system models, such as Reliability Black Diagram (RBD), are used to perform Monte Carlo to evaluate the system. Based thereon, system availability is repeatedly evaluated with the regeneration of parameters before each step. The parameters are restricted by the distribution used. When the probability density function of the random numbers generated is $f(x)$, then the distribution function is represented by:

$$F(x) = \mathbb{P}(t \leq x) = \int_{-\infty}^{x} f(t)\mathrm{d}t\,. \tag{2}$$

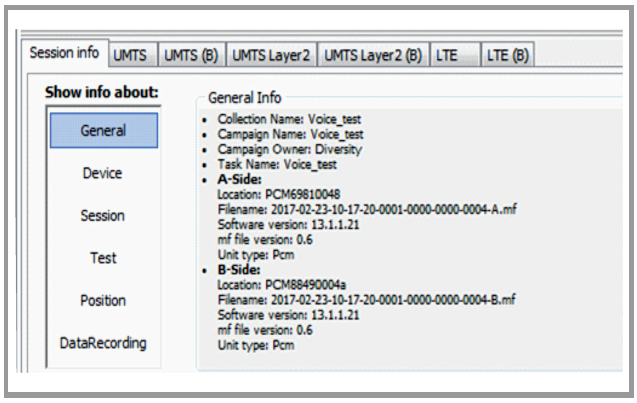

Fig. 4. Session info – general.

In order to perform Monte Carlo, relevant distribution had to be determined in accordance to which the random variables [6] could be generated. As far as listening quality is concerned, Weibull distribution was used to describe it, with is function given by Eq. (3) allowing to generate variables. This decision was motivated by the fact, that Weibull distribution can be adopted to virtually any data.

$$F^{-1}(U) = \theta[-\ln(1-U)]^{\frac{1}{\beta}}. \tag{3}$$

Still, before one can take advantage of this formula, scale parameter θ and shape parameter β have to be determined. Both are present in the formulas for mean $\mathbb{E}(X)$ and variance $\mathrm{Var}(X)$ of the distribution. The parameters were estimated with the assistance of these equations and Microsoft Excel.

$$\mathbb{E}(X) = \theta\Gamma\left(1+\frac{1}{\beta}\right), \tag{4}$$

$$\mathrm{Var}(X) = \theta^2\left[\Gamma\left(1+\frac{2}{\beta}\right) - \Gamma^2\left(1+\frac{1}{\beta}\right)\right]. \tag{5}$$

Monte Carlo values generated for listening quality are summarized in a histogram in the next graph in Fig. 5. The Weibull distribution obtained is skewed left. The shift is reflected in the relation between the extreme values generated and the average, namely by the fact that the average is closer to the maximum than to the minimum.

Speech level is usually characterized with normal distribution and the simulation was performed in accordance with Eq. 2. The only parameters required here were average $\bar{x}$ and standard deviation s. They were taken from the measurement values from Table 1 ($\bar{x} = -25.6$ and $s = 0.43012$) and no additional estimations were needed. Subsequently, relevant formulas to generate 3000 random variables fitting the relevant distribution were used and thus Monte Carlo simulation was performed.

5. Comparison and Conclusions

The last phase was about the comparison of Monte Carlo and measurement values. This comparison is presented in Tables 2 and 3 and contains basic statistical indexes of the obtained results. The relative error in the last column makes it more transparent. As far as listening quality is concerned, it shows that the difference between Diversity- and simulation-obtained average constitutes merely 0.07% of the measurement mean, which is virtually negligible. Similarly, the median determined among randomly generated values is almost the same as the original one. A slightly greater discrepancy is observed for variance and, consequently, for standard distribution. Monte Carlo results are more scattered. Nevertheless, the difference is still relatively small, i.e. remains within 2.5% of the relative error. For the speech level the Monte Carlo values again are very close to Diversity-obtained results. Moreover, they are even more accurate, as the relative error obtained does not exceed 0.04%. The average is most accurate again, while the greatest discrepancy is observed for the median.

The results of the Monte Carlo simulation suggest that the method is indeed effective and allows to replace numerous measurement repetitions or complicated mathematical calculations with a simple simulation. It should also be stated that the relevance of the results obtained within this very

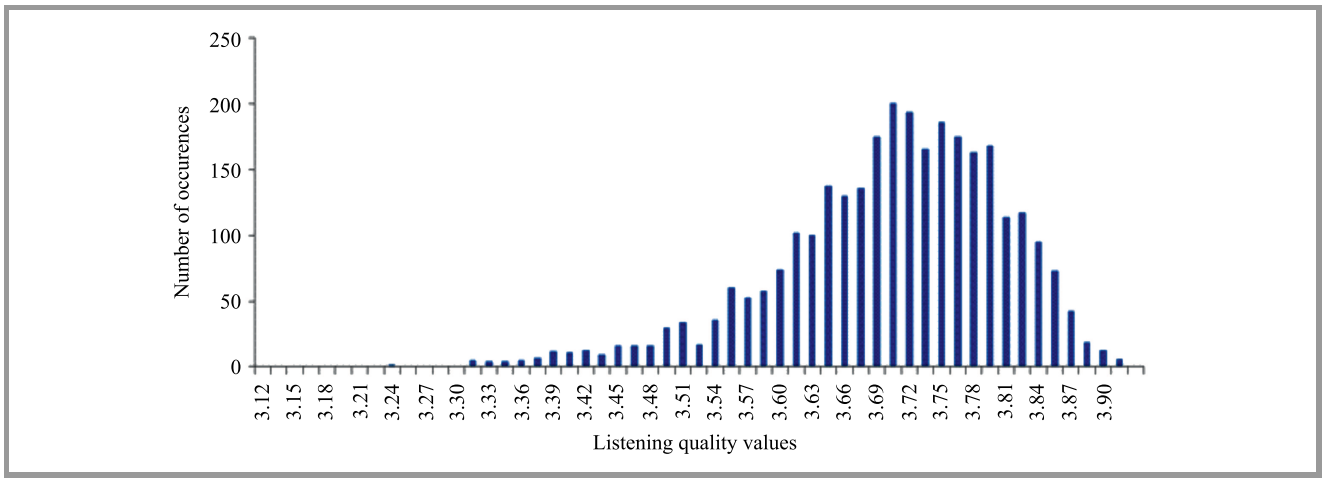

Fig. 5. Histogram of obtained listening quality values using Monte Carlo.

Table 2
Listening quality – comparison of measurement and Monte Carlo simulation

	Measurements	Monte Carlo	$\frac{\lvert X_{meas} - X_{MC} \rvert}{X_{meas}} \times 100\%$
Average ($\bar{x}$)	3.702	3.704	0.07
Median	3.71	3.718	0.22
Standard deviation (s)	0.10895	0.10767	1.17
Variance (s^2)	0.01187	0.01159	2.33
Minimum value	3.54	2.99	x
Maximum value	3.81	3.96	x

Table 3
Speech level – comparison of measurement and Monte Carlo simulation

	Measurements	Monte Carlo	$\frac{\lvert X_{meas} - X_{MC} \rvert}{X_{meas}} \times 100\%$
Average ($\bar{x}$)	−25.6	−25.596	0.01
Median	−25.5	−25.586	0.34
Standard deviation (s)	0.43012	0.42974	0.09
Variance (s^2)	0.185	0.18468	0.17
Minimum value	−26.1	−27.04	x
Maximum value	−25.2	−24.08	x

project could be argued. This is due to a small number of measurements that were taken in the first place, with assistance of the Diversity Benchmarker. Making this number higher would offer information about the scope of simulation and a more reliable scatter of data would be provided. This would allow to obtain more accurate extreme values that could be reflected in the simulation assumption. With more confident measurement the researcher could move on to Monte Carlo simulation.

References

[1] "QoS/QoE framework for the transition from network oriented to service oriented operations", ITU-T E.800 ser. Recom. – Sup. 10, 2016.

[2] "QoS aspects for popular services in mobile networks", Recom. ITU-T E.804, 2014.

[3] SwissQual AG – a Rohde & Schwarz Company, "Company-profile", Feb 2017 [Online]. Available: http://www.mobile-network-testing.com/en/about/company-profile/

[4] "Diversity Hardware Manual 13.0.2", SwissQual AG, 2013.

[5] E. Bauer, X. Zhang, and D. A. Kimber, *Practical System Reliability*, New York: Wiley, 2009 (doi: 10.1002/9780470455401).

[6] L. Devroye, *Non-Uniform Random Variate Generation*, New York: Springer, 1986 (doi: 10.1007/978-1-4613-8643-8).

Grażyna Kadamus obtained her B.Sc. degree in Telecommunications and Computer Science from Lodz University of Technology. Łódź, Poland, in 2017. She is currently continuing her studies for M.Sc. in Management and Production Engineering from the International Faculty of Engineering at Lodz University of Technology.
E-mail: 190095@edu.p.lodz.pl
International Faculty of Engineering
Lodz University of Technology
Żwirki 36
90-001 Łódź, Poland

Małgorzata Langer graduated in Analogues and Digital Circuits of Automatics and got her Ph.D. degree in electronics at Lodz University of Technology (TUL). After several years in international marketing, she joined TUL in 1988, first as an IT specialist at the Institute of Material Science, and then at the Institute of Electronics. She works as an Associate Professor in the telecommunications team and delivers lectures and performs practical sessions (in Polish and in English) for students of various courses. Her main science and research interests are in telecommunications, QoS, QoE, management, non-deterministic object simulation, some aspects of new unconventional technologies in microelectronics, reliability, etc. She is an author and co-author of over 80 publications, including quoted ones, and has been involved in several international, national and university research and didactic programs.
E-mail: malgorzata.langer@p.lodz.pl
Institute of Electronics
Lodz University of Technology
Wólczańska 211/215
90-924 Łódź, Poland

Paper

Throughput Performance Comparison of MPT-GRE and MPTCP in the Fast Ethernet IPv4/IPv6 Environment

Szabolcs Szilágyi, Ferenc Fejes, and Róbert Katona

Department of Informatics Systems and Networks, Faculty of Informatics, University of Debrecen, Hungary

https://doi.org/10.26636/jtit.2018.122817

Abstract—This paper presents the MPT-GRE software, a novel multipath communication technology founded on the Generic Routing Encapsulation (GRE) protocol in UDP tunneling RFC specification. It enables the creation of a GRE protocol-based UDP tunnel built on several communication channels. On the other hand, MPTCP is one of the most typical representatives among multipath communication technologies, basing its operation on the utilization of TCP subflows. The authors compare the path-aggregation capabilities of these two technologies using four Fast Ethernet channels. The tests were carried out with the iperf3 network bandwidth measurement tool, and while transferring data using the FTP protocol over both IPv4 and IPv6.

Keywords— channel capacity aggregation, MPTCP, MPT-GRE, multipath communication, performance analysis, tunneling.

1. Introduction

The Internet communication environment based on the TCP/IP protocol stack provides only one path per communication session for data transfer. The one-path approach is acceptable in the case of systems that only operate with one network interface or a single point of exit towards the Internet. However, most of the devices in use today are factory equipped with multiple network interfaces which, for example, include Ethernet ports for wired networks and multiple radio interfaces for Wi-Fi and mobile data connections (e.g. 3G, LTE).

The classic, single-path based communication technologies are not capable of harnessing the multi-interface capabilities of devices. The communication-related performance (e.g. throughput) can be improved, if the network environments support the use of multiple data paths in a given communication session. Furthermore, in the case of interface malfunction or overload, the capability of automatic handover between the interfaces of a device in a communication session can improve user quality of experience. Several multipath solutions have already been devised, operating in the data link and transport layers [1]–[4]. The most well-known representative among multipath communication technologies is Multipath TCP (MPTCP)[1] situated in the transport layer [5].

A new architecture is introduced in this paper that provides a very easy-to-use extension to the current TCP/IP protocol stack, enabling the use of multiple paths between communication endpoints. The new multipath environment was implemented in the MPT-GRE software tool[2]. The architecture of MPT-GRE is entirely different from that of MPTCP (see Figs. 1 and 2). MPT-GRE provides both TCP and UDP transport protocol support to applications and it operates in the third layer (network layer), while MPTCP operates in the fourth layer (transport layer).

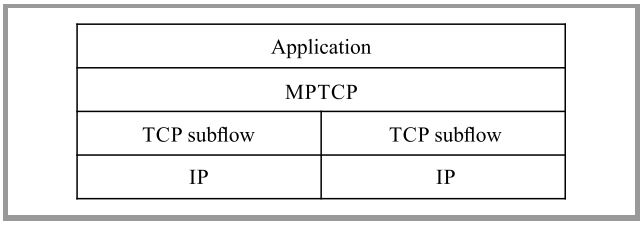

Fig. 1. Architecture of the MPTCP protocol stack.

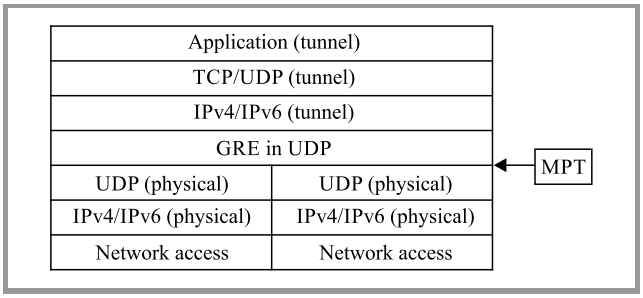

Fig. 2. MPT-GRE conceptual architecture.

The MPT-GRE software was designed on Linux systems with the aim of creating a laboratory setup for measurements, which helped us carry out a performance analysis of its multipath capabilities. Currently it is also available

[1]MPTCP – http://multipath-tcp.org/

[2]MPT-GRE – MultiPath Technology based on Generic Routing Encapsulation in UDP RFC specification: http://irh.inf.unideb.hu/user/szilagyi/mpt/

for Raspbian based systems, and the development of an Android version is in progress [6]–[8]. Our results support the fact that the MPT-GRE multipath solution is capable of efficiently aggregating the throughput of several interfaces used for communication.
The rest of the paper contains a brief look at the operating principles of MPT-GRE and MPTCP in Section 2, while in Section 3 the environment used for measurements is described. Section 4 gives a summary of the results, followed by plans and final conclusions.

2. Multipath Solutions

In this section, we briefly present MPTCP, the most typical representative of these technologies, and then describe the operating principle of the MPT-GRE software library developed.

2.1. MPTCP Operating Principle

The traditional TCP/IP communication infrastructure e.g. [9], is limited to a single IP address per communication endpoint. The current IP technology uses IP address pairs and TCP or UDP port numbers for identifying the communication endpoints (sockets).
MultiPath TCP (MPTCP) operates with an entirely new layered architecture [10]. The new MPTCP sub-layer provides a communication interface to applications, while the TCP sub-flow sub-layers, situated directly below the MPTCP sub-layer, are responsible for creating the multipath communication environment. The TCP protocol operating in the sub-flow sub-layer is responsible for providing flow control and for ensuring reliability (see Fig. 1).
The available literature presents quite a few examples that examine the throughput capabilities of MPTCP. For example, Paasch *et al.* in [11] presented a measurement environment that utilized six 10 Gb links between two endpoints, with an aggregated throughput of 50 Gbps, which is regarded world-wide as the leading performance in the field. Naturally, besides its numerous advantages, MPTCP has a couple of drawbacks:

- tuning of the application layer or the operating system might be necessary to achieve optimal operation,
- operates in the transport layer,
- provides TCP-only support, which can cause problems, e.g. during the usage of multimedia applications.

These problems motivated us to develop a software solution supporting multipath communication that eliminates the aforementioned disadvantages.

2.2. MPT-GRE Operating Principle

The multipath communication architecture is based on the IETF RFC 8086 "GRE in UDP encapsulation" [12]–[14], extending its operating principle to a multipath environment (Fig. 2).
In addition to the classic layered architecture (see e.g. [9]), we introduced a new logical (tunnel) interface (Fig. 2). The layers above the GRE in UDP (tunnel) operate identically to the traditional environment, with the exception that the data arriving from the application layer is sent to a logical (tunnel) interface instead of a physical one. Below the logical interface it is possible to map the communication session to multiple physical interfaces. In practice, the MPT[3] software is situated between these two sections, designed to control the whole operation.
The basic operating principle is as follows. First a logical (tunnel) interface is created on the endpoints, which the applications can use for socket identification. The MPT-GRE software reads the packet arriving to the tunnel interface (IPv4 or IPv6) on the sending host. This packet is encapsulated in a new GRE in UDP segment before being forwarded on a possible physical path. On the receiving host, the header of the GRE in UDP segment is removed before forwarding the embedded data (which is the original packet forwarded from the sender's tunnel interface) to the receiving host's tunnel interface. The (logical) connection between the communicating hosts is of the direct, point-to-point type. With this architecture, no modifications whatsoever are required in the application, as it uses a single logical interface (the tunnel interface) during the entirety of the communication session. In addition, the application can use the UDP transport protocol above the tunnel interface, as the solution is not limited to the TCP protocol like in the case of MPTCP. If the MPT-GRE library uses the UDP protocol during the encapsulation process, retransmission and flow-control services will not be provided below the tunnel interface.
In Fig. 3, the PDU structure of the MPT-based communication is presented. The grey blocks denote the packet arriving from the application layer, which gets forwarded to the logical (tunnel) interface. The MPT-GRE software will read the packet arriving to the tunnel interface and will assign one of the physical interfaces' IP address to it. It has to be noted that the MPT-GRE library is a dual-stack implementation. The separation of the physical and logical IP layer allows for the use of any IP version (IPv4 or IPv6) as well as all combinations, e.g. IPv4 below the tunnel, IPv6 above the tunnel, or *vice versa*. The receiving host listens on the designated UDP port number and after stripping the headers of the incoming packets it forwards the embedded PDUs to the logical interface. Above the tunnel interface, the application layer can normally process the incoming

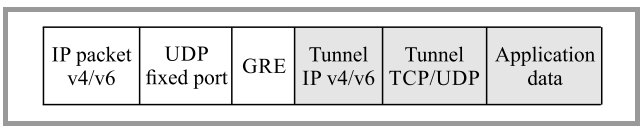

Fig. 3. The PDU structure MPT "GRE in UDP".

[3]MPT and MPT-GRE are interchangeable terms.

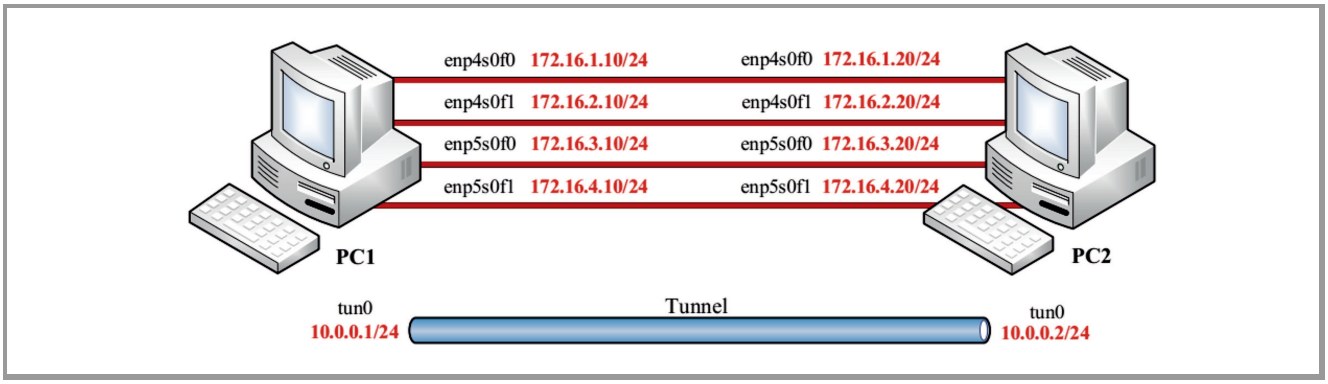

Fig. 4. Four wired paths laboratory measurement environment.

Table 1
IPv4 and IPv6 addressing

Device	Interface	IPv4/IPv6 address prefix	Default gateway
PC1	enp4s0f0	172.16.1.10/24 2001:db8:acad:1::10/64	172.16.1.20/24 2001:db8:acad:1::20/64
	enp4s0f1	172.16.2.10/24 2001:db8:acad:2::10/64	172.16.2.20/24 2001:db8:acad:2::20/64
	enp5s0f0	172.16.3.10/24 2001:db8:acad:3::10/64	172.16.3.20/24 2001:db8:acad:3::20/64
	enp5s0f1	172.16.4.10/24 2001:db8:acad:4::10/64	172.16.4.20/24 2001:db8:acad:4::20/64
	tun0 (only for MPT-GRE)	10.0.0.1/24 fec::1:1/112	–
PC2	enp4s0f0	172.16.1.20/24 2001:db8:acad:1::20/64	172.16.1.10/24 2001:db8:acad:1::10/64
	enp4s0f1	172.16.2.20/24 2001:db8:acad:2::20/64	172.16.2.10/24 2001:db8:acad:2::10/64
	enp5s0f0	172.16.3.20/24 2001:db8:acad:3::20/64	172.16.3.10/24 2001:db8:acad:3::10/64
	enp5s0f1	172.16.4.20/24 2001:db8:acad:4::20/64	172.16.4.10/24 2001:db8:acad:4::10/64
	tun0 (only for MPT-GRE)	10.0.0.2/24 fec::1:2/112	–

packets. The detailed operating principle of MPT-GRE is described in [15] and [16].

3. The Measurement Network Environment

The laboratory environment for the measurements comprised two PCs that were directly connected by wire (Fig. 4). The computers had the following configuration:

- Gigabyte Z77-D3H motherboard with Intel Z77 chipset,
- Intel Core i7-3770K 3.50 GHz processor with 4 cores and 8 threads,
- 4×4 GB 1600 MHz DDR3 SDRAM,
- Intel PT Quad 1000 Gigabit Ethernet server adapter,
- Ubuntu 16.04 LTS (Xenial Xerus) 64-bit operating system with 4.4.0-62-generic Linux kernel module.

Integrated network interface cards were used for remote management purposes and during measurements, the integrated NICs were shut down to avoid excess traffic. The performance measurements were carried out between the 4-port server adapters. Both PCs had one of these installed. As these were Gigabit interfaces, we limited their speed to create the Fast Ethernet measurement environment.
The identically named interface pairs were connected via CAT6 STP cables to create the independent physical paths needed for performing the measurements. The applied addressing scheme is summarized in Table 1.

3.1. MPT-GRE Measurements Setup

Even though we used the same physical laboratory environment for MPT-GRE and MPTCP measurements, the implementations of the two multipath technologies required different configuration steps.
First, the MPT-GRE was downloaded and installed. After the packages were installed, the necessary network parameters in the two basic configuration files were modified.
At the start, we disabled three out of the four interfaces on PC1, and then enabled them one-by-one using the Python script according to the measurement schedule, ensuring the gradual aggregation of the communication channel. We used *iperf3*[4] to measure the throughput, and the *sar*[5] command to examine processor usage. The *tee*[6] program was

[4]https://github.com/esnet/iperf
[5]https://linux.die.net/man/1/sar
[6]http://pubs.opengroup.org/onlinepubs/9699919799/utilities/tee.html

used to log the results into files. Each measurement had a duration of 30 s and was repeated 10 times. Less than 1% deviation could be observed in the results for each set of the repeated measurements. We performed the measurements using all possible IP version combinations in regards to both the tunnel and the physical interfaces (IPv4 over IPv4, IPv4 over IPv6, IPv6 over IPv4, IPv6 over IPv6).
Following the approach of papers [17]–[22], we also carried out for real file transfer performance measurements using scripts.
For FTP performance-analysis we run the scripts on PC1, while PC2 was configured as the FTP server. A 1 GB file was used for each measurement, which was deleted after download completion with the help of the script. We used the *ifstat*[7] tool to display the measurement results. Logging was performed once again with the help of *tee*.

3.2. MPTCP Measurements Setup

We installed MPTCP v0.91 for measurements in *GRUB*[8], which we selected directly after restarting the computer, in order to load the MPTCP kernel module. Next, we configured the routing between the interfaces, and the *mptcp_enabled* and *mptcp_path_manager* parameters.
Finally, with the help of the scripts used for the MPT measurements, we performed the required measurement sequence. At the start, only the first interface was in an active status, the other three were shut down. The appropriately timed reactivation of the interfaces was handled by the script. The MPTCP kernel module was installed on both hosts. The measurement scripts were executed on PC1. Just like in the case of the MPT measurements, we used PC2 as the *iperf3* and FTP server. It has to be noted that for performing the MPTCP measurements, we had to disable the integrated interfaces used for remote access, as MPTCP automatically assigned these to the list of interfaces participating in the MPTCP process. During the MPTCP measurements MPT was not running on the hosts.

4. Measurement Results

4.1. iperf3 Measurements

First, we performed a comparison of the path aggregation capabilities of MPT-GRE and MPTCP. The previously presented *iperf3* command was used for this purpose. As Fig. 5 shows, in the case of MPT-GRE we applied all possible IP version combinations with regards to the physical interfaces and the tunnel interface: IPv4 tunnel over IPv4, IPv6 tunnel over IPv4, IPv4 tunnel over IPv6 and IPv6 tunnel over IPv6. The throughput aggregation capability of the MPT-GRE software minimally decreased compared to the previous list. The same could be observed in the case of MPTCP, where, due to a different implementation procedure, we only examined two cases: when the paths used either IPv4 or IPv6 homogenously. Overall, MPTCP performed slightly better in *iperf3* tests. However, the difference in performance was around 0.9% in all cases. We performed the tests using 1, 2, 3, and 4 interfaces simultaneously. On average, both for MPTCP and MPT-GRE for IPv4, we measured a throughput of 92 Mbps in the case of a single interface, 184 Mbps in the case of two interfaces, 276 Mbps in the case of three interfaces, and 368 Mbps in the case of four interfaces used.

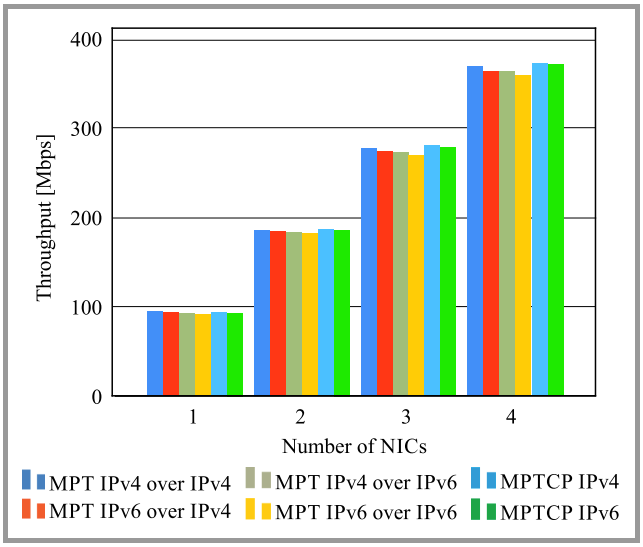

Fig. 5. MPT-MPTCP *iperf3* test comparison. (See color pictures online at www.nit.eu/publications/journal-jtit)

4.2. FTP Measurements

In the next round, the efficiency of MPTCP and MPT-GRE using the FTP protocol was examined. Figure 6 shows the measured download speed of a 1 GB file using four interfaces. The results are close in this case as well, with MPTCP achieving download speed of 368.47 Mbps over IPv4, while in the case of MPT-GRE with IPv4 tunnel over IPv4, 366.89 Mbps was measured.

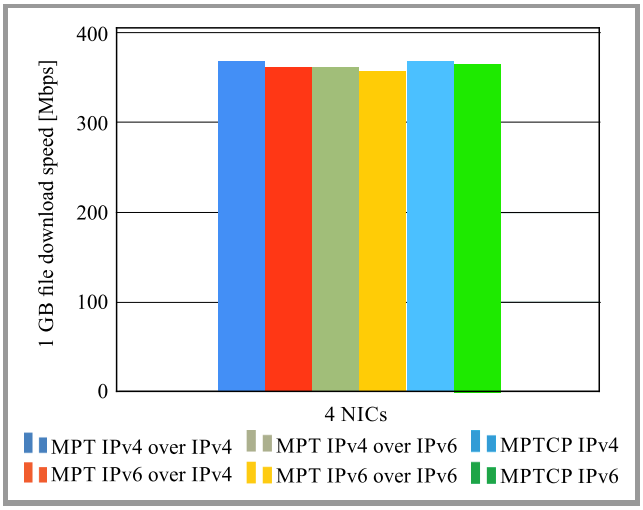

Fig. 6. MPT-MPTCP FTP download speed comparison using 6 interfaces.

[7]https://sourceforge.net/projects/ifstat/
[8]http://www.gnu.org/software/grub/

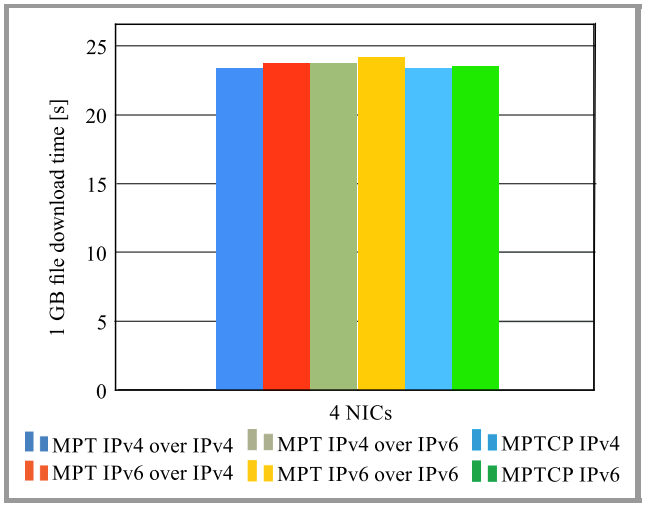

Fig. 7. MPT-MPTCP FTP download time comparison in case of 4 interfaces.

Figure 7 shows the measured download times of a 1 GB file, where values are inversely proportional to Fig. 6. Using MPT-GRE with IPv4 tunnel over IPv4, the 1 GB file was successfully downloaded in 23.41 s, while using MPTCP (IPv4) the duration was around 23.31 s. In case of other sets of measurement results, a minimal deviation could be observed in the file download time.

Figure 8 shows the MPT throughput in an IPv4 tunnel over IPv4 test. Other IP version combinations resulted in similar figures. The result represented with the orange line shows the file download speed measured on the physical interfaces, while the red line shows the throughput measured

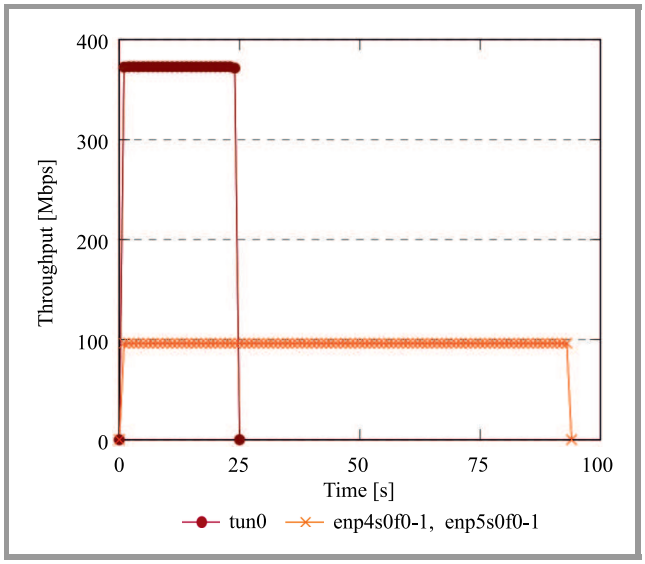

Fig. 8. MPT-GRE IPv4-IPv4 FTP throughput performance using 4 interfaces.

using the tunnel interface. It is clearly visible that in the case the 1 GB file downloaded using a physical interface, the resulting download duration is 94 s with a download speed of around 96.6 Mbps. If the same file is downloaded through the tunnel interface, with 4 parallel physical connections, the download time is reduced to 25 s, while the download speed increases to around 372.76 Mbps. It can be established that using an MPT-GRE based system the time needed to download the file is practically reduced to a quarter, while the maximum download speed is four times that of a traditional single-path solution.

In Fig. 9 we can see the path aggregation performance of MPTCP, similarly during a 1 GB file download. The same can be observed as in the case of MPT-GRE: the download time is reduced to a quarter when utilizing the four physical interfaces at the same time.

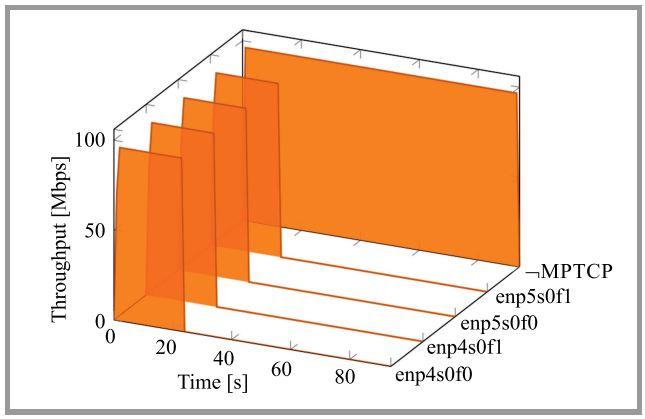

Fig. 9. MPTCP over IPv4 FTP throughput performance using 4 interfaces.

4.3. CPU Utilization in Case of iperf3

In the following section, the CPU utilization results of the MPT-GRE and MPTCP multipath solutions are presented. Figure 10 shows CPU utilization of the MPT and MPTCP solutions while operating with a different number of physical interfaces (1–4), operating over IPv6. This is the most resource-intensive mode of operation. It can be observed that processor utilization is in a linear relationship with the number of physical interfaces, and that the CPU utilization

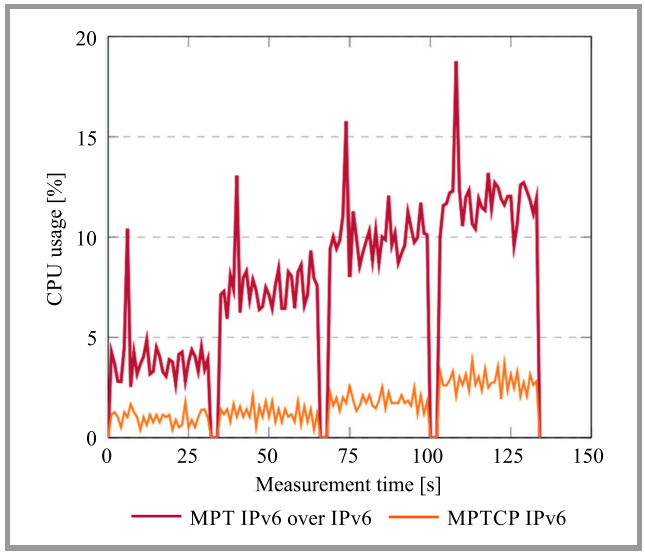

Fig. 10. MPT-MPTCP CPU utilization comparison.

of MPTCP is lower compared to that of MPT-GRE. While the CPU utilization of MPTCP with 4 physical interfaces over IPv6 hovers around the 3% mark, in the case of MPT-GRE with IPv6 tunnel over IPv6 this increases to 12%. Evidently, these are the most critical cases, and when using the other protocol-version combinations the CPU utilization of both solutions is lower.

5. Conclusions

This paper presents two multipath communication systems based on different technologies, comparing their path aggregation capacity, efficiency, and processor utilization. MPTCP is a transport layer, while MPT-GRE is a network layer implementation. In the majority of the measurements MPTCP slightly outperformed MPT-GRE. However, the performance differences were quite minimal. As a result, we highly recommend the use of both technologies. MPTCP for those who primarily concentrate on minimal processor utilization, and MPT for those who would like to communicate over TCP/UDP flexibly with multipath capabilities, e.g. in the case of multimedia traffic (interactive voice, video streaming).
Our future plans include the efficiency review of these two technologies in Gigabit Ethernet and 10 Gigabit Ethernet environments, and the publication of an MPT-GRE RFC draft.

Acknowledgements

This work was supported by the construction EFOP-3.6.3-VEKOP-16-2017-00002. The project was supported by the European Union, co-financed by the European Social Fund.

References

[1] B. Almási and A. Harman, "An overview of the multipath communication technologies", in *Proc. Adv. on Wireless Sensor Networks 2013 Conf. AWSN 2013*, Debrecen, Hungary, 2013, pp. 7–11.

[2] P. Dong, J. Wang, J. Huang, H. Wang, and G. Min, "Performance enhancement of multipath TCP for wireless communications with multiple radio interfaces", *IEEE Transact. on Commun.*, vol. 64, no. 8, pp. 3456–3466, 2016 (doi: 10.1109/TCOMM.2016.2584615).

[3] M. Li, A. Lukyanenko, Z. Ou, A. Ylä-Jääski, S. Tarkoma, M. Coudron, and S. Secci, "Multipath transmission for the internet: A survey", *IEEE Commun. Surveys Tutor.*, vol. 18, no. 4, pp. 2887–2925, 2016 (doi: 10.1109/COMST.2016.2586112).

[4] Y. Yu, S. Fang, K. M. M. Aung, C. H. Foh, H. Li, and Y. Zhu, "A layer 2 multipath solution and its performance evaluation for Data Center Ethernets", *Int. J. of Commun. Sys.*, vol. 27, no. 11, pp. 2555–2576, 2014 (doi: 10.1002/dac.2488).

[5] A. Ford, C. Raiciu, M. Handley, and O. Bonaventure, "TCP extensions for multipath operation with multiple addresses", *RFC 6824, RFC Editor*, Jan 2013 [Online]. Available: http://tools.ietf.org/html/rfc/6824

[6] B. Almási, "A solution for changing the communication interfaces between Wi-Fi and 3G without packet loss", in *2015 38th Int. Conf. on Telecommun. and Signal Proces. TSP*, IEEE, Prague, Czech Republic, 2015, pp. 1–5 (doi: 10.1109/TSP.2015.7296429).

[7] F. Fejes, R. Katona, and L. Püsök, "Multipath strategies and solutions in multihomed mobile environments", in *2016 7th IEEE Int. Conf. on Cognitive Infocommun. CogInfoCom*, IEEE, Wrocław, Poland, 2016, pp. 79–84 (doi: 10.1109/CogInfoCom.2016.7804529).

[8] F. Fejes, S. Rácz, and G. Szabó, "Application agnostic QoE triggered multipath switching for Android devices", in *Proc. 2017 IEEE Int. Conf. on Commun.: Bridging People, Communities, and Cultures, ICC*, Paris, France 2017, pp. 1585–1591 (doi: 10.1109/ICC.2017.7997450).

[9] A. S. Tanenbaum and D. J. Wetherall, *Computer Networks*, Boston: Pearson Education, 2011.

[10] C. Paasch *et al.*, "The MPTCP project official website", [Online]. Available: http://multipath-tcp.org/

[11] C. Paasch, G. Detal, S. Barré, F. Duchêne, and O. Bonaventure, "The fastest TCP connection with multipath TCP", *ICTEAM*, UCLouvain, Louvain-la-Neuve, Belgium, 2013.

[12] B. Almási, M. Kósa, F. Fejes, R. Katona, and L. Püsök, "MPT: A solution for eliminating the effect of network breakdowns in case of HD video stream transmission", *2015 6th IEEE Int. Conf. on Cognitive Infocommun. CogInfoCom*, IEEE, Győr, Hungary, 2015, pp. 121–126 (doi: 10.1109/CogInfoCom.2015/7390576).

[13] S. Szilágyi, "The MPT-GRE project official website", [Online]. Available: http://irh.inf.unideb.hu/user/szilagyi/mpt/

[14] L. Yong, E. Crabbe, X. Xu, and T. Herbert, "GRE-in-UDP encapsulation", *RFC 8086, RFC Editor*, 2017.

[15] B. Almási, G. Lencse and S. Szilágyi, "Investigating the multipath extension of the GRE in UDP technology", *Computer Commun.*, vol. 103, no. C, pp. 29–38, 2017 (doi: 10.1016/j.comcom.2017.02.002).

[16] G. Lencse, S. Szilágyi, F. Fejes, and M. Georgescu, "MPT Network Layer Multipath Library", *IETF Network Working Group, Internet Draft*, Jun 2017 [Online]. Available: https://www.ietf.org/iol/draft-lencse-tsvwg-mpt-01.txt

[17] B. Almási, "Multipath communication – a new basis for the future internet cognitive infocommunication", in *Proc. 2013 IEEE 4th Int. Conf. on Cognitive Infocommun. CogInfoCom*, Budapest, Hungary, 2013, pp. 201–204 (doi: 10.1109/CogInfoCom.2013.6719241).

[18] B. Almási and S. Szilágyi, "Multipath FTP and stream transmission analysis using the MPT software environment", *Int. J. of Adv. Research in Computer and Commun. Engineer.*, vol. 2, no. 11, pp. 4267–4272, 2013.

[19] B. Almási and S. Szilágyi, "Throughput performance analysis of the multipath communication library MPT", in *Proc. 2013 36th Int. Conf. on Telecommun. and Signal Proces. TSP*, Rome, Italy, 2013, pp. 86–90 (doi: 10.1109/TSP.2013.6613897).

[20] B. Almási and S. Szilágyi, "Investigating the throughput performance of the MPT multipath communication library in IPv4 and IPv6", in *Proc. Int. J. of Adv. in Telecommun., Electrotec., Signals and Sys.*, vol. 5, no. 1, pp. 53–60, 2016 (doi: 10.11601/ijates.v5i1.148).

[21] Á. Kovács, "Comparing the aggregation capability of the MPT communications library and multipath TCP", in *Proc. 2016 7th IEEE Int. Conf. on Cognitive Infocommun. CogInfoCom*, Wrocław, Poland, 2016, pp. 157–162 (doi: 10.1109/CogInfoCom.2016.7804542).

[22] G. Lencse and Á. Kovács, "Advanced measurements of the aggregation capability of the MPT multipath communication library", *Int. J. of Adv. in Telecommun., Electrotech., Signals and Sys.*, vol. 4, no. 2, pp. 41–48, 2015 (doi: 10.11601/ijates.v4i2.112).

Szabolcs Szilágyi received his M.Sc. in Electrical Engineering and Computer Science from the University of Oradea, Romania in 2009, and his Ph.D. from the University of Debrecen, Hungary in 2015. He has been working for the Department of Informatics Systems and Networks, Faculty of Informatics, University of Debrecen since 2013. At

present, he is a senior lecturer. The area of his research includes performance analysis of communication networks and investigating multipath communication technologies. He is the new head of the Multipath Communication Research Group at the Faculty of Informatics, University of Debrecen.
E-mail: szilagyi.szabolcs@inf.unideb.hu
Department of Informatics Systems and Networks
Faculty of Informatics
University of Debrecen
26 Kassai Way
4028 Debrecen, Hungary

Ferenc Fejes received his B.Sc. in Computer Engineering from the University of Debrecen in 2015. He is currently working on his master's degree in the same field at the University of Debrecen. He expanded his industrial experience at the Ericsson Traffic Laboratory, Budapest. His research interests include multipath networking, QoS/QoE analysis of wireless networks, open source and experimental technologies.

E-mail: fejes@openmailbox.org
Department of Informatics Systems and Networks
Faculty of Informatics
University of Debrecen
26 Kassai Way
4028 Debrecen, Hungary

Róbert Katona received the B.Sc. degree in Computer Science Engineering from the University of Debrecen, Debrecen, Hungary, in 2016 with a specialization in infocommunication networks. Since 2016, he has been pursuing M.Sc. in the same field at the University of Debrecen. Being a member of the MPT research team at the local Faculty of Informatics, his main research interests include multipath communication networks.

E-mail: robert.k@opmbx.org
Department of Informatics Systems and Networks
Faculty of Informatics
University of Debrecen
26 Kassai Way
4028 Debrecen, Hungary

Paper

Pilot Design for Sparse Channel Estimation in Orthogonal Frequency Division Multiplexing Systems

P. Vimala and G. Yamuna

Annamalai University, Annamalai Nagar, Chidambaram, Tamil Nadu, India

https://doi.org/10.26636/jtit.2018.113817

Abstract—Orthogonal Frequency Division Multiplexing (OFDM) is a well-known technique used in modern wide band wireless communication systems. Coherent OFDM systems achieve its advantages over a multipath fading channel, if channel impulse response is estimated precisely at the receiver. Pilot-aided channel estimation in wide band OFDM systems adopts the recently explored compressive sensing technique to decrease the transmission overhead of pilot subcarriers, since it exploits the inherent sparsity of the wireless fading channel. The accuracy of compressive sensing techniques in sparse channel estimation is based on the location of pilots among OFDM subcarriers. A sufficient condition for the optimal pilot selection from Sylow subgroups is derived. A Sylow subgroup does not exist for most practical OFDM systems. Therefore, a deterministic pilot search algorithm is described to select pilot locations based on minimizing coherence, along with minimum variance. Simulation results reveal the effectiveness of the proposed algorithm in terms of bit error rate, compared to the existing solutions.

Keywords—channel estimation, compressive sensing, minimum coherence, minimum variance, pilot pattern.

1. Introduction

Orthogonal Frequency Division Multiplexing (OFDM) is a multi-carrier modulation technique used in wideband wireless communication systems due to its high spectral efficiency [1]. In OFDM systems, each subcarrier has a narrow bandwidth which ensures signal robustness against frequency selectivity caused by the multipath delay spread. Although coherent, non-coherent and partially coherent detection techniques are deployed in OFDM systems, coherent detection attracts wider interest, as it supports a higher date rate than the other schemes. Coherent communication in OFDM systems allows arbitrary signal constellations for high data rates, but efficient channel estimation strategies are required for detection and decoding of information at the receiver. The channel can be estimated in the receiver using the pilot-aided method, where the receiver makes use of the known transmitted symbols, also known as pilots in, a set of predetermined subcarriers of the OFDM system, or by learning the statistics of the information bearing signals which are referred to as a blind technique. As such an approach involves more complex signal processing and computationally expensive operations to ensure efficient blind methods, pilot-aided methods evoke considerable interest in the recent technologies which are capable of tracking the channel based on coherence time whose duration is in the order of one OFDM symbol [2].

The majority of research concerned with pilot-aided channel estimation is devoted to the selection of pilot locations. Equally spaced pilot locations become the optimal selection when the maximum likelihood (ML) rule is employed in the receiver, which is computationally expensive [3], [4]. Further, several investigations show that many wideband OFDM systems tend, in practice, to have their wireless channel dominated by a relatively small number of coefficients, i.e. most channel coefficients are nearly zero and do not contribute significantly, and the number of effective channel coefficients is relatively much lower than the channel delay spread (length of the channel impulse response). The sparseness of the channel leverages the application of sparse signal processing techniques in the framework of compressive sensing (CS) [5] for channel estimation problems, which can drastically reduce the number of pilots required to estimate the channel, thereby increasing bandwidth efficiency. CS recovery algorithms, such as l1 norm minimization, orthogonal matching pursuit and iterative thresholding, have been adopted for sparse channel estimation, which enables efficient reconstruction of the sparse channel with less pilot overhead than in the case of conventional methods [6]. However, there is no general theory on the optimal pilot selection for sparse channel estimation using CS techniques, such as the optimal equally spaced pilots for conventional channel estimation methods.

A few works of literature deal with the design of a pilot pattern for sparse channel estimation. Deterministic pilot selection [7] is proposed for OFDM systems with the number of subcarriers N being a prime. A pilot generated randomly can be updated by sequentially evolving towards a global optimizer with offline channel data, as discussed in [8]. Pilot design for under water acoustic chan-

nels, based on cluster pilot design and data subcarrier as additional observation for channel estimation, is described in [9]. The tree-based backward pilot generation [10] iteratively removes a subcarrier from N subcarriers of OFDM systems in a backward direction to generate a pilot pattern. Optimum pilot generation by minimizing coherence of the DFT submatrix and cross entropy optimization, to place the pilots at an optimal location, is described in [11], [12]. The first subcarrier is fixed as the first pilot, and the remaining pilot locations are sequentially assigned by minimizing the variance of the multiset formed using the current pilot location set [13]. Statistic serial, parallel and iterative group shrinking was proposed [14] for minimum coherence. Three greedy deterministic pilot search algorithms [15] are stated based on minimizing coherence through a straightforward search.

The remainder of this paper is organized as follows. Section 2 deals with the OFDM system modeling framework and formulates the estimation problem of sparse channel impulse response. In Section 3, optimal pilot design from the Sylow subgroup is analyzed. The proposed deterministic pilot search algorithm is presented in Section 4. The simulation results shown in Section 5 reveal the performance of the proposed algorithm's pilot pattern in sparse channel estimation of wideband OFDM systems and, finally, conclusions are provided in Section 6.

The notations used in this paper are: $\emptyset$, $\setminus$, $|$, $\nmid$, $(.)^T$, $(.)^H$, $(.)^{-1}$, $\|.\|$, $\langle.\rangle$, $\otimes$, $\oplus$, $\lfloor.\rfloor$, $\lceil.\rceil$, and $O(.)$ meaning: empty, exclusion, divide, does not divide, matrix transpose, conjugate transpose, matrix inverse, norm of a vector, inner product of a vector, modulus, multiplication modulo, addition modulo, floor of a value, ceiling of a value and order, respectively.

2. Problem Statement

In this section, we describe the system model for pilot-aided sparse channel estimation in an OFDM system with the canonical discrete time channel model. Assume that information is transmitted through an OFDM symbol that consist of N subcarriers and has a cyclic prefix length of $N/4$. Among N subcarriers, N_p subcarriers are used to transmit pilots with locations represented as $[p_1, p_2, \ldots, p_{N_p}]$, where $1 \leq p_1 < p_2 \ldots < p_{N_p} \leq N$ and $N_d = N - N_p$ subcarriers transmit information. The transmitted and received pilot symbols on pilot subcarrier locations are $x = [x(p_1), x(p_2), \ldots, x(p_{N_p})]^T$ and $y = [y(p_1), y(p_2), \ldots, y(p_{N_p})]^T$ respectively. Then the frequency domain sparse channel estimation of a pilot-aided OFDM system at the receiver can be modeled as:

$$y = Ah + n\,, \tag{1}$$

where $A = X.F_{N_p \times L}$ is a sensing matrix. X is a diagonal matrix of transmitted pilot symbols $X = diag\{x(p_1), x(p_2), \ldots, x(p_{N_p})\}$ and $F_{N_p \times L}$ is a discrete Fourier submatrix constructed by selecting first L columns and N_p rows stated by pilot locations $[p_1, p_2, \ldots, p_{N_p}]$ from a standard Fourier matrix $N \times N$.

$$F_{N_p \times L} = \frac{1}{\sqrt{N}} \begin{bmatrix} 1 & \omega^{p_1} & . & . & . & \omega^{p_1^{(L-1)}} \\ 1 & \omega^{p_2} & . & . & . & \omega^{p_2^{(L-1)}} \\ . & . & . & & & . \\ . & . & & . & & . \\ . & . & & & . & . \\ 1 & \omega^{p_{N_p}} & . & . & . & \omega^{p_{N_p}^{(L-1)}} \end{bmatrix} \tag{2}$$

where $\omega = e^{-j\frac{2\pi}{N}}$ and $n = [n(1), n(2), \ldots, n(N_p)]^T$ is the Additive White Gaussian Noise (AWGN) vector with zero mean and variance σ_n^2. $h = [h(1), h(2), \ldots, h(L)]^T$ is the discrete channel impulse response vector with L coefficients. The multipath wireless channel gives rise to multiple attenuated and delayed copies of transmitted signal at the receiver, due to the number of scatters in the surrounding environment. We consider a transmission over such a multipath wireless channel with L resolvable paths (coefficients), and each path has a complex path gain α_i and a delay spread τ_i. The time domain baseband channel model is given by:

$$h(\tau) = \sum_{i-1}^{L} \alpha_i \delta(\tau - \tau_i)\,, \tag{3}$$

where $\delta(.)$ is a Dirac delta function. The equivalent discrete channel model can be represented as:

$$h(n) = \sum_{i-1}^{L} \alpha_i \delta\big((n - \tau_i)T_s\big)\,, \tag{4}$$

where T_s is the sampling interval which holds a very small value compared to the maximum delay spread for practical wide band wireless channels. In such cases the impulse response h is dominated by relatively few resolvable paths over the maximum paths L, and these channels are often termed as sparse channels. Assuming the frequency domain channel impulse response h is having $\|h\|_0 \leq k \ll L$, then the multipath wireless channel is termed as k *sparse channel*.

The reconstruction of channel impulse response h at the receiver is essential for coherent detection. The competent pilot aided channel estimation for today's wireless systems involves either linear or nonlinear techniques. Conventional pilot-aided methods typically depend on linear reconstruction techniques with the resulting sensing matrix A of N_p rows and L columns, such that $N_p > L$. Considering the inherent sparsity of the wireless channel, the number of pilots N_p is kept lower than maximum channel coefficients L, i.e. $N_p < L$, then system will become an underdetermined system, but improves the system data rate. Thus, linear reconstruction methods do not provide an accurate solution. CS-based methods provide a nonlinear way to reconstruct these under determined systems by exploiting the sparsity of the channel. However, the reliable and efficient reconstruction of sparse vector h by using CS recovery

techniques is based on proper selection of N_p rows for the sensing matrix A from the Fourier matrix, i.e. selection of pilot locations in subcarriers.

3. Optimal Pilot Analysis

Proper selection of the pilot pattern influences the sparse channel estimation of OFDM systems using CS reconstruction algorithms. Indeed, sparse vector h is guaranteed for nonlinear reconstruction by CS if A satisfies the Restricted Isometry Property (RIP).
A sensing matrix A satisfies the RIP of order k if there exists a constant δ such that:

$$(1-\delta)\|h\|_2^2 \leq \|Ah\|_2^2 \leq (1_\delta)\|h\|_2^2 \,, \tag{5}$$

for any k sparse vector. The minimum of all constants δ satisfying the above condition is called the isometric constant δk. But there is no algorithm to check the RIP, since it involves combinatorial computation complexity. Other than RIP, the widely used condition that guarantees the reconstruction of the sparse vector is *coherence* [16].
Coherence μ of a sensing matrix A, is the largest absolute inner product between any two columns a_m and a_n of A:

$$\begin{aligned}\mu(A) &= \max_{1\leq m<n\leq L} \left|\langle a_m, a_n\rangle\right| \\ &= \max_{1\leq m<n\leq L} \left|\sum_{i=1}^{N_p} \left|x(p_i)\right|^2 \omega^{p_i(n-m)}\right| . \end{aligned} \tag{6}$$

Let $c \triangleq n-m$ then

$$\mu(A) = E \max_{1\leq c\leq L-1} \left|\sum_{i=1}^{N_p} \omega^{p_i c}\right| ,$$

where energy of pilot E is treated as one.
Now $\omega = \mathrm{e}^{-\mathrm{j}\frac{2\pi}{N}} = \mathrm{e}^{-\mathrm{j}\theta}$, where $\theta = \frac{q\pi}{N}$.
Then coherence will be:

$$\begin{aligned}\mu(A) &= \max_{1\leq c\leq L-1} \left|\sum_{i=1}^{N_p} \mathrm{e}^{-\mathrm{j}cp_i\theta}\right| \\ &= \max_{1\leq c\leq L-1} \left(N_p + \sum_{i=1}^{N_p}\sum_{j=i+1}^{N_p} 2\cos\Big(c\big((p_i-p_j)\bmod N\big)\theta\Big)\right)^{\frac{1}{2}} \\ \mu(A) &= \max_{1\leq c\leq L-1} \big(N_p + H_c(P)\big)^{\frac{1}{2}} \,, \end{aligned} \tag{7}$$

where

$$H_c(P) = \sum_{i=1}^{N_p}\sum_{j=i+1}^{N_p} 2\cos\Big(c\big((p_i-p_j)\bmod N\big)\theta\Big) \,. \tag{8}$$

A different pilot pattern leads to a different sensing matrix A. The objective function Q for selecting an optimal pilot pattern P is to minimize the coherence of A:

$$Q = \arg\min_A \mu(A) \,. \tag{9}$$

A pilot pattern yields minimum coherence $\mu(A)$ if $\cos\big(c(p_i-p_j)\theta\big)$ holds minimum for all values of c in Eq. (8). If the most of angles $c(p_i-p_j)\theta$ are occupied in the 2nd and 3rd quadrant, then the cosine angle holds minimum. However, for some specific settings, the optimal pilot can be generated from the Cyclic Difference Set (CDS).

Definition for CDS: For the given (N, N_p), if λ is an integer where $\lambda = \frac{N_p(N_p-1)}{N-1}$ and $N_p < N$, then CDS is defined as a set of N_p distinct components selected from N denoted as $(p_1, p_2, \ldots, p_{N_p})$ satisfying that any integer $x(1 \leq x \leq N-1)$ repeats λ times in the set:

$$\{x = p_i - p_j (\bmod N) \,|\, 1 \leq i \neq j \leq N_p\} \,, \tag{10}$$

and the corresponding difference multiset $D = \{a_d\}_{d=1}^{N-1}$, where a_d is the number of pairs (p_i, p_j) in pilot indices set P such that $d = p_i - p_j (\bmod N) \,|\, 1 \leq i \neq j \leq N_p$, $d = 1, 2, \ldots, N-1$. The mean and variance σ_P^2 of the difference multiset are defined as:

$$mean = \frac{1}{N-1}\sum_{i=1}^{N-1} a_{d_i} \,, \tag{11}$$

$$\sigma_P^2 = \sum_{i-i}^{N-1} (a_d - mean)^2 \,. \tag{12}$$

The pilot selection satisfying the definition of CDS is surely the optimal choice for minimum coherence, since the resultant Discrete Fourier Transform (DFT) submatrix achieves the Welch bound. The sufficient condition for CDS to be optimal pilot selection is:

$$L \geq \left\lceil \frac{N}{2} \right\rceil \,. \tag{13}$$

Nevertheless, for many pairs of N and N_p, there is no CDS. Moreover the channel impulse response length L is less than the cyclic prefix of the practical OFDM system.
In the present work for some specific settings, the optimal pilot selection from a p-Sylow subgroup is analyzed and conditions are obtained for a subgroup to act as an optimal pilot selection.

Definition for p-Sylow: Let $(G, .)$ be a group and p be a prime number. If $(G) = p^a m$, where $p \nmid m$, then a subgroup of order p^α is called the p-Sylow subgroup of G.
Existence of the p-Sylow subgroup is guaranteed. If $(G, .)$ is an abelian group, then the p-Sylow subgroup is unique. Let $S \subseteq G$. The subgroup of G generated by S is the smallest subgroup of G containing S and is denoted by (S). (S) is the set of finite products of elements of S and its inverses. For any subgroup H of an abelian group $(G, .)$ and for any $a \in G$, $aH = \{a.h \,|\, h \in H\}$ denotes the coset of H in G.
Now, for a given (N, N_p), the optimal pilot selection that can be generated from a subgroup is analyzed. If N and N_p satisfy the conditions stated in the following theorem, then the p-Sylow subgroup will be an optimal pilot selection.

Theorem 1: For a given (N, N_p), if $(N+1)$ is a prime number q and for some prime p and $N_p = p^\alpha$ for some integer α such that $p^\alpha | N$, $p^{\alpha+1} \nmid N$ with $N_p(N_p-1) = \lambda N$, where λ is an integer and if P is the unique p-Sylow subgroup of the group $(G, \otimes)$ under multiplication $\bmod(N+1)$, then P is a CDS and P is the optimal pilot selection for (N, N_p) for $L \geq \frac{N}{2}$ provided given $p_1, p_2, p_3\, p_4 \in P$, there exist p'_1, p'_2 such that:

$$(p_1 + p_2) - (p_3 + p_4) \equiv (p'_1 - p'_2) \bmod (N+1)\,, \qquad (14)$$

where $G = \{1, 2, \ldots, N\}$.

Proof: Let $F = \{0, 1, 3, \ldots, N\}$ and $\lambda = 1$. Then $(F, \oplus, \otimes)$ is a field where $\oplus$ and $\otimes$ are the addition $(N+1)$ and multiplication $\bmod(N+1)$ respectively. Let $P = (p_1, p_2, p_3, \ldots, p_{N_p})$ be the unique p-Sylow subgroup of $(G, \otimes)$. Let $S \triangleq (p_i - p_j) \bmod (N+1),\ p_i \neq p_j\}$, where $r \in \{1, 2, \ldots, N\}$. Clearly, S is non empty and $O(S) \leq N_p(N_p-1) = N$. Let (S) be the subgroup of $(F, \oplus)$ generated by S. Now, we show that (S) is closed under $\otimes$.

Let $x, y \in (S)$. Suppose $x = s_1 + s_2$, where $s_1, s_2 \in S$. Then $x = \{(p_1 - p_2) + (p_3 - p_4)\} \bmod (N+1)$, where $p_i \in P$.

Similarly $y = \{(p'_1 - p'_2) + (p'_3 - p'_4)\} \bmod (N+1)$, where $p'_i \in P$.

Using the given condition, we can find $p'_i p'_j$ in P such that $x.y = (p'_i - p'_j) \bmod (N+1)$ for some $p'_i, p'_j \in P$. Hence (S) is a subring of F. Since F has no proper subring, $(S) = F$. Now we show that $(S) \setminus \{0\} = S$. Let $y(\neq 0) \in (S)$ and let $y = x_1 + x_2$ where $x_1, x_2 \in S$.

Let $x_1 = (p_1 - p_2) \bmod (N+1)$ and $x_2 = (p_3 - p_4) \bmod (N+1)$. Then:

$$\begin{aligned} x_1 + x_2 &= \{(p_1 + p_2) - (p_3 + p_4) \bmod (N+1) \\ &= (p'_1 - p'_2) \bmod (N+1),\ \text{for some } p'_1, p'_2 \in P, \\ &= x_3,\ \text{for some } x_3 \in S\,;\ \text{thus } (S) \setminus \{0\} = S. \end{aligned}$$

Hence, $S = 1, 2 \ldots N$. Therefore, P is also a CDS and the optimal pilot selection. For any integer $\lambda \neq 1$ the proof is similar.

Corollary: For a given (N, N_p) if N is a prime number q and for some prime p and for some integer α such that $p^\alpha | q-1$, $p^{\alpha+1} \nmid q-1$ with $N_p(N_p-1) = \lambda(N-1)$ and P is the unique p-Sylow subgroup of $(G, \otimes)$, under multiplication $\bmod(N)$ where $G = 1, 2, \ldots, N-1$ such that P satisfies the condition given in theorem 1 then P is the optimal solution.

For the case (N, N_p) where $(N+1)$ is a prime, N_p pilots will be selected from $1, 2, 3, \ldots, N$ whereas in the case (N, N_p), where N is a prime, N_p pilots will be selected from $1, 2, 3, \ldots, N-1$.

The optimal pilot selection for an OFDM system from p-Sylow satisfies the definition of CDS for some specific pairs of (N, N_p). It is no longer an optimal pilot selection for a practical OFDM system with channel length $L < \lceil \frac{N}{2} \rceil$. For example, $\{1, 7, 9, 10, 12, 16, 26, 33, 34\}$ is a 3-Sylow subgroup which is a CDS for $(37, 9)$. It has the coherence $\mu = 2.6458$ for all range of $L \geq \lceil \frac{N}{2} \rceil$. But if $L = 11 < \lceil \frac{N}{2} \rceil$ there exist a set which is neither a subgroup nor a CDS $\{1, 4, 7, 10, 13, 22, 28, 31, 34\}$ having coherence $\mu = 2.1196$ less than obtained by p-Sylow subgroup and CDS. Practical OFDM systems will have a $\frac{N}{4}$ long cyclic prefix which is usually much larger than the length of the channel. Therefore, it is necessary to explore a pilot search algorithm suitable for wideband OFDM systems.

4. Pilot Search Algorithm

This section describes the deterministic procedure for selecting the pilot locations for a given (N, N_p, L). Optimal N_p subcarrier selection from N subcarriers of an OFDM system by exhaustive search among all possible ${}^N C_{N_p}$ DFT submatrices is humanly impossible because of its computational complexity. Here, a deterministic approach is proposed that couples variance and coherence minimization to meet the near-optimal pilot selection. The algorithm starts by assigning the first pilot location and selects the remaining locations, one by one, so that a difference multiset of selected pilot locations achieves minimum variance. The minimum variance pilot pattern will not lead to minimum coherence for small L. Therefore, the algorithm updates every candidate of the selected pilot pattern for minimum coherence from all pilot subcarrier candidates. If the candidate pilot subcarriers are considered to range from 1 to N, there is a possibility for the pilot search algorithm to choose pilot subcarriers close to each other. It decreases the efficiency of the pilot pattern in channel estimation [15]. By defining the neighboring optimal distance for pilot subcarriers, the algorithm will not choose the closest subcarriers. In the proposed algorithm index set I_s defined to contain candidate pilot subcarrier locations at optimal distance. The optimal distance of pilot subcarriers for the given N and L is $c = \lfloor \frac{N}{L} \rfloor$.

The proposed algorithm is summarized as Algorithm 1. Initially, the first pilot location is assigned as number one. Next, the second pilot location is selected from the subset $\widehat{P}_y$ generated using $\widehat{P}_{y-1} \cup n | n \in \{I_s\} \setminus P_{y-1}$ for minimum variance. By repeating this, we obtain the pilot pattern $P = [p_1, p_2 \ldots, p_{N_p}]$. The minimum variance calculation for subset $\widehat{P}_y = \{P_y(1), P_y(2), \ldots, P_y(n)\}$ for each update is given by Eqs. (15)–(19).

Let $P_y = [p_1, p_2, \ldots, p_x]$, where $x \leq N_p$ and $y = 1, 2, \ldots, n$. Then:

$$mean = \frac{1}{N-1} \sum_{i=1}^{N-1} a_{d_i}\,, \qquad (15)$$

where a_d is a element of $D = \{a_d\}_{d=1}^{N-1}$ defined as number of pairs (p_i, p_j) in selected pilot location set P_y such that $d = p_i - p_j (\bmod N) \,|\, 1 \leq i \neq j \leq x$, where $d = 1, 2, \ldots, N-1$, and variance

$$\delta^2_{P_y} = \sum_{i=1}^{N-1} (a_{d_i} - mean)^2\,. \qquad (16)$$

Algorithm 1: Pseudocode for proposed algorithm

Input: N, N_p, L, t
Initialize: $I_{temp} = \emptyset$, $I_P = \emptyset$, $P_c = \emptyset$, $c = \left\lfloor \frac{N}{L} \right\rfloor$
$I_s = \{1, 1+c, 1+2c, \ldots, N\}$: $\|I_s\| = M$
For $m = 1, 2, \ldots, M$, $P_1 = I_s(m)$
Generate subset $\widehat{P}_2$ by $P_1 \cup n | n \in \{I_s\} \setminus P_1$
Obtain $I = [P_2(1), P_2(2), \ldots, P_2(t)]$ according to Eq. (17)
For $y = 3, 4, 5, \ldots, N_p$,
For $x = 1, 2, \ldots, t$, $P_{y-1} = I(x)$
Generate subset $\widehat{P}_y$ by $P_{y-1} \cup n | n \in \{I_s\} \setminus P_{y-1}$
Obtain $I = [P_y(1), P_y(2), \ldots, P_y(t)]$ according to Eq. (17)
$I_{temp} \Leftarrow [I_{temp}, I]$
End for x
Obtain I from I_{temp} according to Eq. (17)
End for y
For $z = 1, 2, \ldots, t$
P_{N_p}, $z = I(z)$
For $y = N_p, N_{p-1}, \ldots, 1$
$P'_{N_p,z} = [p_{1,z}, p_{2,z}, \ldots, p_{y,z} = \emptyset, \ldots, p_{N_p,z}]$
For $x = 1, 1+c, 1+2c, \ldots, \leq N$
If $x \notin P_{N_p,z}$
$\widehat{P} = [p_{1,z}, p_{2,z}, p_{y,z} = x, \ldots, p + N_p, z]$
End if
End for x
Obtain $P'_{N_p,z}$from $\widehat{P}$ according to Eq. (19)
End for y
$I_p(z) = P'_{N_p,z}$
End for z
Obtain $P_c(m)$ from I_p according to Eq. (19)
End for m
$P = \arg\min_P \mu(A)_{P_c}$
Output: pilot pattern P.

To achieve a greater degree of accuracy, instead of selecting a pilot pattern with the least variance, we select t sets of pilot patterns (group selection) having a minimum variance in every pilot location update. The t sets are selected with least $\sigma^2_{P_y}$ among n updated set $P = [P_y(1), P_y(2), \ldots, P_y(n)]$ as:

$$I = [P_y(1),\ P_y(2), \ldots, P_y(t)]\,, \tag{17}$$

where $y = 2,\ 3,\ 4,\ \ldots,\ N_p$ and $P_y(1) = P_y(i),\ P_y(2) = P_y(j) \ldots | 0 \leq \sigma^2_{P_y(i)} \leq \sigma^2_{P_y(j)} \leq \ldots$.

The procedure is repeated for every one of the values from index set I_s as first pilot location. The resulting t sets of pilot pattern obtained from the first loop is:

$$I = [P_{N_p}(1), P_{N_p}(2), \ldots, P_{N_p}(t)]\,, \tag{18}$$

where $P_{N_p}(i) = [p_{1,i}, p_{2,i}, \ldots, p_{N_p,i}]$. All t selected pilot patterns are updated for minimum coherence. Every n-th entry of a pilot pattern P_{N_p} can be updated by selecting the best form $I_s \setminus \{P_{N_p}(j) \,|\, j = 1, 2, \ldots, N_p,\ j \neq n\}$. From the resulting pilot location collection set P, select a pilot location with minimum coherence as:

$$P \Leftarrow \arg\min_P \mu(A)_{P(i)},\ i = 1, 2, 3, \ldots\,. \tag{19}$$

5. Simulation Results

The theoretical distance between the pilot locations is verified practically by simulating the proposed algorithm for

Table 1
Coherence of a pilot pattern generated with various distances selected between pilot subcarriers

N	N_p	L	Distance	μ
256	16	50	1	4.6868
			3	4.8937
			4	4.4308
			5	**4.3887**
			6	10.8125

Table 2
List of pilot patterns generated for various (N, N_p, L), using the proposed algorithm

N	N_p	μ	Pilot pattern	L
64	6	2.6131	1, 5, 9, 17, 33, 45	15
	6	2.6131	1, 13, 29, 33, 37, 53	16
	9	2.5326	1, 5, 13, 21, 29, 33, 37, 49	
73	9	2.7284	1, 11, 12, 14, 17, 26, 42, 47, 65	37
		2.7201	1, 9, 13, 17, 21, 29, 33, 53, 57	18
128	6	2.8840	5, 21, 49, 53, 61, 113	30
	9	3.1350	5, 21, 37, 41, 45, 49, 73, 113, 121	
	12	3.2558	1l, 29, 33, 41, 45, 49, 53, 69, 81, 85, 105, 113	
	14	3.3785	1, 5, 9, 17, 25, 29, 37, 61, 65, 69, 81, 105, 109 121	
256	12	4.1823	1, 6, 21, 41, 81, 146, 151, 156, 176, 201, 211, 246	50
	13	4.3591	1, 6, 31, 41, 46, 81, 86, 141, 151, 206, 211, 226, 236	
	16	4.3887	1, 6, 16, 21, 26, 41, 46, 51, 66, 121, 126, 156, 181, 191, 211, 221	
	23	4.8822	1, 6, 11, 21, 26, 31, 36, 46, 66, 71, 81, 86, 106, 116, 136, 141, 151, 156, 181, 196, 206, 226, 236	
	12	4.0496	1, 29, 73, 77, 93, 97, 101, 109, 129, 141, 153, 161, 165, 201, 217, 245	
	16	4.4308	1, 29, 73, 77, 93, 97, 101, 109, 129, 141, 153, 161, 165, 201, 217, 245	
	24	4.8550	1, 13, 49, 57, 61, 73, 77, 93, 117, 121, 141, 145, 149, 161, 169, 177, 181, 189, 193, 201, 217, 225, 233, 253	
512	40	6.8674	1, 6, 11, 16, 21, 26, 31, 36, 51, 66, 71, 81, 91, 101, 126, 171, 176, 181, 191, 216, 221, 236, 266, 271, 276, 291, 296, 306, 351, 376, 381, 396, 401, 411, 421, 446, 461, 481, 486	90
	27	6.3813	1, 16, 21, 46, 56, 76, 81, 106, 111, 151, 186, 201, 206, 211, 251, 256, 286, 301, 326, 371, 411, 421, 471, 481, 486, 491, 501	93
1024	16	4.4653	1, 21, 41, 101, 141, 161, 221, 261, 321, 341, 421, 601, 621, 661, 761, 801	50

various distances. Table 1 proves that the minimum distance that should be maintained between the pilot locations is $\lfloor \frac{N}{L} \rfloor$ which is 5 for $N = 256$ and $L = 50$.

The pilot patterns generated using the proposed algorithm for various pairs of (N, N_p, L) are presented in Table 2. The results show that if N is a prime, coherence of the proposed algorithm's pilot pattern meets the Welch lower bound and prove the effectiveness of the proposed algorithm. For example, $(N, N_p, L) = (73, 9, 37)$ coherence of the proposed algorithm's pilot location achieves the Welch bound 2.8284. Comparison of coherence obtained by the proposed algorithm with algorithms used in practice for various (N, N_p, L) values is presented in Table 3.

Table 3
Comparison of coherence obtained by the proposed algorithm and by existing pilot search algorithms

N	N_p	L	Algorithm	μ
256	16	60	Stochastic serial search [12]	4.7021
			Greedy deterministic [13]	4.8630
			Proposed algorithm	**4.4308**
256	16	50	Tree based backward with 11 branches [8]	4.9189
			Greedy deterministic [13]	4.5261
			Proposed algorithm	**5.8757**
256	13	50	Mahdi-Khosravi & Saeed-Mashhadi [11]	5.8757
			Proposed algorithm	**4.3591**

An QPSK OFDM system is constructed with 256 subcarriers and 16 of them are used as pilot subcarriers for pilot-aided channel estimation. A discrete sparse channel h is realized with 5 dominant coefficients, randomly placed over the maximum of 50 channel coefficients. A typical discrete channel realization is shown in Fig. 1. The channel estimation performance of the pilot pattern generated using the proposed algorithm is evaluated at the receiver based on the knowledge of the sensing matrix A and the received pilots vector y using greedy iterative orthogonal matching pursuit (OMP) [17]. The normalized mean square error (MSE) associated with channel vector h and estimated channel $\hat{h}$ is calculated by:

$$MSE = \frac{\left\|h - \hat{h}\right\|_2^2}{\left\|h\right\|_2^2}. \tag{20}$$

MSE comparison for channel estimation using the proposed and different pilot selection algorithms, comprising, in practice, over 105 iterations for each signal to

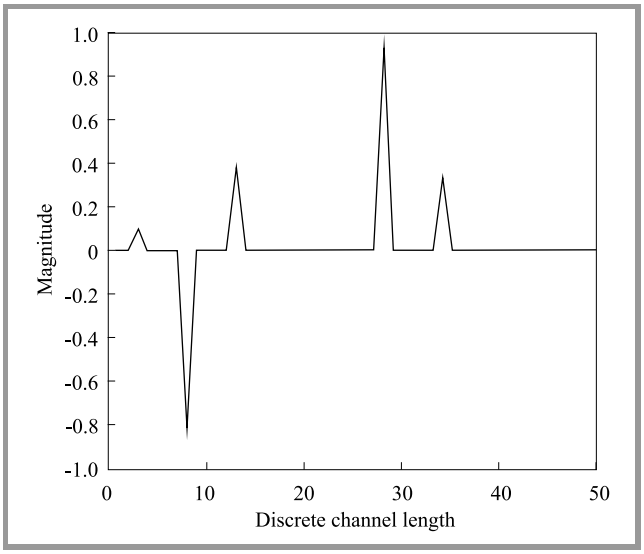

Fig. 1. Typical channel impulse response with 5 dominant coefficients over the maximum discrete channel length.

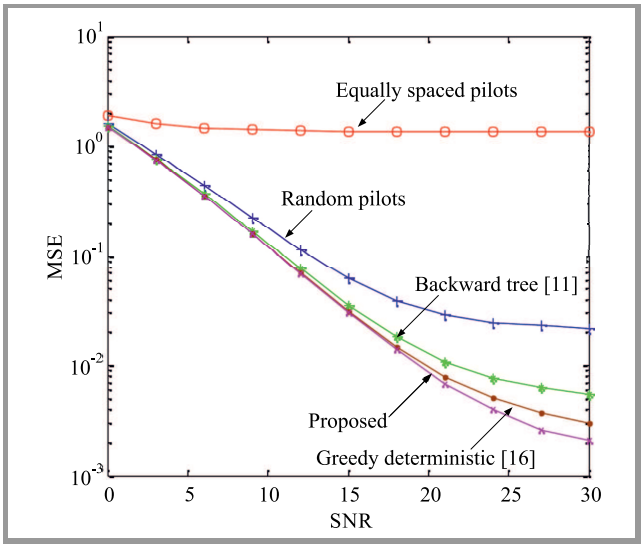

Fig. 2. MSE performance comparison for channel estimation with pilot patterns generated using different schemes for $(N, N_p, L) = (256, 16, 50)$.

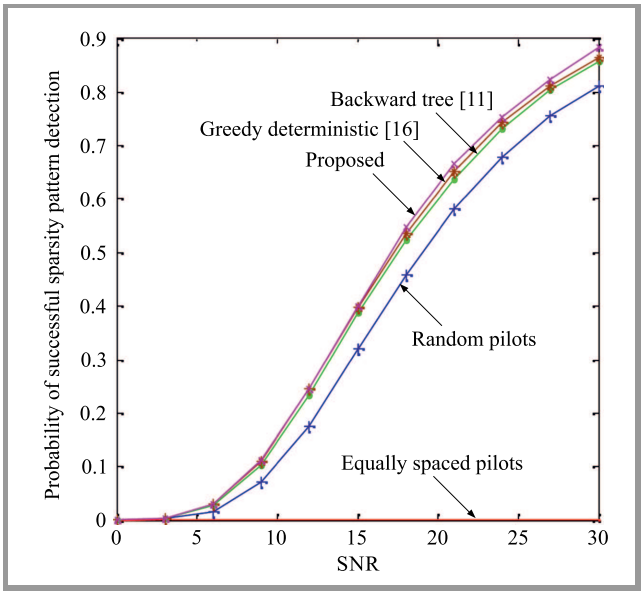

Fig. 3. Detection performance of OMP using proposed and different pilot schemes for $(N, N_p, L) = (256, 16, 50)$.

noise ratio (SNR), is plotted in Fig. 2. The equally spaced conventional pilots and random pilots suggested for the sparse channel are also considered for comparison purposes. Equally spaced pilots are not optimized to minimum coherence and there is no benefit in using them for sparse channel estimation and for random pilot generation, which is difficult for practical systems. We observe that the proposed pilot pattern significantly improves the performance of MSE compared to existing schemes used in practice, with reduced coherence. Detection performance of the sparse reconstruction algorithm gives the percentage of cases of exact recovery of the sparse channel from the received pilots. The comparison of sparse channel detection performance of OMP is presented

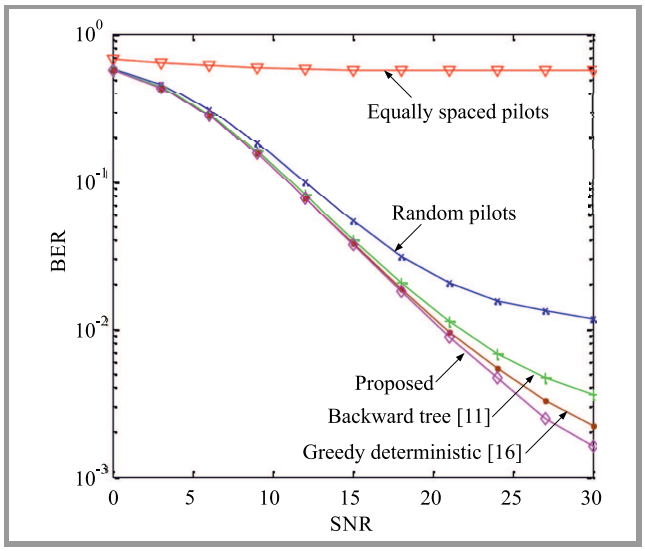

Fig. 4. BER performance comparison of channel estimation for pilot patterns generated using different schemes for $(N, N_p, L) = (256, 16, 50)$.

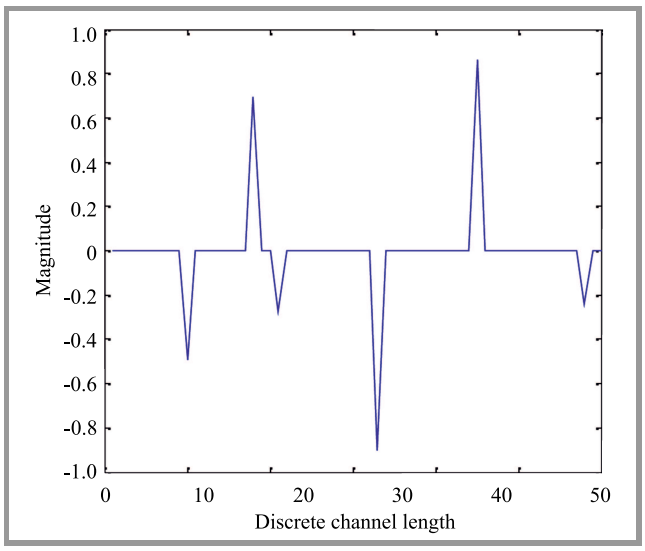

Fig. 5. Typical channel impulse response with 6 dominant coefficients over the maximum discrete channel coefficients $L = 60$.

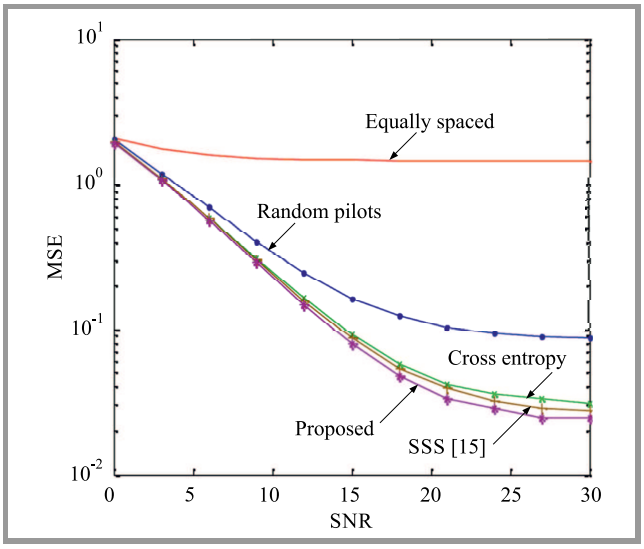

Fig. 6. MSE performance comparison of channel estimation for pilot patterns generated using different schemes for $(N, N_p, L) = (256, 16, 60)$.

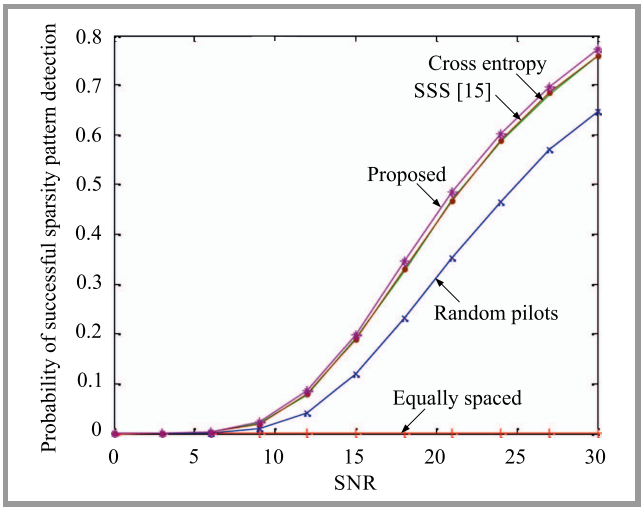

Fig. 7. Detection performance of OMP using proposed and different pilot schemes for $(N, N_p, L) = (256, 16, 60)$.

in Fig. 3. Transmitted data detection performance is shown in Fig. 4 as Bit Error Rate (BER). Performance of the proposed pilot search algorithm is also evaluated for a channel with 6 dominant coefficients spread over the maximum length of 60 in an QPSK OFDM system channel estimation to verify the robustness of the proposed algorithm. Figure 5 represents a typical channel implementation for $L = 60$.

MSE channel estimate, detection performance of the channel estimation algorithm and BER of detected data are given in Figs. 6–8, respectively, for $L = 60$ and show the effectiveness of the proposed pilot search algorithm compared to pilot search algorithms used in practice. The running time of the proposed algorithm required to generate pilots with the length of 16, for the channel length

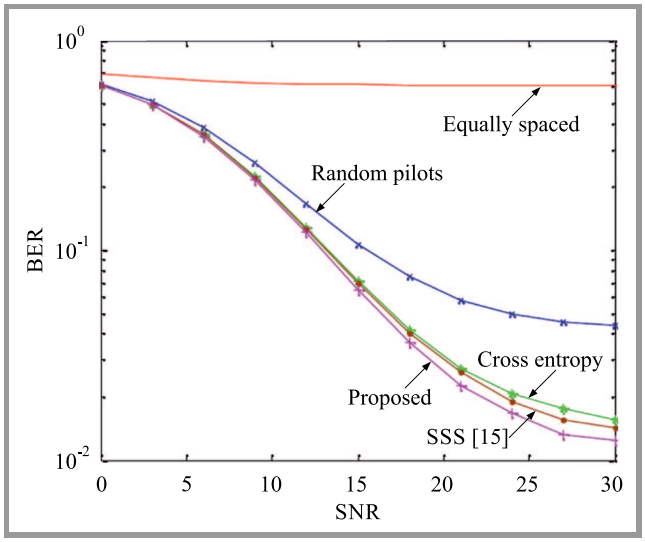

Fig. 8. BER performance comparison of channel estimation for pilot patterns generated using different schemes for $(N, N_p, L) = (256, 16, 60)$.

of $L = 50$ and 60, is 111 and 188 s over 256 subcarriers, respectively.

6. Conclusions

In this paper, we investigated pilot selection for pilot-aided sparse channel estimation in wide band OFDM systems. Sufficient conditions are derived to guarantee that p-Sylow is the optimal pilot pattern for some (N, N_p, L). We have proposed a deterministic procedure to select the pilot pattern for given (N, N_p, L). If N is a prime, then the proposed algorithm achieves the Welch bound, confirming its effectiveness. Simulation results show that the pilot pattern generated using the proposed scheme significantly improves the key metrics of wireless systems, including MSE and BER, compared to the existing methods with minimized coherence.

References

[1] Y. S. Cho, J. K. Won, Y. Y. Chung, and G. Kang, *MIMO-OFDM Wireless Communication with MATLAB*. Singapore: Wiley & Sons (Asia), 2010 (doi: 10.1002/9780470825631).

[2] Y. Li, "Pilot-symbol-aided channel estimation for OFDM in wireless systems", *IEEE Trans. on Vehicular Technol.*, vol. 49, no. 4, pp. 1207–1215, 2000 (doi: 10.1109/25.875230).

[3] M. H. Hsieh and Ch. H. Wei, "Channel estimation for OFDM Systems Based on comb-type pilot arrangement in frequency selective fading channels", *IEEE Trans. on Consumer Electron.*, vol. 44, no. 1, pp. 217–225, 1998 (doi: 10.1109/30.663750).

[4] R. Negi and J. Cioffi, "Pilot tone selection for channel estimation in a mobile OFDM system", *IEEE Trans. on Consumer Electron.*, vol. 44, no. 3, pp. 1122–1128, 1998 (doi: 10.1109/30.713244).

[5] D. L. Donoho, "Compressed sensing", *IEEE Trans. on Inform. Theory*, vol. 52, no. 4, pp. 1289–1306, 2006 (doi: 10.1109/TiT.2006.871582).

[6] W. U. Bajwa, "New information processing theory and methods for exploiting sparsity in wireless Systems", Ph.D. Dissertation, University of Wisconsin, Madison, WI, USA, 2009.

[7] L. Applebaum *et al.*, "Deterministic pilot sequences for sparse channel estimation in OFDM systems", in *Proc. of 17th Int. Conf. on Digit. Sig. Process. DSP 2011*, Corfu, Greece, 2011, pp. 1–7 (doi: 10.1109/ICDSP.2011.6005021).

[8] Ch. Qi and L. Wu, "Optimized Pilot placement for sparse channel estimation in OFDM systems", *IEEE Sig. Process. Lett.*, vol. 18, no. 12, pp. 749–752, 2011 (doi: 10.1109/LSP.2011.2170834).

[9] Ch. R. Berger, J. Gomes, and J. M. F. Moura, "Study of pilot designs for cyclic-prefix OFDM on time-varying and sparse underwater acoustic channels", in *Proc. of IEEE Oceans Conf.*, Santander, Spain, 2011, pp. 1–8 (doi: 10.1109/Oceans-Spain.2011.6003627).

[10] Ch. Qi and L. Wu, "Tree-based backward pilot generation for sparse channel estimation", *Electron. Lett.*, vol. 48, no. 9, pp. 501–503, 2012 (doi: 10.1049/el.2012.0010).

[11] J. Ch. Chen, Ch. K. Wen, and P. Ting, "An efficient pilot design scheme for sparse channel estimation in OFDM systems", *IEEE Commun. Lett.*, vol. 17, no. 7, pp. 1352–1355, 2013 (doi: 10.1109.LCOMM.2013.051313.122933).

[12] P. Pakrooh, A. Amini, and F. Marvasti, "OFDM pilot allocation for sparse channel estimation", *EURASIP J. of Adv. Sig. Process.*, vol. 59, no. 1, pp. 1–9, 2012 (doi: 10.1186/1687-6180-2012-59).

[13] M. Khosravi and S. Mashhadi, "Joint pilot power pattern design for compressive OFDM channel estimation", *IEEE Commun. Lett.*, vol. 19, no. 1, pp. 50–53, 2013 (doi: 10.1109/LCOMM.2014.2371036).

[14] Ch. Qi *et al.*, "Pilot design scheme for sparse channel estimation in OFDM systems", *IEEE Trans. on Vehicular Technol.*, vol. 64, no. 4, pp. 1493–1505, 2015 (doi: 10.1109/TVT.2014.2331085).

[15] S. Hadi, S. Masoumian, and B. M. Tazehkand, "Greedy deterministic pilot pattern algorithms for OFDM sparse channel estimation", *Wirel. Personal Commun.*, vol. 84, no. 2, pp. 1119–1132, 2015 (doi: 10.1007/s11277-015-2679-5).

[16] D. L. Donoho and X. Huo, "Uncertainty principles and ideal atomic decomposition", *IEEE Trans. on Inform. Theory*, vol. 47, no. 7, pp. 2845–2862, 2001 (doi: 10.1109/18.959265).

[17] A. Ganesh, Z. Zhou, and Y. Ma, "Separation of a subspace signal: Algorithms and conditions", in *Proc. of IEEE Int. Con. on Acoust. Speech Sig. Process. ICASSP 2009*, Taipei, Taiwan, 2009, pp. 3141–3144 (doi: 10.1109/ICASSP.2009.4960290).

P. Vimala received her B.Sc. in Electronics and Communication Engineering from Jayaram College of Engineering, Trichy, Tamil Nadu, India in 2000 and M.Sc. in Process Control and Instrumentation Engineering from Annamalai University, Chidambaram, Tamilnadu, India in 2010. She is currently working as an Assistant Professor at the Department of Electronics and Communication Engineering, Faculty of Engineering and Technology, Annamalai University. Her current research areas include digital signal processing, sparse signal processing, digital communication and wireless communication.

E-mail: vimalakathirau@gmail.com
Department of Electronics and Communication Engineering
Annamalai University
Tamil Nadu, India

G. Yamuna received her B.Sc. in Electronics and Communication Engineering from National Institute of Technology (NIT), Trichy, Tamil Nadu, India in 1987. She received her M.Sc. in Power Systems from Annamalai University in 1991. She received her Ph.D. in Electrical Engineering from Annamalai University in 2010. She has published many technical papers in national and international conferences and journals. Currently, she is working as a Professor at the Department of Electronics and Communication Engineering, Faculty of Engineering and Technology, Annamalai University, Tamil Nadu, India. She is an associate editor and reviewer for several national and international journals. Her research interests include signal processing, image processing, wireless communication systems, antenna design and information security.

E-mail: yamuna.sky@gmail.com
Department of Electronics and Communication Engineering
Annamalai University
Tamil Nadu, India

Paper

An Optimized Propagation Model based on Measurement Data for Indoor Environments

Marco Morocho-Yaguana, Patricia Ludeña-González, Francisco Sandoval, Betty Poma-Vélez, and Alexandra Erreyes-Dota

Department of Computer Science and Electronic, Universidad Técnica Particular de Loja, Loja, Ecuador

https://doi.org/10.26636/jtit.2018.117217

Abstract—Propagation is an essential factor ensuring good coverage of wireless communications systems. Propagation models are used to predict losses in the path between transmitter and receiver nodes. They are usually defined for general conditions. Therefore, their results are not always adapted to the behavior of real signals in a specific environment. The main goal of this work is to propose a new model adjusting the loss coefficients based on empirical data, which can be applied in an indoor university campus environment. The One-slope, Log-distance and ITU models are described to provide a mathematical base. An extensive measurement campaign is performed based on a strict methodology considering different cases in typical indoor scenarios. New loss parameter values are defined to adjust the mathematical model to the behavior of real signals in the campus environment. The experimental results show that the model proposed offers an attenuation average error of 2.5% with respect to the losses measured. In addition, comparison of the proposed model with existing solutions shows that it decreases the average error significantly for all scenarios under evaluation.

Keywords—indoor, ITU model, log-distance model, loss measurement, one-slope model, path loss, propagation measurement, propagation models, radio propagation.

1. Introduction

Indoor environments are the most difficult scenarios in which communication systems operate, because the density of wireless communications is increasing on a daily basis, and the number of active devices is growing rapidly. Therefore, it is necessary to understand the nature of indoor propagation to predict the effects on electromagnetic signals through a propagation model.

The goal of propagation models is to determine the probability of successful operation of a communication system. It is an important factor in communication network planning. If the model is too conservative, the network could be very expensive. If it is too liberal, it can have low performance. Thus, fidelity of the model must be adapted to the network application [1]. It can be classified as a deterministic model, empiric model and as a combination of the two [2], depending on the environment characteristics available and their stability over time [3].

Since the indoor environment is more unfavorable than a typical outdoor scenario, determining a good propagation model is complicated, mainly due to the high variability in building structure and building materials [4]. Moreover, the propagation level can be radically affected by the interaction between obstacles, for instance, people motion or the closing of the doors. For this reason, the deterministic model is not usually used for indoor environments.

In the literature, there are many models providing for a number of parameters, for instance attenuation between floors [5] and optical phenomena, such as reflections [6]. Mathematical expressions are needed that model the specific indoor environmental conditions with more precision. Most models rely on the exponential law, with the propagation loss exponent depending on the frequency of operation [7], meaning that propagation is different for each frequency band.

Obtaining a mathematical model realistically reflecting the specific construction characteristics, such as type of building structure, shape of zones, wall thickness, type of materials used and separation distances between obstacles, is a complex task [8], [9]. For example, for 2.4 GHz WLAN systems there are data for underground mines [10], space platforms [11] and airports [12]. Paper [13] compares different models in building offices, concluding that the standard deviation of the error between the estimation and measurement model is around 6 dB. For the 914 MHz band, article [14] presents a simple exponential model where the error in the loss calculus by a block of data is around 6 dB on average and, 9 dB in the worst case scenario. All these models are empirical.

In the literature, it is not easy to find empirical models based on extensive measurement campaigns, enabling losses to be determined and later adapted to a mathematical model, because it is an expensive and difficult task requiring high performance equipment and demanding that a strict methodology be followed [15], [16].

Among the most popular indoor empirical models is the One-slope model (OSM), which assumes a linear depen-

dence between path losses (in dB) and the logarithm of the distance between the transmitter and the receiver. It is a simple model, but is usually characterized by a high percentage of error because it does not take into account the environment characteristics in the calculus [17]. Another model is the Log-distance model [18] that is a combination of the modified power law and log-normal fading based on empirical data. Finally, the International Telecommunication Union (ITU) has a loss model resuming in recommendation P.1238 [19]. It is based on empirical construction coefficients obtained through a measurement campaign that calculates the losses per trip in five different types of offices for the frequency range from 900 MHz to 100 GHz.

The goal of this paper is to propose a new model based on typical prediction models but with an adjustment of building campus environment parameters through an extensive measurement campaign, to obtain coefficients that are closer to real conditions.

This paper is organized as follows. Section 2 presents the indoor propagation models calculus and parameters. Section 3 describes the methodology for the measurement campaign and how the data is analyzed. In Section 4, the proposed model to calculate losses on the campus is described. The results are discussed in Section 5. Section 6 concludes the paper.

2. Indoor Propagation Models

In the indoor propagation environment, there are similar mechanisms (reflection, diffraction, and scattering) to those existing in outdoor environments. However, the indoor environment is considered more hostile [1]. For instance, inside a building, the signal levels can change by opening or closing a door [18].

Three key models, namely One-slope, Log-distance, and ITU indoor path loss models, are presented here.

2.1. One-slope Model (OSM)

In the One-slope indoor propagation model, a linear dependence between the path loss (PL) and the logarithm of the length d of the path is assumed, as can be seen in Eq. (1):

$$\text{PL [dB]} = \text{PL}(d_0) + 10 \cdot n_{\text{OSM}} \log d\,, \tag{1}$$

where $\text{PL}(d_0)$ represents the path loss at the reference distance equal to 1 m or Free-Space Path Loss (FSPL) for distance d [1], and n_{OSM} is the loss exponent. It is evident that OSM does not consider the random effects occurring in the propagation [20]. Table 1 presents the values of the attenuation coefficient when different environments at the frequency of 915 MHz are considered.

Table 1
One-slope model attenuation coefficient for indoor environments

Environment (915 MHz)	n_{OSM} [dB]
Building (LOS)	1.6 to 2
Building (NLOS) same floor	2 to 4
Building (NLOS) through 1–3 floors	4 to 6

2.2. Log-distance Model

It is a generic model frequently used in the literature to predict the propagation loss. It is logarithmically dependent on the distance, is used for a wide range of environments, and is expressed as:

$$\text{PL [dB]} = \text{PL}(d_0) + 10 \cdot n_{\text{LD}} \log \frac{d}{d_0} + X_\sigma\,, \tag{2}$$

where $\text{PL}(d_0)$ is defined as in Subsection 2.1, n_{LD} denotes the path loss exponent, and X_σ is a normal random variable with zero mean (in dB) and standard deviation of σ. X_σ includes in the model the shadowing effect and it is equal to zero in the case of no shadowing. Finally, Table 2 presents empirical values to path loss exponent and standard deviation for various indoor wave propagation cases [18].

Table 2
Path loss exponent and standard deviation for indoor environments

Location	Frequency [MHz]	n_{LD} [dB]	σ [dB]
Retails stores	914	2.2	8.7
Grocery store	914	1.8	5.2
Office, hard partition	1500	3.0	7.0
Office, soft partition	900	2.4	9.6
Office, soft partition	1900	2.6	14.1
Textile/chemical	1300	2.0	3.0
Textile/chemical	4000	2.1	7.0
Paper/cereals (LOS)	1300	1.8	6.0
Metalworking (LOS)	1300	1.6	5.8
Metalworking (NLOS)	1300	3.3	6.8

Table 3
ITU attenuation coefficient for indoor environments

Environment (900 MHz)	n_{ITU} [dB]
Open space	20
Indoor propagation (office)	33
Corridor	18
Walls	40

2.3. ITU-R (P.1238) Indoor Model

The ITU model is a radio propagation model that predicts the indoor path loss inside a closed area, e.g. inside a building, and is given by [1]:

$$\text{PL [dB]} = 20 \cdot \log f + n_{\text{ITU}} \cdot \log d + L_f(p) - 28\,, \tag{3}$$

where f is the frequency in MHz, n_{ITU} represents the distance power loss coefficient. The representative values for the attenuation coefficient for indoor environments are showed in Table 3 [19]. Additionally, in Eq. (3), d is the distance in meters, $L_f(p)$ is the floor penetration loss factor, and p denotes the number of floors between the transmitter and the receiver, in this case 0.

3. Methodology

3.1. Scenarios

Two buildings were chosen on the Universidad Técnica Particular de Loja (UTPL), Loya, Equador, campus to allow examination of indoor propagation models in the presence of different cases. The two buildings are described below:

1. **Building type A**: It comprises four floors with office areas, movable partitions and wooden cubicle desks, meeting rooms and laboratories with different equipment (only on the fourth floor). The exterior walls are constructed with bricks and have wide windows. The corridors in this building have a minimum length of 14 m and a maximum length of 22 m, and a minimum width between 1.76 and 7.65 m depending on the floor. In addition, in this building there are two types of doors: wooden doors (4 cm thick), and mixed doors (wood-glass) (0.8 cm thick).

2. **Building type B**: It has five floors with classrooms and auditoriums. The measurements were only made on three floors of the building. The exterior walls are constructed with brick and metal structure. In this building the measurements were made in corridors, doors, and windows. The corridors on the first and second floors have dimensions of 40×4.50 m, and on the third floor 40×3.20 m. There are wooden doors that are 4 cm thick.

There are 9 measurements cases, divided in two situations: NLOS (Fig. 1) with obstacles (cases 1–7) and LOS (Fig. 2) with free space (cases 8–9). Obstacles 1 to 7 are wooden doors (4 cm), glass doors (0.8 cm), wooden-glass doors (4 cm), gypsum walls (7.5 cm), wooden walls covered with

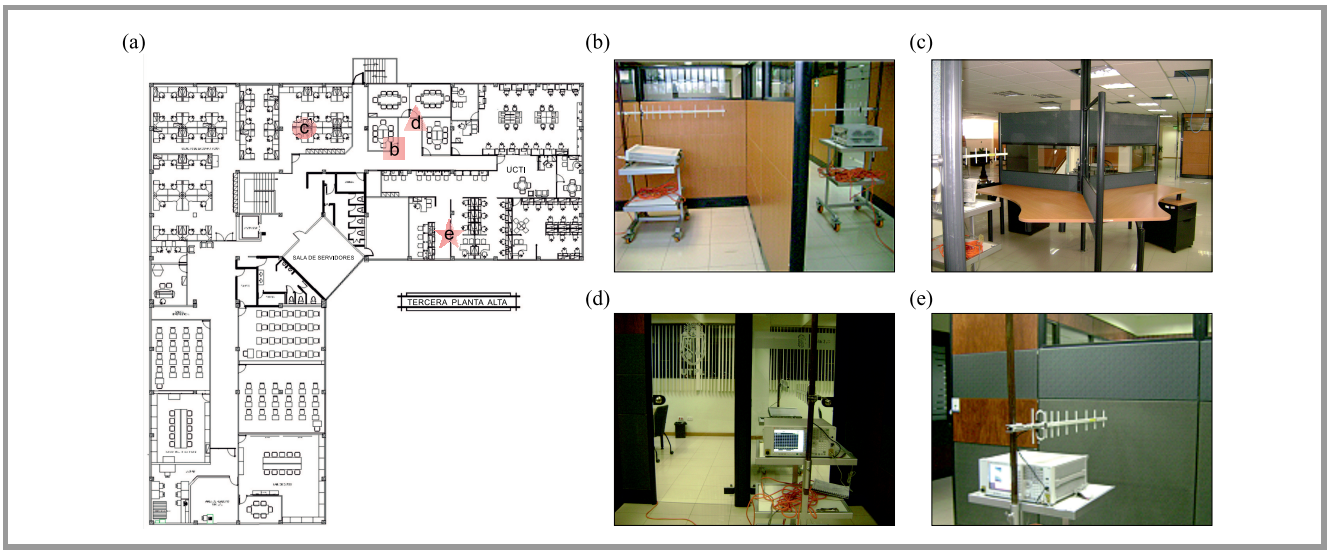

Fig. 1. NLOS type building: (a) architectural plan, (b) gypsum walls, (c) wood with glass and metal intersecting cubicles, (d) glass doors, and (e) wooden walls covered with textile and glass.

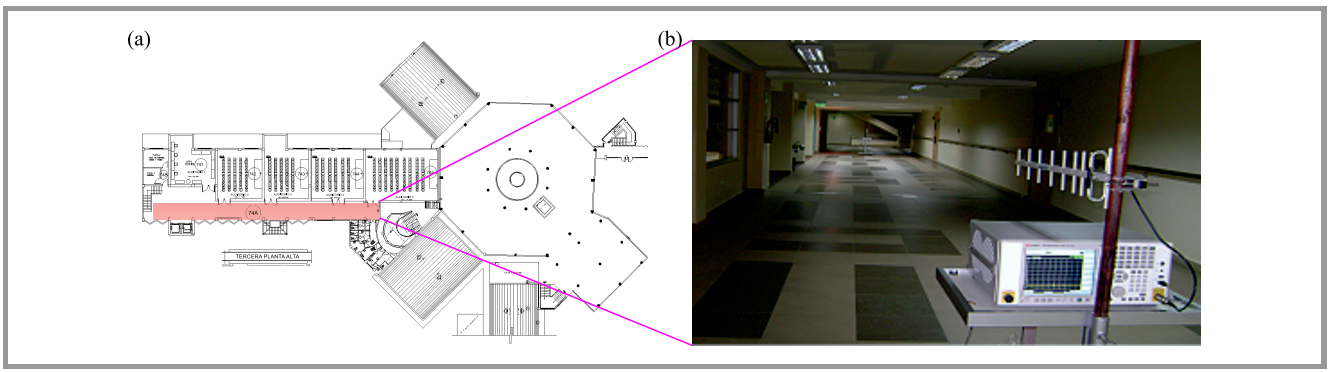

Fig. 2. LOS type building: (a) architectural plan and (b) corridors.

textile and glass (9 cm), partitions (wood with metal joints) and wood with glass and metal intersecting cubicles (9 cm), respectively. The LOS situation is present in corridors: case 8 with the length of up to 22 m, and case 9 with the length of over 22 m.

3.2. Equipment

The measurement equipment consists of:

- Keysight ECE Vector Signal Generator N5172B-50, 9 kHz – GHz at the transmitter,
- Keysight Signal Analyzer N9000A-507, of 9 kHz – 7.5 GHz at the receiver,
- two antennas Yagi TG-Y915-14 that have the gain of 14 dBi each one.

3.3. Experimental Procedure

Before starting the test, the transmitter and receiver antennas are positioned on metal supports at the height of 1.2 m. The transmit power is adjusted to –40 dBm at 915 MHz, and the receiver is configured in the 900 MHz band (902–928 MHz) with a central frequency of 915 MHz (see Fig. 3).

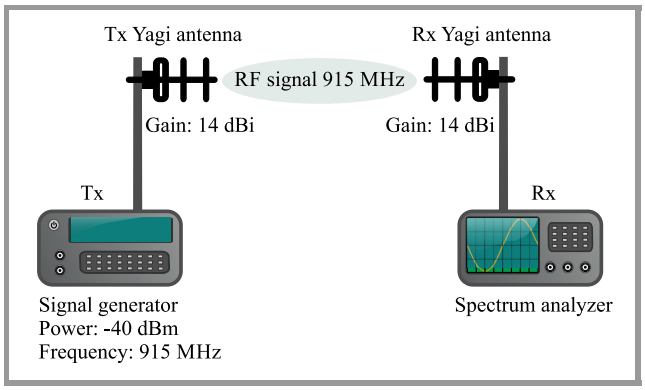

Fig. 3. Overview of the measurement setup.

The transmitter and the receiver are positioned at the distance corresponding to the case to be measured. Thus for the specific situation:

- **NLOS** doors, walls, separators, and cubicles – the transmitter and receiver are placed at an initial distance of 0.50 m. Then, measurements are made by moving the transmitter in a straight line in 0.25 m steps (Fig. 4).
- **LOS** halls, and corridors – the transmitter and receiver are located at the same initial distance as in NLOS. Measurements are then taken every 0.5 m, to the maximum value of 40 m, like in Fig. 5.

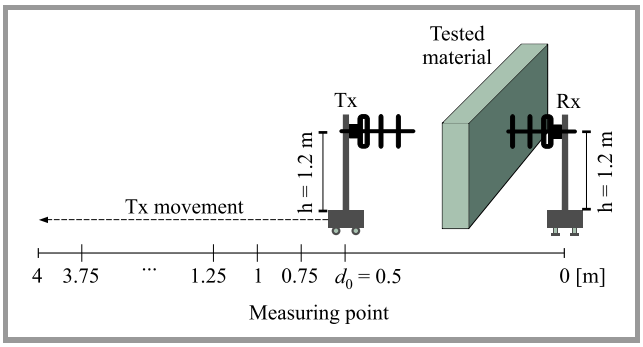

Fig. 4. NLOS measurement: doors, walls, partitions, and cubicles.

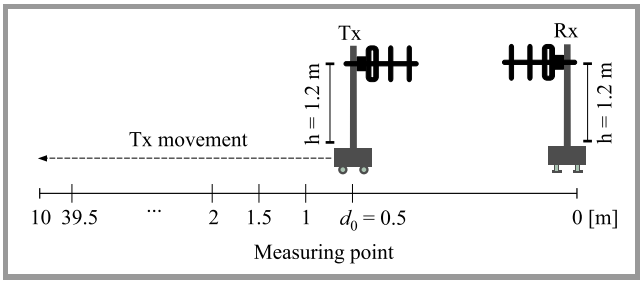

Fig. 5. LOS measurement: corridors.

4. Proposed Model

The objective of this work is to propose a model, with the specific coefficients used in loss prediction models adjusted to a university campus scenario, that can be used in similar environments.

As mentioned in previous sections, the typical models of propagation include the FSPL model, which calculates the loss that results from a line-of-sight path through free space and that depends on the square of the distance. Then, losses typical of a specific scenario are introduced through attenuation coefficients. Such models generally provide loss coefficients (different for each infrastructure) which, according to measurements that have been made at specific locations, are not feasible to use. For this reason, new loss coefficients must be obtained to have a model that is better adjusted to the actual behavior of indoor communications systems on a university campus.

Values obtained in the measurement campaign sere as baseline data for this task, as explained in Section 3. In order to obtain n, it clears this value from:

$$L_{\text{total}}\ [\text{dB}] = \text{PL}(d_0) + n \cdot \log \frac{d}{d_0} + X_\sigma\ , \tag{4}$$

where PL is FSPL, d is the distance and L_{total} represents the path losses, which is calculated replacing the values in the load balance expression:

$$P_{\text{RX}}\ [\text{dB}] = P_{\text{TX}} + G_A - L_{\text{total}}\ , \tag{5}$$

where P_{RX} is the reception power (obtained in the measurement campaign), P_{TX} is the transmission power and G_A is the sum of antennas gain in transmission and reception.

Then, with the measured values we calculate the standard deviation (σ) and the correction factor (CF). For each case, the standard deviation σ is calculated with the variance S of the measured average values through $\sigma^2 = S$.

Table 4
Attenuation parameters for tested cases

Case	Description	CF [dB]	n [dB]	σ [dB]
1	Wood doors	42.23	10.55	0.97
2	Glass doors	40.30	6.99	1.23
3	Mixed doors (wood-glass)	41.31	9.81	0.73
4	Gypsum walls	42.20	11.17	1.02
5	Textile-wood-glass walls	41.79	8.54	1.39
6	Textile-wood-glass divisions	44.06	9.73	2.86
7	Textile-wood-glass-metallic cubicles	42.05	20.85	4.26
8	Short corridor ($<$ 22 m)	41.76	9.91	2.52
9	Long corridor ($>$ 22 m)	41.99	12.14	3.97

Table 4 shows the attenuation coefficients and the respective standard deviation for different cases. Finally, the new coefficients are inserted in the defined model of Eq. (2), where $\mathrm{PL}(d_0)$ is replaced by CF according to the obtained measured values, so, the proposed model is resumed in Eq. (6):

$$\mathrm{L_{total}}\ [\mathrm{dB}] = \mathrm{CF} + n \cdot \log d + X_\sigma\ . \tag{6}$$

5. Results

In this section, a comparative analysis is presented, discussing results based on the average error. The average error is the relation between calculated attenuation and the measured attenuation.
Figure 6 depicts the measured attenuation versus calculated attenuation through the proposed model for cases 1 to 7.

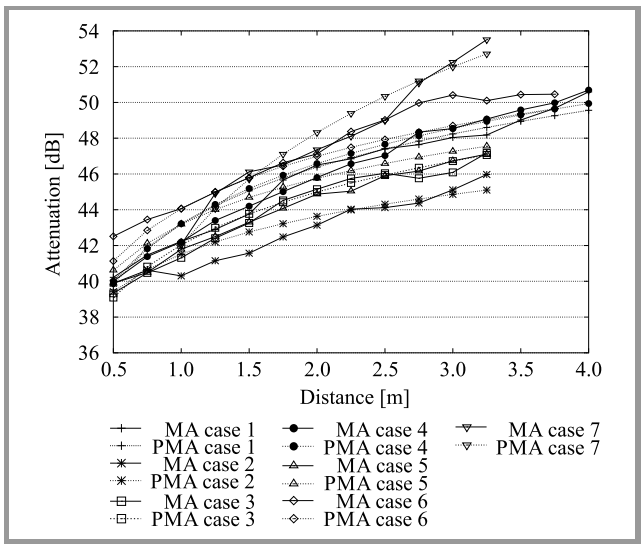

Fig. 6. Measured attenuation (MA) and proposed model attenuation (PMA) for obstacles (cases 1–7).

Every 25 cm, wood, glass and mixed doors (corresponding to cases 1, 2 and 3) increase the attenuation to 0.72, 0.63 and 0.85 dB, respectively. The curves indicate clearly that glass doors represent the lower attenuation for the set of obstacles. The average error for them equals 0.46, 0.56 and 0.36 dB respectively. In addition, the results for cases 4 (gypsum walls) and 5 (wood walls) are showed; the average error is 0.54 dB and 1.03 dB, respectively. The attenuation for case 6 is around 0.87 dB for each 25 cm and the error is 0.76 dB. With cubicles (case 7) present in the area, the highest fluctuation rate is registered, and the average error equals 0.66 dB.

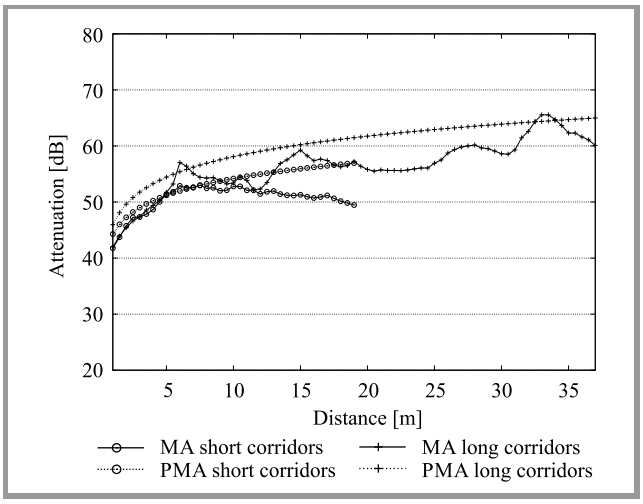

Fig. 7. Measured attenuation (MA) and proposed model attenuation (PMA) for cases 8 and 9.

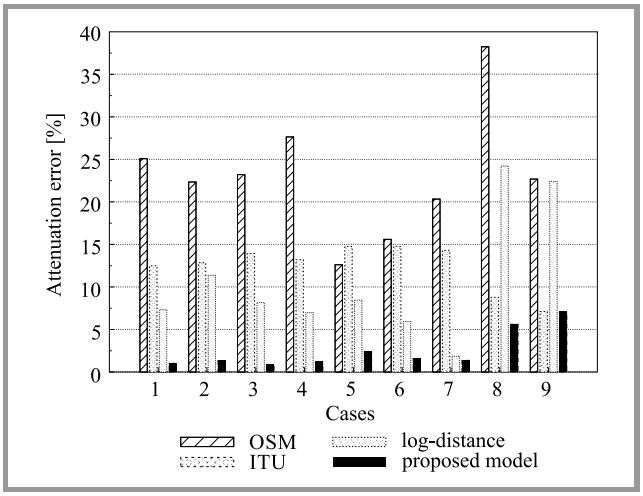

Fig. 8. Theoretical models versus proposed model attenuation error for indoor environments.

The attenuation for cases 8 and 9 is depicted in Fig. 7. The measured values show that the attenuation in short corridors is lower than in long corridors, with the variation of around 3 dB and peaks up to 7.96 dB. The error is 2.83 dB and 3.9 dB, respectively. Abrupt changes in attenuation curves are mainly due to the multipath effect caused by the variability of the indoor environment.

Figure 8 shows the average error for the theoretical models and the proposed model. For cases 1 to 7, the optimized model has lower average percentages of error of attenuation (smaller than 3%) in relation to OSM, ITU and Log-distance models, whose average values equal 21.0%, 13.8% and 7.2%, respectively, versus 1.4% of the proposed model. Moreover, for cases 8 and 9, OSM has an error of 30.5%, ITU model error is 8.0% and Log-distance error is 23.3% versus 6.3% of the proposed model.

Among the mathematical models, the worst model that predicts the losses is the OSM with the error greater than 25%, versus Log-distance model values of around 7.5%. The Log-normal model has the lowest error percentage. It presents a better behavior for case 7 with 0.47%, compared to the optimized model. But for cases 8 and 9, ITU is a better adjusted model. For example, for case 9, the error is 0.07% for the proposed model. Nevertheless, ITU presents a measured attenuation variability of up to 11.59 dB, versus 6.79 dB of the proposed model.

6. Conclusions

In this paper, some typical propagation models have been analyzed. An extensive measurement campaign was performed based on a strict methodology. With these results a new model was proposed. The proposed model specifies coefficients (n and σ) for structures, shapes, materials, and obstacles typical of a campus environment.

All approaches were have been analyzed, compared and the results are discussed. Theoretical models have a high error percentage – mainly the One-slope model with values between 12% and 27%. Log-distance and ITU models have a better performance for the scenarios under study, with different obstacles and corridors considered. The proposed model decreases the attenuation error by approximately 10 dB, meaning that the models analyzed have been optimized. Low error percentages are obtained in all scenarios. The proposed model presents the average measured attenuation data error of 2.5%.

References

[1] J. S. Seybold, *Introduction to RF Propagation*. Wiley, 2005.

[2] U. Naik and V. N. Bapat, "Adaptive empirical path loss prediction models for indoor WLAN", *Wirel. Personal Commun.*, vol. 79, no. 2, pp. 1003–1016, 2014 (doi: 10.1007/s11277-014-1914-9).

[3] I. Dey, G. G. Messier, and S. Magierowski, "Joint fading and shadowing model for large office indoor WLAN environments", *IEEE Trans. on Antennas and Propag.*, vol. 62, no. 4, pp. 2209–2222, 2014 (doi: 10.1109/TAP.2014.2299818).

[4] J. H. Jung, J. Lee, J. H. Lee, Y. H. Kim, and S. C. Kim, "Ray-tracing-aided modeling of user-shadowing effects in indoor wireless channels", *IEEE Trans. on Antennas and Propag.*, vol. 62, no. 6, pp. 3412–3416, 2014 (doi: 10.1109/TAP.2014.2313637).

[5] M. Sasaki *et al.*, "Path loss characteristics between different floors from 0.8 to 37 GHz in indoor office environments", in *Proc. 21st Int. Symp. on Antennas and Propag. ISAP 2016*, Ginowan, Okinawa, Japan, 2016.

[6] N. G. Fernández, "Modelo de Cobertura en Redes Inalámbricas Basado en Radiosidad por Refinamiento Progresivo", Doctoral Thesis, Universidad de Oviedo, Spain, 2006 (in Spanish).

[7] A. Samuylov, D. Moltchanov, Y. Gaidamaka, V. Begishev, R. Kovalchukov, P. Abaev, and S. Shorgin, "SIR analysis in square-shaped indoor premises", in *Proc. 30th Eur. Conf. on Modelling and Simul. ECMS 2016*, Regensburg, Germany, 2016, pp. 692–697 (doi: 10.7148/2016-0692).

[8] I. Rodriguez, H. C. Nguyen, N. T. Jorgensen, T. B. Sorensen, and P. Mogensen, "Radio propagation into modern buildings: Attenuation measurements in the range from 800 MHz to 18 GHz", in *Proc. 80th Veh. Technol. Conf. VTC Fall 2014*, Vancouver, DC, Canada, 2014, pp. 1–5 (doi: 10.1109/VTCFall.2014.6966147).

[9] O. Felekoglu, "Propagation and performance analysis for a 915 MHz wireless IR image transfer system", Ph.D. dissertation, Naval Postgraduate School, Monterey CA, USA, 2005 [Online]. Available: http://hdl.handle.net/10945/2155

[10] C. Nerguizian, C. L. Despins, S. Affès, and M. Djadel, "Radio-channel characterization of an underground mine at 2.4 GHz", *IEEE Trans. on Wirel. Commun.*, vol. 4, no. 5, pp. 2441–2453, 2005 (doi: 10.1109/TWC.2005.853899).

[11] O. Fernandez, M. Domingo, and R. P. Torres, "Experimental Analysis of wireless data transmission systems in space platforms", *IEEE Antennas and Propag. Mag.*, vol. 46, no. 4, pp. 38–60, 2004 (doi: 10.1109/MAP.2004.1373998).

[12] T. Chrysikos, G. Georgopoulos, S. Kotsopoulos, and D. Zevgolis, "Site-specific validation of indoor RF models for commercial propagation topologies at 2.4 GHz", in *Proc. 7th Int. Symp. on Wirel. Commun. Syst. ISWCS 2010*, York, United Kingdom, 2010, pp. 681–685 (doi: 10.1109/ISWCS.2010.5624276).

[13] F. Capulli, C. Monti, M. Vari, and F. Mazzenga, "Path Loss Models for IEEE 802.11 a Wireless Local Area Networks", in *Proc. 3rd Int. Symp. on Wirel. Commun. Syst. . ISWCS 2006*, Valecia, Spain, 2006, pp. 621–624 (doi: 10.1109/ISWCS.2006.4362375).

[14] S. Y. Seidel and T. S. Rappaport, "914 MHz path loss prediction models for indoor wireless communications in multifloored buildings", *IEEE Trans. on Antennas and Propag.*, vol. 40, no. 2, pp. 207–217, 1992 (doi: 10.1109/8.127405).

[15] T. S. Rappaport, G. R. MacCartney, M. K. Samimi, and S. Sun, "Wideband millimeter-wave propagation measurements and channel models for future wireless communication system design", *IEEE Trans. on Commun.*, vol. 63, no. 9, pp. 3029–3056, 2015 (doi: 10.1109/TCOMM.2015.2434384).

[16] M. Tolstrup, *Indoor Radio Planning: A Practical Guide for 2G, 3G and 4G*. Wiley, 2015.

[17] A. Hrovat, G. Kandus, and T. Javornik, "A survey of radio propagation modeling for tunnels", *IEEE Commun. Surveys Tutor.*, vol. 16, no. 2, pp. 658–669, 2014 (doi: 10.1109/SURV.2013.091213.00175).

[18] T. S. Rappaport, *Wireless Communications – Principles and Practice*. Upper Saddle River, NJ, USA: Prentice Hall PTR, 2002.

[19] ITU-T Recommendation P.1238-9, "Propagation Data and Prediction Methods for the Planning of Indoor Radiocommunication Systems and Radio Local Area Networks in the Frequency Range 300 MHz to 100 GHz", ITU, Geneva, July 2017 [Online]. Available: http://www.itu.int/rec/RREC-P.1238/eu

[20] C. Monti, A. Saitto, and D. Valletta, "Indoor radio channel models for IEEE 802.15.4 technology", in *Proc. 2nd Int. EURASIP Worksh. on RFID Technol. RFID 2008*, Budapest, Hungary, 2008.

Marco Morocho-Yaguana received his M.Sc. in Engineering from the Moscow Technical University of Communications and Informatics. He is a professor at the Computer Science and Electronics Department (DCCE) and Coordinator for the engineering degrees in electronics and telecommuni-

cations at Universidad Técnica Particular de Loja since 2016. His research interests focus on the wave propagation, antennas and electromagnetism.
E-mail: mvmorocho@utpl.edu.ec
Department of Computer Science and Electronic
Universidad Técnica Particular de Loja
C/. Marcelino Champagnat S/N
1101608 Loja, Ecuador

Patricia Ludeña-González received her B.Sc. degree in Electronic and Telecommunications Engineering from Universidad Técnica Particular de Loja (UTPL) in 2005. She has an M.Sc. in Telecommunications Networks since 2011 from the Rey Juan Carlos University in Spain. She is a Ph.D. Candidate at Universidad Politécnica de Madrid in Spain. She is a professor at the Computer Science and Electronics Department (DCCE) in UTPL since 2005. Her research interests focus on the optimization of protocols, traffic engineering, wave propagation in wireless telecommunications and new technology networks in rural wireless networks deployments.
E-mail: pjludena@utpl.edu.ec
Department of Computer Science and Electronic
Universidad Técnica Particular de Loja
C/. Marcelino Champagnat S/N
1101608 Loja, Ecuador

Francisco Alberto Sandoval Noreña received his B.Sc. degree in Electronics and Telecommunications Engineering from Universidad Técnica Particular de Loja (UTPL), and an M.Sc. degree in Electrical Engineering from the Pontifícia Universidade Católica do Rio de Janeiro (PUC-RIO), in 2008, and 2013, respectively. He is currently pursuing a Ph.D. degree in Electrical Engineering with École de Technologie Supérieure (University of Quebec), Canada. He has worked, since October 2008, at UTPL as an auxiliary professor at the Computer Science and Electronics Department (DCCE). His research interests include wireless communications, communication theory, signal processing, and RF propagation.
E-mail: fasandoval@utpl.edu.ec
Department of Computer Science and Electronic
Universidad Técnica Particular de Loja
C/. Marcelino Champagnat S/N
1101608 Loja, Ecuador

Betty Poma-Vélez is an Electronics and Telecommunications engineer at the Universidad Técnica Particular de Loja (2016). She is focusing on Networking and TIC enterprises. Her research interests focus around telecommunications, mainly radiofrequency propagation and wireless communications.
E-mail: bppoma@utpl.edu.ec
Department of Computer Science and Electronic
Universidad Técnica Particular de Loja
C/. Marcelino Champagnat S/N
1101608 Loja, Ecuador

Alexandra Erreyes-Dota has been an Electronics and Telecommunications engineer at the Universidad Técnica Particular de Loja (UTPL) since 2016. She contributed research articles to the UTPL magazine in 2009 and 2010. Her research interests are: wave propagation in wireless telecommunications, wireless sensor networks, information management and communication technologies.
E-mail: ajerreyes1@utpl.edu.ec
Department of Computer Science and Electronic
Universidad Técnica Particular de Loja
C/. Marcelino Champagnat S/N
1101608 Loja, Ecuador

Paper

Numerical Evaluation of Electromagnetic-wave Penetration at Normal Incidence through an Inhomogeneous-wave Approach

Alessandro Calcaterra[1], Fabrizio Frezza[1], Patrizio Simeoni[2], and Nicola Tedeschi[1]

[1] *Department of Information Engineering, Electronics and Telecommunications, La Sapienza University of Rome, Rome, Italy*
[2] *National Transport Authority (NTA), Dublin, Ireland*

https://doi.org/10.26636/jtit.2018.124218

Abstract— This paper presents numerical scenarios concerning penetration in a lossy medium that can be obtained by radiating inhomogeneous electromagnetic waves. Former papers approached this problem, both analytically and numerically, finding requirements and limits of the so-called "deep-penetration" condition, which consists of a wave transmitted in a lossy medium having an attenuation vector whose direction forms the angle of ninety degrees with the normal to the separation surface. The deep-penetration condition always requires an oblique incidence, therefore is not practical in many applications. For this reason, we are interested here in finding whether an inhomogeneous wave guarantees larger penetration than the one obtainable with homogeneous waves, even when the incident wave is normal to the separation surface between two media, i.e. when the deep-penetration condition is not satisfied. We are also interested in verifying numerically whether the lossy-prism structure may achieve larger penetration than the one obtainable through traditional leaky-wave antennas, and we also wish to propose a lossy-prism design more realistic than the one previously presented in the literature.

Keywords—deep-penetration, electromagnetic simulation, leaky-wave antennas, lossy prism.

1. The Scenario

In this article, we study a typical near-field problem, in which antennas generate electromagnetic radiation that propagates first in the air, for a short distance (near-field), here approximated by a vacuum, and then impinges normally to the separation surface with a lossy medium. Such a problem represents a typical air-coupled antenna scenario. In [1], [2], authors found analytical requirements and restrictions of the so-called "deep-penetration" condition. The problem studied in such papers is the incidence of an inhomogeneous plane wave, incoming from a lossless medium, on a planar and infinite separation surface with a lossy medium. Those papers found conditions in which the transmitted wave generated in the lossy medium attenuates along the interface – this guarantees infinite penetration. In realistic scenarios, i.e. when the electromagnetic field is generated by a finite source, the deep-penetration condition can only be supported in a limited spatial region. It was observed that leaky-wave antennas [3], [4] can be employed to generate an electromagnetic field suitable for deep penetration in near-field [5].

Moreover, it was demonstrated in [1], [2], that the deep-penetration condition can only be obtained for oblique incidence. Such a condition, as highlighted in [6], is not very practical for many applications, where, instead, normal incidence is recommended. We investigate here the penetration achievable in the normal incidence condition employing leaky-wave antennas, we numerically verify the role played by the incidence angle, and finally, the lossy prism proposed in [6] is numerically studied in a suitable antenna structure to verify its penetration properties. The design proposed here is a numerical prototype which intends to serve as an input to lossy-prism antennas design for practical and realistic scenarios.

2. Normal Incidence of Inhomogeneous and Homogeneous Plane Waves

In Fig. 1, the incidence of an inhomogeneous wave on a separation surface between a lossless and a lossy medium is illustrated: $\boldsymbol{\beta}_1$ represents the phase vector of the incident wave, $\boldsymbol{\alpha}_1$ the attenuation vector of the incident wave, $\boldsymbol{\beta}_2$ the phase vector of the transmitted wave, and finally $\boldsymbol{\alpha}_2$ the attenuation vector of the transmitted wave. ξ_1 is the angle of incidence, and the angles formed by $\boldsymbol{\beta}_2$ and $\boldsymbol{\alpha}_2$ with the normal to the separation surface are defined as ξ_2 and ζ_2, respectively. In the lossy medium region, the amplitude α_2 of the vector $\boldsymbol{\alpha}_2$ needs to be always different from zero, but the ζ_2 angle can assume different values.

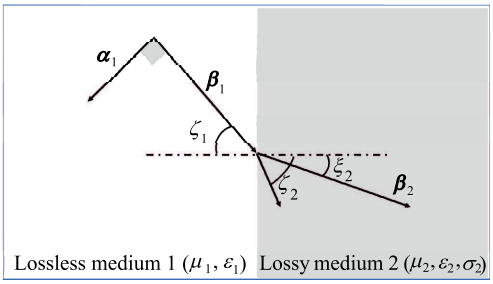

Fig. 1. Theoretical geometry of the problem: an incident inhomogeneous-plane wave characterized by a phase vector $\boldsymbol{\beta}_1$ and an attenuation vector $\boldsymbol{\alpha}_1$ is generated in a lossless medium and it impinges on an infinite and planar separation surface with a lossy medium generating a transmitted wave whose phase vector is indicated by $\boldsymbol{\beta}_2$ and attenuation vector is indicated with $\boldsymbol{\alpha}_2$.

The tangential component of the electromagnetic field is conserved at the interface between two media [7]. It follows that, in the case of an incident homogeneous wave ($\boldsymbol{\alpha}_1 = 0$), $\zeta_2 = 0$. When the incident wave is inhomogeneous, in turn, it must necessarily be $\zeta_2 > 0$ [7].

It is therefore reasonable to expect that, even when $\xi_1 = 0$ in Fig. 1, the penetration obtained through inhomogeneous waves needs to be larger than the one that can be obtained by employing a homogeneous incident wave, simply because the presence of a $\zeta_2 > 0$ angle results in a transmitted wave which does not attenuate in the direction orthogonal to the separation surface. To demonstrate this, let us impose $\xi_1 = 0$ and let us define with $\hat{\mathbf{x}}$ and $\hat{\mathbf{z}}$ the unit vectors parallel and perpendicular to the separation interface, respectively. We can write:

$$\begin{aligned} \boldsymbol{\alpha}_2 &= \alpha_{2t}\hat{\mathbf{x}} + \alpha_{2n}\hat{\mathbf{z}} \\ \boldsymbol{\beta}_2 &= \beta_2\hat{\mathbf{z}} \end{aligned}. \tag{1}$$

Let us now define with $\mathbf{k}_2$ the wave vector of the transmitted wave, with $\mathbf{k}_1$ the wave vector of the incident wave, and with k_2 the amplitude of $\mathbf{k}_2$. It is [7]:

$$\begin{aligned} \mathbf{k}_2 &= \boldsymbol{\beta}_2 - \mathrm{j}\boldsymbol{\alpha}_2 \\ \mathbf{k}_1 &= \boldsymbol{\beta}_1 - \mathrm{j}\boldsymbol{\alpha}_1 \end{aligned}. \tag{2}$$

From Eqs. (1)–(2):

$$\begin{aligned} \beta_2^2 &= \mathrm{Re}^2 k_2 + \alpha_{2t}^2 + \alpha_{2n}^2 \\ \beta_2\alpha_{2n} &= \mathrm{Im}\, k_2 \end{aligned} \tag{3}$$

Therefore:

$$\beta_2^4 - \left(\mathrm{Re}^2 k_2 + \alpha_{2t}^2\right)\beta_2^2 - \mathrm{Im}^2 k_2 = 0\,. \tag{4}$$

Taking twice the positive sign, β can be found from the bi-quadratic Eq. (4):

$$\beta_2 = \frac{1}{\sqrt{2}}\sqrt{\mathrm{Re}^2 k_2 + \alpha_{2t}^2 + \sqrt{\left(\mathrm{Re}^2 k_2 + \alpha_{2t}^2\right)^2 + 4\,\mathrm{Im}^2 k_2}}\,. \tag{5}$$

At a given frequency, k_2 depends only on the medium [7], therefore it does not change modifying ξ_1. But then, from Eq. (5), we can see that the larger α_{2t} is, the larger β_2 becomes, and consequently, from the second equation in (3), α_{2n} needs to get smaller. Therefore, the penetration-depth increases. The minimum value of β_2 is obtained when $\alpha_{2t} = 0$, i.e. in the case of an impinging homogeneous wave, as expected.

The demonstration presented in this section is purely mathematical, we need to choose an appropriate physical inhomogeneous wave to validate the finding.

In [8], different kinds of inhomogeneous waves are studied, and it is shown that the leaky wave is the only one which is not bound to the separation surface between a lossless and a lossy medium. This waveform is the most suitable for our exploration, because it can be locally approximated by an inhomogeneous plane wave. Moreover, such a waveform can be easily generated through well-known structures named leaky-wave antennas [3], [4].

Unfortunately, as written earlier, such a wave can be supported only for a limited distance from the antenna aperture. This constraint limits the advantage in terms of penetration that can be obtained employing those structures over the one achievable through more traditional antenna design (e.g. horns).

3. The Two-dimensional Leaky-wave Antenna

The first objective of this paper is to extend, and complete, the study presented in [9] related to the penetration that can be obtained employing the two-dimensional planar antenna designed in [10]. This antenna is, in principle, equivalent to the substrate-superstrate leaky-wave antenna (see [11], [12]) as demonstrated in [13], but it does not present the disadvantage of a high-permittivity layer. Two-dimensional and periodic leaky-wave antennas have the advantage of creating a pencil beam at broadside, which is the direction of interest here, employing a very simple feeder. A mono-dimensional and periodic antenna could also represent a suitable solution because, even though those structures present a natural stop-band at broadside [3], [4], examples are present in literature of projects that can guarantee broadside radiation employing those structures [14], [15]. Anyway, the mono-dimensional periodic LWAs still require challenging design for achieving the stop-band suppression at broadside.

For all reasons exposed above, the two-dimensional and periodic leaky-wave antenna was selected for some preliminary promising qualitative results in terms of penetration depth, in [9].

The antenna is designed to radiate at 12 GHz, mainly to allow an easy comparison with former inhomogeneous-wave penetration studies, such as [5] and [9], where such a frequency was chosen. The antenna, which is assumed of infinite dimension in [10], was modelled on CST Microwave

Studio Software [16] (see Fig. 18) using a structure of 22×12 patches according to the geometry illustrated in Fig. 2, where patch and periodicity dimensions are also listed, such dimensions are chosen in agreement with the values suggested in [9] and [10]. Rogers RT5870 was chosen as the medium for the substrate (relative permittivity $\varepsilon_r = 2.33$, relative permeability $\mu_r = 0$), and losses in the substrate were neglected. The thickness of the substrate

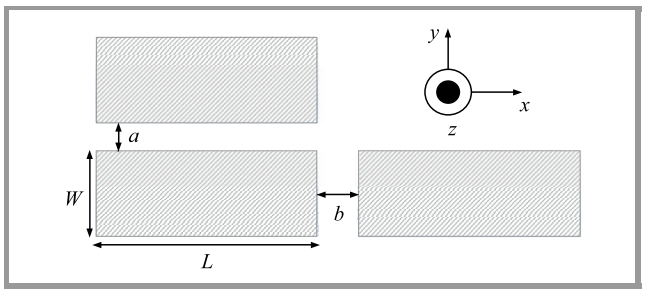

Fig. 2. Patch structure of the two-dimensional leaky-wave antenna: $L = 11$ mm, $W = 3$ mm, $b = 2$ mm, and $a = 1$ mm. Metal patches were designed assuming PEC as a material to speed-up the simulation.

in this antenna controls the beam direction for a given frequency [10], [17], i.e. for the n-th mode, it is (Eq. (2) in [10]):

$$h_s = \lambda_0 \cdot \frac{n}{2\sqrt{\varepsilon_r - \sin^2 \theta_p}}, \tag{6}$$

where θ_p is the scanning angle. Having chosen the $n = 1$ radiation mode, from $\varepsilon_r = 2.33$, and from the operating frequency of 12 GHz, it follows:

$$h_s = 0.025 \cdot \frac{1}{2\sqrt{2.33}} \approx 0.0082 \text{ m}. \tag{7}$$

The value indicated by Eq. (7) was modified into $h_s = 8.40$ mm after having run the parameter sweep option of CST on the beam direction.

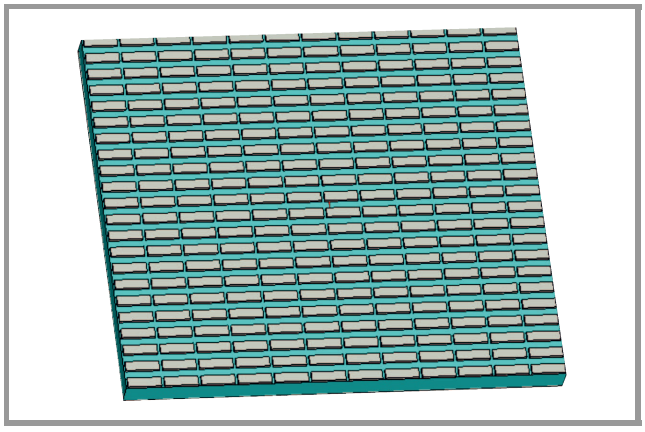

Fig. 3. Two-dimensional leaky-wave antenna design on CST Microwave Studio. (See color pictures online at www.nit.eu/publications/journal-jtit)

The radiation pattern on the E-plane generated by this leaky-wave antenna is shown in Fig. 4, while the radiation pattern for the H-plane is shown in Fig. 5.

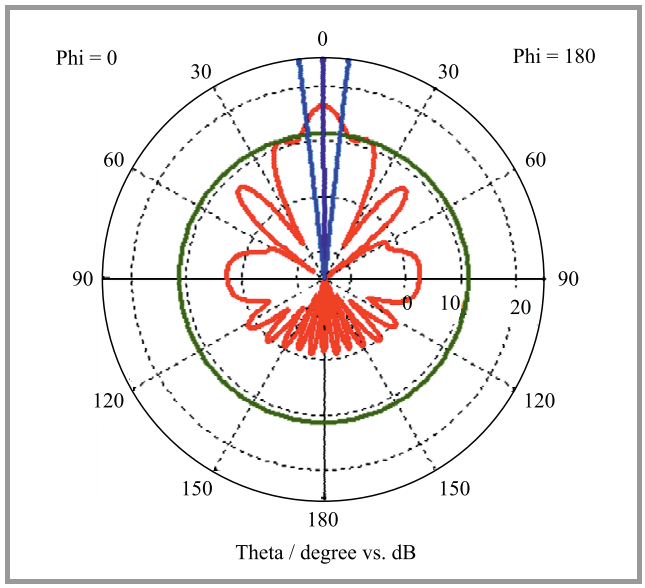

Fig. 4. Broadside radiation pattern on the E-plane.

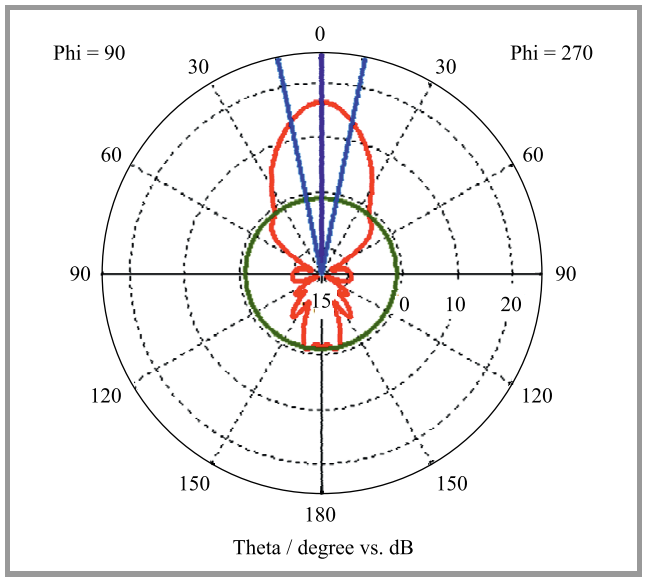

Fig. 5. Broadside radiation pattern on the H-plane.

The E-plane has grating lobes due to the presence of the surface wave which is mostly directed on such a plane, in perfect agreement with the behavior exposed in [10] and [17]. The antenna was fed by a $\frac{1}{2}\lambda$ horizontal dipole placed at a distance $h_d = 0.5h_s$ from the antenna ground plane. The dipole does not represent a practical, realistic feeding, but it can be replaced, for instance, by a microstrip slot [18] on a hypothetical prototype.

To compare the penetration produced by this antenna with the one produced by more commonly used antennas, a lossy medium, characterized by a conductivity $\sigma = 0.05$ S/m, unitary relative permittivity and unitary relative permeabil-

ity was designed and positioned at a distance $d = \frac{3}{2}\lambda$ from the antenna aperture, as shown in Fig. 6. The choice of a unitary relative permittivity for the lossy medium is fundamental to avoid the influence of the incidence angle on the penetration. A relative permittivity $\varepsilon_r = 1$ and a low enough value of conductivity σ, such as the value chosen, allow to neglect reflections independently of the incidence angle: such a choice permits to compare antennas radiating at different angles. Different choices for the lossy medium could potentially complicate the comparison because the behavior in terms of penetration could strongly depend on the incidence angle (e.g. pseudo-Brewster angle or total transmission [19]). Moreover, $\varepsilon_r = 1$ and $\sigma = 0.05$ S/m were assumed in previous deep-penetration studies (see for instance [9]), therefore the choice made here allows a direct comparison with the literature.

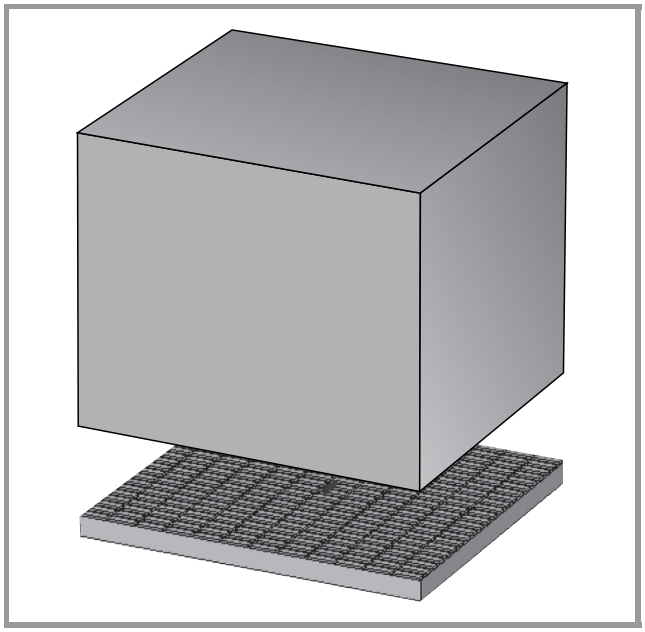

Fig. 6. Lossy medium positioned above the antenna aperture: note that the lossy medium base is chosen as large as the aperture, to avoid radiation entering from the lateral faces of the lossy prism.

The distance $d = \frac{3}{2}\lambda$ was chosen in accordance with the criteria that request the lossy medium to be inside the radiating near-field region [5].

4. Homogeneous-wave Antennas

Pyramidal- and circular-horn antennas were designed to act as a comparison for the penetration achieved by the two-dimensional periodic leaky-wave antenna. An almost omnidirectional antenna, and in particular a $\frac{1}{2}\lambda$ dipole [20], was also simulated to serve as reference for the minimum achievable penetration. All mentioned antennas were optimized to radiate at a frequency of 12 GHz, because a direct penetration comparison is possible only when both frequencies and lossy media are equivalent.

4.1. Circular-horn Antenna

The circular-horn antenna was designed following the procedure illustrated in [21]. The radius of the aperture resulted $r_c = 25.4$ mm. Perfect Electric Conductor (PEC) was chosen as metal for the structure, to increase the simulation speed, and the antenna was fed by means of a waveguide port. The amplitude of the scattering reflection coefficient at the first port (S_{11}) is illustrated in Fig. 7.

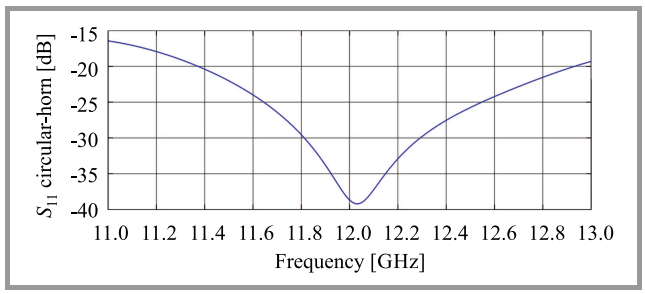

Fig. 7. Amplitude of the S_{11} scattering parameter for the circular-horn antenna, the resonance at $f_0 = 12$ GHz is visible.

A lossy medium equivalent to the one used for the periodic two-dimensional LWA was posed, again, at a distance $d = \frac{3}{2}\lambda$ from the antenna aperture. The CST design of the structure is shown in Fig. 8.

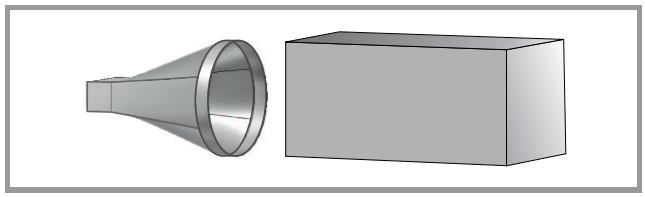

Fig. 8. Design of the circular-horn antenna with a lossy medium posed at a distance $d = \frac{3}{2}\lambda$ from the antenna aperture, note that the lossy prism base is as large as the antenna aperture to guarantee the infinite planar separation surface approximation in near-field condition.

4.2. Pyramidal-horn Antenna

The pyramidal-horn antenna was designed having aperture dimensions of 107.8×137.4 mm. The metal for the horn antenna enclosure was approximated with a PEC, and the antenna was fed by means of a waveguide port. The amplitude of the S_{11} scattering parameter for this antenna is shown in Fig. 9.
A lossy medium equivalent to the one used for the periodic two-dimensional LWA was posed, again, at a distance $d = \frac{3}{2}\lambda$ from the antenna aperture. The CST design of the structure is shown in Fig. 10.

4.3. Dipole Antenna

A 0.5λ dipole antenna was also designed. Obviously such an antenna is not expected to have high performance in terms of penetration, but it was designed to act as a reference, so that the improvement in penetration introduced by

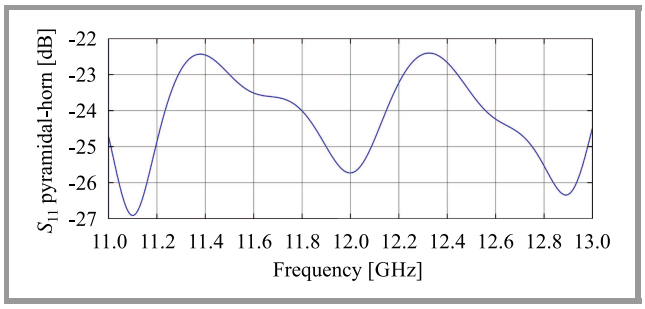

Fig. 9. Amplitude of the S_{11} scattering parameter for the pyramidal-horn antenna, this antenna presents clear broadband characteristics.

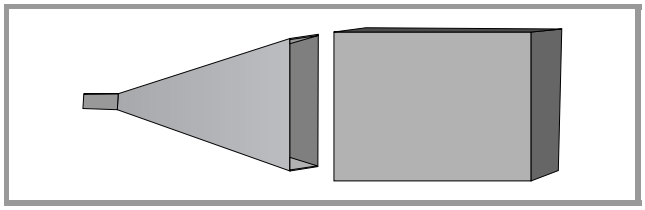

Fig. 10. Design of the pyramidal-horn antenna with a lossy medium posed at a distance $d = \frac{3}{2}\lambda$ from the antenna aperture, note that the lossy prism base is as large as the antenna aperture to guarantee the infinite planar separation surface approximation in near-field condition.

the LWA with respect to the horn antenna could be compared against the improvement that the horn antenna would introduce with respect to a non-directive antenna, such as the dipole chosen. The dipole arms were assumed PEC, again, and the dipole was fed by a discrete port between the arms, as shown in Fig. 11.

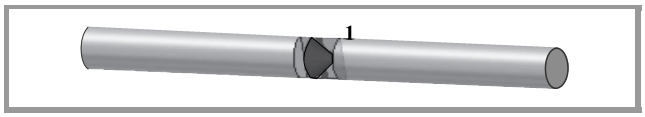

Fig. 11. Design of a $\frac{1}{2}\lambda$ dipole antenna, fed by a discrete port.

5. Simulation Results

5.1. Penetration Comparison

Let us assume, without loss of generality, the direction of the maximum amplitude of the electric field, which for the designed antennas corresponds to the direction normal to both antenna aperture and interface with the lossy medium, along the z axis. To compare the penetration achieved by the antennas illustrated in the previous paragraph, the amplitude of the electric field $|\mathbf{E}|$ was first evaluated using the E-field monitor option of CST Microwave Studio for all the antennas, then results were exported to Matlab for further processing. In Matlab, the value of the field at the separation interface with the lossy medium: $E_{\text{if}}^{\text{MAX}} = |\mathbf{E}(0,0,1.5\lambda)|$ was extracted first. Then, every sample of the field, such that $E_z = |\mathbf{E}(0,0,z)|$, where $z > \frac{3}{2}\lambda$ was normalized by such a value. The normalized electric field curve obtained is therefore:

$$|\mathbf{E}_{\text{zn}}| = \frac{|\mathbf{E}(0,0,z)|}{E_{\text{if}}^{\text{MAX}}}, \text{where } z > \frac{3}{2}\lambda\,. \tag{8}$$

We evaluated this normalized curve for all antennas: the results are presented in Fig. 12. The curve for the planar two-dimensional LWA presents a higher penetration in the lossy medium. However, as expected, the slope of the curve is always negative, even at the interface. This is due to a low amplitude of propagation and attenuation vectors which must result in $\zeta_2 < 90°$. A second, important result, is that the best performances for the homogeneous wave generators are obtained through the pyramidal antenna. By visual inspection it is also possible to verify that the advantage introduced by the LWA on the pyramidal horn is comparable with the one that the pyramidal horn has on the dipole, at least up to approximately 60 mm inside the lossy medium, i.e. $\frac{12}{5}\lambda$.

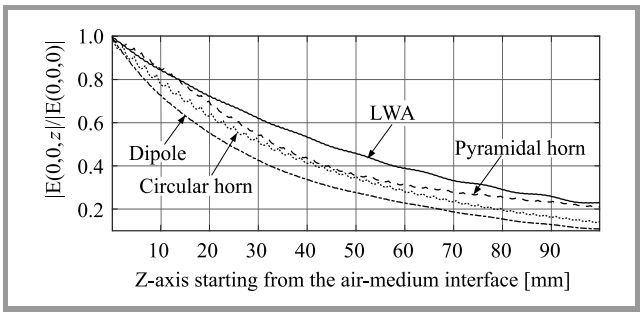

Fig. 12. Comparison between electric-field amplitudes produced by various antennas and propagating inside a lossy non-magnetic medium, of relative permittivity $\varepsilon_r = 1$ and conductivity $\sigma = 0.05$ S/m; the fields are evaluated as described by Eq. (8).

5.2. Results Varying the Conductivity

In [1] and [2], the deep-penetration condition is verified from an analytical-theoretical point of view, and in [5] preliminary results demonstrate that the deep-penetration condition can be met employing simple uniform leaky-wave structures such as the Menzel antenna [22], [23].
In [5], the field generated by the Menzel antenna is studied for different values of the lossy-medium conductivity σ, but no comparison is performed with other antennas. Here, instead, simulations are performed to compare the difference of electric-field penetration between the pyramidal-horn antenna and the two-dimensional LWA through:

$$f(z) = E^{\text{LWA}}(0,0,z) - E^{\text{HORN}}(0,0,z)\,, \tag{9}$$

where $E^{\text{LWA}}(0,0,z)$ and $E^{\text{HORN}}(0,0,z)$ represent the normalized electric fields inside the lossy medium for the LWA and pyramidal-horn antenna, respectively – Eq. (8). Equation (9) is evaluated for different values of conductivity σ of the lossy medium, while its relative permittivity and permeability are kept constant ($\varepsilon_r = 1$ and $\mu_r = 1$). Other antennas, mentioned in the previous paragraph, were not

considered in this comparison because they provide lower penetration than the one achievable by the pyramidal horn, see Fig. 12. The result is given in Fig. 13, where every curve represents the difference between the amplitudes of the electric fields, normalized as in Eq. (8), produced by the LWA and the horn antennas, respectively, for a specific conductivity value of the lossy medium. We can observe that increasing the σ value of the lossy medium the penetration performance of the two antennas tends to align, while when σ diminishes LWA penetration becomes noticeably higher.

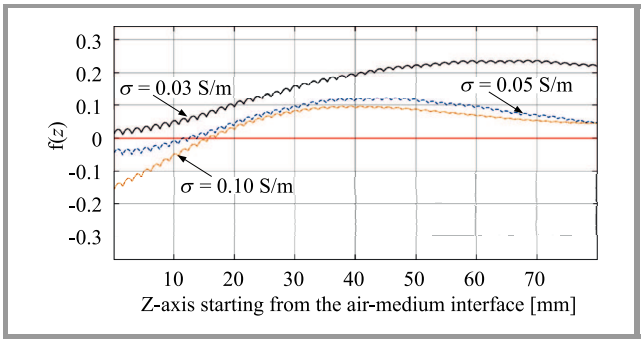

Fig. 13. Difference between normalized electric-field amplitudes generated by a planar leaky-wave antenna and a pyramidal-horn antenna inside the medium computed according to Eq. (9). Curves are shown for conductivity values of $\sigma = 0.03$ S/m, $\sigma = 0.05$ S/m, and $\sigma = 0.1$ S/m. Relative permittivity and permeability are $\varepsilon_r = 1$ and $\mu_r = 1$, respectively.

This result confirms the theoretical results found in [6] for inhomogeneous plane waves.

5.3. Results Varying the Incident Angle

Finally, it was important to verify the property demonstrated for plane waves in [1], [2] for which a larger incidence angle would result in a deeper penetration in a lossy medium through inhomogeneous waves. As the two-dimensional patch LWA presents a very low amplitude of the attenuation vector $\boldsymbol{\alpha}$, it follows that the best penetration condition is guaranteed by an incidence angle $\xi_1 = 45°$. Anyway, such an angle cannot easily be exploited with the designed antenna for the presence of the -1 space harmonic of TM_0 surface wave [10], whose perturbation effect, mainly on the E-plane, is larger for larger values of the scanning angle. It is not possible to increase the incidence angle by rotating either the antenna or the lossy medium, because doing so could cause the lossy medium to enter inside the reactive near-field zone. This would change the nature of the problem that is studied here. For the LWA analyzed here, the effects of the surface wave were considered negligible when $\xi_1 \leq 30°$, therefore $\xi_1 = 30°$ was chosen as the maximum value for the incidence angle. Leaky-wave antennas perform a frequency scan, but here, we needed to compare the penetration at different angles without varying the frequency. Therefore, we had to re-design the antenna increasing the substrate thickness. From Eq. (6), it follows that $h_s = 8.7$ mm: $h_s = 8.9$ mm was chosen after the parameter-sweep optimization in CST. We needed to guarantee that the second order mode would not appear at broadside when the first mode reaches the angle of 30°. This requirement translates into a minimum value for the relative permittivity, which can be evaluated imposing Eq. (6) for both $n = 1$ and $n = 2$ modes, and comparing the two (see Eq. (5) of [10]), obtaining the:

$$\varepsilon_r > \frac{4}{3}\sin^2\theta_p\,. \tag{10}$$

In particular $\varepsilon_r > 1/3$ is required for the antenna designed here. The permittivity value chosen in this paper ($\varepsilon_r = 1$) respects this condition, and therefore guarantees the absence of higher-order modes at the desired angle. It is clear that the chosen amplitude for the substrate permittivity would guarantee the absence of the second order mode even when the $n = 1$ mode would be at endfire ($\varepsilon_r > 4/3$, i.e. the case illustrated in Eq. (5) of [10]).

The result of the investigation is shown in Fig. 14. The penetration obtained by the oblique beam at 30° is slightly larger than the one obtained by broadside radiation, as expected according to the theoretical results found in [1], [2].

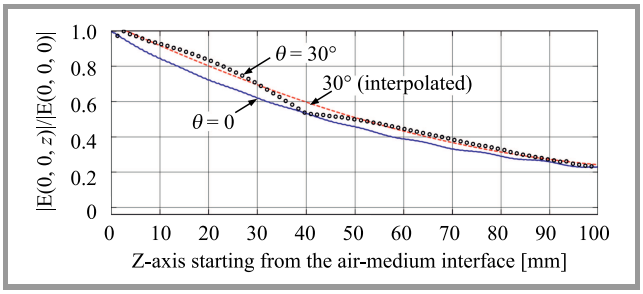

Fig. 14. Normalized electric field amplitude inside the lossy medium – Eq. (8) for broadside radiation ($\xi_1 = 0°$) and for $\xi_1 = 30°$. The lossy medium has conductivity $\sigma = 0.05$ S/m and relative permittivity $\varepsilon_r = 1$. The field is generated by the two-dimensional periodic LWA at a frequency of 12 GHz.

6. Leaky Wave Through a Two-dimensional Lossy Prism

Recently, it has been demonstrated, analytically, that a two-dimensional lossy prism, firstly introduced in [24], may achieve a larger penetration than the one obtained by conventional leaky-wave antennas [6]. The first numerical prototype of this geometrical structure was presented in [25]. In that paper, the prism was illuminated by the far-field generated by a customary horn antenna. Such a setup cannot easily lead to a suitable antenna design, so we analyze here an alternative, and more practical, feeding structure. We propose to position the lossy prism at the aperture of a TEM-horn antenna, i.e. a two-dimensional horn antenna also known in the literature as dihedral horn [26]: a TEM antenna allows a full control of the beam incidence angle on the lossy prism. The vertex of the lossy prism, indicated

with χ in [6], is set to 90°, as suggested in [6]. It makes sense to verify whether the electromagnetic field can penetrate more deeply inside the lossy medium in this case, where the illumination is not exactly a plane wave, as it was, instead, in [6]. The proposed structure was designed in Comsol Multiphysics, and it is illustrated in Fig. 15.

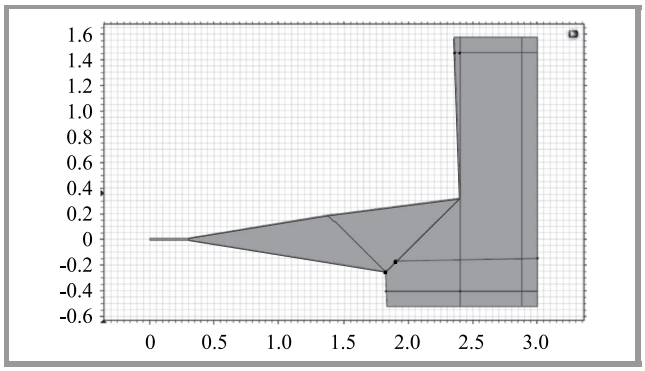

Fig. 15. Comsol simulation of a two-dimensional TEM-horn antenna having a lossy prism attached to the aperture.

The lossy prism was chosen to be of the non-magnetic kind and having a relative complex permittivity of $\varepsilon_r = 1 - \mathrm{j}0.05$. The two-dimensional horn antenna radiates at a frequency of 12 GHz. At such a frequency, the conductivity of the prism is $\sigma = 0.005$ S/m. It is possible to obtain the amplitudes of attenuation vector α_3, and phase vector β_3 of the generated inhomogeneous wave using the formulas presented in [6], which are reported here for the case of interest:

$$\begin{aligned} k_0 &= \omega\sqrt{\mu_0\varepsilon_0} = 252.167972 \text{ rad/m} \quad , \\ \beta_3 &= \frac{k_0}{\sqrt{2}}\sqrt{1+\sqrt{1+\left(\frac{2\varepsilon''_{r2}}{\sin(2\xi_3)}\right)}} = \\ &= 252.48220 \text{ rad/m} \quad , \\ \alpha_3 &= \frac{k_0}{\sqrt{2}}\sqrt{-1+\sqrt{1+\left(\frac{2\varepsilon''_{r2}}{\sin(2\xi_3)}\right)}} = \\ &= 12.5927 \text{ rad/m} \quad , \\ \frac{\beta_3}{k_0} &= \frac{252.48220}{252.167972} = 1.00125 \quad . \end{aligned} \tag{11}$$

Again, PEC was used for the horn structure, and PML was chosen for the boundary conditions of the simulation domain. A two-dimensional map of the electric field generated in a vacuum by the considered structure is shown in Fig. 16. Here, we can clearly see the effect of diffraction of the electromagnetic wave caused by the prism's wedge, because the prism is not much larger than the wave front as hypothesized in [6].

The amplitude of the phase vector β_3 was evaluated on Comsol, based on the assumption that the generated wave was inhomogeneous. From such a hypothesis, it follows:

$$E_y(x) = E_0 \mathrm{e}^{-\mathrm{j}\mathbf{k}_3\cdot\mathbf{r}} = E_0 \mathrm{e}^{-\mathrm{j}\beta_x x}\mathrm{e}^{-\boldsymbol{\alpha}\cdot\mathbf{r}} \tag{12}$$

so,

$$\ln E_y(x) = \ln E_0 - \mathrm{j}\beta_x x - \boldsymbol{\alpha}\cdot\mathbf{r} \tag{13}$$

and, finally:

$$\mathrm{Im}\left[\ln E_y(x)\right] = \mathrm{Im}\left[\ln E_0\right] - \beta_x x \,. \tag{14}$$

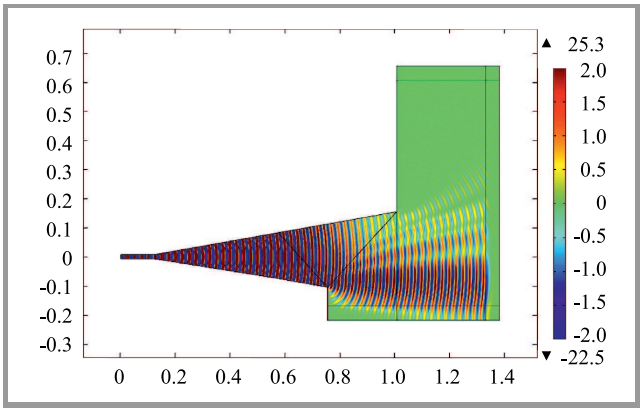

Fig. 16. Near-field radiation (V/m) of the horn lossy prism structure in vacuum: it can be observed that the radiation is directed normally to the separation interface. (See color pictures online at www.nit.eu/publications/journal-jtit)

Exporting some samples of the amplitude of the phase vector β_x in the direction normal to the lossy medium interface, and averaging the obtained values (as the phase vector amplitude presents a spatial periodicity), it was obtained $\beta_3/k_0 = 1.00119$. This value is in very good agreement with the one expected from [6], and it is only slightly lower, because the wave generated by this structure is not plane. After having confirmed that the lossy prism behaves as expected, we introduced the lossy medium already treated in the previous sections of this paper. The simulation results are shown in Fig. 17.

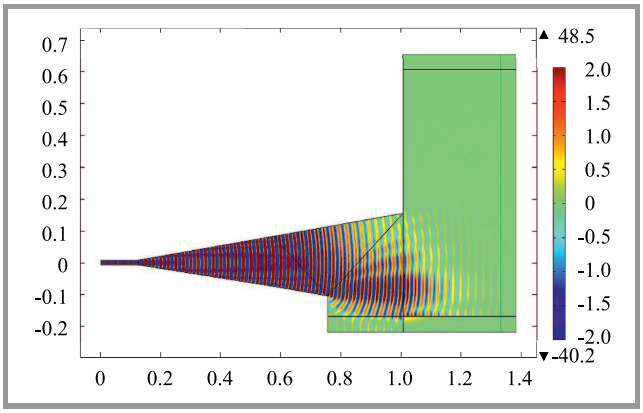

Fig. 17. Simulation of the horn-prism structure penetration on a lossy medium having unitary relative permittivity and permeability, and with conductivity $\sigma = 0.05$ S/m, the electric-field amplitude is expressed in V/m.

The amplitude of the field on the direction of maximum penetration was exported on Matlab and compared against

the penetration produced by the two-dimensional antenna presented in the previous paragraph. The result is displayed in Fig. 18.

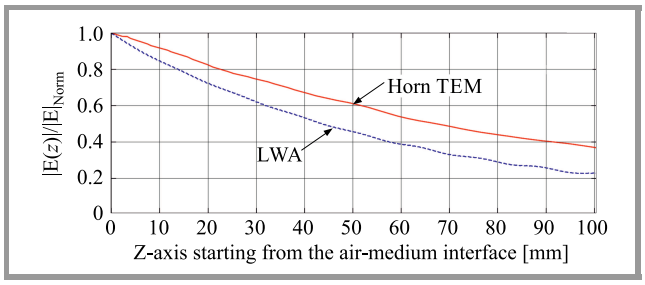

Fig. 18. Normalized electric-field amplitudes of horn-prism structure and two-dimensional leaky-wave antenna inside a non-magnetic lossy medium, with relative permittivity $\varepsilon_r = 1$ and conductivity $\sigma = 0.05$ S/m – Eq. (8).

The horn-prism structure clearly presents higher penetration, as predicted in [6]. This comes at the cost of loss of energy that gets dissipated inside the prism.

The base of the prism considered in this paper is as large as the two-dimensional TEM-horn antenna aperture. This choice reduces the losses in the prism to a minimum, but it is not ideal, because the theory was developed for an infinite long prism. We need therefore to confirm that the choice made does not compromise the expected behavior. Let us enlarge the base of the two-dimensional lossy prism, obtaining the antenna shown in Fig. 19.

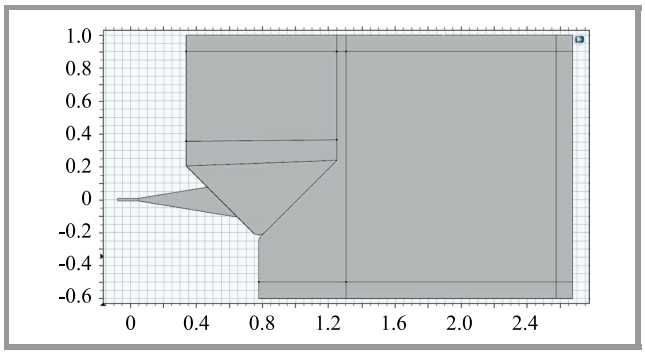

Fig. 19. Comsol simulation of a two-dimensional TEM-horn antenna device with lossy prism dimensions larger than the TEM-horn antenna aperture dimensions.

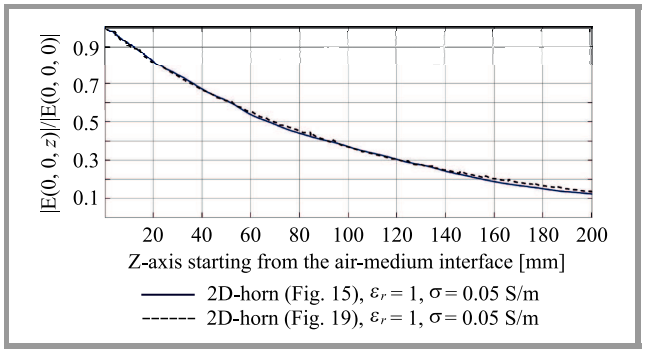

Fig. 20. Normalized electric-field amplitude achieved by employing the antenna illustrated in Fig. 19 compared with the one obtained by the antenna of Fig. 15 on a non-magnetic lossy medium, having relative permittivity $\varepsilon_r = 1$ and conductivity $\sigma = 0.05$ S/m – Eq. (8).

Let us, again, try to penetrate the lossy medium of unitary relative permittivity and conductivity of 0.05 S/m. The result of the comparison is available in Fig. 20. The two prisms show almost identical behavior: that is expected, noting that the original prism phase vector amplitude differs from the ideal one only by 6 ppm.

7. Lossy Prism Penetration on Realistic Media

A fundamental task is the evaluation of the penetration produced by the two-dimensional lossy prism on media having non-unitary permittivity, and in particular on media that can be encountered in realistic applications such as Ground Penetrating Radar (GPR). To perform such a task, we will consider clay, whose relative permittivity varies from 2 to 4, and conductivity varies depending on the humidity from 10^{-7} S/m (extremely dry clay), up to 10^{-1} S/m (extremely wet clay). We will consider here three samples having relative permittivity $\varepsilon_r = 3$ and conductivity $\sigma = 10^{-7}$ S/m, $\sigma = 10^{-5}$ S/m, and, finally, $\sigma = 10^{-3}$ S/m. We are going to predict analytically the expected penetration-curve behavior and then we will illustrate numerical simulations that will compare the penetration achieved by the lossy prism to the one achieved employing the customary horn antenna shown in Fig. 10.

7.1. Analytical Expectations for the Ideal Lossy Prism

The curve describing the amplitude of the electric field inside the lossy medium considered in the previous section does not resemble a horizontal line, as one would expect in the case of a deep-penetration condition (see Fig. 18). Let us analyze the reasons for this behavior approximating, again, the field produced by the lossy prism with a single inhomogeneous plane wave. Let us consider an inhomogeneous wave impinging normally on the separation surface with a lossy medium: with reference to Fig. 1, it is: $\xi_1 = \xi_2 = 0$, $\zeta_1 = 90°$, $0 < \zeta_2 < 90°$. It is then possible to evaluate the amplitude of the angle ζ_2 by knowing the amplitude of the attenuation vector of the incident wave through the generalized Snell laws and the separability conditions:

$$\begin{cases} \beta_2^2 - \alpha_2^2 = \mathrm{Re}\, k_2^2 \\ 2\beta_2\alpha_2 \cos(\zeta_2 - \xi_2) = 2\beta_2\alpha_2 \cos\zeta_2 = \mathrm{Im}\, k_2^2 \\ \alpha_2^2 \sin^2\zeta_2 = \alpha_1^2 \end{cases} . \quad (15)$$

Employing simple algebraic manipulations, we can write:

$$\begin{cases} 4\left(\mathrm{Re}\, k_2^2 + \alpha_2^2\right)\cdot\alpha_2^2\left(1 - \sin^2\zeta_2\right) = \mathrm{Im}^2 k_2^2 \\ \alpha_2^2 \sin^2\zeta_2 = \alpha_1^2 \end{cases} . \quad (16)$$

Now, setting $\sin^2\zeta_2 = \chi$ and substituting the second in the first of (16), a second-order equation in χ is obtained:

$$\left(\mathrm{Re}\,k_2^2\chi + \alpha_1^2\right)(1-\chi) = \frac{\mathrm{Im}^2 k_2^2}{4\alpha_1^2}\chi^2 \Rightarrow$$

$$\left(\mathrm{Re}\,k_2^2 + \frac{\mathrm{Im}^2 k_2^2}{4\alpha_1^2}\right)\chi^2 + \left(\alpha_1^2 - \mathrm{Re}\,k_2^2\right)\chi - \alpha_1^2 = 0\,.$$

We assumed a working frequency of $f_0 = 12$ GHz and we designed a lossy prism such that $\alpha_1 = 12.5927$ rad/m, see Eq. (11). For the medium considered in the previous paragraph $\sigma = 0.05$ S/m, $\mu_r = 1$, and $\varepsilon_r = 1$. In that case Eq. (17) predicts $\zeta_2 \approx 53.26°$. The component of the attenuation vector along the z axis is, in this case, not negligible with respect to the component along the interface. If, instead, $\mu_r = 1$, $\varepsilon_r = 3$, and $\sigma = 10^{-7}$ S/m are assumed in Eq. (17), we obtain $\zeta_2 \approx 89.9999°$. In this scenario the lossy prism approximates very well the "deep-penetration condition" and therefore it would penetrate almost indefinitely inside the lossy medium. The field inside the medium approximates a line parallel to the z axis because the component of $\boldsymbol{\alpha}$ along the z axis and responsible for the exponential attenuation inside the lossy medium is, in this case, negligible. When $\mu_r = 1$, $\varepsilon_r = 3$, and $\sigma = 10^{-3}$ S/m are considered, $\zeta_2 \approx 89.5°$. Also in this case, the curve describing the penetration should still be approximated as a line in the interval taken in this simulation (about 100 mm). In all considered cases the prism is expected to penetrate inside the lossy medium more deeply than the pyramidal horn.

7.2. Numerical Results

Let us now take the antenna shown in Fig. 19 and let us apply it to the three different configurations of clay considered. The penetration is, again, evaluated through the expression given in Eq. (8), and results are compared against the ones obtained by employing the customary pyramidal-horn antenna of Fig. 10. Results of the comparisons for the three media are shown in Figs. 21, 22, and 23, respectively. As expected, the field generated by the horn antenna decreases exponentially in the direction normal to the separation surface (it must be $\zeta_2 = 0$ in Fig. 1), while the field produced by the TEM-horn antenna equipped with the lossy prism presents a slope that, in the interval taken, resembles a line. The attenuation produced by the lossy medium on the inhomogeneous field generated is almost in perfect agreement with the value expected by Eq. (17) when $\sigma = 0.05$ S/m and $\varepsilon_r = 1$, but in the cases shown in Figs. 21–23, in which the conductivity has a lower amplitude, the attenuation produced on the field generated by the TEM-horn antenna is found to be slightly larger than the one predicted for the plane-wave. The attenuation on the wave due to the finite nature of the source is predominant in this case on the attenuation introduced by the lossy medium.

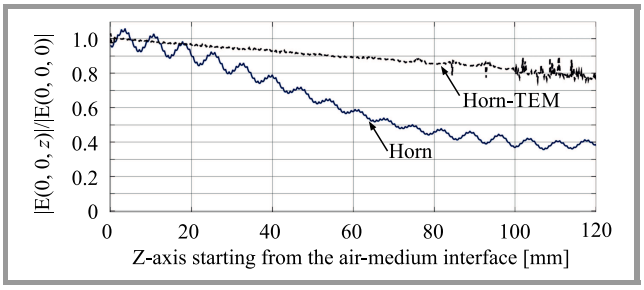

Fig. 21. Amplitudes of normalized electric fields generated by the lossy-prism antenna (dashed line) and a customary horn antenna evaluated inside a non-magnetic lossy medium having permittivity $\varepsilon_r = 3$ and conductivity $\sigma = 10^{-7}$ S/m in the direction normal to the separation interface and normalized by the field at the separation interface – Eq. (8).

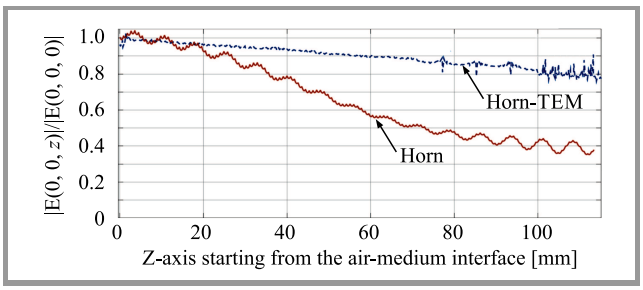

Fig. 22. Amplitudes of normalized electric fields generated by the lossy-prism antenna (dashed line) and a customary horn antenna evaluated inside a non-magnetic lossy medium having permittivity $\varepsilon_r = 3$ and conductivity $\sigma = 10^{-5}$ S/m in the direction normal to the separation interface and normalized by the field at the separation interface – Eq. (8).

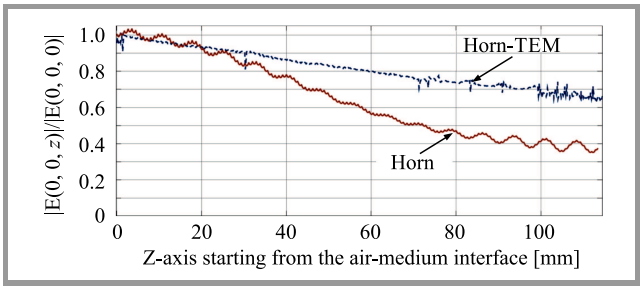

Fig. 23. Amplitudes of normalized electric fields generated by the lossy-prism antenna (dashed line) and a customary horn antenna evaluated inside a non-magnetic lossy medium having permittivity $\varepsilon_r = 3$ and conductivity $\sigma = 10^{-3}$ S/m in the direction normal to the separation interface and normalized by the field at the separation interface – Eq. (8).

8. Conclusions

In this paper, a larger penetration achievable by inhomogeneous waves was investigated numerically by simulating common horn antennas and inhomogeneous-wave generators. Attention was paid to broadside radiation, which represents a common requirement for many practical applications, highlighting that the inhomogeneous radiation may be not only a necessary condition, but also a sufficient condi-

tion for achieving penetration larger than the one achievable by commonly used and more traditional antenna geometries. It was verified, at least for the numerical scenarios considered, that the closer the losses in the medium get to the condition of deep-penetration, the higher the difference in penetration between homogeneous and inhomogeneous waves. It was also verified that the expectation that higher penetration is achieved increasing the incidence angle is confirmed by numerical simulations employing realistic waveforms and not only by the former analytical plane-wave demonstrations, as done in previous works presented in the literature. Finally, we concentrated on the recently proposed geometry of the lossy prism structure, showing that, where losses in the prism are an acceptable compromise, this structure can guarantee deeper penetration than the one obtainable through other leaky-wave antennas presented in the literature [3]. The deep penetration employing a lossy prism comes at the price of dissipation of energy in form of heating, so, the energy available at the separation interface between lossless and lossy media is lower than the one produced by the feeding antenna, this may be suitable only in certain scenarios, as discussed in the paper.

9. Future work

The simulations exposed in this paper show encouraging results but they are still early-stage outcomes that will need to be confirmed by operating a larger number of comparisons. A more realistic tapered TEM antenna, such as the one presented in [27], should be considered. Moreover, the results given here are valid for a single frequency, while the impact on UWB applications and antennas should also be evaluated. Further simulations will have to be performed to demonstrate the suitability of this structure to interesting scenarios such as hyperthermia or Ground Penetrating Radar. Those simulations could require a re-design and further optimization of the antenna proposed here. Moreover, penetration is only one factor to be evaluated in antenna design, realistic applications will need also to consider important characteristics such as phase-center stability and bandwidth.

Acknowledgements

The authors are deeply indebted to the GPR COST Action TU1208 and its network activities that made this study possible.

References

[1] F. Frezza and N. Tedeschi, "Deeply penetrating waves in lossy media", *Optics Letters*, vol. 37, no. 13, pp. 2616–2618, 2012 (doi: 10.1364/OL.37.002616).

[2] F. Frezza and N. Tedeschi, "On the electromagnetic power transmission between two lossy media: discussion", *J. of the Opt. Soc. of America A*, vol. 29, no. 11, pp. 2281–2288, 2012 (doi:10.1364/JOSAA.29.002281).

[3] A. A. Oliner and D. R. Jackson, "Leaky-Wave Antennas", in *Antenna Engineering Handbook*, 4th Edition, Chap. 11, John Volakis Editor, McGraw Hill Professional, 2007.

[4] D. R. Jackson and A. A. Oliner, "Leaky-wave antennas", in *Modern Antenna Handbook* (C. A. Balanis, Ed.), pp. 325-367, New York: Wiley, 2008.

[5] P. Baccarelli, F. Frezza, P. Simeoni, and N. Tedeschi, "Inhomogeneous Wave Penetration in Lossy Media", in *Proc. Int. Symp. on EM Theory EMTS 2016*, Espoo, Finland, 2016 (doi: 10.1109/URSI-EMTS.2016.2016.7571523).

[6] F. Frezza, P. Simeoni, and N. Tedeschi, "Analytical Investigation on a New Approach for achieving Deep Penetration in a Lossy medium: the Lossy Prism", *J. of Telecommun. and Infor. Technol.*, no. 3, pp. 17–24, 2017 (doi: 10.26636/jtit.2017.119917).

[7] F. Frezza, *A Primer on Electromagnetic Fields*. Springer, 2015.

[8] F. Frezza and N. Tedeschi, "Electromagnetic inhomogeneous waves at planar boundaries: tutorial", *J. of the Opt. Soc. of America A*, vol. 32, no. 8, pp. 1485–1501, 2015 (doi: 10.26636/jtit.2017.119917).

[9] F. Frezza, S. Leo, F. Mangini, N. Tedeschi, and P. Simeoni, "Deep Penetration in Lossy Media Through Non Uniform Electromagnetic Waves", in *Proc. the Third TU1208 Action Gen. Meeting*, London, United Kingdom, 2015, Aracne.

[10] T. Zhao, D. R. Jackson, J. T. Williams, H. Y. D. Yang, and A. A. Oliner, "2-D Periodic Leaky-Wave Antennas-Part I: Metal Patch Design", *IEEE Transact. on Antennas and Propag.*, vol. 53, no. 11 pp. 3505–3514, 2005 (doi: 10.1109/TAP.2005.858579).

[11] N. G. Alexopoulos and D.R. Jackson, "Fundamental superstrate (cover) effects on printed circuit antennas", *IEEE Transact. on Antennas and Propag.*, vol. AP-32, pp. 807–816, 1984 (doi: 10.1109/TAP.1984.1143433).

[12] D. R. Jackson and N. G. Alexopoulos, "Gain Enhancement method for Printed Circuit Antennas", *IEEE Transact. on Antennas and Propag.*, vol. AP-33, pp. 976–987, 1985.

[13] M. Ettore, "Analysis and design of efficient planar leaky-wave antennas", Ph. D. Thesis, University of Siena, 2008.

[14] P. Burghignoli, G. Lovat, and D. R. Jackson, "Analysis and optimization of leaky-wave radiation at broadside from a class of 1-D periodic structures", *IEEE Transact. on Antennas and Propag.*, vol. 54, no. 9, pp. 2593–2604, 2006 (doi: 10.1109/TAP.2006.880725).

[15] S. Paulotto, P. Baccarelli, F. Frezza, and D. R. Jackson, "A novel technique for open-stopband suppression in 1-D periodic printed leaky-wave antennas", *IEEE Transactions on Antennas and Propagation*, vol. 57, no. 7, pp. 1894-1906, 2009 (doi: 10.1109/TAP.2009.2019900).

[16] CST Microwave Studio, "Version 2014", Darmstadt (Germany), CST GmbH, 2014.

[17] T. Zhao, D. R. Jackson, J. T. Williams, and A. A. Oliner, "General formulas for 2-D leaky-wave antennas", *IEEE Transact. on Antennas and Propag.*, vol. 53, no. 11, pp. 3525–3533, 2005 (doi: 10.1109/TAP.2005.856315).

[18] R. Garg, *Microstrip antenna design handbook*, Boston, MA: Artech House, 2001.

[19] F. Frezza and N. Tedeschi, "Total transmission of inhomogeneous electromagnetic waves at planar interfaces", *Phys. Rev. A*, vol. 92, 053853, 2015 (doi: 10.1103/PhysRevA.92.053853).

[20] C. A. Balanis, *Antenna theory: analysis and design,* New York: Wiley, 2016.

[21] CST, "Workflow Example Horn Antenna", *CST Microwave Studio Training Class*, 2009.

[22] W. Menzel, "A new travelling-wave antenna in microstrip", in *Proc. 8th Eur. Microwave Conf.*, Paris, France, 1978, pp. 302–306 (doi: 10.1109/EUMA.1978.332503).

[23] A. A. Oliner and K. S. Lee, "Microstrip leaky wave strip antennas", in *Proc. IEEE Int. Symp. on Antennas and Propag.*, Philadelphia, PA, USA, 1986, pp. 443–446 (doi: 10.1109/APS.1986.1149629).

[24] N. Tedeschi and F. Frezza, "An analysis of the inhomogeneous wave interaction with plane interfaces", in *Proc. Gen. Ass. and Scient. Symp. URSI GASS*, Beijing, China, 2014, pp. 109–112 (doi: 10.1109/URSIGASS.2014.6929097).

[25] N. Tedeschi, V. Pascale, F. Pelorossi, and F. Frezza, "Generation of inhomogeneous electromagnetic waves by a lossy prism", in *Proc. Int. Symp. on EM Theory EMTS 2016*, Espoo, Finland, 2016 (doi: 10.1109/URSI-EMTS.2016.7571534).

[26] S. A. Schelkunoff and H. T. Friis, *Antennas Theory and Practice*, New York: Wiley, 1952.
[27] S. Bassam and J. Rashed-Mohassel, "A Chebyshev tapered TEM horn antenna", *PIERS Online*, vol. 2, no. 6, pp. 706–709, 2016 (doi: 10.2529/PIERS060902041831).

Alessandro Calcaterra received his B.Sc. and M.Sc. degrees in Electronic Engineering with full marks and honors, both from the University of Rome "La Sapienza" in 2014 and 2017, respectively. During his academic career he attended two different advanced courses, in which he could deeply improve his knowledge on the electromagnetic theory, on the characteristics of materials at microwave frequencies and on leaky-wave antennas. In particular, the latter represents his main topic of interest that he could enhance by attending the ESoA course on "Leaky-waves and periodic structures for antenna applications" in 2017. At the moment, he is enrolled in the Ph.D. course in Electromagnetism at the University of Rome "La Sapienza", studying the deep-penetration phenomenon and how to achieve it using inhomogeneous waves such as leaky ones.

E-mail: alessandro.calcaterra@uniroma1.it
Department of Information Engineering, Electronics and Telecommunications
La Sapienza University of Rome
via Eudossiana 18
00184 Rome, Italy

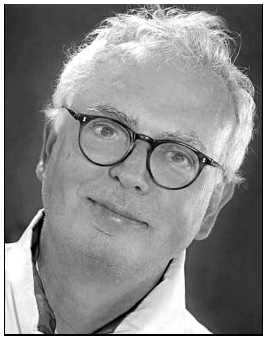

Fabrizio Frezza received the "Laurea" degree (cum laude) in Electronics Engineering and the Ph.D. degree in Applied Electromagnetics and Electrophysical Sciences from La Sapienza University of Rome, Italy, in 1986 and 1991, respectively. He joined the Department of Electronics, Sapienza University of Rome, in 1986, where he was a Researcher from 1990 to 1998, a Temporary Professor of Electromagnetic Fields from 1994 to 1998, and an Associate Professor from 1998 to 2004. He has been a Full Professor of Electromagnetic Fields with Sapienza University of Rome since 2005. His current research interests include guiding structures, antennas and resonators for microwaves and millimeter waves, numerical methods, scattering, optical propagation, plasma heating, anisotropic media, artificial materials, and metamaterials.

E-mail: fabrizio.frezza@uniroma1.it
Department of Information Engineering, Electronics and Telecommunications
La Sapienza University of Rome
via Eudossiana 18
00184 Rome, Italy

Patrizio Simeoni received both the "Laurea" (degree) in Electronic Engineering and the Ph.D. in Mathematical Models for Engineering, Electromagnetics and Nanosciences from "La Sapienza" University of Rome, Italy. He worked as an embedded, software and system engineer from 2002. As a software engineer, he developed firmware on both DSPs and controllers, device drivers and user-level applications. As a system engineer he collaborated in the design of solutions for telecommunication and transport projects. His main research topic in electromagnetism is the study of electromagnetic-wave penetration in lossy media. Since 2012, he has been employed in the National Transport Authority, Ireland, as a senior technical engineer in the Integrated Ticketing System project.

E-mail: patrizio.simeoni@nationaltransport.ie
National Transport Authority (NTA)
Dún Scéine
Harcourt Lane
Dublin 2
Dublin, Ireland

Nicola Tedeschi received the M.Sc. degree in Electronic Engineering and the Ph.D. degree from La Sapienza University of Rome, Rome, Italy, in 2009 and 2013, respectively. Currently, he is a Postdoctoral Fellow with La Sapienza University of Rome. He was a visiting student with the Department of Radio Science and Engineering, Aalto University, Espoo, Finland, in 2012. His research interests include electromagnetic scattering by objects near interfaces, propagation of inhomogeneous waves in dissipative media, and characterization of dispersive properties of natural and artificial materials.

E-mail: nicola.tedeschi@uniroma1.it
Department of Information Engineering, Electronics and Telecommunications
La Sapienza University of Rome
via Eudossiana 18
00184 Rome, Italy

Paper

Minimum Array Elements for Resolution of Several Direction of Arrival Estimation Methods in Various Noise-Level Environments

Ismail El Ouargui[1], Said Safi[1], and Miloud Frikel[2]

[1] *Department of Mathematics and Informatics, Sultan Moulay Slimane University, Beni Mellal, Morocco*
[2] *GREYC Lab UMR 6072 CNRS, ENSICAEN, Caen, France*

https://doi.org/10.26636/jtit.2018.119417

Abstract—The resolution of a Direction of Arrival (DOA) estimation algorithm is determined based on its capability to resolve two closely spaced signals. In this paper, authors present and discuss the minimum number of array elements needed for the resolution of nearby sources in several DOA estimation methods. In the real world, the informative signals are corrupted by Additive White Gaussian Noise (AWGN). Thus, a higher signal-to-noise ratio (SNR) offers a better resolution. Therefore, we show the performance of each method by applying the algorithms in different noise level environments.

Keywords—covariance matrix, direction of arrival, geolocation, resolution, noise, smart antenna.

1. Introduction

Direction-of-arrival (DOA) estimation [1], [2] aims essentially to find the direction of arrival of multiple signals, which can be in the form of electromagnetic or acoustic waves, impinging on a sensor or antenna array. The requirement for DOA estimation arises from the needs of locating and tracking [3] signal sources in both civilian and military applications, such as search and rescue, law enforcement, sonar, seismology, and emergency call locating.

A large amount of work has been performed on DOA algorithms, e.g. [4]–[6]. In [2] Krim *et al*. presented an interesting comparative study between a set of DOA estimation algorithms, such as beamforming techniques and subspace-based methods. The basic idea of beamforming techniques [7]–[9] is to steer, electronically, the array in one direction at a time and measure the output power, so when the steered direction coincides with a DOA of a signal, the maximum output power will be observed. The scheme leads essentially to the formation of an appropriate form of output power that will be strongly related to the DOA.

Although beamforming techniques are simple to implement and require low computational time and power, they suffer from their poor resolution. For this reason, we introduce the concept of subspaces and propose the subspace-based methods [10], [11] that use the decomposition of the output data covariance matrix to benefit from the orthogonality of the two subspaces: the signal subspace and the noise subspace. Other methods have been proposed recently to overcome the computational load provided by the decomposition of the data covariance matrix, such as the propagator [12], [13] and the partial propagator [14].

Obviously, it has been proven [1], [15] that the accuracy and resolution of DOA estimation can be affected by several factors such as the number of the impinging sources, the number of array elements, the SNR, number of snapshots and angle differences [16]. In this paper, we focus on a study of the resolution capability of several DOA estimation algorithms by selecting the minimum array elements needed to separate closely spaced signals in different noise level environments. Our aim is to analyze the resolution performance of those methods, and at the same time, show their sensitivity against the noise. The study is restricted to one-dimensional signals that are assumed to be narrowband [17] and corrupted by a uniform Additive White Gaussian Noise (AWGN), impinging on a Uniform Linear Array (ULA).

2. Problem Modeling

Before presenting the data model, authors consider the same assumptions taken in [1]:

- isotropic and linear transmission medium,
- far-field,
- narrowband,
- the noise is AWGN.

Consider a ULA consisting of M identical elements that are aligned and equally spaced on a line by a distance Δ, receiving a wavefield generated by d narrowband sources in the presence of an AWGN, as presented in Fig. 1 [1].

The data received by the antenna array elements can be expressed as:

$$\mathbf{x}(t) = \mathbf{A}\mathbf{s}(t) + \mathbf{n}(t), \tag{1}$$

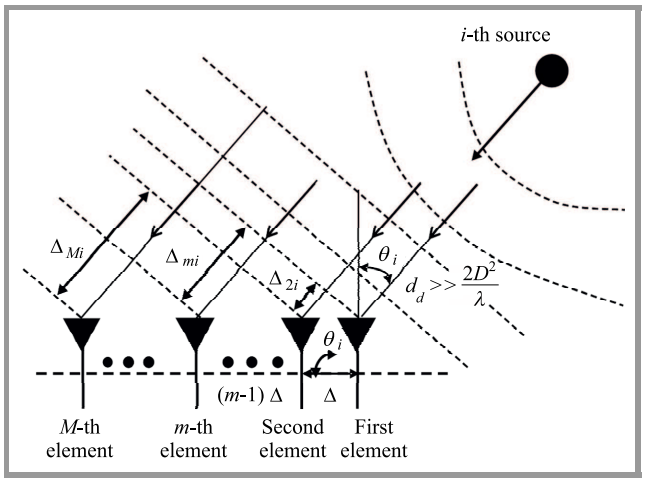

Fig. 1. Data model for DOA estimation of d sources with a linear array of the M element.

where $\mathbf{x}(t) = [x_1(t)\ x_2(t) \ldots x_M(t)]^T$ denotes the received array data vector, $\mathbf{s}(t) = [s_1(t) \ldots s_d(t)]^T$ denotes the source waveform vector, $\mathbf{n}(t) = [n_1(t)\ n_2(t) \ldots n_M(t)]^T$ is the vector of the uncorrelated additive noise in the array.

$\mathbf{A} = [\mathbf{a}(\theta_1)\,\mathbf{a}(\theta_2) \ldots \mathbf{a}(\theta_d)]$ denotes the steering matrix containing the steering column vectors $\mathbf{a}(\theta_i)$ defined as:

$$\mathbf{a}(\theta_i) = \begin{bmatrix} 1 & \mathrm{e}^{\frac{\mathrm{j}2\pi\Delta}{\lambda}\sin(\theta_i)} & \ldots & \mathrm{e}^{(M-1)\frac{\mathrm{j}2\pi\Delta}{\lambda}\sin(\theta_i)} \end{bmatrix}^T,$$

where Δ is the element spacing which satisfies $\Delta \leq \frac{\lambda}{2}$, λ is the wavelength of the propagating signals, and θ_i is the unknown direction of arrival of the i-th source.

The noise is assumed to be uncorrelated between array elements, and to have identical variance σ^2 in each element. Under this assumption, the $M \times M$ spatial covariance matrix of the data received by an array can be defined as:

$$\mathbf{R_{xx}} = E[\mathbf{x}(t)\mathbf{x}^H(t)] = \mathbf{A}\mathbf{R}_{ss}\mathbf{A}^H + \sigma^2 I_M\,, \tag{2}$$

where $(.)^H$ is the conjugate transposition, E is the expectation operator and $\mathbf{R}_{ss} = E[\mathbf{s}(t)\mathbf{s}^H(t)]$ is the $d \times d$ signal covariance matrix.

In practice, the exact $\mathbf{R_{xx}}$ is hard to find, due to the limited number of data sets received by the array, but it can be estimated by:

$$\mathbf{R_{xx}} \simeq \widehat{\mathbf{R}}_{\mathbf{xx}} = \frac{1}{N}\sum_{t=1}^{N}\mathbf{x}(t)\mathbf{x}^H(t) = \frac{1}{N}\mathbf{X}\mathbf{X}^H\,, \tag{3}$$

where $\mathbf{X}$ denotes the noise corrupted signal (or data) matrix composed of N snapshots of $\mathbf{x}(t)$, $1 \leq t \leq N$. Many DOA estimation algorithms basically try to extract the information from this array data covariance matrix.

Knowing the data model, and before dealing with our principal aim, which is to study the resolution capability of several popular DOA estimation techniques by showing the minimum array elements they require to split two nearby sources, here is a brief overview about these techniques.

3. Algorithms

3.1. Conventional Beamforming

Conventional beamforming [7], also known as the Bartlett spectrum, is one of the beamforming techniques which are based on an electronic steering of the array in one direction at a time, and measure the output power, so when the steered direction coincides with a DOA of a signal, the maximum output power is observed.

An array can be steered electronically just as an antenna can be steered mechanically by designing a weight vector $\mathbf{w}$ and combining it with the data received by the array elements to form a single output signal $\mathbf{y}(t)$:

$$\mathbf{y}(t) = \mathbf{w}^H\mathbf{x}(t)\,. \tag{4}$$

By taking N snapshots, the total averaged output power of an array is given by:

$$\mathbf{P}(\mathbf{w}) = \frac{1}{N}\sum_{n=1}^{N}|\mathbf{y}(t_n)|^2 = \frac{1}{N}\sum_{n=1}^{N}\mathbf{w}^H\mathbf{x}(t_n)\mathbf{x}^H(t_n)w = \\ = \mathbf{w}^H\widehat{\mathbf{R}}_{\mathbf{xx}}w\,. \tag{5}$$

The conventional beamforming method consists of $\mathbf{w} = \mathbf{a}(\theta)$ with θ being the scanning angle, and the steering vector $\mathbf{a}(\theta)$ is defined as:

$$\mathbf{a}(\theta) = \begin{bmatrix} 1 & \mathrm{e}^{\frac{\mathrm{j}2\pi\Delta}{\lambda}\sin(\theta)} & \ldots & \mathrm{e}^{(M-1)\frac{\mathrm{j}2\pi\Delta}{\lambda}\sin(\theta)} \end{bmatrix}^T,$$

where Δ is the element spacing which satisfies $\Delta \leq \frac{\lambda}{2}$, λ is the wavelength of the propagating signals.

In practice, $\mathbf{w} = \mathbf{a}(\theta)$ is normalized as:

$$\mathbf{w}_{Bartlett} = \frac{\mathbf{a}(\theta)}{\sqrt{\mathbf{a}^H(\theta)\mathbf{a}(\theta)}}\,. \tag{6}$$

Thus, the output power is obtained as:

$$\mathbf{P}_{Bartlett}(\theta) = \frac{\mathbf{a}^H(\theta)\widehat{\mathbf{R}}_{\mathbf{xx}}\mathbf{a}(\theta)}{\mathbf{a}^H(\theta)\mathbf{a}(\theta)}\,. \tag{7}$$

3.2. Capon's Beamformer

The conventional beamforming method has a poor resolution. We can increase the resolution by adding array elements, as will be shown further. However, to overcome this problem, Capon [8] proposed a method that uses the degrees of freedom to form a beam in the look direction and at the same time the nulls in other directions. For a particular look direction, Capon's method uses all but one of the degrees of the freedom to minimize the array output power while using the remaining degrees of freedom to constrain the gain in the look direction to be unity:

$$\min\mathbf{P}(\mathbf{w}) = 0 \quad \text{subject to} \quad \mathbf{w}^H\mathbf{a}(\theta) = 1\,. \tag{8}$$

Thus, the weight vector is expressed as:

$$\mathbf{w}_{Capon} = \frac{\widehat{\mathbf{R}}_{\mathbf{xx}}^{-1}\mathbf{a}(\theta)}{\mathbf{a}^H(\theta)\widehat{\mathbf{R}}_{\mathbf{xx}}^{-1}\mathbf{a}(\theta)}. \tag{9}$$

By combining this weight vector with the Eq. (5), the output power is:

$$\mathbf{P}_{Capon}(\theta) = \frac{1}{\mathbf{a}^H(\theta)\widehat{\mathbf{R}}_{\mathbf{xx}}^{-1}\mathbf{a}(\theta)}. \tag{10}$$

3.3. Linear Prediction

Linear prediction [9] aims to minimize the mean output power of the array, subject to the constraint that the weight on a selected element is unity. The weight vector is given by:

$$\mathbf{w}_{LP} = \frac{\widehat{\mathbf{R}}_{\mathbf{xx}}^{-1}\mathbf{u}}{\mathbf{u}^H\widehat{\mathbf{R}}_{\mathbf{xx}}^{-1}\mathbf{u}} \tag{11}$$

and the power spectrum is:

$$\mathbf{P}_{LP} = \frac{\mathbf{u}^H\widehat{\mathbf{R}}_{\mathbf{xx}}^{-1}\mathbf{u}}{\left|\mathbf{u}^H\widehat{\mathbf{R}}_{\mathbf{xx}}^{-1}\mathbf{a}(\theta)\right|^2}, \tag{12}$$

where $\mathbf{u}$ is a column vector of all zeros except for the selected element, which is equal to 1. This selected element corresponds to the position of the selected element in the array. There is no criterion for the proper choice of this element.

3.4. Maximum Entropy

Maximum entropy [18] is similar to the linear prediction method, it is based on an extrapolation of the covariance matrix. The extrapolation is selected with maximized signal entropy, where its maximum is achieved by searching for the coefficients of an auto-regressive model that minimize the expected prediction error:

$$\mathbf{w} = \min\ \mathbf{w}^H\widehat{\mathbf{R}}_{\mathbf{xx}}\mathbf{w}\ \text{ subject to }\ \mathbf{w}^H\mathbf{e}_i = 1, \tag{13}$$

where $\mathbf{e}_i$ is a column vector of all zeros except for the i-th element, which is equal to 1.

Developing the computations leads to achieving the following power spectrum:

$$\mathbf{P}_{MEM} = \frac{1}{\mathbf{a}(\theta)\mathbf{C}_i\mathbf{C}_i^H\mathbf{a}(\theta)}, \tag{14}$$

where $\mathbf{C}_i$ is the i-th column of the inverse of $\widehat{\mathbf{R}}_{\mathbf{xx}}$.

3.5. MUSIC

Multiple Signal Classification (MUSIC) [10] is considered as one of the most popular subspace-based techniques. It uses the property of orthogonality between the two subspaces, the signal subspace and the noise subspace. The eigen-decomposition of the covariance matrix can be expressed as:

$$\mathbf{R}_{\mathbf{xx}} = \mathbf{A}\mathbf{R}_{ss}\mathbf{A}^H + \sigma^2\mathbf{I}_M = \mathbf{U}_s\Lambda_s\mathbf{U}_s^H + \sigma^2\mathbf{U}_n\mathbf{U}_n^H, \tag{15}$$

where $\mathbf{U}_s$ is the matrix that contains the eigenvectors (the signal eigenvectors) corresponding to the d largest eigenvalues of $\mathbf{R}_{\mathbf{xx}}$, $\mathbf{U}_n$ is the matrix that contains eigenvectors (the noise eigenvectors) corresponding to the $M-d$ smallest eigenvalues of $\mathbf{R}_{\mathbf{xx}}$, the diagonal matrix Λ_s contains the M largest eigenvalues. Since the eigenvectors in $\mathbf{U}_n$, are orthogonal to $\mathbf{A}$, we have:

$$\mathbf{U}_n\mathbf{a}(\theta_i) = 0 \quad i = 1, \ldots, d. \tag{16}$$

Using this property, the power spectrum of MUSIC technique is:

$$\mathbf{P}_{MUSIC} = \frac{1}{\mathbf{a}^H(\theta)\mathbf{U}_n\mathbf{U}_n^H\mathbf{a}(\theta)}. \tag{17}$$

3.6. Minimum Norm

The minimum norm technique can be seen as an enhancement of the MUSIC algorithm, it consists in finding the DOA estimate by searching for the peaks in the power spectrum:

$$\mathbf{P}_{MN} = \frac{1}{|\mathbf{w}^H\mathbf{a}(\theta)|^2}. \tag{18}$$

By determining the array weight $\mathbf{w}$, which is of minimum norm [18] we find the spectrum:

$$\mathbf{P}_{MN} = \frac{1}{|\mathbf{a}^H(\theta)\mathbf{U}_n\mathbf{U}_n^H\mathbf{W}\mathbf{U}_n\mathbf{U}_n^H\mathbf{a}(\theta)|}, \tag{19}$$

where the matrix $\mathbf{W} = \mathbf{e}_1\mathbf{e}_1^T$ ($\mathbf{e}_1$ is the first vector of a $M \times M$ matrix) is needed to make the matrix dimensions match mathematically.

3.7. The Propagator Method

To reduce the computational complexity of the methods that are based on the eigen-decomposition. The propagator method [12], [13], [19] exploits the partition of the data covariance matrix defined as:

$$\widehat{\mathbf{R}}_{\mathbf{xx}} = \begin{pmatrix}\widehat{\mathbf{R}}_1\\ \widehat{\mathbf{R}}_2\end{pmatrix}, \tag{20}$$

where $\widehat{\mathbf{R}}_1$ is a square matrix of size $d \times M$ and $\widehat{\mathbf{R}}_2$ is a matrix of size $(M-d) \times M$. The propagator operator is defined as:

$$\begin{cases}\widehat{\mathbf{R}}_2 = \Psi_{21}\widehat{\mathbf{R}}_1\\ \Psi_{21} = \widehat{\mathbf{R}}_2\widehat{\mathbf{R}}_1^{\dagger}\end{cases}, \tag{21}$$

where $\widehat{\mathbf{R}}_1^{\dagger}$ is the pseudo-inverse of $\widehat{\mathbf{R}}_1$ defined as $\widehat{\mathbf{R}}_1^{\dagger} = \left(\widehat{\mathbf{R}}_1^H\widehat{\mathbf{R}}_1\right)^{-1}\widehat{\mathbf{R}}_1^H$. Then the noise subspace constructed by this operator is given by $\mathbf{U}_n = [\Psi_{21}, \mathbf{I}_{M-d}]$, and the power spectrum is:

$$\mathbf{P}_{Pr} = \frac{1}{\mathbf{a}^H(\theta)\mathbf{U}_n\mathbf{U}_n^H\mathbf{a}(\theta)}. \tag{22}$$

3.8. The Partial Propagator

Unlike the propagator method, the partial propagator [14] only needs to use the partial covariance matrix and reduce the computation complexity. The partial propagator is based on partitioning the steering matrix into three blocks under the assumption $M > 2d$. The steering matrix is partitioned as:

$$\mathbf{A} = \begin{pmatrix} \mathbf{A}_1 \\ \mathbf{A}_2 \\ \mathbf{A}_3 \end{pmatrix}, \tag{23}$$

where $\mathbf{A}_1$, $\mathbf{A}_2$ and $\mathbf{A}_3$ are matrices of size: $d \times d$, $d \times d$, $(M-2d) \times d$ respectively. Using this partition, the partial correlation matrix are defined as:

$$\begin{aligned} \mathbf{R}_{12} &= E\left[\mathbf{X}(t)(1:d,:)\mathbf{X}^H(t)((d+1):2d,:)\right] = \\ &= \mathbf{A}_1 \mathbf{R}_{ss} \mathbf{A}_2^H, \end{aligned} \tag{24}$$

$$\begin{aligned} \mathbf{R}_{31} &= E\left[\mathbf{X}(t)((2d+1):M,:)\mathbf{X}^H(t)(1:d,:)\right] = \\ &= \mathbf{A}_3 \mathbf{R}_{ss} \mathbf{A}_1^H, \end{aligned} \tag{25}$$

$$\begin{aligned} \mathbf{R}_{32} &= E\left[\mathbf{X}(t)((2d+1):M,:)\mathbf{X}^H(t)(d+1:2d,:)\right] = \\ &= \mathbf{A}_3 \mathbf{R}_{ss} \mathbf{A}_2^H, \end{aligned} \tag{26}$$

where $\mathbf{X}$ is the matrix defined in Eq. 3. Based on these partitions, we define a matrix $\mathbf{U}_n$ as:

$$\mathbf{U}_n = \begin{bmatrix} \mathbf{R}_{32}\mathbf{R}_{12}^{-1} & \mathbf{R}_{31}\mathbf{R}_{21}^{-1} & -2\mathbf{I}_{M-2d} \end{bmatrix} \tag{27}$$

for which we have: $\mathbf{U}_n\mathbf{A} = 0$. So, similarly to MUSIC and the propagator methods, we can form the power spectrum as follows:

$$\mathbf{P}_{Partial} = \frac{1}{\mathbf{a}^H(\theta)\mathbf{U}_n\mathbf{U}_n^H\mathbf{a}(\theta)}. \tag{28}$$

4. Experimental Results

This section focuses on testing the resolution capability of each algorithm mentioned in Section 3. We determine the minimum number of the array antennas required to separate two far field sources that are spaced with an angular distance of 5°. The simulation is done by taking $d = 4$ sources impinging on a ULA of identical antennas with element spacing equaling to the half of the input signal wavelength, the number of snapshots is fixed at $N = 200$. Since the SNR highly influences on the resolution, four different noise level environments are considered in this study, which are $SNR_1 = -10$ dB, $SNR_2 = 0$ dB, $SNR_3 = 10$ dB, and $SNR_4 = 20$ dB. The number of array elements is thus varied until we find the minimum satisfying the resolution of the second and the third sources which are closely separated (5°). All the simulations are made using Matlab R2016b, the noise is a random process generated using a Matlab function and the signals are assumed to be snapshots of demodulated electromagnetic sources. Differentiation between the different sources is detected by vision. The degree of sensitivity to the number of array elements is different for the individual methods. This is why we notice, for some methods, that there's a small valley and a big one for others.

In the following figures, we show some of the simulations that we have performed. We present the response of each method for two values of the number of antennas, before and after resolution, at the noise level of $SNR_2 = 0$ dB.

We start with the conventional beamformer. Figure 2 represents the spectrum before and after resolution and the number of array elements used.

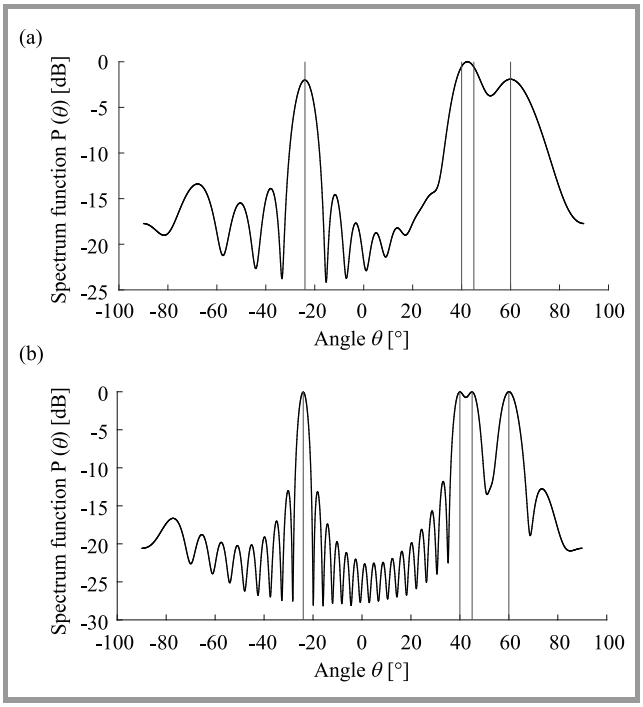

Fig. 2. Bartlett's spectrum: (a) before – 14 elements and (b) after – 30 elements.

We remark that as mentioned in Section 3, Bartlet's method has a poor resolution. Indeed, it requires about 30 elements as a minimum to slightly separate our two close sources.

Figure 3 shows the result obtained by using the Capon's beamformer technique.

With the Capon's beamformer, we start having a low number of elements needed to separate the two close sources (14 elements). It performs much better than the conventional beamformer at the resolution level, but as illustrated in Fig. 3, the separation is not complete. To achieve better resolution while using this method, we should add more elements.

Figure 4 shows the spectrum obtained by using the linear prediction method and choosing the selected element for $\mathbf{u}$ in Eq. (12) as the element in the center.

The linear prediction method performs well. As can be seen clearly in the Fig. 4, the two close sources are well separated once we use 12 array elements.

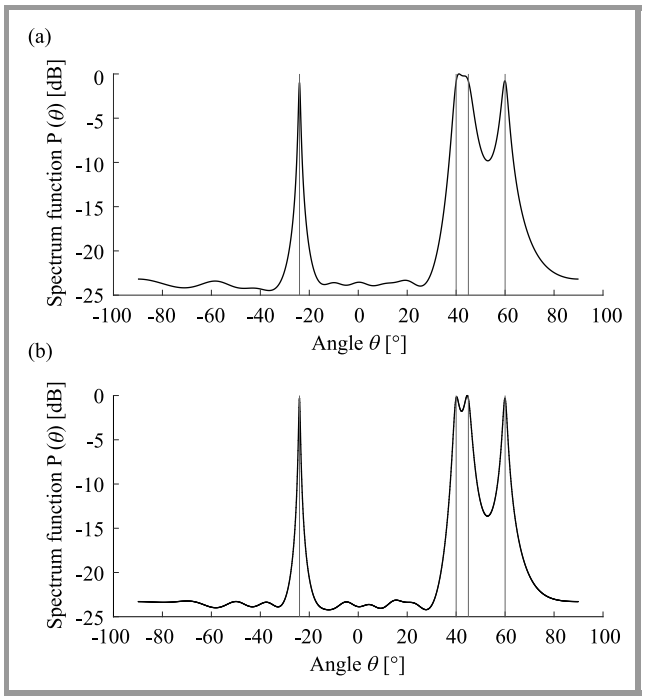

Fig. 3. Capon's spectrum: (a) before – 12 elements and (b) after – 14 elements.

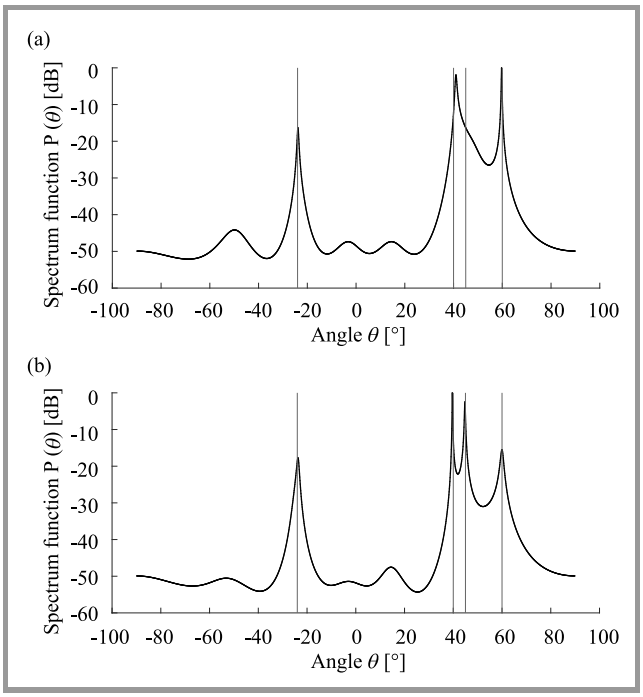

Fig. 5. Maximum entropy spectrum: (a) before – 13 elements and (b) after – 14 elements.

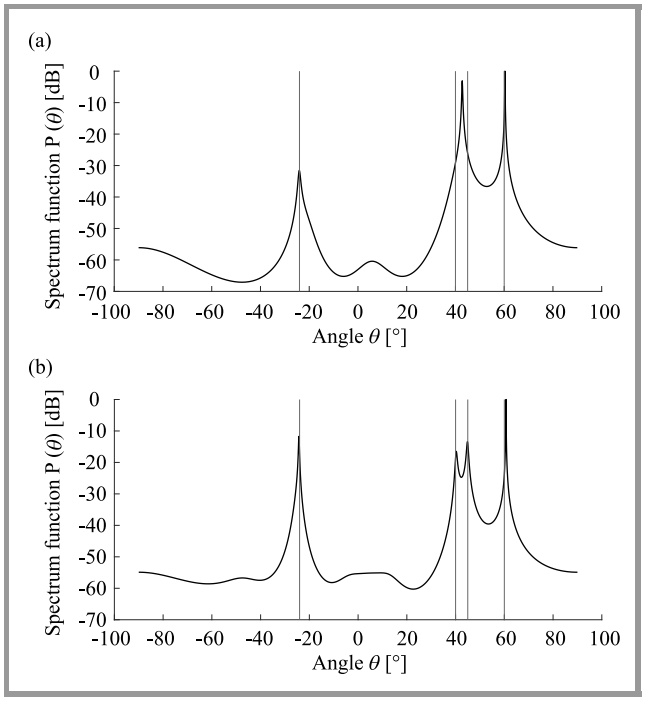

Fig. 4. Linear prediction spectrum: (a) before – 11 elements and (b) after – 12 elements.

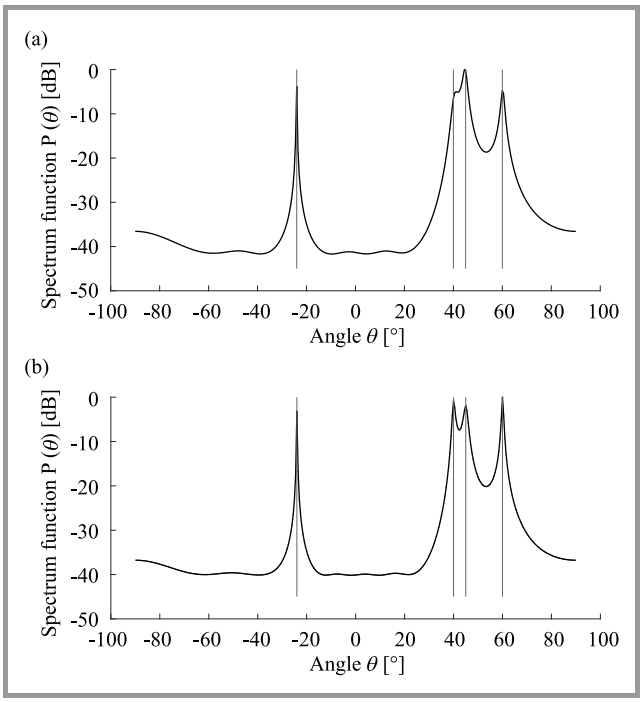

Fig. 6. MUSIC spectrum: (a) before – 9 elements and (b) after – 10 elements.

Figure 5 shows the result obtained by using the maximum entropy method by choosing $\mathbf{e}_i$ as the element in the center. As illustrated in Fig. 5, the maximum entropy method performs well too and allows to have a good resolution by using 14 array elements.

Figure 6 represents the result obtained by using the MUSIC method. With MUSIC, we could achieve a good resolution using only 10 array elements in this noise level. In addition, one can notice that the spectrum contains no secondary lobes which makes MUSIC be one of the most performing DOA estimation algorithms.

We now see the performance of minimum norm in Fig. 7. Minimum norm seems to be the best performing technique at this noise level among all the methods discussed earlier.

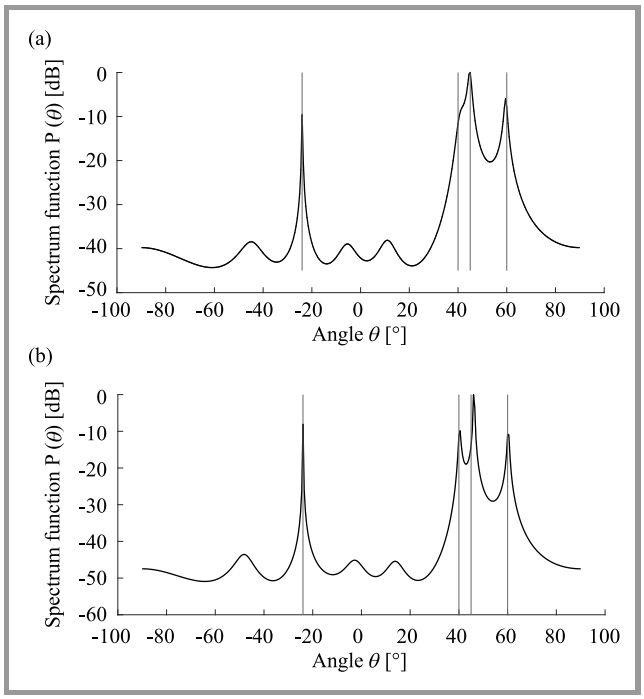

Fig. 7. Minimum norm spectrum: (a) before – 8 elements and (b) after – 9 elements.

It only needs 9 elements to give a good and clear resolution of the second and the third sources as illustrated in Fig. 7. We will see further the results found at other noise levels. The next spectrum is the propagator's one, it's represented in Fig. 8.

The propagator method requires 14 elements as a minimum to provide a clear resolution of the two close sources.

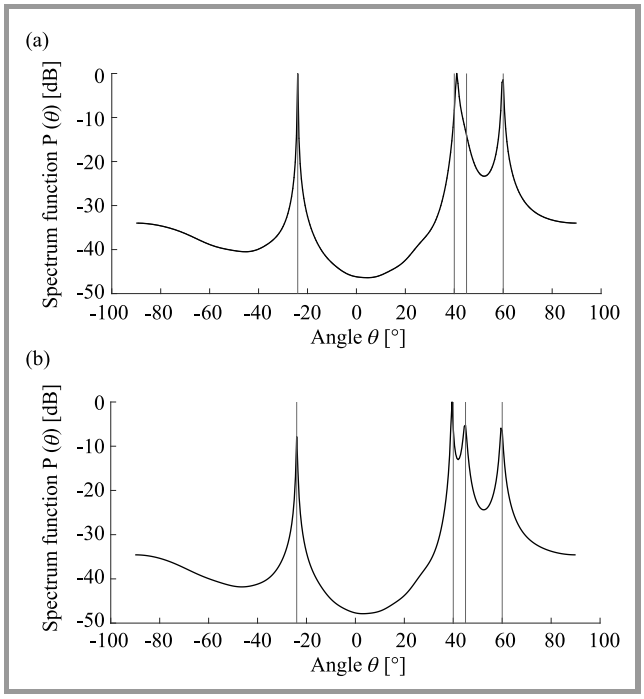

Fig. 8. Propagator spectrum: (a) before – 13 elements and (b) after – 14 elements.

Although the number of array elements required is higher than minimum norm and MUSIC, the big advantage of the propagator method is lower level of complexity compared with the eigen-decomposition-based methods [16].

We finally deal with the partial propagator method, its spectrum is illustrated in Fig. 9.

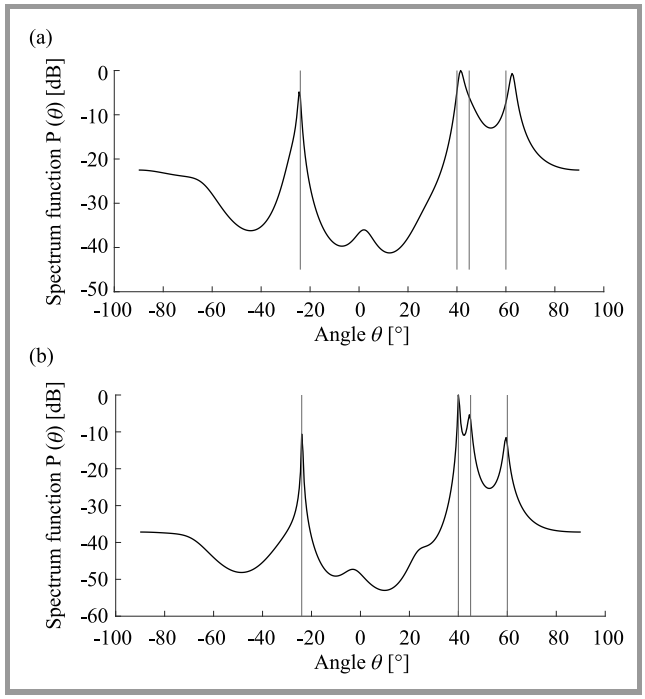

Fig. 9. Partial-propagator spectrum: (a) before – 10 elements and (b) after – 11 elements.

The partial propagator method needs at least 11 elements as a minimum to separate clearly the two close sources, which is also a good result of high resolution. In addition, the partial propagator performs well in the presence of a colored noise [14], and it also reduces the computational complexity compared to the propagator method.

We now discuss the resolution capability of these methods in four noise levels, namely $SNR_1 = -10$ dB, $SNR_2 = 0$ dB, $SNR_3 = 10$ dB, and $SNR_4 = 20$ dB.

Figure 10 illustrates the number of array elements needed for each method at the different noises levels, to resolve the two closely separated sources.

The first remark to be made here is that the Bartlett's spectrum is not influenced very much by the noise. Indeed, the minimum array elements remain stable for all the noise levels, and this can be explained by the fact that noise eigenvalues (the smallest ones) of the covariance matrix $\widehat{\mathbf{R}}_{\mathbf{xx}}$ do not have much influence in Eq. (7) because it's in the numerator of the equation, unlike the other methods which have the covariance matrix or some of its characteristics (like the noise subspace) in the denominator. As can be seen in Fig. 10, in noisy environments (low SNR), the minimum norm method performs better than all the others methods, by requiring fewer array elements for the resolution. On the other hand, one can see that in a high SNR environ-

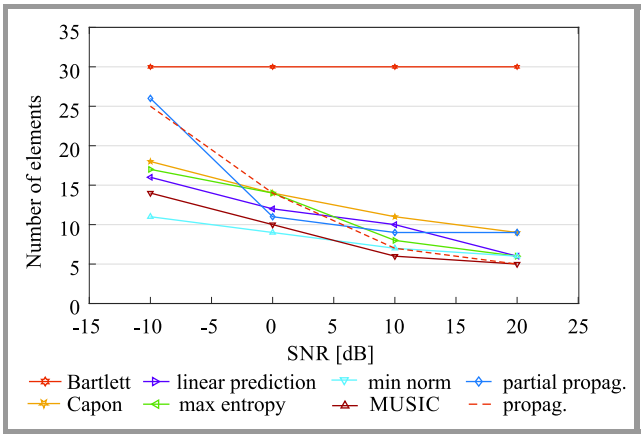

Fig. 10. Minimum elements needed for resolution in each SNR level.

ment, the MUSIC method is the best performing one. One can also note that in the noise-level SNR_4 the propagator requires the same number of elements as MUSIC.
However, an experimental verification of the proposed study in the research laboratory using physical materials is a direction for future work.

5. Conclusion

In this paper we have discussed the performance analysis related to the resolution capability of several DOA algorithms. The noise was assumed to be AWGN and the sources were narrowband and far-field impinging on a uniform linear array. The algorithms have been simulated under four different noise level environments. For each noise level, we have presented the performance of the resolution of the algorithms by searching the minimum array elements needed to separate two closely spaced sources. The results shown that in noisy environments, the minimum norm algorithm is the best performing one and requires fewer elements to separate the close sources. The minimum norm algorithm is more significant and in the same time the less sensitive to noise. Otherwise, in clean environments, MUSIC performs well and requires less array elements.

References

[1] Z. Chen, G. Gokeda, and Y. Yu, *Introduction to Direction-of-Arrival Estimation*. Boston: Artech House, 2010.

[2] H. Krim and M. Viberg, "Two decades of array signal processing research: The parametric approach", *IEEE Sig. Process. Mag.*, vol. 13, no. 4, pp. 67–94, 1996 (doi: 10.1109/79.526899).

[3] M. Frikel, S. Safi, and Y. Khmou, "Focusing operators and tracking moving wideband sources", *J. of Telecommun. and Inform. Technology*, no. 4, pp. 53–59, 2016.

[4] V. Krishnaveni, T. Kesavamurthy, and B. Aparna, "Beamforming for direction-of-arrival (DOA) estimation – A survey", *Int. J. of Comp. Appl.*, vol. 61, no. 11, 2013 (doi: 10.5120/9970-4758).

[5] B. Liao, Z.-G. Zhang, and S.-C. Chan, "DOA estimation and tracking of ULAs with mutual coupling", *IEEE Trans. on Aerospace and Elec. Syst.*, vol. 48, no. 1, pp. 891–905, 2012 (doi: 10.1109/TAES.2012.6129676).

[6] L. Badidi and L. Radouane, "A neural network approach for DOA estimation and tracking", in *Proc. of the 10th IEEE Worksh. on Statistical Sig. and Array Process.*, Pocono Manor, PA, USA, 2000, pp. 434–438 (doi: 10.1109/SSAP.2000.870161).

[7] M. S. Bartlett, "Periodogram analysis and continuous spectra", *Biometrika*, vol. 37, no. 1/2, pp. 1–16, 1950 (doi: 10.2307/2332141).

[8] J. Capon, "High-resolution frequency-wavenumber spectrum analysis", *Proc. of the IEEE*, vol. 57, no. 8, pp. 1408–1418, 1969 (doi: 10.1109/PROC.169.7278).

[9] J. Makhoul, "Linear prediction: A tutorial review", *Proc. of the IEEE*, vol. 63, no. 4, pp. 561–580, 1975 (doi: 10.1109/PROC.1975.9792).

[10] R. Schmidt, "Multiple emitter location and signal parameter estimation", *IEEE Trans. on Antennas and Propag.*, vol. 34, no. 3, pp. 276–280, 1986 (doi: 10.1109/TAP.1986.1143830).

[11] J. Xin and A. Sano, "Computationally efficient subspace-based method for direction-of-arrival estimation without eigendecomposition", *IEEE Trans. on Sig. Process.*, vol. 52, no. 4, pp. 876–893, 2004 (doi: 10.1109/TSP.2004.823469).

[12] S. Marcos, A. Marsal, and M. Benidir, "The propagator method for source bearing estimation", *Sig. Process.*, vol. 42, no. 2, pp. 121–138, 1995 (doi: 10.1016/0165-1684(94)00122-G).

[13] M. Frikel, "Localization of sources radiating on a large antenna", in *Proc. of the 13th Eur. Sig. Process. Conf. EUSIPCO 2005*, Antalya, Turkey, 2005, pp. 1–4.

[14] J. Chen, Y. Wu, H. Cao, and H. Wang, "Fast algorithm for DOA estimation with partial covariance matrix and without eigendecomposition", *J. of Sig. and Inform. Process.*, vol. 2, no. 4, pp. 266–269, 2011 (doi: 10.4236/jsip.2011.24037).

[15] H. Tang, "DOA estimation based on MUSIC algorithm", Bachelor thesis, Linneuniversitetet Kalmar, Vaxjo, Sweden, 2014.

[16] Y. Khmou, S. Safi, and M. Frikel, "Comparative study between several direction of arrival estimation methods", *J. of Telecommun. and Inform. Technol.*, no. 1, pp. 41–48, 2014.

[17] J. Foutz, A. Spanias, and M. K. Banavar, "Narrowband direction of arrival estimation for antenna arrays", *Synthesis Lect. on Antennas*, vol. 3, no. 1, pp. 1–76, 2008 (doi: 10.2200/S00118ED1V01Y200805ANT008).

[18] L. C. Godara, "Application of antenna arrays to mobile communications, Part II: Beam-forming and direction-of-arrival considerations", *Proc. of the IEEE*, vol. 85, no. 8, pp. 1195–1245, 1997 (doi: 10.1109/5.622504).

[19] S. Bourennane, C. Fossati, and J. Marot, "About noneigenvector source localization methods", *EURASIP J. on Adv. in Sig. Process.*, Article ID 480835, pp. 1–14, 2008 (doi: 10.1155/2008/480835).

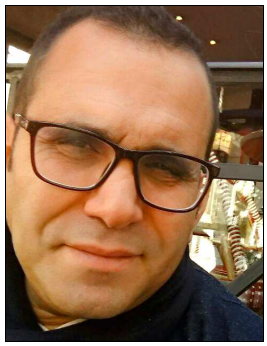

Miloud Frikel received his Ph.D. degree from the Center of Mathematics and Scientific Computation CNRS URA 2053, France, in array processing. Currently, he is with the GREYC laboratory (CNRS URA 6072) and the ENSI-CAEN as an Assistant Professor. From 1998 to 2003, he was with the Signal Processing Lab, Institute for Systems and Robotics, Institute Superior Tecnico, Lisbon, as a researcher in the field of wireless location and statistical array processing, after being a research engineer in a software company in Munich, Germany. He worked at the Institute for Circuit and Signal Processing of the Technical University of Munich. His research interests span several areas, including statistical signal and array

processing, cellular geolocation (wireless location), space time coding, direction finding and source localization, blind channel identification for wireless communication systems, and MC-CDMA systems.
E-mail: mfrikel@greyc.ensicaen.fr
GREYC UMR 6072 CNRS
Ecole Nationale Supérieure d'Ingénieurs
de Caen (ENSICAEN)
B. Maréchal Juin 6
14050 Caen, France

Ismail El Ouargui received a B.Sc. degree in Computer Science and an M.Sc. degree from the faculty of Science and Technics Beni Mellal, Morocco, in 2014 and 2016, respectively. He is currently working towards the Ph.D. degree in Computer Science and Signal Processing from Sultan Moulay Slimane University, Morocco. His research interests include statistical signal, array processing and sparse signal recovery techniques and their applications in source localization, wireless communications.
E-mail: ielouargui@gmail.com
Department of Mathematics and Informatics
Sultan Moulay Slimane University
Beni Mellal, Morocco

Said Safi received his B.Sc. degree in Physics (Electronics) from Cadi Ayyad University, Marrakech, Morocco in 1995, M.Sc. degree from Chouaib Doukkali University and Cadi Ayyad University, in 1997 and 2002, respectively. He served a Professor of information theory and telecommunication systems at the National School for applied Sciences, Tangier, Morocco, from 2003 to 2005. Since 2006, he has been a Professor of applied mathematics and programming at Polydisciplinary Faculty, Sultan Moulay Slimane University, Beni Mellal, Morocco. In 2008 he received a Ph.D. degree in Telecommunication and Informatics from the Cadi Ayyad University. In 2015 he received the degree of Professor in Sciences at Sultan Moulay Slimane University. His general interests span the areas of communications and signal processing, estimation, time-series analysis, and system identification subjects on which he has published 35 journal papers and more than 70 conference papers. Current research topics focus on transmitter and receiver diversity techniques for single- and multi-user fading communication channels, and wide-band wireless communication systems.
E-mail: safi.said@gmail.com
Department of Mathematics and Informatics
Sultan Moulay Slimane University
Beni Mellal, Morocco

Paper

Alarm Correlation in Mobile Telecommunications Networks based on *k*-means Cluster Analysis Method

Artur Maździarz

Systems Research Institute, Polish Academy of Science, Warsaw, Poland

https://doi.org/10.26636/jtit.2018.124518

Abstract— Event correlation and root cause analysis play a fundamental role in the process of troubleshooting all technical faults and malfunctions. An in-depth, complicated multiprotocol analysis can be greatly supported or even replaced by a troubleshooting methodology based on data analysis approaches. The mobile telecommunications domain has been experiencing rapid development recently. Introduction of new technologies and services, as well as multivendor environment distributed across the same geographical area create a lot of challenges in network operation routines. Maintenance tasks have been recently becoming more and more complicated, time consuming and require big data analyses to be performed. Most network maintenance activities are completed manually by experts using raw network management information available in the network management system via multiple applications and direct database queries. With these circumstances considered, identification of network failures is a very difficult, if not an impossible task. This explains why effective yet simple tools and methods providing network operators with carefully selected, essential information are needed. Hence, in this paper efficient approximated alarm correlation algorithm based on the *k*-means cluster analysis method is proposed.

Keywords— alarm correlation, alarm patterns, cluster analysis, mobile telecommunication network, root cause analysis.

1. Introduction

The history of mobile telecommunication started in the late 1970s, when analog telephony standards were introduced to cover basic voice calls. The entire family of these analog systems is referred to as 1G. In the 1990s, the digital age of mobile communication began along with the introduction of the so-called 2G technology. Technology development, driven by moving towards mobile data transfers with ever higher speeds, resulted in the introduction of 2.5G (GPRS), 3G and 4G/LTE standards. Currently, the telecommunication community is working on the development and introduction of the 5G standard, which is supposed to be ready for use by 2020 [1].

The generic diagram a mobile telecommunication network is presented in Fig. 1.

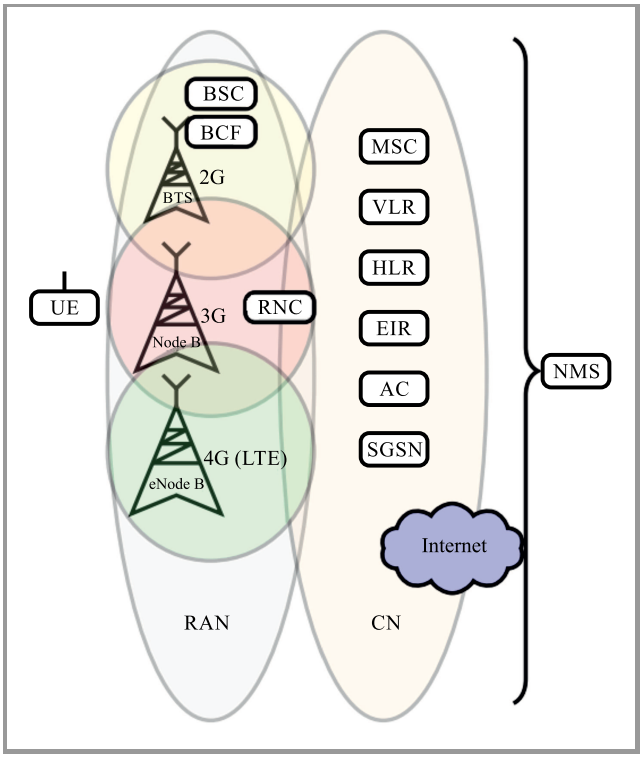

Fig. 1. Typical architecture of a mobile telecommunication network.

A mobile telecommunication network consists of two major functional subsystems: the radio access network (RAN) and the core network (CN).

RAN is responsible for managing radio resources, including strategies and algorithms for controlling power, channel allocation and data rate. It allows the user terminal equipment (UE) to access network services. The RAN consists of the following elements, depending on the technology used: 2G base station controller (BSC), 3G radio network controller (RNC), base station control function (BCF), 2G base transceiver station (BTS), 3G base transceiver station (NodeB), enhanced node B, 4G base transceiver station (eNodeB) and transceiver (TRX).

The CN is mainly responsible for high-level traffic aggregation, routing, call control/switching, user authentication

and charging. Some of the CN subsystems are: 2G, 3G mobile switching center (MSC), 2G, 3G visitor location register (VLR), 2G, 3G home location register (VLR), 2G, 3G authentication center (AC), 2G, 3G equipment identity register (EIR), 2G, 5G service GPRS support node (SGSN) [1]–[3].
The entire network is managed by the network management system, the so-called NMS, which provides several network management functionalities. One of the primary functions of the NMS is fault management. It is a term used in the network management domain, focusing on processes related to diagnosing and fixing network faults.
In the paper, we propose the approximated network faults diagnosing methodology based on the cluster analysis *k*-means algorithm.
The paper is organized as follows: In Section 2 we briefly introduce the Network Fault Management domain. Section 3 introduces novel alarm correlation methodology based on k-means clustering approach. Section 4 illustrates experiments and results achieved. Finally concluding remarks are given in Section 5.

2. Preliminaries and Problem Statement

The fault management domain of the network is characterized by a few definitions and notations that are central to this paper [4].

- **event** is an exceptional condition occurring in the operation of hardware or software within the network managed; an *instantaneous occurrence* at a time,
- **event correlation** is the process of establishing relationships between network events,
- **root causes**, are events that can cause other events but are not caused by other events; they are associated with an *abnormal state* of network infrastructure,
- **error** is a discrepancy between an observed or computed value or condition and a true value or condition, assumed to be correct,
- **failure** or **fault** is considered to be a kind of an error,
- **symptoms** are external manifestations of failures (errors) which are observed as alarms.

Fault diagnosis usually involves three processes: fault detection, fault localization (also known as fault isolation or root cause analysis) and testing the possible hypotheses [4].
Fault detection is the process of collecting information related to malfunctions of the network's components (network elements) in the form of alarms [4].
Fault localization or root cause analysis (RCA) is the process of identifying the causes of faults. It comprises several stages of correlating events (including alarms) which occurred over a certain period of time, and requires technical knowledge about the system analyzed [4], [5].
Alarm correlation is the process of grouping alarms which refer to the same problem, in order to highlight those which indicate the possible root cause [6].
The advantages of automating RCA and alarm correlation routines are numerous. By automating the troubleshooting process, we shorten the time needed for identifying a potential source of the problem, which impacts the duration of downtimes and quality of service (QoS) figures for the network in question. Short troubleshooting times bring benefits in the form of satisfying the terms of customers' service level agreements (SLAs). In addition, less skilled personnel can be involved in network operation tasks, thus reducing network maintenance costs [7].
There are several root cause analysis techniques described in the literature. We can divide them into three major categories: artificial intelligence techniques, model traversing and the so-called fault propagation model techniques [4]. All techniques are based either on predefined expert system knowledge, network static information or network dynamic information. The static knowledge comes from the topology and system structure. The dynamic network information is connected with the functional behavior of the network [4], [8], [9]. The methodology proposed in this paper helps discover relations between alarms generated by the network, thus contributing to analysis of static and dynamic network characteristics in the RCA process.
The amount of data to be analyzed and the limited analysis lead time pose a major challenge while troubleshooting faults in such a complex system like a telecommunication network. These two factors play a key role in fast problem resolution and minimize consequences for end users. The volume of troubleshooting data processed during propagation of faults in a large network can easily exceed several dozens of alarms per second. For those faults that impact the usability of the network by considerable amounts of end users, the resolution time is crucial and has a big financial impact on the service provider. To cope with the problem referred to above, the data correlation methodology should be characterized by fast processing, as well as by easy interpretation and reliable quantification of the results.
Medium size mobile telecommunication networks consist of several thousand of network elements, including RAN and CN subsystems. With all functional dependencies between network elements taken into consideration, the entire network is very complex. There are a lot of network elements, and each of them can potentially generate alarms. As per the fault management objective, network alarms collected by NMS should be correlated and the potential root cause of the problem should be identified within a short time. Analysis of alarm symptoms which leads to discovering the root cause of the problem is covered by the alarm correlation and root cause analysis processes. This paper focuses on the alarm correlation process which works on the alarm data sets. Each raw alarm data record contains several alarm attributes:

- **time of alarm**, this attribute contains the date and time with the precision of one second,

- **alarm number**, a unique number which identifies the fault. Usually the alarm numbers are divided into ranges representing a specific subsystem, network element type and alarm type,
- **alarm type** can be specified as communication, or for example equipment type,
- **alarm description** inside the alarm frame is a very short, compact description of the fault that usually contains a brief description (a few words) of what has happened,
- **alarm severity** specifies the importance of the fault and describes the alarm class. It can take one of the following logical values: critical, major, medium, minor or warning,
- **name of the object** is the object identification label which clearly identifies the network element which has generated the alarm event,

In the case of a fault of a specific network element, the alarm rate can reach several dozen alarms per second. Usually, failures related to one network element cause other network components to send relevant alarms as well. Additional troubleshooting difficulty in a complex system like a mobile telecommunication network stems from the number of network elements, as well as from their geographical distribution. In the attached example a set of BTSes connected to the BSC via BCFs is considered. The transmission problem related to the connection between the BSC and BCFs generates several alarms from BCFs and BTSes. The example shows how one problem triggers a string of alarms for all related network elements. If outage of critical network elements occurs, the network management system is flooded by large quantities of alarms. In these conditions, the operator has very limited time to diagnose what and where has happened. This is the reason behind the need to develop fast and simple methods to deal with big amount of symptom-describing data (alarms). It is worth mentioning that apart from the fast alarm correlation methodology, the additional goal is to work on reducing the amount of data (alarms) which are being analyzed. This is achieved by identifying repeatable alarm patterns which can be analyzed as one atomic entity to simplify the correlation process and to reduce amount of data to be processed.
In the following section a methodology is proposed which addresses most of the abovementioned challenges involving the correlation of alarms in mobile telecommunication networks.

3. Proposed Methodology Approach using Cluster Analysis in RCA

There are several RCA methods proposed in the literature which relate to the subject of correlating alarm symptoms. In general, the methods are complicated and difficult to be implemented in practice. Therefore, this approach to alarm correlation is fast and practical.
As mentioned in Section 2, each alarm has six major attributes: occurrence time, number, description, type, severity, name of the alarming object (network element). All attributes can be used in the RCA process. The most important alarm attribute, which plays a fundamental role in troubleshooting, is alarm occurrence time. It is the main factor used for alarm correlation in this proposal.
In the approach presented, the alarm correlation methodology focuses on discovering, within the alarm data set, those which occurred within a short period of time. Hence, in this paper we will use the cluster analysis domain, assuming alarm occurrence as the clustering attribute. Practice shows that alarms which represent causal sequences of events may be grouped into clusters with limited time intervals. The alarm clusters identified constitute an alarm correlation hypothesis, which should be further analyzed by domain experts. Apart from the correlation of alarms, the goal is to find the root cause of the sequence of clustered alarms. Practice shows that the first alarm in the cluster (based on the occurrence time) is usually the root cause. It may happen that multiple incidents occur within the same time interval. In such a case, it is always the expert's role to evaluate the alarm clusters and to validate the alarm correlation hypothesis proposed.
The nature of the alarm flow reflects certain physicality of the incident within the network. The alarms which are related are either collected at the same time or are generated by network elements with a certain delay. In practice, it has been observed that correlated alarms can occur within intervals of 1–2 s. In the light of the above, it is essential to establish a fast methodology for discovering, within alarm data sets, alarms clusters characterized by the difference between alarm occurrence of approximately 2 seconds. Hence, we define the correlation criterion as the interval between the occurrence of alarms within the cluster.
Figure 2 illustrates two alarm cluster examples. The first cluster includes three alarm events $\{e_1, e_2, e_3\}$ that occurred at the same time, the second cluster consists of three alarm events $\{e_4, e_5, e_6\}$ which occurred sequentially, with a one second delay.

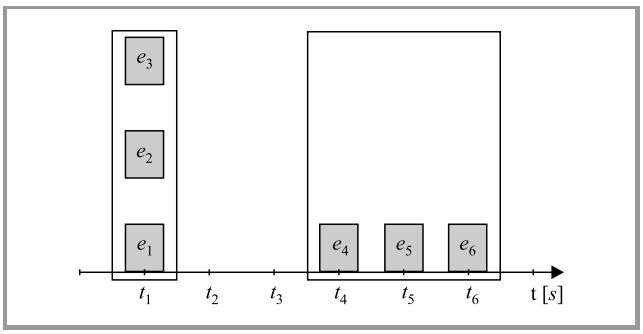

Fig. 2. Visualization of alarm correlation.

The cluster analysis domain offers techniques satisfying the objective of the method that consists in discovering clusters

of alarms. For the analysis, we selected the k-means clustering method for a filtered set of network elements known as a topology chain.

Each topology chain consists of network elements which share the same parent as the root of the topology. Typically, the roots are the main components of the network architecture and contain several child objects to perform the individual function. According to an alternative definition, the root object is the object which does not possess a parent, it is the first object in the hierarchy of a given type. An example of a topology chains is presented in Fig. 3.

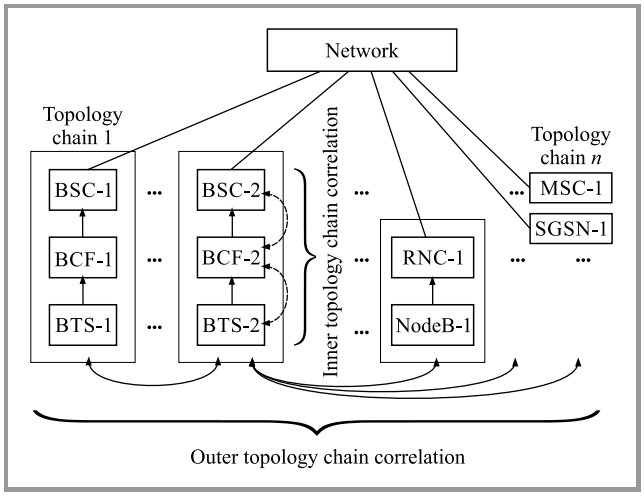

Fig. 3. Mobile telecommunication network topology and correlation view.

The term cluster analysis was used for the first time in 1954 in the context of analyzing anthropological data [10]. The k-means algorithm is recognized as the most important algorithm in the entire history of data mining [11], [12]. It represents the so-called combinatorial family of clustering algorithms. The cluster analysis, also known as classification without supervision, has two major characteristics. The clusters are unknown a priori and we do not dispose of the learning set. The goal of the analysis is to discover and group disjoint sets of data which are sharing similar characteristics (qualitative or quantitative features). In this type of analysis, the goal is to propose a data set split maximizing similarity features inside the sets and, at the same time, minimizing similarity between the disjoint sets. The same task can be translated into minimizing object dissimilarities inside the sets (clusters) and maximizing dissimilarities between sets. The cluster analysis process is based on the comparison of data set observations, resulting in generating groups of data which are more similar to each other within the group, than to objects from other groups (clusters). The popular methods of measuring dissimilarities, described in the literature concerned with cluster analysis, include the following: Euclidean distance, squared Euclidean distance, Minkowski distance, Mahalanobis distance, cosine distance and power distance [13]–[16]. In the approach presented, we analyze the time of occurrence of the alarms within the network, which is noted as: $X = \{x_1, \ldots, x_N\}$. The observations have labels assigned $i \in \{1, \ldots, N\}$. The squared Euclidean distance in the time domain is used as the correlation measure:

$$d(x_i, x_j) = \| x_i - x_j \|^2 . \tag{1}$$

The general principle of combinatorial clustering is based on the analysis of three characteristics: the total sum of dissimilarities between sample elements (T – total), the sum of dissimilarities between sample elements belonging to the same cluster (W – within), the sum of dissimilarities between sample elements belonging to different clusters (B – between).

The characteristics presented satisfy the following inquiry: $T = W + B$. For a given data set the value of T is constant and we target to minimize W or maximize B characteristics across all possible assignments of data set elements to the clusters [13], [16].

We denote dissimilarities between observations as $d(x_i, x_j)$ and we also define classificator $C(i)$, the function which based on the input maps the data to specific class, in our case the cluster. Classificator $C(i)$ returns cluster number ($k \in K$) for each observation i, j from the input data set.

Following the above notations, we can define W as [13], [16]:

$$W(C) = \frac{1}{2} \sum_{k=1}^{K} \sum_{C(i)=k} \sum_{C(j)=k} \| x_i - x_j \|^2 , \tag{2}$$

$$\overline{x}_k = \frac{1}{N_k} \sum_{C(j)=k} x_j , \tag{3}$$

$$W(C) = \sum_{k=1}^{K} N_k \sum_{C(i)=k} \| x_i - \overline{x}_k \|^2 , \tag{4}$$

where: $\overline{x}_k$ is the mean vector associated with k-th cluster denoted as m_k and it is called centroid for cluster k, and N_k is the number of elements in cluster k.

Inquiry (4) serves as a basis for an entire family of algorithms referred to as k-means method algorithms.

The idea behind the k-means algorithm can be specified as follows [13]:

1. Propose clusters distribution determining means (centroids) of the clusters $\{m_1, \ldots, m_k\}$.
2. Assign the observations to the closest cluster based on its distance to the centroid.
3. Update the centroids based on the observations values assigned to the clusters.
4. Repeat steps 1–3 until centroids do not change and the observations do not change their assignments.

The steps referred to above accomplish the following optimization task which can be seen as a variance minimization task [17]:

$$\min_{C, \{m_k\}_1^K} \sum_{k=1}^{K} N_k \sum_{C(i)=k} \| x_i - m_k \|^2 . \tag{5}$$

An important note for this method is that we have to specify the number of clusters K in advance, and that the number of clusters we predefine should be lower than the number of elements in the sample N ($K < N$) [13], [16].
In this paper we focus on practical applications of the *k*-means method. As the *k*-means method requires specifying the number of clusters for the analysis, we perform the analysis by iterating the number of clusters K from 1 up to the value of $\overline{K} < N$. The proposed correlation methodology is based on applying the *k*-means iterative algorithm to pre-filtered data sets which represent the so-called topology chains and can be described by the following inquiry:

$$\sum_{\substack{topology\\chain}} \left(\max_{K/c \leq 3} \left(\min_{C,\{m_k\}_1^K} \sum_{k=1}^{K} N_k \sum_{C(i)=k} \| x_i - m_k \|^2 \right) \right). \quad (6)$$

In the proposed approach, we introduced an additional parameter which is used as the clustering criterion. It is the average Euclidean squared distance between the observations in cluster c. The coefficient c is expressed by the relation of within-cluster sum of squared distances between the observations (the average squared distance between the observations within the cluster in the time domain) to the number of observations in the cluster (*cluster_size*):

$$c = \frac{average\_squared\_distance\_within\_cluster}{cluster\_size}.$$

From the alarm correlation point of view, the squared distance up to 3 s (distance of 1.73 s) is a reasonable value for general fault management in mobile telecommunication networks.
The alarm correlation methodology proposed in this paper can be summarized by the following steps:

1. Pre-processing – decomposing alarm data sets into smaller parts, following the root object filtering criteria (generation of topology chains),
2. Applying the *k*-means iterative algorithm, along with the time correlation criteria for each of the filtered topology chains from step 1 (this part requires multiple execution, due to *k*-means algorithm's stability issue),
3. Formulating the RCA hypothesis list based on results of step 2,
4. RCA analysis performed by domain experts.

In the experiment, we used the `R` package and the *k*-means function implemented in this environment. The *k*-means function in `R` offers several algorithms like Lloyd, Forgy, and MacQueen [18]–[22]. Lloyd's, MacQueen's and Forgey's (for continues cases) algorithms follow an intuitive, definition-based approach by repeatedly computing and assigning the observations to the closest center (centroid) [23]. By default, the `R` package uses the *k*-means algorithm implementation proposed by Hartigan and Wong.

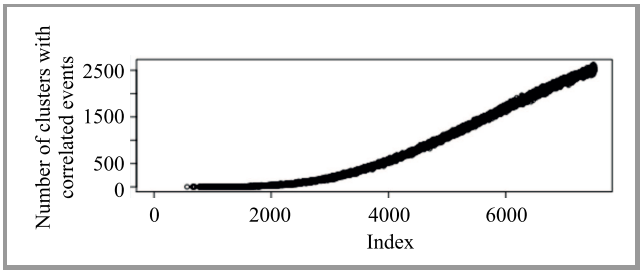

Fig. 4. Number of clusters satisfying the correlation objective, identified for the entire sample, with no topology filtering.

Experiments show that the number of clusters discovered by iterating the k-means method is growing non-linearly until we reach the K clusters split. It is illustrated by the results presented in Fig. 4. In addition, the processing of the algorithm is time consuming (computational complexity $O(n^3k)$, where n is the size of the data sample, k is the number of clusters) and results in a processing time of several hours for a data set containing several thousand alarms.
Due to above constraints and in consideration of the role of topology filtering in the RCA analysis, we have proposed an additional pre-processing step, which makes the methodology more efficient and acceptable from the point of view of the processing time.
The additional step consists in dividing the data set into subsets containing alarms belonging to one topology chain (following one topology root network element). The topology pre-filtering step introduces a very useful property of the *k*-means iterative methodology. It introduces a global maximum to the function between the number of clusters satisfying the correlation objective and the total number of clusters generated. This property, shown in Fig. 5, is observed for the first time and was not described in any paper in the past as per the author's knowledge.
This approach also addresses technical specificities of the correlation which shows that the majority of correlated events originate from the same topological chain. This type of correlation is called inner topology correlation. It is also possible to execute an outer topology correlation by com-

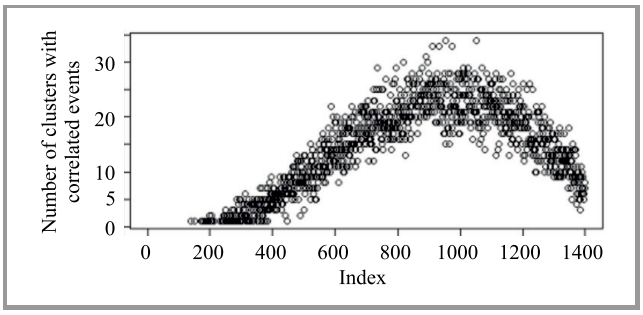

Fig. 5. Number of clusters satisfying the correlation objective (number of observations per split, where $c \leq 3$), as the function of the number of splits K for sample 1. The global maximum of 34 clusters satisfying the correlation objective was achieved for the value of 954 and 1051 total clusters generated for a sample containing 1400 alarms.

paring the centroids and alarms associated with them with inner topology correlation sets.

An example of the distribution of topology chains in a mobile telecommunication network is presented in Fig. 3. This methodology of correlation enables us to identify the method of partitioning the data set which maximizes the number of clusters for given correlation criteria, within a reasonable time. It is an optimal clustering solution which we seek for each data set, as we expand the maximum number of clusters for a given data set. The method can be used selectively for a chosen topology chain, or as the concatenation of several or all topology chains.

4. Results and Examples

The presented examples of partitioning performed on real alarm data samples are from a live mobile operator network. The data set which has been selected for simulations had 1440813 alarms divided into several sample sets. The data set which is analyzed in the example contains 7517 alarms. For the inner topology chain analysis we selected one BSC (BSC-1) which filters 1600 alarms belonging to that topology chain. The data originates from a heterogeneous, live mobile network containing 2G, 3G and 4G network elements, and was collected between July 2014 and May 2015. The data sample selected for analysis contains 28 BSCs and 27 RNCs.

As mentioned earlier, the *k*-means algorithm results depend on the initial conditions. This means that the starting centroids selected for the analysis, as well as the convergence process of each iteration result in a different number of clusters computed by the algorithm. Situations are also experienced where, for given number of clusters, the algorithm does not converge in within a specified limit of iterations or, where solutions are trapped in the local extremum. The above factors mean that each iteration run finishes with a different amount of detected clusters, as well as with a different amount of clusters matching the events correlation criteria specified: $\frac{average\_squared\_distance\_within\_cluster}{cluster\_size} \leq 3$.

Regardless of the specificities referred to above, the approximated iterated k-means algorithm proposed herein selects major clusters from the data set and the results are satisfactory. It can be seen that the main clusters, especially those with several events, are discovered by each iteration of the algorithm.

Figure 4 presents the algorithm's output for the entire data set containing 7517 alarms, without topological prefiltering. The test took 4 hours to perform in this case. We can see that iteration of the *k*-means algorithm for non-filtered data generates a number of clusters growing in a non-linear trend. Figure 5 presents output of the *k*-means iterative algorithm which was run on a pre-filtered data subset representing alarms belonging to the BSC-1 network element topology chain.

From the RCA perspective, each cluster which satisfies the correlation objective ($c \leq 3$) represents a cause of the first alarm or of several alarms from the cluster identified. The algorithm generates only a filtered correlation hypothesis, which has to be verified by an expert before assuming repairs of the network [5]. The experiments confirmed effectiveness of the methodology in question. In all clusters which satisfy the correlation criteria ($c \leq 3$), the troubleshooting hypothesis has been verified very quickly. It is worth mentioning that during the root cause hypothesis verification stage, topology is the factor that should always be taken into account. The proposed methodology takes into consideration topological aspects of the troubleshooting process by analyzing topology chain correlations. Thus, by default, we take into consideration the topological relation between the network elements generating alarms.

4.1. Alarm Inner Topology Correlation Example Discussion

For the example and discussion we selected one of 34 clusters identified by the *k*-means algorithm iterations with the centroid value of 82482.667 for inner topology correlations related to the BSC-1 topology chain. It represents one of

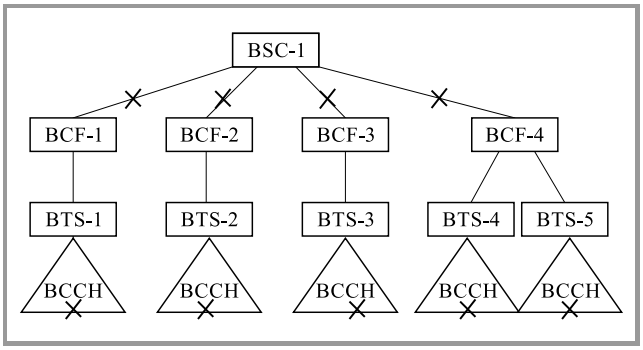

Fig. 6. Alarm correlation example.

Table 1
2G alarm correlation example

Time of event occurrence	Alarm type	Network element
82481	BTS O&M link failure	BSC-1/BCF-2
82481	BTS O&M link failure	BSC-1/BCF-4
82481	BTS O&M link failure	BSC-1/BCF-3
82481	BTS O&M link failure	BSC-1/BCF-1
82484	BCCH missing	BSC-1/BCF-4/BTS-4
82484	BCCH missing	BSC-1/BCF-4/BTS-5
82484	BCCH missing	BSC-1/BCF-1/BTS-1
82484	BCCH missing	BSC-1/BCF-3/BTS-3
82484	BCCH missing	BSC-1/BCF-2/BTS-2

the clusters for a global maximum split of 954 clusters for the data set sample. The fault illustration is presented in Fig. 6. Table 1 describes alarms used in the example. The transmission type of alarm in the network element (BCF) is causing problems with the radio broadcasting channel in another network element (BTS). The rectangle below the BTS shown in the picture symbolizes the radio network sector which is broadcast by the BTS. Inside the sector there is one radio channel component (BCCH), which plays a signaling role for the sector. The broadcast common channel (BCCH) is handling signaling communication in the sector and allows UE to log in to the network. Due to BCCH missing, there is no traffic in this sector. The problem is affecting all sectors.

5. Summary and Conclusions

In the experiment conducted, we have been analyzing several dozens of data samples with alarms from a real life mobile telecommunication network. The *k*-means iterative clustering methodology for data pre-filtered topology-wise is a very effective approach enabling to discover alarm correlation clusters (potential root cause analysis hypothesis). We have proposed an approximated alarm correlation algorithm which employs the *k*-means method for the topology chain data set by iterating the number of clusters from 0 up to K $(K < N)$. In the first stage, we propose to execute so-called inner topology chain correlation, which may be followed by an outer topology chain correlations analysis. The inner topology chain correlation iterations are characterized by reaching global maximums for the function of cluster numbers satisfying the correlation criteria:$(\frac{average\_squared\_distance\_within\_cluster}{cluster\_size} \leq 3)$ to the total number of clusters generated. This feature implies the possibility to limit the number of *k*-means function iterations to the value linked with the described maximum, which will additionally reduce the execution time. It has been observed that a vast majority of the correlated alarms originate from the inner topology chain correlation analysis, and that they play a fundamental role in selecting the event correlation hypothesis. The tests confirmed that the computation time of inner topology correlations is very reasonable in terms of practical alarm correlation. Partitioning operations for samples containing between 1200 and 2000 alarms took 10–15 s maximum.

In addition, from the overall RCA process perspective, the centroids identified indicate the moments in time which the troubleshooting engineer should pay special attention to. It has been also proven that data clustering significantly reduces the size and the quantity of the data analyzed, which makes the analysis process (network problem troubleshooting) much faster and more efficient. As far as final conclusions concerning the root cause of the faults are concerned, we need to consider other alarm attributes as well. These include: severity, number, description, type, network element type and name. There is one more practical conclusion related to the experiment. The correlation method can be used to create the so-called suppression alarm rules in the NMS. The suppression rules can be discovered after offline analysis of correlated alarms from the network and they reduce number of alarms being analyzed. For example, all alarms labeled as "BTS O&M link failure" and "BCCH missing" from the case presented in Fig. 6, identified within the same network element, can be suppressed by 1 alarm labeled "Traffic outage". This approach is similar to the pattern recognition concept, where patterns in data set analyzed are recognized and where predefined data subsets are used for further analysis and classification of data [24], [25].

References

[1] M. Lopa and J. Vora, "Evolution of mobile generation technology: 1G to 5G and review of upcoming wireless technology 5G", *Int. J. of Modern Trends in Engineer. and Research*, vol. 2, no. 10, pp. 281–290, 2015.

[2] K. Singh, S. Thakur, and S. Singh, "Comparison of 3G and LTE with other generation", *Int. J. of Comput. Applic.*, vol. 121. no. 6, pp. 42-47, 2015.

[3] A. Kumar, J. Sengupta, and Y. Liu, "3GPP LTE: the future of mobile broadband", *Wirel. Person. Commun.*, vol. 62, pp. 671–686, 2012 (doi: 10.1007/s11277-010-0088-3).

[4] M. Steinder and A. S. Sethi, "A survey of fault localization techniques in computer networks", *Science of Comput. Program.* vol. 53, pp. 165–194, 2004 (doi: 10.1016/j.scico.2014.01.010).

[5] S. K. Bhaumik, "Root cause analysis in engineering failures", *Transact. of the Ind. Instit. of Metals*, vol. 63, no. 2–3, pp. 297–299, 2010 (doi: 10.1007/s12666-010-0040-y).

[6] A. Bouillard, A. Junier, and B. Ronot "Alarms correlation in telecommunication networks", INRIA, pp. 17, 2013, [Online]. Available: https://hal.inria.fr/hal-00838969 (accessed on May 7, 2018).

[7] A. Samba, "A Network management framework for emerging telecommunications networks", in *Modeling and Simulation Tools for Emerging Telecommunication Networks. Needs, Trends, Challenges and Solutions*, A. N. Ince and E. Topuz, Eds. New York: Springer, 2006.

[8] P. Hong and P. Sen, "Incorporating non-deterministic reasoning in managing heterogeneous network faults", in *Proc. 2nd IFIP/IEEE Int. Symp. on Integrated Network Manag.*, Washington, DC, USA, 1991.

[9] M. T. Sutter and P. E. Zeldin, "Designing expert systems for real time diagnosis of self-correcting networks", *IEEE Network*, vol. 2, no. 5, pp. 43–51, 1998 (doi: 10.1109/65.17979) .

[10] A. Jain, "Data clustering: 50 years beyond k-means", *Pattern Recog. Let.*, vol. 31, no. 8, pp. 651–666, 2010 (doi: 10.1016/j.patrec.2009.09.011).

[11] H. Steinhaus, "Sur la division des corp materiels en parties", *Bullet. of the Polish Acad. of Sciences*, vol. 4, no. 12, pp. 801–804, 1956 [in French].

[12] X. Wu, *et. al.* "Top 10 algorithms in data mining", *Knowl. and Infor. Sys.*, vol. 14, no. 1, pp. 1–37, 2007 (doi: 10.1007/s10115-007-0114-2).

[13] T. Hastie, R. Tibshirani, and J. Friedman, *The Elements of Statistical Learning.* New York: Springer, Series in Statistics, 2001.

[14] S. T. Wierzchoń and M. A. Kłopotek, *Algorithms of Cluster Analysis*, Warsaw: Wyd. IPI PAN, 2015.

[15] A.-L. Jousselme and P. Maupin, "Distances in evidence theory: Comprehensive survey and generalizations", *Int. J. of Approx. Reason.*, vol. 53, no. 2 pp. 118–145, 2012 (doi: 10.1016/j.ijar.2011.07.00C).

[16] J. Koronacki and J. Ćwik, *Statystyczne systemy uczące się*. Warszawa: Exit, 2008 [in Polish].

[17] L. Morissette and S. Chariter, "The k-means clustering technique: General considerations and implementation in Mathematica", *Tutor. in Quantit. Methods for Psychol.*, vol. 9, no. 1, pp. 15–24, 2013 (doi: 10.20982/tqmp.09.1.p015).

[18] J. MacQueen, "Some methods for classifications and analysis of multivariate observations", in *Proc. of the Fifth Berkeley Symposium on Mathematical Statistics and Probability, Volume 1: Statistics*, L. M. Le Cam and J. Neyman, Eds. Berkeley, CA, USA: University of California Press, pp. 281–297, 1967.

[19] J. A. Hartigan and M. A. Wong, "Algorithm AS 136: A K-means clustering algorithm", *J. of the Royal Statis. Soc. Series C (Appl. Statistics)*, vol. 28, pp. 100–108, 1979, (doi: 10.2307/2346830).

[20] E. W. Forgy, "Cluster analysis of multivariate data: efficiency vs. interpretability of classifications", *Biometrics*, vol. 21, pp. 768–769, 1965.

[21] S. P. Lloyd, "Least squares quantization in PCM", *Transact. on Infor. Theory*, vol. 28, no. 2, pp. 128–137, 1982 (doi: 10.1109/TIT.1982.1056489).

[22] R documentation help of kmeans function [Online]. Available: https://www.rdocumentation.org/packages/stats/versions/3.5.0/topics/kmeans (accessed on May 7, 2018).

[23] M. Telgarsky and A. Vattani, "Hartigan's Method: k-means clustering without Voronoi", in *Proc. 13th Int. Conf. on Artif. Intel. and Statistics AISTATS*, Chia, Sardinia, Italy, 2010.

[24] G. H. Ball and D. J. Hall, *ISODATA: a novel method of data analysis and pattern classification*. Menlo Park, CA: Stanford Research Institute, 1965.

[25] *Pattern recognition*, A. Pinz, T. Pock, H. Bischof, and F. Leberl, Eds. New York: Springer, 2012 (doi: 10.1007/978-3-642-32717-9).

Artur Maździarz received his M.Sc. in Telecommunications Engineering from the Warsaw University of Technology, Faculty of Electronics and Information Technology, in 1999. Since 1999 he has been linked with the Nokia corporation, holding different engineering and management positions – all of them concerning Network Management Systems. Currently, he is a Ph.D. candidate at the Systems Research Institute of the Polish Academy of Science. His scientific research focuses on fault propagation models, event correlation and root cause analysis in mobile telecommunication networks.

E-mail: artur.mazdziarz@nokia.com
Systems Research Institute
Polish Academy of Science
Newelska 6
01-447 Warsaw, Poland

Information for Authors

Journal of Telecommunications and Information Technology **(JTIT)** is published quarterly. It comprises original contributions, dealing with a wide range of topics related to telecommunications and information technology. **All papers are subject to peer review**. Topics presented in the JTIT report primary and/or experimental research results, which advance the base of scientific and technological knowledge about telecommunications and information technology.

JTIT is dedicated to publishing research results which advance the level of current research or add to the understanding of problems related to modulation and signal design, wireless communications, optical communications and photonic systems, voice communications devices, image and signal processing, transmission systems, network architecture, coding and communication theory, as well as information technology.

Suitable research-related papers should hold the potential to advance the technological base of telecommunications and information technology. Tutorial and review papers are published only by invitation.

Manuscript. TEX and LATEX are preferable, standard Microsoft Word format (.doc) is acceptable. The authors JTIT LATEX style file is available:
http://www.nit.eu/for-authors

Papers published should contain up to 10 printed pages in LATEX authors style (Word processor one printed page corresponds approximately to 6000 characters).

The manuscript should include an abstract about 150200 words long and the relevant keywords. The abstract should contain statement of the problem, assumptions and methodology, results and conclusion or discussion on the importance of the results. Abstracts must not include mathematical expressions or bibliographic references.

Keywords should not repeat the title of the manuscript. About four keywords or phrases in alphabetical order should be used, separated by commas.

The original files accompanied with pdf file should be submitted by e-mail: redakcja@itl.waw.pl

Figures, tables and photographs. Original figures should be submitted. Drawings in Corel Draw and PostScript formats are preferred. Figure captions should be placed below the figures and can not be included as a part of the figure. Each figure should be submitted as a separated graphic file, in .cdr, .eps, .ps, .png or .tif format. Tables and figures should be numbered consecutively with Arabic numerals.

Each photograph with minimum 300 dpi resolution should be delivered in electronic formats (TIFF, JPG or PNG) as a separated file.

References. All references should be marked in the text by Arabic numerals in square brackets and listed at the end of the paper in order of their appearance in the text, including exclusively publications cited inside. Samples of correct formats for various types of references are presented below:

[1] Y. Namihira, Relationship between nonlinear effective area and mode field diameter for dispersion shifted fibres, *Electron. Lett*., vol. 30, no. 3, pp. 262264, 1994.

[2] C. Kittel, *Introduction to Solid State Physics*. New York: Wiley, 1986.

[3] S. Demri and E. Orłowska, Informational representability: Abstract models versus concrete models, in *Fuzzy Sets, Logics and Knowledge-Based Reasoning*, D. Dubois and H. Prade, Eds. Dordrecht: Kluwer, 1999, pp. 301314.

Biographies and photographs of authors. A brief professional authors biography of up to 200 words and a photo of each author should be included with the manuscript.

Galley proofs. Authors should return proofs as a list of corrections as soon as possible. In other cases, the article will be proof-read against manuscript by the editor and printed without the author's corrections. Remarks to the errata should be provided within one week after receiving the offprint.

A copy of the JTIT is provided to each author of paper published.

Journal of Telecommunications and Information Technology has entered into an electronic licencing relationship with EBSCO Publishing, the worlds most prolific aggregator of full text journals, magazines and other sources. The text of *Journal of Telecommunications and Information Technology* can be found on EBSCO Publishings databases. For more information on EBSCO Publishing, please visit www.epnet.com.

(*Contents Continued from Front Cover*)

INSTYTUT ŁĄCZNOŚCI
PAŃSTWOWY INSTYTUT BADAWCZY

Editorial Office

National Institute
of Telecommunications
Szachowa st 1
04-894 Warsaw, Poland

tel. +48 22 512 81 83
fax: +48 22 512 84 00
e-mail: redakcja@itl.waw.pl
http://www.nit.eu

JOURNAL OF TELECOMMUNICATIONS AND INFORMATION TECHNOLOGY 2/2013